



HAL
open science

Synthèse guidée par des précurseurs de nanomatériaux à conversion ascendante pour la photocatalyse dans le proche infrarouge

Bhagyesh Purohit

► **To cite this version:**

Bhagyesh Purohit. Synthèse guidée par des précurseurs de nanomatériaux à conversion ascendante pour la photocatalyse dans le proche infrarouge. Catalysis. Université de Lyon, 2021. English. NNT : 2021LYSE1049 . tel-03593408

HAL Id: tel-03593408

<https://theses.hal.science/tel-03593408>

Submitted on 2 Mar 2022

HAL is a multi-disciplinary open access archive for the deposit and dissemination of scientific research documents, whether they are published or not. The documents may come from teaching and research institutions in France or abroad, or from public or private research centers.

L'archive ouverte pluridisciplinaire **HAL**, est destinée au dépôt et à la diffusion de documents scientifiques de niveau recherche, publiés ou non, émanant des établissements d'enseignement et de recherche français ou étrangers, des laboratoires publics ou privés.



N°d'ordre NNT: 2021LYSE1049

THESE de DOCTORAT DE L'UNIVERSITE DE LYON

opérée au sein de
l'Université Claude Bernard Lyon 1

Ecole Doctorale N° 52
Ecole Doctorale de Physique et Astrophysique

Spécialité de doctorat : Physique

Soutenue publiquement le 15/03/2021, par:

Bhagyesh PUROHIT

Precursors-guided synthesis of upconverting nanomaterials for near-infrared driven photocatalysis

Devant le jury composé de:

M. GOLDNER Phillippe, DR-CNRS, ChimieParisTech - PSL	Rapporteur
Mme. HEMMER Eva, Assistant Professor, Université de Ottawa	Rapporteur
Mme. DANTELLE Géraldine, CR-CNRS, Université Grenoble Alpes	Examinatrice
M. PAROLA Stéphane, Professeur, Université de Lyon	Examineur
M. LEDOUX Gilles, DR-CNRS, Université de Lyon	Directeur de thèse
M. MISHRA Shashank, Maître de Conférences, HDR, Université de Lyon	Co-directeur de thèse
Mme. BLANCHARD Juliette, CR-CNRS, Université Pierre et Marie Curie	Invitée

Université Claude Bernard –Lyon 1

Administrateur provisoire de l'Université	M. Frédéric FLEURY
Président du Conseil Académique	M. Hamda BEN HADID
Vice-Président du Conseil d'Administration	M. Didier REVEL
Vice-Président du Conseil des Etudes et de la Vie Universitaire	M. Philippe CHEVALLIER
Vice-Président de la Commission de Recherche	M. Jean-François MORNEX
Directeur Général des Services	M. Pierre ROLLAND

Composantes santé

Département de Formation et Centre de Recherche en Biologie Humaine	Directrice : Mme Anne-Marie SCHOTT
Faculté d'Odontologie	Doyenne : Mme Dominique SEUX
Faculté de Médecine et Maïeutique Lyon Sud - Charles Mérieux	Doyenne : Mme Carole BURILLON
Faculté de Médecine Lyon-Est	Doyen : M. Gilles RODE
Institut des Sciences et Techniques de la Réadaptation (ISTR)	Directeur : M. Xavier PERROT
Institut des Sciences Pharmaceutiques et Biologiques (ISBP)	Directrice : Mme Christine VINCIGUERRA

Composantes & départements de sciences & technologie

Département Génie Electrique et des Procédés (GEP)	Directrice : Mme Rosaria FERRIGNO
Département Informatique	Directeur : M. Behzad SHARIAT
Département Mécanique	Directeur M. Marc BUFFAT
Ecole Supérieure de Chimie, Physique, Electronique (CPE Lyon)	Directeur : Gérard PIGNAULT
Institut de Science Financière et d'Assurances (ISFA)	Directeur : M. Nicolas LEBOISNE
Institut National du Professorat et de l'Education	Administrateur Provisoire : M. Pierre CHAREYRON
Institut Universitaire de Technologie de Lyon 1	Directeur : M. Christophe VITON
Observatoire de Lyon	Directrice : Mme Isabelle DANIEL
Polytechnique Lyon	Directeur : Emmanuel PERRIN
UFR Biosciences	Administratrice provisoire : Mme Kathrin GIESELER
UFR des Sciences et Techniques des Activités Physiques et Sportives (STAPS)	Directeur : M. Yannick VANPOULLE
UFR Faculté des Sciences	Directeur : M. Bruno ANDRIOLETTI

*To my parents
and the whole family
for their constant support and belief in me*

*Comparison with myself brings improvement, comparison with
others brings discontent*

*If not now, then when? and
If not us, then who?*

*You cannot get more than what you deserve and before you
deserve.*

Acknowledgements

First of all, I would like to thank my supervisors, **Dr Gilles Ledoux** and **Dr Shashank Mishra** for providing me with the opportunity to work on this interesting project. It was a big learning experience for me not only concerning science but also about the management of time and resources. Also, I am thankful to you for being patient while answering some very basic and silly doubts. I learned a lot from both of you, especially how not to waste time and to be dedicated to your work. The inspiration and encouragement that you both provided during all stages of my thesis were very crucial and much needed. I thank you both also for providing me with an opportunity to attend so many conferences and for the opportunity to visit the University of Oslo for a month.

The constant support and motivation from my parents, sister and the whole family gave me inspiration and reasons to believe in myself. Not only regarding this thesis but whatever I became is all because of your support and guidance.

My greatest of thanks also goes to **Benoit, Christophe, David and Yannick** for helping me out in many calculations, TEM analyses and discussions. Also, I am grateful to **Nicholas** for teaching me TEM and answering so many naive questions anytime I asked. I would also like to thank **Thibaut** for giving me time to help me out in many scientific manipulations. I thank **Per-Anders** also for being a great mentor and teaching me ALD from the very basics.

Furthermore, I thank all my colleagues at ILM and IRCELYON: especially **Sweta**, for your teaching, motivation, scientific discussions, support and proofreading of the thesis. You taught me how to use many instruments right from the start of my thesis, I hope we meet again somewhere in our future academic or professional career path.

Lama, thanks for motivating me always to be chilled out even in the ultra stressful times; **Ashkan**, thank you for being a great colleague and friend and I am grateful to you to listen to all the sad, bad and good stories from me; **Amira**, thank you a lot for always being supportive and no matter how busy you were, you always helped me out; **Lionel**, thank you for all the troubles I gave you during these two years and bearing the 'good french' that I spoke all the times in the office. **Shefali**, thank you for answering all the basic chemistry doubts I had and supporting me throughout your stay at IRCELYON; **Akash**, thank you for always being one call away whenever I needed you; **Austin and Mariana**, I thank you for being excellent officemates and also for bringing the office 14-021 back from dead (I was all alone there for a long time ;P).

Clara, we have become great friends during your stay in Lyon and I will always carry the memories with me. A lot of thanks also to **Bridge, Meryem, Maria** for making the stressful time of my thesis writing less worrying. I will thank **Iama** again for being the starting point of our friendship.

I would also like to thank **Sonu** for always supporting me in all the low and high times throughout this thesis. I really admire your simplicity and supportive nature and I thank you for being a genuine friend. I would also like to thank **Rahul, Vardan, Shantanu** and **Nitin** for the weekend talks during all this time.

Finally, I would like to thank **Lucie, Sarah, Miguel, Dolores, Ahmad, Saly, Roua, Oleksandra, An, Alex, Diane, Sameh, Christopher** and all C'Durable, IRCELYON members; **Max, Mathilde, Arsene, Gaetan, Hoshang, Zhu, Tomas** and all Luminescence, iLM members

Contents

List of Figures.....	v
List of tables	xiii
List of Schemes.....	xv
Abstract	xvii
Résumé.....	xix
General Introduction.....	1
References.....	5
Chapter 1 Literature review	9
1.1. Solar photocatalysis.....	9
1.2. TiO ₂ as a robust photocatalyst and its limitations.....	10
1.3. Upconversion as a solution	13
a). Upconversion in detail.....	14
1.4. References.....	25
Chapter 2 Synthesis and upconversion studies of NaGdF ₄ :Yb ³⁺ , Tm ³⁺ nanoparticles: A comparison of anhydrous versus hydrous synthesis.....	33
2.1. Introduction.....	33
2.2. Results and discussion.....	34
2.2.1. Anhydrous synthesis of NaGdF ₄ : Yb ³⁺ , Tm ³⁺ nanoparticles from thermal decomposition of designed precursors [NaLn(TFA) ₄ (diglyme)] (Ln = Gd, Tm, Yb): influence of solvents and dopant percentage on the crystal phase of up-converting NPs	34
2.2.2. Hydrous synthesis of NaGdF ₄ : Yb ³⁺ , Tm ³⁺ NPs from the co-precipitation reaction of hydrated inorganic salts at room temperature.....	42
2.2.3. Comparative upconversion studies	47
2.3. Conclusions and perspectives	53
2.4. References.....	54
Chapter 3 Precursor-guided synthesis of LiYF ₄ :Yb ³⁺ , Tm ³⁺ nanoparticles having comparable efficiency with single crystals	63
3.1. Introduction.....	63
3.2. Results and discussion.....	64
3.2.1. Synthesis and characterization of novel anhydrous molecular precursors	64
3.2.2. Synthesis of undoped and Yb ³⁺ , Tm ³⁺ co-doped LiYF ₄ nanoparticles from the thermal decomposition of anhydrous precursors	72
3.2.3. Comparative upconversion study of LiYF ₄ :Yb ³⁺ , Tm ³⁺ nanoparticles and bulk single crystals	96
3.3. Conclusions and perspectives	100

3.4. References.....	101
Chapter 4 Synergistic UV upconversion mechanism in LiYF ₄ : Yb ³⁺ , Tm ³⁺ nanocrystals (Dual Laser Excitation/ Excited-state absorption spectroscopic studies and sun-like excitation).....	107
4.1. Introduction.....	107
4.2. Results and discussion.....	108
4.2.1. Synthesis and characterization (structural and morphological) of upconverting nanoparticles.....	108
4.2.2. Experimental setup	110
4.2.3. Upconversion studies	111
4.2.4. Excited-state excitation spectroscopic studies	112
4.3. Conclusions and perspectives	123
4.4. References.....	124
Chapter 5 TiO ₂ -LiYF ₄ :Yb ³⁺ , Tm ³⁺ nanocomposites for near-IR driven photocatalysis.....	127
5.1. Introduction.....	127
5.2. Results and discussion.....	128
5.2.1. Synthesis of UCNPs-TiO ₂ nanocomposites	128
5.2.2. Upconversion studies	138
5.2.3. Photocatalytic studies	140
5.3. Conclusions and perspectives	143
5.4. References.....	144
Chapter 6 Experimental.....	149
6.1. Chemicals and general instrumentation procedures	149
6.2. Experimental setup	151
6.2.1. Upconversion measurements	151
6.2.2. Photocatalysis setup.....	152
6.3. Synthesis of anhydrous precursors	152
6.3.1. Method A.....	153
6.3.2. Method B for the synthesis of (3)-(6)	154
6.4. Synthesis of sodium-based UCNPs	155
6.4.1. Using anhydrous precursors.....	155
6.4.2. Using hydrous precursors.....	156
6.5. Synthesis of lithium-based UCNPs.....	157
6.5.1. Synthesis of Yb ³⁺ , Tm ³⁺ doped LiYF ₄ matrices with different synthesis conditions	158
6.6. Synthesis of UCNPs-TiO ₂ nanocomposites	161
6.6.1. Oleic acid-modified TiO ₂ @UCNPs nanocomposites.....	161

6.6.2. Aminoalcohols modified TiO ₂ @UCNPs nanocomposites	161
6.6.3. UCNPs embedded TiO ₂ metallogels	162
6.7. References	163
Chapter 7: Conclusions and perspectives.....	165
7.1. Conclusions.....	165
7.2. Perspectives.....	166
7.2.1. Optimization of energy transfer between UCNPs and TiO ₂ for efficient photocatalysis ..	166
7.2.2. Photocatalytic experiments under direct sunlight	169
7.3. References.....	171
Appendix A: Research output related to this thesis.....	173
A1. Publications	173
A2. Oral Presentations.....	173
A3. Poster presentation.....	174
A4. Awards and Grants.....	174

List of Figures

Figure 0.1: The absorption and emission range of three types of upconversion materials concerning AM 1.5 spectrum (QN-UC (purple): upconversion in quantum nanostructures; TTA-UC (purple): triplet-triplet annihilation upconversion; RED-UC (green): rare-earth-doped upconversion materials). ⁷	3
Figure 1.1: Schematic diagram of the photocatalytic reaction ⁶	10
Figure 1.2: Solar spectrum showing the useful share of photons for TiO ₂ based photocatalysis.....	11
Figure 1.3: Working principle of triplet-triplet annihilation upconversion (TTA-UC). ²³	14
Figure 1.4: Energy level diagram for codoped Tm ³⁺ and Yb ³⁺ system; adapted from Dulick et al. (Journal of Luminescence 1991 , 48–49, 517–521) and Bensalah et al. (Optical Materials 2004 , 26 (4), 375–383).....	18
Figure 2.1: Powder XRD of NaGdF ₄ : Yb ³⁺ , Tm ³⁺ NPs obtained from the thermal decomposition of SSPs in a 1:1 mixture of ODE + OA (a).	36
Figure 2.2: Powder XRD of NaGdF ₄ : Yb ³⁺ , Tm ³⁺ NPs obtained from the thermal decomposition of SSPs in a 1:1 mixture of ODE + OM (b).	36
Figure 2.3: Conversion of as-prepared mixed-phase NaGd _{5/6} Yb _{1/6} F ₄ : 0.8% Tm ³⁺ NPs (13% α + 87% β) to pure β -phase after calcination at 350 °C.	38
Figure 2.4: FT-IR spectra of NaGd _{5/6} Yb _{1/6} F ₄ : 0.8% Tm ³⁺ NPs obtained from a) thermal decomposition of the single-source precursors [NaLn(TFA) ₄ (diglyme)] (Ln = Gd, Yb, Tm) at 290 °C in a 1:1 mixture of 1-octadecene + oleylamine.	38
Figure 2.5: TEM, HR-TEM and associated FFT of the NaGd _{5/6} Yb _{1/6} F ₄ : 0.8% Tm ³⁺ NPs obtained from the thermal decomposition of the single source precursors (SSP) [NaLn(TFA) ₄ (diglyme)] (Ln = Gd, Yb, Tm) at 290°C in a 1:1 mixture of 1-octadecene + oleylamine. The HR-TEM image in (c) shows an interreticular spacing of 0.302 nm related to the β -phase, whereas the FFT of the second particle in (d) corresponds to the diffraction pattern of a cubic crystal structure (α -phase) in the zone axis [01-1] (e). Size distribution of these nanoparticles (f).	40
Figure 2.6: TEM (a), HRTEM (b) FFT analysis (c) and EDX analysis (d) of NaGd _{5/6} Yb _{1/6} F ₄ : 0.8% Tm ³⁺ NPs obtained from high temperature decomposition of NaLn(TFA) ₄ (diglyme) (Ln = Gd, Tm, Yb) in the mixture of 1-octadecene and oleylamine. The crystal structure corresponds to cubic NaGdF ₄ (ICDD file # 04-019-0931).	41
Figure 2.7: TEM (a, b), HRTEM (c) and corresponding FFT analysis (d, e) of NaGd _{2/3} Yb _{1/3} F ₄ : 1% Tm ³⁺ NPs obtained from the high temperature decomposition of NaLn(TFA) ₄ (diglyme) (Ln = Gd, Tm, Yb) in	

the mixture of 1- octadecene and oleic acid. The crystal structure corresponds to cubic NaGdF ₄ (ICDD file # 04-019-0931).	42
Figure 2.8: Powder XRD of NaGdF ₄ : Yb ³⁺ , Tm ³⁺ NPs obtained from co-precipitation reaction of hydrated inorganic salts at room temperature.....	43
Figure 2.9: TEM images of NaGd _{5/6} Yb _{1/6} F ₄ : 1.2% Tm ³⁺ (a) and NaGd _{5/6} Yb _{1/6} F ₄ : 0.8% Tm ³⁺ (b) NPs obtained from room temperature co-precipitation using hydrated inorganic salts Ln(NO ₃) ₃ ·xH ₂ O (Ln = Gd, Tm, Yb), NaNO ₃ and NH ₄ F in ethylene glycol. HR-TEM (c) and associated FFT analysis (d) of β-NaGd _{5/6} Yb _{1/6} F ₄ : 0.8% Tm ³⁺ NPs. The FFT corresponds to the diffraction pattern of a hexagonal crystal structure (β-phase) in the zone axis [001] (e)	44
Figure 2.10: TEM images of NaGd _{2/3} Yb _{1/3} F ₄ : 0.3% Tm ³⁺ (a) and NaGd _{5/6} Yb _{1/6} F ₄ : 1.2% Tm ³⁺ (b) NPs obtained from room temperature co-precipitation using hydrated inorganic salts Ln(NO ₃) ₃ ·xH ₂ O (Ln = Gd, Tm, Yb), NaNO ₃ and NH ₄ F in ethylene glycol.....	45
Figure 2.11: Size distribution curves along with the length (a) and width (b) of NaGd _{5/6} Yb _{1/6} F ₄ : 1.2% Tm ³⁺ nanorods obtained from room temperature co-precipitation using hydrated inorganic salts Ln(NO ₃) ₃ ·5H ₂ O (Ln = Gd, Tm, Yb), NaNO ₃ and NH ₄ F in ethylene glycol.....	45
Figure 2.12: FT-IR spectrum of NaGd _{5/6} Yb _{1/6} F ₄ : 0.8% Tm ³⁺ nanorods obtained from room temperature co-precipitation using hydrated inorganic salts Ln(NO ₃) ₃ ·5H ₂ O (Ln = Gd, Tm, Yb), NaNO ₃ and NH ₄ F in ethylene glycol.	46
Figure 2.13: Thermogravimetric analysis (TGA) and derivative thermogravimetry (DTG) analysis of NaGd _{5/6} Yb _{1/6} F ₄ : 0.4%Tm ³⁺ NPs obtained from the room temperature co-precipitation using hydrated inorganic salts Ln(NO ₃) ₃ ·5H ₂ O (Ln = Gd, Tm, Yb), NaNO ₃ and NH ₄ F in ethylene glycol.	46
Figure 2.14: Up-conversion studies ($\lambda_{exc} = 972$ nm CW Laser, and slit width = 0.5 mm for entry and exit) of NaGdF ₄ : Yb ³⁺ , Tm ³⁺ NPs obtained from the thermal decomposition method.	48
Figure 2.15: Upconversion emission spectra for NaGdF ₄ : Yb ³⁺ , Tm ³⁺ _hyd synthesized using hydrated inorganic salts Ln(NO ₃) ₃ ·5H ₂ O (Ln = Gd, Tm, Yb) with 972 nm CW laser excitation (slit width = 2 mm for both entry and exit), showing classical Tm ³⁺ emission for samples with different ratio of sensitizers and activators.	48
Figure 2.16: Up-conversion studies comparing the emission intensity of NaGd _{5/6} Yb _{1/6} F ₄ : 0.8% Tm ³⁺ _anhyd and NaGd _{5/6} Yb _{1/6} F ₄ : 0.8% Tm ³⁺ _hyd samples.	50
Figure 3.1: (a) Perspective view of [Li(TFA)(THF)] _∞ (2) with displacement ellipsoids drawn at the 30% probability level. (b) One-dimensional structure of 2. H-atoms on the THF ligand have been omitted for clarity. Symmetry codes: (i) 2-x, 1-y, -z; (ii) 2+x, -1+y, z;	67

Figure 3.2: (a) Perspective view of [Gd(TFA) ₃ (monoglyme)] (4) with displacement ellipsoids drawn at the 50% probability level. (b) One-dimensional structure of 4 . H-atoms on monoglyme ligand have been omitted for clarity. Atom colour scheme same as shown in Figure 3.1.....	68
Figure 3.3: (a) Perspective view of [Yb(TFA) ₃ (monoglyme)] (6) with displacement ellipsoids drawn at the 50% probability level. (b) One-dimensional structure of 6 . H-atoms on monoglyme ligand have been omitted for clarity.	69
Figure 3.4: FT-IR spectra of 1-6	71
Figure 3.5: TGA (a) and DTG (b) curves of anhydrous monoglyme complex of metal trifluoroacetate.	72
Figure 3.6: TGA (a) and DTG (b) curves of hydrated trifluoroacetate of lithium and yttrium.	72
Figure 3.7: powder x-ray diffraction pattern of undoped LiLnF ₄ (Ln = Y (a), Yb (c)) prepared by thermal decomposition of anhydrous molecular precursors in 1:1 ratio of ODE and OA. The synthesis using the Gd precursors yielded in the mixture of GdF ₃ and LiF (b) instead of LiGdF ₄ . The ticks below the plot indicate the respective positions of the reflection for that particular phase.....	74
Figure 3.8: Transmission electron microscopy images of a) undoped LiYF ₄ and b) undoped LiYbF ₄ prepared by thermal decomposition of anhydrous molecular precursors.....	74
Figure 3.9: Rietveld refinement performed on X-ray diffraction pattern of a series of doped LiYF ₄ with fixed ratio of sensitizer (Yb ³⁺) but different ratio of activators (Tm ³⁺) (Yb = ~20%; Tm = 0.4%, 0.8%, 1.2%. The ticks below the plot indicate the respective positions of the reflection for that particular phase.	76
Figure 3.10: Transmission electron microscopy images of LiY _{5/6} Yb _{1/6} F ₄ : 0.4% Tm ³⁺ (a), LiY _{5/6} Yb _{1/6} F ₄ : 1.2% Tm ³⁺ (b) and LiY _{5/6} Yb _{1/6} F ₄ : 0.8% Tm ³⁺ (c).....	77
Figure 3.11: Difference in the upconversion emission intensities of the samples prepared with a different doping concentration of activator ions (Tm ³⁺) while keeping sensitizer (Yb ³⁺) at a fixed concentration. These spectra were measured from dry powder under similar excitation condition for all the samples.....	78
Figure 3.12: TGA and DTG curves of LiYF ₄ doped with 20% Yb ³⁺ and 0.4% Tm ³⁺	79
Figure 3.13: Temperature-dependent upconversion response of LiY _{5/6} Yb _{1/6} F ₄ : 0.4% Tm ³⁺	80
Figure 3.14: Rietveld refinement performed on X-ray diffraction pattern of three different samples prepared using different ratios of ODE and OA. The ticks below the plot indicate the respective positions of the reflection for that particular phase.	81
Figure 3.15: Transmission electron microscopy images of different LiY _{5/6} Yb _{1/6} F ₄ : 0.4% Tm ³⁺ samples prepared by varying the ratio of ODE to OA as a) 1:3, b) 3:1, and c) 1:1	83

Figure 3.16: Difference in the upconversion emission intensities of the samples prepared using three different ratios of solvents (ODE and OA). These spectra were measured from dry powder in the same excitation condition for all three samples.	84
Figure 3.17: Rietveld refinement performed on X-ray diffraction pattern of three different samples prepared by taking different concentrations of precursors. The ticks below the plot indicate the respective positions of the reflection for that particular phase	85
Figure 3.18: Transmission electron microscopy images of different $\text{LiY}_{5/6}\text{Yb}_{1/6}\text{F}_4$: 0.4% Tm^{3+} samples prepared by varying the concentration of precursors and their size distribution. a) 0.520 mmol/ml; b) 0.175 mmol/ml.....	86
Figure 3.19: Difference in the upconversion emission intensities of the samples prepared using different concentration of precursors. These spectra were measured from dry powder in the same excitation condition for all three samples.....	87
Figure 3.20: Rietveld refinement of powder X-ray diffraction pattern of different samples prepared by decomposition of anhydrous precursors at varied temperatures (from 270°C - 315°C). These peaks have been indexed with tetragonal LiYF_4 and orthorhombic YF_3	88
Figure 3.21: Williamson-Hall (W-H) plot derived from powder X-ray diffraction data of different samples prepared by decomposition of anhydrous precursors at varied temperatures (from 270 °C – 315 °C). The sample decomposed at 295 °C has negative strain (compression) whereas other samples have positive values of strain (tensile strain).....	89
Figure 3.22: Unit cell, bond length and bond angle values for the crystal structure of different samples decomposed at different temperature (270 °C-315 °C).....	90
Figure 3.23: Powder diffraction pattern showing a shift in the peak position for one sample decomposed at 295 °C.	90
Figure 3.24: Transmission electron microscopy images of $\text{LiY}_{5/6}\text{Yb}_{1/6}\text{F}_4$: 0.4% Tm^{3+} samples prepared by decomposing anhydrous precursors at different temperature (from 270 °C – 315 °C).....	92
Figure 3.25: Variation of upconversion emission intensity of samples prepared at different temperatures (270 °C-315 °C).	93
Figure 3.26: A plot of upconversion fluorescence peak intensity (green) against lattice strain of doped particle/ rod and core-shell particle/rod and Yb doped LaPO_4 nanorod (reported by P. Ghosh et al and A. Kar et al). ^{40,43}	94
Figure 3.27: Incident power-dependent upconversion studies of $\text{LiY}_{5/6}\text{Yb}_{1/6}\text{F}_4$: 0.4% Tm^{3+} prepared by decomposing anhydrous molecular precursors at different temperatures (270 °C, 290 °C, 295 °C, and 315 °C). These samples are excited by a 973 nm CW laser.....	95

Figure 3.28: Transmission electron microscopy images of $\text{LiY}_{5/6}\text{Yb}_{1/6}\text{F}_4$: 0.4% Tm^{3+} samples taken at a different course of reaction from 30 min to 2 h. These images clearly show the formation of diamond morphology of nanoparticles is guided through small spherical seeds which aligns themselves in accordance to their minimum surface energy to get the most thermodynamic stable phase and morphology.	96
Figure 3.29: Upconversion emission spectra obtained under 10 W/cm^2 for the nanocrystals studied (black line) and for a single crystal (red) of the similar composition obtained by a modified Bridgman method. The doping concentrations have been measured by EDS	97
Figure 3.30: Comparative upconversion quantum yield of the sample prepared using anhydrous molecular precursors versus the quantum yield of samples prepared at different laboratories as already reported (*) by Meijer et al. ⁵⁰	99
Figure 4.1: Energy level diagram for Tm^{3+} and Yb^{3+} as reported by Dulick and collaborators ¹¹ and also by Bensalah et al. ¹²	108
Figure 4.2: Powder XRD spectrum of $\text{LiY}_{5/6}\text{Yb}_{1/6}\text{F}_4$: 0.4% Tm^{3+} nanocrystals	109
Figure 4.3: TEM and HR-TEM (inset) images of $\text{LiY}_{5/6}\text{Yb}_{1/6}\text{F}_4$: 0.4% Tm^{3+} nanocrystals as well as the size distribution deduced from the analysis of 235 particles.....	109
Figure 4.4: Experimental setup for excited state emission spectroscopic measurements.....	111
Figure 4.5: Upconversion spectra of $\text{LiY}_{5/6}\text{Yb}_{1/6}\text{F}_4$: 0.4% Tm^{3+} nanocrystals under a 973 nm excitation wavelength with an incidence power density of 4.32 W/cm^2 (a). Energy level diagram for Yb^{3+} - Tm^{3+} codoped system (b). The luminescence intensity variations of the principal emission components for the excitation intensity of the IR laser (c).	111
Figure 4.6: Various Tm^{3+} transitions under different excitation conditions.....	113
Figure 4.7: lifetime in the excited state $^3\text{H}_4 \rightarrow ^3\text{H}_6$ under different excitation schemes (continuous wave and pulsed laser).	114
Figure 4.8: Excitation spectra of the $^1\text{G}_4 \rightarrow ^3\text{H}_6$ transition with (black) or without (red) the CW IR laser at 100 mW/cm^2	115
Figure 4.9: Emission spectra of Tm^{3+} ions in $\text{LiYF}_4:\text{Yb}^{3+}, \text{Tm}^{3+}$ nanocrystals under dual excitation (black line) of a CW IR laser ($\sim 1 \text{ W/cm}^2$) at 973 nm and an OPO laser at 446.45 nm or simple excitation with the IR laser (dashed red line) or with the OPO laser (thick green line).....	116
Figure 4.10: Excitation spectra of the $^1\text{D}_2 \rightarrow ^3\text{H}_6$ transition of Tm^{3+} ions in $\text{LiYF}_4:\text{Yb}^{3+}, \text{Tm}^{3+}$ nanocrystals.....	117
Figure 4.11: lifetime in the excited state of the emission at 360 nm ($^1\text{D}_2 \rightarrow ^3\text{H}_6$) under two different excitation schemes.	118
Figure 4.12: Emission spectra of Tm^{3+} ions in $\text{LiYF}_4:\text{Yb}, \text{Tm}$ nanocrystals under dual excitation.	119

Figure 4.13: Emission intensity of the $^1D_2 \rightarrow ^3H_6$ of Tm^{3+} ions in $LiYF_4:Yb^{3+}$, Tm^{3+} nanocrystals under dual excitation (black line) of a CW IR laser at 973 nm and an LED centred at 460 nm.	120
Figure 4.14: Total emission in the range 360-370 nm Tm^{3+} ions in $LiYF_4:Yb$, Tm nanocrystals ($^1D_2 \rightarrow ^3H_6$) under dual excitation of a CW IR laser at 973 nm and a LED centred at 460 nm (M455L1 from Thorlabs) with varying intensity.	121
Figure 4.15: Measured spectra of the Xe lamp and filter used to excite the nanoparticles under sun-like excitation.	122
Figure 5.1: Contribution of different radiation in the solar spectrum. ¹⁶	128
Figure 5.2: TEM images of $TiO_2@LiY_{5/6}Yb_{1/6}F_4: 0.4\% Tm^{3+}$ NPs using oleic acid as a capping ligand..	129
Figure 5.3: N, N-dimethylaminoethanol (dmeaH) (a) and N-methyl diethanolamine (mdeaH ₂) (b) ligands used as capping ligands in the present study.	130
Figure 5.4: Transmission electron microscopy images of TiO_2 coated $LiY_{5/6}Yb_{1/6}F_4: 0.4\% Tm^{3+}$ samples when N, N-dimethyl ethanolamine was used as functionalizing ligand. The top left image clearly shows the coating of amorphous TiO_2 on well crystalline $LiYF_4$ nanoparticle which is further confirmed by calculating d spacing of 0.46 nm corresponding to (101) planes of tetragonal $LiYF_4$. The STEM image on the top right and subsequent EDX mapping data show a nearly uniform coating of TiO_2 around $LiYF_4$ nanocrystals.	131
Figure 5.5: STEM imaging and EDX mapping of TiO_2 coated $LiY_{5/6}Yb_{1/6}F_4: 0.4\% Tm^{3+}$ upconverting nanoparticles using N-methyl diethanolamine as a functionalizing ligand.	131
Figure 5.6: Blank and UCNPs-embedded TiO_2 metallogels synthesized using controlled hydrolysis and condensation of $Ti(OEt)_4$ in the presence of varying amounts of $LiY_{5/6}Yb_{1/6}F_4: 0.4\% Tm^{3+}$ NPs (a). The varied intensity of Tm^{3+} luminescence with different doping percentage of up-converting $LiY_{5/6}Yb_{1/6}F_4: 0.4\% Tm^{3+}$ nanoparticles in TiO_2 metallogels (b). The nanoparticles are uniformly embedded in TiO_2 gel as observed from the output blue luminescence.	133
Figure 5.7: Characterization of undoped dried TiO_2 metallogel. Powder X-ray diffraction pattern of dried TiO_2 metallogel with and without heat treatment and evolution of its crystalline anatase form with an increase in calcination temperature from 200°C to 400°C (a). Thermogravimetric analysis (TGA) and differential thermogravimetric (DTG) curve of undoped TiO_2 dried gel (b). N_2 adsorption and desorption isotherms of dried microporous TiO_2 gel both in the calcined and non-calcined state with different surface areas (c), the distribution of pore volume with average pore diameter (d). ...	135
Figure 5.8: Characterization of UCNPs embedded TiO_2 metallogels. Powder X-ray diffraction pattern of Pure $LiY_{5/6}Yb_{1/6}F_4: 0.4\% Tm^{3+}$ and it's composite with TiO_2 metallogel with and without heat treatment (a). N_2 adsorption and desorption isotherms of undoped TiO_2 dried gel and TiO_2 gels embedded with different percentages of $LiY_{5/6}Yb_{1/6}F_4: 0.4\% Tm^{3+}$ (b). TEM and EDX spectroscopic	

studies of 10% UCNP-TiO ₂ sample before calcination of the dried gel. The HRTEM image shows lattice fringes corresponding to the (112) plane of tetragonal LiYF ₄ (c).	137
Figure 5.9: Up conversion emission studies for non-coated LiYF ₄ :20% Yb ³⁺ ,0.5% Tm ³⁺ and titania coated LiYF ₄ :20% Yb ³⁺ ,0.5% Tm ³⁺ using different ligands for functionalization, upon 972 nm CW laser excitation. These spectra are normalized with respect to ¹ G ₄ → ³ F ₄ Tm ³⁺ transition.	139
Figure 5.10: power variation upconversion emission studies for undoped TiO ₂ dried gel and LiY _{5/6} Yb _{1/6} F ₄ : 0.4% Tm ³⁺ doped TiO ₂ samples upon 973 nm CW laser excitation. These spectra are normalized for ¹ G ₄ → ³ F ₄ Tm ³⁺ transition.	140
Figure 5.11: Experimental setup for degradation of methylene blue (MB).....	140
Figure 5.12: Photodegradation study of methylene shown by the relative change in concentration blue using Xe lamp under infrared irradiation band (above 800nm) (a). Natural logarithm of the ratio of initial concentration (C ₀) and final concentration (C) for understanding degradation kinetics (b). UV-Vis absorption spectra showing degradation of methylene blue c) 10% UCNPs-TiO ₂ and d) 5% UCNPs-TiO ₂ nanocomposites. First-order rate constants, k (hour ⁻¹), of different UCNPs-TiO ₂ catalyst for the degradation of MB (e).	142
Figure 7.1: Experimental setup a) and representative figure for the different sample prepared by varying the thickness of the yttrium layer using atomic layer deposition (ALD) technique b).....	167
Figure 7.2: Emission spectra for different thin film samples with varying separation layer (YF ₃) thickness.....	168
Figure 7.3: Photodegradation study of methylene shown by the relative change in concentration blue using Xe lamp under visible irradiation band (420 - 780 nm)	170

List of tables

Table 2.1: Different crystalline phases and crystallite size of the NaGdF ₄ : Yb ³⁺ , Tm ³⁺ NPs obtained from the thermal decomposition of SSPs [NaLn(TFA) ₄ (diglyme)] (Ln = Gd, Yb, Tm) at 290 °C in 1:1 mixture of 1-Octadecene + Oleic acid or 1-Octadecene + Oleylamine.	39
Table 2.2: Upconversion quantum yield (QY) and energy conversion efficiency(ECE) of NaGd _{5/6} Yb _{1/6} F ₄ : 0.8% Tm ³⁺ _anhyd at different power densities of the IR laser for different spectral regions: the under-script UV represents the region between 250 and 375nm, 475 corresponds to the region 430-530 nm, 648 corresponds to 635-665 nm, 700 corresponds to 670-720 nm, 802 corresponds to 730-870 nm. Finally, the total stands for the whole 250-900 nm region.....	52
Table 2.3: Upconversion quantum yield (QY) and energy conversion efficiency (ECE) of NaGd _{5/6} Yb _{1/6} F ₄ : 0.8% Tm ³⁺ _hyd at different power densities of the IR laser for different spectral regions: the under-script UV represents the region between 250 and 375nm, 475 corresponds to the region 430-530 nm, 648 corresponds to 635-665 nm, 700 corresponds to 670-720 nm, 802 corresponds to 730-870 nm. Finally, the total stands for the whole 250-900 nm region.....	52
Table 3.1: Selected bond lengths (Å) and angles (°) for 2	67
Table 3.2: Selected bond lengths (Å) and angles (°) for 4	69
Table 3.3: Selected bond lengths (Å) and angles (°) for 6	70
Table 3.4: Rietveld refinement parameters of powder X-ray diffraction pattern of different samples prepared with different ratio of solvents during thermal decomposition.....	82
Table 3.5: Rietveld refinement parameters of powder X-ray diffraction pattern of different samples prepared with different concentration of precursors during thermal decomposition.....	86
Table 3.6: upconversion Quantum yield (QY) and energy conversion efficiency(ECE) at different intensities of the IR laser for different spectral regions: the under-script UV represents the region between 250 and 375nm, 451 corresponds to the region 440-460 nm, 480 to the region 461-507 nm, 649 to the region 620-732 nm, 794 to the region 733-880 nm. Finally, the total stands for the whole 250-900 nm region.	98
Table 6.1: Crystallographic and refinement data for complexes 2 , 4 and 5	151
Table 6.2: Synthesis of NaGdF ₄ : x% Yb ³⁺ , y% Tm ³⁺ _anhyd in the mixture of 1-octadecene and oleylamine	155
Table 6.3: Synthesis of NaGdF ₄ : x% Yb ³⁺ , y% Tm ³⁺ _anhyd in the mixture of 1-octadecene and oleic acid	156
Table 6.4: The amount of precursors used to synthesize NaGdF ₄ : x% Yb ³⁺ , y% Tm ³⁺ _hyd in ethylene glycol at room temperature.	157

Table 6.5: The amount of precursors used to synthesize undoped LiYF_4 and LiYbF_4 matrices using anhydrous precursors by thermal decomposition at 290°C	158
Table 6.6: The amount of precursors used to synthesize doped LiYF_4 with varying ratio of Tm^{3+} using anhydrous precursors by thermal decomposition at 290°C	159
Table 6.7: The amount of precursors used to synthesize $\text{LiY}_{5/6}\text{Yb}_{1/6}\text{F}_4$: 0.4% Tm^{3+} in a decomposition mixture containing a different ratio of 1-octadecene and oleic acid.....	159
Table 6.8: The amount of precursors used for studying the effect of their concentration on the resultant $\text{LiY}_{5/6}\text{Yb}_{1/6}\text{F}_4$: 0.4% Tm^{3+} UCNPs.	160
Table 6.9: The amount of precursors used for studying the effect of decomposition temperature on the resultant $\text{LiY}_{5/6}\text{Yb}_{1/6}\text{F}_4$: 0.4% Tm^{3+} UCNPs.....	160
Table 6.10: The amount of precursors used for studying the effect of time of decomposition on the resultant $\text{LiY}_{5/6}\text{Yb}_{1/6}\text{F}_4$: 0.4% Tm^{3+} UCNPs.	161

List of Schemes

Scheme 2.1: Synthesis of NaGdF ₄ : Yb ³⁺ , Tm ³⁺ nanoparticles using anhydrous precursors.	35
Scheme 3.1: Synthesis of anhydrous lithium precursors 1 and 2	65
Scheme 3.2: Synthesis of anhydrous lanthanide precursors 3-6	65
Scheme 3.3: Common bonding modes observed for the trifluoroacetate ligand in metal complexes.	66
Scheme 5.1: Different steps for the synthesis of TiO ₂ @UCNPs shell-core structure using amino alcohols as functionalising ligand.	130

Abstract

The utilization of solar energy to solve environmental problems such as water detoxification, air purification and hydrogen production has attracted great interest from the scientific community over the last two decades. Solar photocatalysis is an interesting avenue to target all these environmental issues. Currently, technologies do not yet allow for the efficient use of a significant portion of the solar spectrum, namely the infrared, which corresponds to nearly ~48% of the total solar spectrum. This thesis aims at preparing nanocomposite materials that use these low energy solar photons by converting them into high energy UV and visible photons and then using them for classical photocatalysis. To achieve this, two major aspects of the preparation of this modified photocatalyst were emphasized. Firstly, the synthesis of materials that could efficiently convert currently unused photons and secondly, the preparation of their composite with TiO₂, the most widely used photocatalyst.

This doctoral thesis focuses on an approach based on "upconversion" to extend the range of use of the solar spectrum. To achieve this goal, two optimization strategies were addressed. The optimization of the quantum efficiency of upconversion nanoparticles (UCNPs) using new anhydrous precursors and, the preparation of UCNPs-TiO₂ nanocatalyst using metallo gels and/or core-shell structures. Finally, we test the objective of using low energy infrared solar photons by performing photocatalysis under IR irradiation only using the platform developed in this work.

Keywords: Solar photocatalysis; Upconversion; upconverting nanomaterials; anhydrous precursors; photocatalyst; NIR induced photocatalysis; TiO₂; UCNP.

Résumé

L'utilisation de l'énergie solaire pour résoudre des problèmes environnementaux tels que la détoxification de l'eau, la purification de l'air et la production d'hydrogène a suscité un grand intérêt de la part de la communauté scientifique au cours des deux dernières décennies. La photocatalyse solaire est une piste intéressante pour cibler toutes ces questions environnementales. Actuellement, les technologies ne permettent pas encore d'utiliser efficacement une partie importante du spectre solaire, à savoir l'infrarouge, qui correspond à près de ~48 % du spectre solaire total. Cette thèse vise à préparer des matériaux nanocomposites qui utilisent ces photons solaires à faible énergie en les convertissant en photons UV et visibles à haute énergie et en les utilisant ensuite pour la photocatalyse classique. Pour y parvenir, l'accent a été mis sur deux aspects majeurs de la préparation de ce photocatalyseur modifié. Premièrement, la synthèse de matériaux qui pourraient convertir efficacement les photons actuellement inutilisés et deuxièmement, la préparation de leur composite avec TiO₂, le photocatalyseur le plus largement utilisé.

Cette thèse de doctorat se concentre sur une approche basée sur l'« upconversion » afin d'étendre la gamme d'utilisation du spectre solaire. Pour atteindre cet objectif, deux stratégies d'optimisation ont été abordées. L'optimisation du rendement quantique des nanoparticules à upconversion en utilisant de nouveaux précurseurs anhydres et, la préparation de photo-catalyseur nanocomposite UCNPs-TiO₂ en utilisant des métallogels et/ou des structures coeur-coquille. Pour finir nous testons l'objectif de l'utilisation des photons solaires infrarouges à faible énergie en réalisant une photocatalyse sous irradiation IR uniquement en utilisant la plate-forme développée dans ce travail.

Mots-clés : Photocatalyse solaire ; Upconversion ; nanomatériaux d'upconversion ; précurseurs anhydres ; photocatalyseur ; photocatalyse induite par le proche infrarouge ; TiO₂ ; UCNP

General Introduction

After one century of intense use of non-renewable resources and the constant increase of energy consumption (~559.8 EJ in 2012)¹ and wastewater treatment demand, the global demand for energy by the year 2050 won't be completely fulfilled by available oil and gas reserves. The exhaustion of these reserves soon is the major challenge we are facing right now. The equitable distribution and universal accessibility of solar energy is an important aspect of utilizing solar energy for our daily energy needs. We are utilizing the sun's energy not only in direct forms such as by using photovoltaics for electricity production² or photocatalysis for waste treatment³ etc. but also indirectly through biomass utilization^{4,5} and harnessing wind power.⁶

As we know that a large amount (~100,000 terawatts) of solar energy is insolated to the earth surface⁷ and the maximum effective energy required to fulfil our daily needs is relatively small (18 TW-year).⁸ So, to use solar energy to its maximum potential, we need to focus our attention more on either improving the light trapping optics or on the materials that can enhance the absorption spectrum of the devices.

In the current scenario, the solar photon energy conversion is still lacking the utilization of a major part of the solar spectrum. Therefore, the majority of the systems (photovoltaics, photocatalytic etc.) that convert solar energy for their utilization in application such as electricity production and wastewater treatment, waste a major portion of incident solar light that can be utilised otherwise.⁹ Such devices which are based on the classical method of utilization of solar energy are somehow limited by their absorption threshold, which means that the incident photons which does not correspond to their bandgap energy cannot be harvested, rather they will either be converted into heat or lost due to some other processes such as cross-relaxation, back-transfer, non-radiative decay etc..^{10,11}

To enhance the utilization of solar influx many strategies have been introduced which are still in a nascent state where many improvements are being currently implemented. Methods such as co-sensitization with light-absorbing molecular complexes (dye sensitization),¹² surface Plasmon resonance induced by preparing Z-scheme heterojunction,^{13,14} increasing the light collection by preparing hybrid single and multi-layered structures,¹⁵ and by spectral conversion of currently unused light using upconverting nanostructures.^{7,16,17}

The use of upconversion for solar applications can eliminate the inability of conventional photocatalysts to harvest a broad range of solar irradiation. Semiconductor photocatalyst has achieved immense interest from past few decades due to their ability to directly utilize solar radiation, but due

to their limited bandgap tunability, they are restricted to respond only to a small portion of solar light primarily ultraviolet (UV), therefore limiting them to gain maximum achievable efficiency. Out of many strategies for increasing the output efficiency of conventional solar energy-driven systems, only very few are utilizing one of the biggest regions of the solar spectrum, –Infrared, which consists of ~50% energy of the solar spectrum. Hence, for practical applications, this strategy to use IR photons (700-2500 nm) for solar-driven catalytic systems is desirable. Photon upconversion is a nonlinear, anti-Stokes optical process, that can make these conventional photocatalytic systems outperform by converting the otherwise unused low energy photons into high energy photons and channelling them properly into the different energy levels of the photo catalysts.^{16,18,19} This process is observed in many systems such as rare-earth-doped materials, organic dyes, quantum nanostructures etc. Out of which, upconversion in lanthanide-doped crystals has been most notably observed (see Figure 0.1), particularly due to their longer lifetimes (~microseconds to milliseconds), allowing sequential absorption of two or more excitation photons with lower energy and producing high-energy luminescence emissions.^{7,9,12} In addition, the intra 4f transitions in the lanthanide ions makes electron transitions within themselves less susceptible to their surrounding environmental changes.

For solar photocatalytic applications, the most widely used conventional photocatalyst such as TiO₂ has a bandgap of 3.2 eV (anatase), due to which its light absorption is limited to wavelengths below 365 nm only. To increase its efficiency there are many advances out of which major attention was caught by the use of upconverting materials with conventional and classical photocatalysis.^{17,18,20} There are also numerous rare earth metals ions-based upconverting photocatalytic systems available, but since the spectral upconversion of NIR/visible photons into UV photons is not straightforward, their upconversion quantum yield is low,^{21,22} hence making people reluctant about their actual use in NIR photocatalysis.²³ These findings are also justified by preliminary results by Ying Chen et al¹⁹ justifying NIR driven photocatalysis under solar excitation.

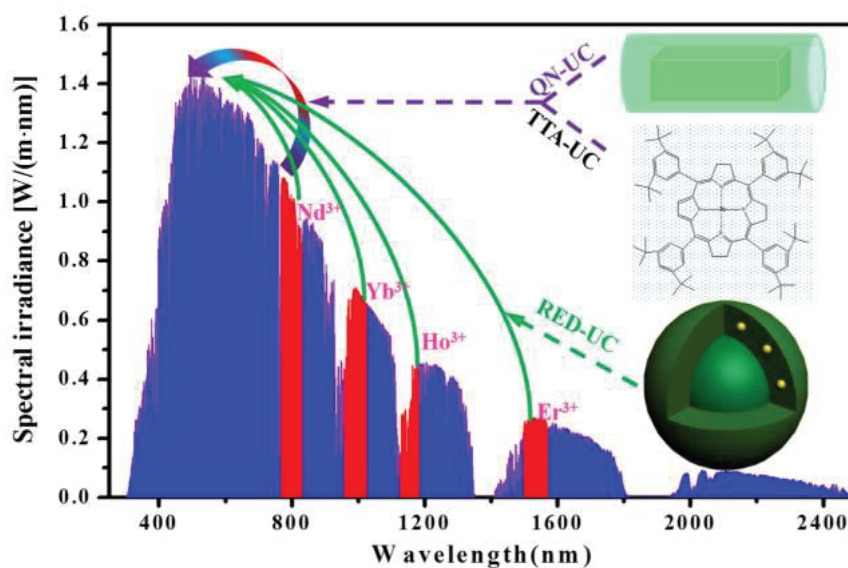


Figure 0.1: The absorption and emission range of three types of upconversion materials concerning AM 1.5 spectrum (QN-UC (purple): upconversion in quantum nanostructures; TTA-UC (purple): triplet-triplet annihilation upconversion; RED-UC (green): rare-earth-doped upconversion materials).⁷

This doctoral thesis focuses on the upconversion-based approach for the extended utilization of the solar spectrum. To achieve this objective, this thesis is organized as an intermix of optimization of quantum efficiency upconverting nanomaterials using novel anhydrous precursors and preparation of UCNPs–TiO₂ nanocomposite photocatalyst using metallogels and core-shell strategy.

Structurally, this thesis is divided into 7 chapters. The first chapter briefs the motivation behind this work and emphasizes the necessity of improving upconversion efficiency via different chemical routes by studying the existing literature on this subject. This state of the art survey of literature regarding the growth of solar photocatalysis and the role of upconversion nanomaterials in its applicability develops the premise for the coming chapters.

The second chapter focuses on sodium-based upconverting nanostructures and describes the importance of the use of anhydrous precursors over widely used hydrous precursors. In the first part of this chapter, the effect of combining different solvents during thermal decomposition of anhydrous precursors and their impact on the phase and purity of the resultant upconverting nanoparticles is studied. During this study, we also optimised the ideal concentration of the dopant ions. Following this, the optical output efficiency (upconversion quantum yield) of sodium-based upconverting nanostructures prepared using both anhydrous and hydrous precursors is measured. This chapter concludes with an important idea that the use of anhydrous precursors could be a benchmark for obtaining bright luminescent upconverting nanoparticles with improved optical throughput.

After establishing the importance of anhydrous precursors for obtaining brighter upconverting nanoparticles, we investigate other methods to obtain higher upconversion UV emission (< 380 nm).

With this objective, in chapter 3, Lithium-based upconverting nanostructures have been explored in detail. In this chapter, we started by explaining the synthesis of novel anhydrous monoglyme precursors for the upconverting nanoparticles. After thoroughly characterizing these precursors, we studied the synthesis of upconverting nanoparticles under different synthesis conditions. Starting with choosing lanthanide ions for the host matrix, we then varied numerous parameters such as i) Effect of ratio of dopant ions ii) The effect of the ratio of solvents, iii) Effect of concentration of precursors and iv) Effect of reaction time which affect the phase, morphology and optical output of the upconverting nanoparticles. This chapter encompasses a great number of factors for obtaining lithium-based upconverting nanoparticles with high optical emission. At the end of this chapter, a comparative study of the output emission intensity of the best performing upconverting nanoparticle with its bulk counterpart which has identical dopant concentration is performed.

Chapter 4, provides evidence concerning the use of near-infrared (NIR) photons for photocatalytic applications. In this chapter, we justified that if correct conditions exist, the sequential absorption of photons of different wavelengths even with non-laser sources (LED) can yield high energy UV photons. This study bridges the gap between different opinions towards the idea of NIR induced photocatalysis.

Chapter 5, presents two different strategies to prepare nanocomposites of upconverting nanoparticles with classical photocatalyst TiO_2 . Here, we followed two different strategies for preparing novel photocatalyst synthesis. First, active core-shell strategy, where two different ligands have been used as a functionalizing agent for the TiO_2 @UCNPs synthesis. The second strategy is based on the preparation of transparent UCNP- TiO_2 metallogels, following which we performed dye degradation studies to assess the photocatalytic activity of these metallogels.

Chapter 6, describes in detail the experimental procedure for the preparation of novel anhydrous molecular precursors and upconverting nanoparticles and their composites with TiO_2 . The details about the experimental setup for upconversion and quantum yield measurement is also discussed.

Finally, chapter 7 concludes all the major findings regarding the techniques used for the improvement of upconversion emission of lanthanide-doped nanoparticles and their perspective for the improvisation of the photocatalytic activity of their respective nanocomposites with TiO_2 .

References

- (1) World Energy Assessment: *Energy and the Challenge of Sustainability*; Goldemberg, J., UNDP, Eds.; New York, NY, **2000**.
- (2) Saga, T. Advances in Crystalline Silicon Solar Cell Technology for Industrial Mass Production. *NPG Asia Materials* **2010**, *2* (3), 96–102. <https://doi.org/10.1038/asiamat.2010.82>.
- (3) Spasiano, D.; Marotta, R.; Malato, S.; Fernandez-Ibañez, P.; Di Somma, I. Solar Photocatalysis: Materials, Reactors, Some Commercial, and Pre-Industrialized Applications. A Comprehensive Approach. *Applied Catalysis B: Environmental* **2015**, *170–171*, 90–123. <https://doi.org/10.1016/j.apcatb.2014.12.050>.
- (4) Vermaas, W. An Introduction to Photosynthesis and Its Applications, <https://web.archive.org/web/19981203020943/http://photoscience.la.asu.edu/photosyn/education/photointro.html>.
- (5) Miyamoto, K. Energy Conversion by Photosynthetic Organisms. In *Renewable biological systems for alternative sustainable energy production*; FAO Agricultural Services Bulletin.
- (6) Wind Energy Basics, <https://www.energy.gov/eere/wind/wind-energy-basics>.
- (7) Shang, Y.; Hao, S.; Yang, C.; Chen, G. Enhancing Solar Cell Efficiency Using Photon Upconversion Materials. *Nanomaterials (Basel)* **2015**, *5* (4), 1782–1809. <https://doi.org/10.3390/nano5041782>.
- (8) Key World Energy Statistics 2015. **2015**, 81.
- (9) Schulze, T. F.; Schmidt, T. W. Photochemical Upconversion: Present Status and Prospects for Its Application to Solar Energy Conversion. *Energy Environ. Sci.* **2014**, *8* (1), 103–125. <https://doi.org/10.1039/C4EE02481H>.
- (10) Rabouw, F. T.; Prins, P. T.; Villanueva-Delgado, P.; Castelijns, M.; Geitenbeek, R. G.; Meijerink, A. Quenching Pathways in NaYF₄: Er³⁺, Yb³⁺ Upconversion Nanocrystals. *ACS Nano* **2018**, *12* (5), 4812–4823. <https://doi.org/10.1021/acsnano.8b01545>.
- (11) Wang, F.; Wang, J.; Liu, X. Direct Evidence of a Surface Quenching Effect on Size-Dependent Luminescence of Upconversion Nanoparticles. *Angewandte Chemie International Edition* **2010**, *49* (41), 7456–7460. <https://doi.org/10.1002/anie.201003959>.

- (12) Paramasivam, I.; Jha, H.; Liu, N.; Schmuki, P. A Review of Photocatalysis Using Self-Organized TiO₂ Nanotubes and Other Ordered Oxide Nanostructures. *Small* **2012**, *8* (20), 3073–3103. <https://doi.org/10.1002/sml.201200564>.
- (13) Li, X.; Yang, K.; Yu, C.; Zhang, K.; Yang, S.; Zhu, L.; Ji, H.; Dai, W.; Fan, Q.; Huang, W. Broadband Photocatalysis Using a Z-Scheme Heterojunction of Au/NaYF₄: Yb, Er/WO₃·0.33H₂O-W₁₈O₄₉ via a Synergetic Strategy of Upconversion Function and Plasmonic Effect. *Inorg. Chem. Front.* **2019**, *6* (11), 3158–3167. <https://doi.org/10.1039/C9QI00823C>.
- (14) Li, S.; Miao, P.; Zhang, Y.; Wu, J.; Zhang, B.; Du, Y.; Han, X.; Sun, J.; Xu, P. Recent Advances in Plasmonic Nanostructures for Enhanced Photocatalysis and Electrocatalysis. *Advanced Materials* **2020**, *6* (33), 2000086. <https://doi.org/10.1002/adma.202000086>.
- (15) Li, X.; Zuo, X.; Jiang, X.; Li, D.; Cui, B.; Liu, D. Enhanced Photocatalysis for Water Splitting in Layered Tin Chalcogenides with High Carrier Mobility. *Phys. Chem. Chem. Phys.* **2019**, *21* (14), 7559–7566. <https://doi.org/10.1039/C9CP00088G>.
- (16) Avram, D.; Patrascu, A. A.; Istrate, M. C.; Cojocaru, B.; Tiseanu, C. Lanthanide Doped TiO₂: Coexistence of Discrete and Continuous Dopant Distribution in Anatase Phase. *Journal of Alloys and Compounds* **2020**, 156849. <https://doi.org/10.1016/j.jallcom.2020.156849>.
- (17) Tang, Y.; Di, W.; Zhai, X.; Yang, R.; Qin, W. NIR-Responsive Photocatalytic Activity and Mechanism of NaYF₄: Yb, Tm@TiO₂ Core-Shell Nanoparticles. *ACS Catal.* **2013**, *3* (3), 405–412. <https://doi.org/10.1021/cs300808r>.
- (18) Zhao, J.; Xu, J.; Jian, X.; Xu, J.; Gao, Z.; Song, Y.-Y. NIR-Light Driven Photocatalysis on Amphiphilic TiO₂ Nanotubes for Controllable Drug Release. *ACS Appl. Mater. Interfaces* **2020**, acsami.0c04260. <https://doi.org/10.1021/acsami.0c04260>.
- (19) Chen, Y.; Mishra, S.; Ledoux, G.; Jeanneau, E.; Daniel, M.; Zhang, J.; Daniele, S. Direct Synthesis of Hexagonal NaGdF₄ Nanocrystals from a Single-Source Precursor: Upconverting NaGdF₄: Yb³⁺, Tm³⁺ and Its Composites with TiO₂ for Near-IR-Driven Photocatalysis. *Chemistry – An Asian Journal* **2014**, *9* (9), 2415–2421. <https://doi.org/10.1002/asia.201402347>.
- (20) Wielopolski, M.; Linton, K. E.; Marszałek, M.; Gulcur, M.; Bryce, M. R.; Moser, J. E. Harvesting UV Photons for Solar Energy Conversion Applications. *Phys. Chem. Chem. Phys.* **2014**, *16* (5), 2090–2099. <https://doi.org/10.1039/C3CP54914C>.

- (21) Kraft, M.; Würth, C.; Palo, E.; Soukka, T.; Resch-Genger, U. Colour-Optimized Quantum Yields of Yb, Tm Co-Doped Upconversion Nanocrystals. *Methods Appl. Fluoresc.* **2019**, *7* (2), 024001. <https://doi.org/10.1088/2050-6120/ab023b>.
- (22) Kaiser, M.; Würth, C.; Kraft, M.; Hyppänen, I.; Soukka, T.; Resch-Genger, U. Power-Dependent Upconversion Quantum Yield of NaYF₄: Yb³⁺, Er³⁺ Nano- and Micrometer-Sized Particles – Measurements and Simulations. *Nanoscale* **2017**, *9* (28), 10051–10058. <https://doi.org/10.1039/C7NR02449E>.
- (23) Zhang, Q.; Yang, F.; Xu, Z.; Chaker, M.; Ma, D. Are Lanthanide-Doped Upconversion Materials Good Candidates for Photocatalysis? *Nanoscale Horiz.* **2019**, *4* (3), 579–591. <https://doi.org/10.1039/C8NH00373D>.

Chapter 1 Literature review

1.1. Solar photocatalysis

With our current exponential increase in energy demands, it would be very difficult to meet all our energy needs by the end of this century with the currently used non-renewable energy resources.¹ Alternative source such as solar, wind or geothermal energy, which are reliable, consistent and more importantly renewable would play a major role shortly. This is particularly relevant for the case of solar energy where its conversion into chemical or electrical energy could be governed by natural photo-assisted reactions. So, it would be a very important and sustainable solution for the energy and environmental problems if we could utilize solar energy for the generation of hydrogen energy or detoxification of organic pollutants by an eco-friendly route.²

One of such photochemical reactions is photocatalysis, which is most widely studied and has a powerful influence in many industries such as hygiene and sanitation, environmental protection such as water treatment and air purification, architecture and construction etc.³⁻⁵

In general, the whole idea of photocatalytic reaction could be briefly categorized into three steps as shown in Figure 1.1. The first step is the absorption of photons by the semiconductor photocatalyst and the subsequent generation of electron-hole pairs. Depending on the energy of incoming photons, if the energy of these photons is higher than the bandgap of these semiconductors ($E_{\text{photons}} > E_{\text{gap}}$) then these photogenerated electrons and holes can be separated. The second step involves the migration of these charge carrier species to the surface of the photocatalyst. The driving force is the internal electric field. It is a crucial process, as the tendency of these charge carriers to recombine is high. Finally, after the successful transfer of these charge carriers to the surface of the catalyst, the already adsorbed molecules (or water from the solution) will react with these photo generated charge carriers.⁶

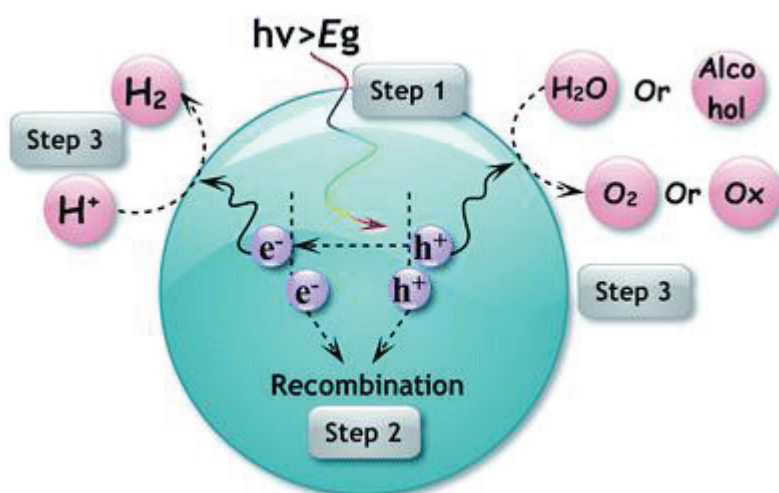


Figure 1.1: Schematic diagram of the photocatalytic reaction⁶.

It was in the mid-1990s that the photocatalytic products found their way to markets, first in Japan and later in America and Europe. By 2009, the total volume of solar photocatalysis based products was around \$848 million, which increased greatly to \$1.4 billion in 2013, \$1.5 billion in 2014 and the forecast of compound annual growth rate (CAGR) equivalent to 12.6%, might take this market to \$2.9 billion by the end of 2020.⁷

1.2. *TiO₂ as a robust photocatalyst and its limitations.*

A major share among these photocatalyst is held by titanium dioxide (TiO₂), which is mainly a UV based semiconductor photocatalyst. TiO₂ has three crystal structures i.e., anatase, rutile and brookite. The anatase phase of TiO₂ generally has the highest photoactivity compared to other phases. It has a band gap of 3.2 eV, which limits its absorption only to UV light (< 380 nm). With such a semiconductor-based photocatalyst, the utilization of direct sunlight is only feasible when the energy of incoming photons exceeds the bandgap energy between the conduction and valence band. Therefore, for TiO₂, only high energy solar photons ($\lambda < 380 \text{ nm}$), can activate the catalyst and trigger photocatalysis. Regrettably, more than 90% of the sunlight cannot be utilized for its activation, as the total share of UV light photons in the solar spectrum is only ~5% and out of it, ~1% is being utilized by TiO₂ (Figure 1.2).

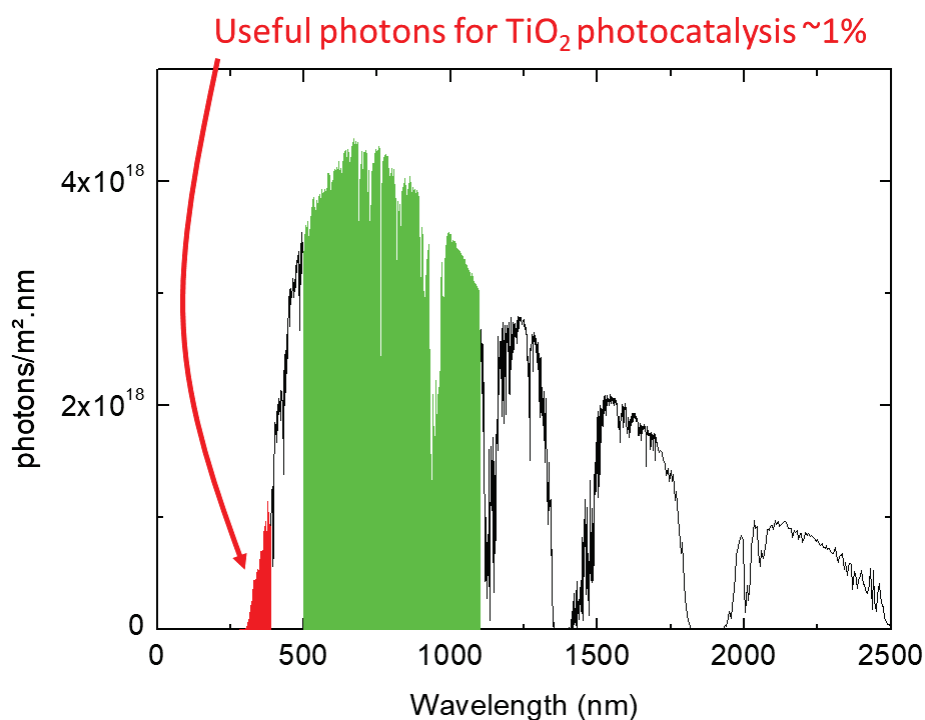


Figure 1.2: Solar spectrum showing the useful share of photons for TiO₂ based photocatalysis.

In literature, many efforts have been devoted to tackling these issue of non-utilization of most of the solar spectra and higher probability of recombination by modifying the bandgap of TiO₂. The reduction of the optical bandgap is one of the strategies to enable visible light photocatalysis with TiO₂. This reduction has been achieved by either introducing intermediate states in the bandgap using elemental doping or narrowing the bandgap itself. The introduction of some noble metals (such as Fe³⁺, V⁵⁺, Cu⁺, Ag⁺), non-metals (such as N), low bandgap semiconductors (such as Cu₂Se), or lanthanide ions (La, Ce, Nd etc) or even wrapping TiO₂ with graphene layers has been proven efficient methods for enhancing the range of photocatalytic activity of TiO₂. For example;

Navio et al.⁸ showed that doping of Fe³⁺ into the TiO₂ samples could provide a monophasic material without observing any separate iron oxide phases. This iron-doped titanium oxide has shown higher surface hydroxyl densities making them a potential candidate for photocatalysis.

A step further, Yuan et al.⁹ showed that by co-doping of Zn²⁺ and Fe³⁺ into titania, cooperative enhancement in the photoactivity could be observed. Due to change in the morphology of nanoparticles, they achieved a two-fold increase in the photocatalytic decomposition of phenol under optimum conditions (pH = 7; 1.5 and 3 mol% of Zn and Fe, respectively).

Chao et al.¹⁰ suggested that the addition of Ag⁺ dopant into the TiO₂ powder could accelerate the phase transformation from anatase to rutile, this reduces the grain size of the anatase

phase however the specific surface area increases on this transformation. An optimum balance of the dopant concentration (2-6%) has a positive effect on photocatalytic activity. Also, as reported by Seery et al.,¹¹ the slight doping of Ag⁺ can significantly increase the absorption of TiO₂ in the visible region. Silver ions can also enhance the electron-hole pair separation, leading to enhanced photocatalytic efficiency of TiO₂.

The doping of V⁵⁺ and Mn⁺ has also a positive effect on the photocatalytic activity of TiO₂ thin films towards propanol degradation as reported by Yamashita et al.¹² The implantation of these ions alters the electronic structure of the TiO₂ surface layer, shifting its absorption band slightly into the visible region.

Copper being an effective electron trapper could reduce the probability of electron-hole recombination as reported by Tseng et al.¹³ By reducing CO₂ in NaOH aqueous solution under UV irradiation, they were able to produce methanol; showing the enhancement of photocatalytic efficiency of Cu loaded TiO₂.

Choi et al.,¹⁴ in their research showed the redshift in the absorption of N-doped TiO₂ up to 468 nm, with a significantly narrow bandgap of 2.65eV.

Many low bandgap semiconductors such as CdS, CdSe have also been used to enhance the photocatalytic activity of TiO₂. One such semiconductor, Ag₂Se, when doped with commercial TiO₂ shows the much higher catalytic activity as reported by Mishra et al.¹⁵ They showed great improvement in the degradation of formic acid by the addition of silver selenide nanoparticles with TiO₂.

The use of rare-earth ions for photocatalytic reactions was first reported by Yu et al.¹⁶ Back in 1998 they showed that La₂O₃ modified TiO₂ shows promising photocatalytic activity for the oxidation of acetone in the gas phase.

In another study, Du et al.,¹⁷ used different lanthanide ions including Ce, Y, Pr, Sm to modify the commercial TiO₂ and observed the effect of doping variable amount of lanthanide ions into TiO₂ towards the degradation of methylene blue under UV irradiation.

Other studies including the degradation of phenol using Cerium doped TiO₂ by Fan et al.,¹⁸ degradations of p-nitrophenol using europium and ytterbium-doped TiO₂ by Ranjit et al.¹⁹ are among the first few reports concerning the photocatalytic degradation of organics in solution.

But all these attempts were made to either enhance the utilization of UV or extend its absorption up to only visible radiation. Generally, the addition of such dopant ions or molecules enhances the photocatalytic activity in the visible region, but the activity in UV irradiation is compromised. A major portion of the solar spectra (~48%) was still not explored by these techniques.

1.3. Upconversion as a solution

In principle, the utilization of the invisible infrared region of solar spectra by these classical photocatalysts would only be possible if we could couple such photocatalytic systems with materials that could act as wavelength converters. In other words, a material that could absorb infrared radiation and emit light that is energetically higher than the incoming light. Such emissions were already discovered as of anti-Stokes band in Raman scattering, but these emissions were of the order of kT and quite often not observed (low efficiency) due to thermal quenching. Thankfully, the proposal of Bloembergen²⁰ regarding the addition of infrared photons with the visible photons to produce other visible photons of higher energy and the subsequent ground-breaking discovery of a phenomenon of sequential energy transfer of photons or APTE effect (French acronym: **A**ddition de **P**hotons par **T**ransfert d'**E**nergie) back in 1966 by F. Auzel made it possible to observe the anti-Stokes emission with energies 10-100 times greater than kT . He came up with a completely revolutionising idea regarding the transfer of energy in rare-earth ions. His understanding of energy transfers as the transfer of only the energy differences not the absolute energy in the Yb/Er and Yb/Tm couples indeed provided the evidence for sequential transfer of energy from more than two photons.²¹ Before his discovery the sequential transfer of energy was a very less probable idea as the means such as laser excitation and optical fibre confinement were yet to be discovered at that time. This phenomenon was later termed 'upconversion', as the low energy photons are being converted to higher energy photons in this process.

Photon upconversion is essentially a non-linear optical process and could be observed primarily in lanthanide ions (lanthanide-based upconversion) and in some aromatic organic compounds (TTA-based upconversion). It is a process of sequential absorption of two or more photons by metastable, long-lived energy states. This sequential absorption leads to the population of a highly excited state from which upconversion emission occurs. Both these processes are based on the interaction of similar kind of excited states. For lanthanide-based upconversion, it is the transition between 4f energy levels and for TTA based upconversion it is the first excited state of the TTA emitter molecules. To understand more about the process of upconversion (both lanthanide and TTA based upconversion) and to realize its importance and applicability for our application in photocatalysis, we

will now carefully look at the brief journey of upconversion in the past decades. We will talk about the evolution of both these approaches but our prime focus would be to observe lanthanide-based upconversion in great detail.

a). Upconversion in detail

The upconversion based on organic materials (**TTA based upconversion**) was first proposed back in 1962 by Parker et al. where they called it “anti-Stokes delayed fluorescence”. They proposed that to observe such phenomenon in organic chromophores, two separate species are needed (a donor and an acceptor) and they successfully presented this phenomenon in two different molecular systems. First a combination of phenanthrene (donor), and naphthalene (acceptor), and second proflavine hydrochloride (donor) and anthracene as an acceptor.²² The working principle of TTA based upconversion involves a series of steps: absorption of low energy photons by sensitizer (Step 1), followed by an intersystem crossing (ISC, Step 2). The third step is the energy transfer between the triplet states of donor and acceptor ions (TET, Step 3). With the help of a second donor molecule, a second emitter molecule gets excited (triplet-triplet annihilation, Step 4) and the subsequent interaction between these emitter molecules could observe the delayed fluorescence.²³ A descriptive schematic to help visualize these step is shown in Figure 1.3

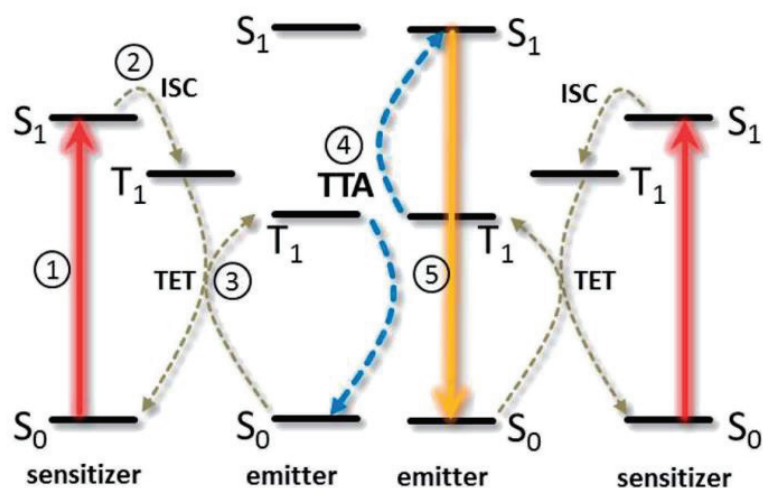


Figure 1.3: Working principle of triplet-triplet annihilation upconversion (TTA-UC).²³

This scheme of upconversion, being very reliable and easily achievable has been explored for a long time in a variety of solar energy-based applications. In the domain of solar photovoltaics, the incorporation of TTA based up-convertors could revolutionize the solar cells by addressing the inefficacy of complex manufacturing and minimization of the series connections.

Even though this process was known to us for a long time, its first successful implementation was not done until 2006, when Balushev et al demonstrated the photon upconversion with concentrated solar lights for a solution of DPA (diphenylanthracene) sensitized with 2 wt% PdOEP (palladium(II) octaethylporphyrin) with more than 1% external efficiency.²⁴

Furthermore, the research lead by Schmidt et al.^{23,25} focuses a lot on increasing the efficiency of solar cells. In 2012, they came up with a proof of concept of the third-generation photovoltaic device by making the first integrated a-Si: H/TTA-UC device. A multi-layered device coupled by a-Si: H p-i-n cell and a TTA-solution with porphyrins (PQ₄Pd and their derivatives) as sensitizers and a polycyclic aromatic hydrocarbon Rubrene (5,6,11,12-tetraphenyltetracene) as annihilator/ emitter was used as a model and was further improved by Schulze et al.²⁶ with an enhancement of 0.2% under 19 solar excitations.

In addition to the application in traditional photochemistry for photovoltaics, the application of TTA based upconverters in the domain of photocatalysis is also growing. In 2012, the first proof of concept photoelectrochemical device utilising the TTA based upconversion for water splitting has been given by Khnayzer et al.²⁷ They made a system by combining WO₃ semiconductor ($E_g = 2.7$ eV) with benchmark upconversion composition of palladium(II) octaethylporphyrin (PdOEP) and 9,10-diphenylanthracene (DPA) in toluene and enables the utilization of sub-bandgap non-coherent photons at low power density.

Later that year Kim et al.²⁸ reported the first instance of aqueous phase photosensitization of Pt loaded WO₃ semiconductor. In this system, they achieved the photon upconversion directly in the aqueous phase by encapsulating the solvent phase containing the DPA/platinum(II)-octaethyl-porphyrin (PtOEP) (sensitizer/emitter) pair in a rigid polymer shell in the form of aqueous dispersible microcapsules.

After this proof of concept of encapsulated TTA based upconversion, significant focus has been given to the fabrication of more complex and robust samples using silica. Because the surface functionalization on the silica surface is easier along with its ease to be synthesized in nanoscale dimensions, such a structurally advanced system has found a wide range of applications. In this field, more detailed research has been done by Kim's group, including the decoration of such silica encapsulated TTA upconverters with CdS which resulted in aqueous phase photocatalytic oxidation.^{29,30}

Although the TTA based upconversion has shown a promising role in the domain of photocatalysis, they are still limited by the broadband utilization of the solar spectrum.³¹ Most of the currently used TTA based upconversion systems are limited to Vis-Vis or Vis-UV upconversion, so this is why lanthanide-based upconverting materials have attracted considerable attention during the past decade or so. They have excellent tunability from near-infrared to deep UV emissions. Even though the upconversion quantum efficiency of lanthanide-based upconverters is lower than TTA based upconverters, the wide applicability of such materials and their ease of incorporation with semiconductor nanocrystals of classical photocatalyst makes them more versatile for photocatalytic applications.

The upconversion based on lanthanoids (**lanthanide-based upconversion**) as briefly discussed before, has a different working principle than the upconversion from organic molecules. Since this thesis is primarily based on the use of lanthanide-based upconverting systems for the photocatalytic application, I would like to first describe very briefly the theory of such upconverting systems.

The upconversion luminescence in the lanthanides originates due to their very peculiar electronic property. They are most stable in trivalent form (Ln^{3+}) with an electronic configuration of $4f^n 5s^2 5p^6$ where n varies from 0 to 14. The inner filled $4f$ electrons in these trivalent ions are shielded by $5s^2$ and $5p^6$ subshells. This results in the reduction in electron and phonon coupling which is why the lanthanide ions show sharp and narrow emission bands. When these ions are present in a crystal matrix then due to the crystal field generation, a large number of the excited f states have a lifetime long enough so that the transition between the f - f energy levels become possible. Generally, these inorganic upconversion materials consist of a crystalline host matrix and a dopant ion (usually lanthanide ions in a small concentration). A very important parameter to be taken care of concerning such upconverting systems is the ion to ion distance and their spatial arrangement. The choice of crystalline host lattice is therefore very important as it determines the distance between the dopant ions and brings these luminescent centres to the optimal position.^{32,33} From this essential requirement we can say that the property of the host matrix and its interaction with the dopant ion is a very crucial consideration for the upconversion process. An ideal host matrix should be a) optically transparent for the particular choice of dopant ions, i.e. there should be no optical transitions concerning the matrix itself; b) they should have very low phonon energy so that the excited states can have longer lifetimes, otherwise many electronic transitions will be lost in the form of lattice vibrations.³⁴ Many choices are available as the host matrices mainly including oxides and halides. Both of these matrices have their unique virtue depending on which ideal host matrix could be chosen. Oxides usually are more stable chemically and thermally but have relatively higher phonon energy (>500 - 1000 cm^{-1}) than halides,

whereas the halides which have very low phonon energies suffer from a lack of chemical stability. Halides such as -chlorides, -bromides, and -iodides generally exhibit very low phonon energies ($<300\text{ cm}^{-1}$), but they are hygroscopic, which limits their usage in many applications. Fluorides on the other hand are best compromise with lower phonon energy ($\sim 400\text{ cm}^{-1}$) compared to oxides and more stable than other halides. This is why our study is primarily focused on fluoride based matrices.

Regarding the doping of lanthanide ions, it can be either a single ion or co-doping of two lanthanide ions. For a single ion-doped the essential requirement of the lanthanide ion is to have a similar energy gap between three or more subsequent energy levels, so that sequential absorption with a single monochromatic source could be possible. The suitable choice of lanthanide ions fulfilling these criteria are Er^{3+} , Tm^{3+} and Ho^{3+} , out of which the efficiency of Er^{3+} is particularly higher than the other two choices. To have a clearer understanding the detailed energy level diagram for a codoped system is presented in figure xxx. For such systems, one of the dopant ion, called sensitizer, absorbs excitation light, then transfers it nonradiatively to a nearby dopant ion, called an activator. After multiple energy transfer, once the activator ion's excited states have enough build-up of energy, it emits light of a shorter wavelength than the excitation source. The most common choice for sensitizer ions is Yb^{3+} ions primarily because of two reasons; a) it has single and relatively strong absorption in the visible-infrared spectrum and b) its ${}^2\text{F}_{7/2} \rightarrow {}^2\text{F}_{5/2}$ transition matches very well with electronic transitions in generally used activators such as Er^{3+} and Tm^{3+} . The concentration is an important factor because if the sensitizer concentration is too high then the cross-relaxation energy loss would overtake the average energy transfer to the activator ion, resulting in a decrease in upconversion emission. The concentration of sensitizer and activator usually should be not higher than 20-25 mol% (but X. Liu et al.³⁵ showed energy transfer even at higher doping percentage up to 50%) and 1-2 mol% respectively. For the last two decades, the major number of papers published are related to rare-earth-doped nano-fluorides. When compared with the bulk upconverting materials, the nanomaterials suffer a drawback of lower upconversion quantum yield due to greater availability of surface resulting in more surface defects. But the vast applicability of nanoparticles in a variety of domains including biological imaging, drug loading and releasing and photocatalysis etc. pushes the interest of the scientific community to have better upconversion quantum yields in nanostructures.³⁶

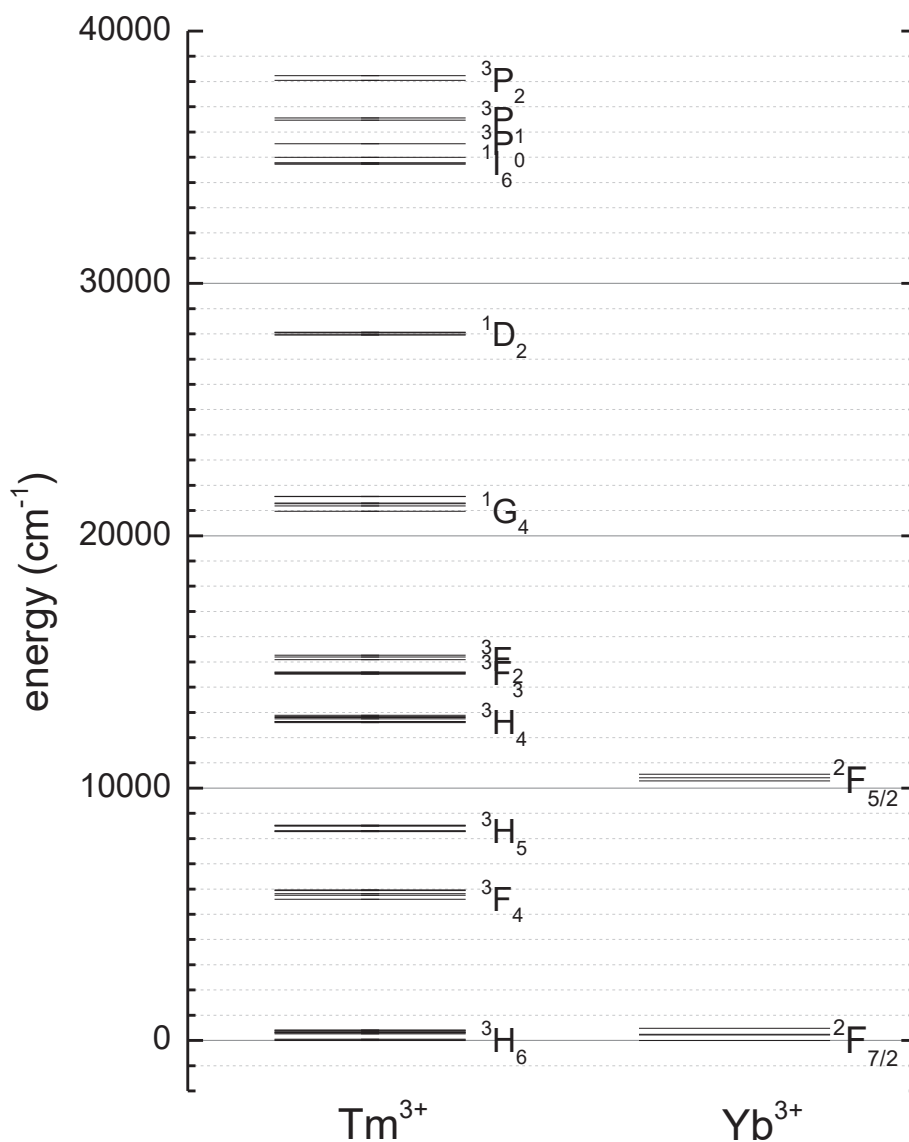


Figure 1.4: Energy level diagram for codoped Tm³⁺ and Yb³⁺ system; adapted from Dulick et al. (*Journal of Luminescence* **1991**, 48–49, 517–521) and Bensalah et al. (*Optical Materials* **2004**, 26 (4), 375–383)

i). Lanthanide trifluoride materials (LnF₃)

In the late 1960s and early 1970s, the optical properties of bulk LaF₃: Yb³⁺, Er³⁺³⁷ and bulk YF₃: Yb³⁺, Er³⁺³⁸ were studied. The first synthesis of LaF₃ nanoparticles is reported in 2001 by Dang et al.,³⁹ although for a completely different application. It motivated Stouwadam et al.⁴⁰ to synthesize a variety of combination with Er³⁺, Nd³⁺ and Ho³⁺ doped LaF₃ nanoparticles and they proposed a modified method for their preparation that led to better re-dispersibility of these nanoparticles, which is an important property that finds potential applications in the telecommunication sector.

Also, Chow, Yi et al.⁴¹ in 2005, reported Yb/Er, Yb/Ho and Yb/Tm co-doped LaF₃ with high re-dispersibility and fluorescence output. The synthesis methods for YF₃, YbF₃ have also been intensely investigated.

Yan and Li et al.⁴² also in 2005, reported a two-step synthesis procedure for Yb³⁺, Er³⁺ co-doped YF₃ nanoparticles. They reported a unique sonochemistry assisted hydrothermal route for their synthesis and demonstrated red, green and even blue emission in such system when excited with infrared light.

Similarly, many other strategies for the synthesis of lanthanide-based upconverting nanomaterials have been reported in much detail by Wang et al.⁴³, but one particular synthesis of a flexible polymeric display using YF₃: Yb³⁺/Er³⁺ system by Tsujiuchi et al.⁴⁴ has also attracted much attention.

Later on, the synthesis of LaF₃ nanocrystals by Zhang et al.⁴⁵ using single-source precursors such as La(CF₃COOH) in the mixture of oleic acid and 1-octadecene at high temperature opened up a new path towards the synthesis of sub-20 nm uniform upconverting nanoparticles.

ii). Lanthanide tetrafluoride nanoparticles (M(RE)F₄; M=Li, Na, K; RE=Rare Earth)

Upconversion based on bulk, microcrystalline and NaYF₄ has been extensively studied in the past decades and one of the very first few reports by Menyuk et al.⁴⁶ in 1972, showed great upconversion emission efficiency of a few per cent in NaYF₄: Yb, Er phosphor. In the subsequent years when the demand and availability of means of producing nanoparticles increased, many groups devoted their research to the synthesis of lanthanide-doped NaYF₄ nanoparticles. During the initial years, the most frequently studied was Ln³⁺: NaYF₄ upconverting system.

The first synthesis of small luminescent NaYF₄ nanocrystals was developed by Heer et al.⁴⁷ and was based on the co-precipitation method performed in the high boiling solvent *N*-(2-hydroxyethyl) ethylenediamine (HEEDA). They observed good upconversion efficiency for the cubic phase of Yb, Er and Yb, Tm codoped NaYF₄ nanoparticles. The size distribution however was rather broad (5-30 nm). In the same year Yi et al.⁴⁸ prepared cubic phase of Yb³⁺/Er³⁺ codoped NaYF₄ particles by co-precipitation of rare earth chlorides with NaF in the presence of EDTA (ethylenediamine tetraacetic acid). They obtained narrow size distribution but the size was ranging from 32-46 nm. Not only cubic but hexagonal phase (which has higher

upconversion efficiency) of NaYF₄: Yb³⁺, Er³⁺ were prepared in acetic acid solution by Zeng et al.,⁴⁹ their reported average particle size was 25 nm.

After 2005, considerable focus was given to the method based on thermal decomposition of metal trifluoroacetates (single-source precursors) given originally by Zhang et al.⁴⁵ The main advantage of utilizing single-source precursors of trifluoroacetates is the quick formation of fluorine compounds at a higher temperature. There were many reports which utilize a slightly modified method for the preparation of NaLnF₄ than the one described by Zhang et al.⁴⁵ The first one after was given by Yi et al.⁵⁰ in 2006 where they prepared sub-10 nm NaYF₄:Yb³⁺, Er³⁺ nanoparticles by thermal decomposition in pure oleylamine at around 330°C. These particles had excellent dispersibility in organic solvents, were uniform in shape and also showed a narrow size distribution.

The following year, Boyer et al.⁵¹ reported the synthesis of both Yb, Er and Yb, Tm doped monodispersible NaYF₄ nanocrystals with an average size of ~27 nm via thermal decomposition in the mixture of octadecene and oleic acid. In 2009, Zhang et al.⁵² reported a different method of preparation of hexagonal NaYF₄ by replacing metal trifluoroacetates with in-situ produced rare-earth oleates, NaOH and NH₄F.

However, in 2010, the synthesis of new single-source heterometallic precursors by Mishra et al.⁵³ opened up new prospects for the synthesis of sub-50 nm particles without the need of any surfactant or capping agent. His approach of controlled synthesis could result in either cubic or hexagonal phase NaYF₄ nanocrystals just by varying the decomposition temperature. The approach was unique also in the sense that since the reaction was carried out in an inert atmosphere and all the precursors chosen, were anhydrous, it significantly reduced the surface OH groups, as evident from their results. This thesis also presents some results (chapter 2) emphasizing the improved quality of upconverting nanoparticles compared to identically doped nanoparticles prepared by other synthetic techniques. In 2012, Mishra et al.⁵⁴ and his group reported a detailed study about the synthesis of the novel heterometal organic complex as the first single-source precursors for upconverting nanoparticle synthesis. He reported the improved thermal response of such anhydrous hetero-metallic complexes over the widely used hydrated precursors. In 2014, using similar single-source precursors, Chen et al.⁵⁵ reported a direct synthetic method for Yb³⁺, Tm³⁺ doped NaGdF₄. The quality of nanoparticles prepared via this technique was very good, considering the results presented by them

regarding their nanocomposite formation with TiO_2 and the subsequent performance in direct sunlight.

In addition to these thermal decomposition methods, other synthetic procedures such as hydrothermal and microwave-assisted synthesis also gained interest in these years. Wang et al.⁵⁶ have studied extensively the solvothermal synthesis of lanthanide fluoride-based materials LnF_3 and NaLnF_4 . When they reacted $\text{Ln}(\text{NO}_3)_3$ and NH_4F at pH 4-5 in the temperature range of 80-180 °C, they obtained hollow structures. The pioneering work by Wang et al.⁴³ in 2005, for synthesizing a new method based on liquid-solid-solution (LSS) growth for the synthesis of lanthanide fluoride materials is also worth mentioning. Their synthesis was based on a phase transfer and separation occurring at the interfaces of the liquid-solid and solid-solution phases. Using microwave synthetic method, Wang, Nann et al.^{57,58} synthesized oleate capped nanoparticles of NaYF_4 , $\text{Na}(\text{Li})\text{YF}_4$, and LiYF_4 at 290 °C in only 5 min under microwave irradiation. The nanoparticles obtained are of cubic phase with a particle size of 10 nm. They further extended this study and investigated the effect of reaction parameters such as time, concentration etc.

While in the last decade the majority of works have focused on NaYF_4 / NaGdF_4 or LnF_3 hosts,^{59,60} there have been some reports on other alternative hosts, such as LnOF , KYF_4 , BaYF_3 and LiYF_4 . The LiYF_4 can provide very large anti-Stokes emission up to the deep UV (265 nm), and hence can be used to overcome many challenges including undesirable non-radiative energy transfer, cross-relaxations etc. To the best of our knowledge, for the first time, Yi et al.⁶¹ in 2007, reported the synthesis of LiYF_4 : Yb^{3+} , Er^{3+} nanoparticles using trifluoroacetate precursors. The ideal reaction temperature for the synthesis of crystalline LiYF_4 as suggested by them was however very high (340 °C).

Later in 2009, Mahalingam et al.⁶² synthesized tetragonal phase LiYF_4 nanoparticles with diamond shape with a very narrow size distribution (average size ~80 nm). Another very detailed upconversion energy transfer analysis in Er^{3+} , Yb^{3+} doped LiYF_4 nanocrystals was done by Secu et al.⁶³ showing the effect of a high concentration of lanthanide ions ceramic glasses

After going through the history of upconverting nanoparticle synthesis, we come back to our motivation behind the use of upconversion for photocatalysis. In the context of upconversion semiconductor-based photocatalyst, the upconversion materials could serve as the frequency converters that can harvest low energy sub-bandgap photons and convert them to UV or vis photons via an efficient fluorescent energy transfer process. Following this, the converted photons can be

reabsorbed by the surrounding semiconductor and thus can induce the electron-hole pair separation in the semiconductor. A more efficient and direct transfer of energy from upconverting material to the surrounding semiconductor via non-radiative transfer could increase the yield of charge carriers in the classical semiconductor and therefore would be the potential solution of our problem of non-utilization of low energy photons of the solar spectrum. In other words, including upconversion materials with TiO₂ will extend the absorption edge up to the NIR region and therefore higher photocatalytic efficiency could be achieved. By looking at the great virtue of upconverting materials a lot of work has been done in photocatalysis, most of which is devoted to pollutant removal (dye degradation). The recent World Bank data (2011) states that discharge from the textile industries accounts for nearly 20% of the total industrial pollution.⁶⁴ Hence research community have taken some serious steps towards pollutant removal using eco-friendly strategies. Although, in the photocatalysis community, it is a matter of great debate about the similarity and dissimilarity between classical photocatalysis and photocatalytic degradation of organic pollutants. It is worth mentioning that the mechanism of absorption of photons and the charge carrier dynamics are very much identical in both of these cases.⁶⁵

The core-shell nanostructures have been explored for many photocatalytic dye degradation studies due to the added benefit of size and morphological control. In this regard, Zhang et al.⁶⁶ in 2013, presented a facile hydrothermal route for the synthesis of NaYF₄: Yb³⁺, Tm³⁺@TiO₂ core-shell nanocomposites. The micro rods prepared by this method showed excellent photocatalytic activity towards methylene blue degradation (~90% degradation in 12h under 980 nm NIR laser irradiation). They emphasized the importance of optimal thickness of TiO₂ coating on the upconverting material.

Another report concerning the degradation of methylene blue (MB) using near-infrared radiation was presented by Tang et al.⁶⁷ in 2013. They synthesized NaYF₄: Yb³⁺, Tm³⁺@TiO₂ composite via solvothermal route. They presented a NIR-responsive photocatalytic mechanism that could be helpful for the structural design and functionality of such composite materials.

The NIR induced photocatalytic mechanism for the degradation of Rhodamine B (RhB) was given by Wang et al.⁶⁸ They compared the photocatalytic activity of core-shell and physical mixture of the composite of upconverting nanoparticles and TiO₂. The better utilization of NIR light for photocatalysis was observed in core-shell nanocomposites.

More studies on the decolouration of Methylene Blue, Methyl Orange and Rhodamine B was carried out under 980 nm laser irradiation by Xu et al.,⁶⁹ Chatti et al.⁷⁰

In 2014, Chen et al.⁵⁵ reported the enhanced photocatalytic performance (towards methylene blue degradation) of upconverting nanoparticle modified TiO₂ (14.5%) compared to classical TiO₂ (4.5%) under direct sunlight. Their research focused more on maximizing the upconversion from the nanoparticles for their further utilization by TiO₂. Their reports about the degradation of MB under direct sunlight shows potential for real-life photocatalytic applications.

Later on, in 2015, Su et al.⁷¹ reported the synthesis of uniform coating over hydrophobic NaYF₄: Yb³⁺, Tm³⁺ nanoplates and demonstrated the photocatalytic activity under near-infrared as well as ultraviolet lights source. They emphasized the effect of both upconversion fluorescence of the core and surface properties of the shell on photocatalytic activities.

With continuous progress over years, researchers came up with enhanced upconversion and therefore higher photoactivity from ternary and even quaternary photocatalysts. Wang et al.⁷³ reported a new strategy of integrating NaYF₄: Yb, Tm@core shell structures with graphene for demonstrating enhanced NIR driven photocatalysis. They reported significantly degradation of MB (81% in 12h), MO (46% in 12h) and phenol (30% in 12h) under NIR irradiation.

To summarize the key points from the state of the art, we can conclude that to achieve efficient solar photocatalysis using upconverting nanomaterials (as the frequency convertors) and their incorporation with classical photocatalyst such as titania (TiO₂), there are several key points to be kept in mind. The primary concern to deal with should be to enhance and maximize the upconversion emission from the system as much as possible. Many strategies have been suggested to deal with this issue, but they still need improvement. The secondary concern that needed to be addressed is the interaction of these upconverting nanoparticles (UCNPs) with the photocatalyst. The energy transfer between UCNPs and TiO₂ need to be optimized.

In this thesis, we tried to address some of these issues in details such as obtaining an upconverting nanomaterial system with its performance equivalent to the bulk upconverting phosphor. This is achieved by using anhydrous molecular precursors for their synthesis. The second issue we addressed is the optimization of the UCNPs-TiO₂ junction. As we saw from the recent studies that the coupling between TiO₂ and UCNPs should be efficient enough so that most significant losses

could be overcome, we, in this thesis explored many different strategies that could potentially improve the UCNPs-TiO₂ junction and thus our aim of direct utilization of sunlight would become feasible.

1.4. References

- (1) Dincer, I. Renewable Energy and Sustainable Development: A Crucial Review. *Renewable and Sustainable Energy Reviews* **2000**, *4* (2), 157–175. [https://doi.org/10.1016/S1364-0321\(99\)00011-8](https://doi.org/10.1016/S1364-0321(99)00011-8).
- (2) Nozik, A. J.; Miller, J. Introduction to Solar Photon Conversion. *Chem. Rev.* **2010**, *110* (11), 6443–6445. <https://doi.org/10.1021/cr1003419>.
- (3) Spasiano, D.; del Pilar Prieto Rodriguez, L.; Olleros, J. C.; Malato, S.; Marotta, R.; Andreozzi, R. TiO₂/Cu(II) Photocatalytic Production of Benzaldehyde from Benzyl Alcohol in Solar Pilot Plant Reactor. *Applied Catalysis B: Environmental* **2013**, *136–137*, 56–63. <https://doi.org/10.1016/j.apcatb.2013.01.055>.
- (4) *Applications of Titanium Dioxide Photocatalysis to Construction Materials*; Ohama, Y., Van Gemert, D., Eds.; Springer Netherlands: Dordrecht, **2011**. <https://doi.org/10.1007/978-94-007-1297-3>.
- (5) Ismail, A. A.; Bahnemann, D. W. Photochemical Splitting of Water for Hydrogen Production by Photocatalysis: A Review. *Solar Energy Materials and Solar Cells* **2014**, *128*, 85–101. <https://doi.org/10.1016/j.solmat.2014.04.037>.
- (6) Yaoguang, Y. Recent Advances in Rare-Earth Elements Modification of Inorganic Semiconductor-Based Photocatalysts for Efficient Solar Energy Conversion: A Review. *JOURNAL OF RARE EARTHS* **2015**, *33* (5), 10.
- (7) Photocatalysts: Technologies and Global Markets: AVM069B | BCC Research <https://www.bccresearch.com/market-research/advanced-materials/photocatalysts-technologies-markets-report.html>.
- (8) Navío, J. A.; Colón, G.; Macías, M.; Real, C.; Litter, M. I. Iron-Doped Titania Semiconductor Powders Prepared by a Sol-Gel Method. Part I: Synthesis and Characterization. *Applied Catalysis A: General* **1999**, *177* (1), 111–120. [https://doi.org/10.1016/S0926-860X\(98\)00255-5](https://doi.org/10.1016/S0926-860X(98)00255-5).
- (9) Yuan, Z.; Jia, J.; Zhang, L. Influence of Co-Doping of Zn(II)+Fe(III) on the Photocatalytic Activity of TiO₂ for Phenol Degradation. *Materials Chemistry and Physics* **2002**, *73* (2), 323–326. [https://doi.org/10.1016/S0254-0584\(01\)00373-X](https://doi.org/10.1016/S0254-0584(01)00373-X).

- (10) Chao, H. E.; Yun, Y. U.; Xingfang, H. U.; Larbot, A. Effect of Silver Doping on the Phase Transformation and Grain Growth of Sol-Gel Titania Powder. *Journal of the European Ceramic Society* **2003**, *23* (9), 1457–1464. [https://doi.org/10.1016/S0955-2219\(02\)00356-4](https://doi.org/10.1016/S0955-2219(02)00356-4).
- (11) Seery, M. K.; George, R.; Floris, P.; Pillai, S. C. Silver Doped Titanium Dioxide Nanomaterials for Enhanced Visible Light Photocatalysis. *Journal of Photochemistry and Photobiology A: Chemistry* **2007**, *189* (2), 258–263. <https://doi.org/10.1016/j.jphotochem.2007.02.010>.
- (12) Yamashita, H.; Harada, M.; Misaka, J.; Takeuchi, M.; Ikeue, K.; Anpo, M. Degradation of Propanol Diluted in Water under Visible Light Irradiation Using Metal Ion-Implanted Titanium Dioxide Photocatalysts. *Journal of Photochemistry and Photobiology A: Chemistry* **2002**, *148* (1), 257–261. [https://doi.org/10.1016/S1010-6030\(02\)00051-5](https://doi.org/10.1016/S1010-6030(02)00051-5).
- (13) Tseng, I.-H.; Chang, W.-C.; Wu, J. C. S. Photoreduction of CO₂ Using Sol-Gel Derived Titania and Titania-Supported Copper Catalysts. *Applied Catalysis B: Environmental* **2002**, *37* (1), 37–48. [https://doi.org/10.1016/S0926-3373\(01\)00322-8](https://doi.org/10.1016/S0926-3373(01)00322-8).
- (14) Choi, H.; Antoniou, M. G.; Pelaez, M.; de la Cruz, A. A.; Shoemaker, J. A.; Dionysiou, D. D. Mesoporous Nitrogen-Doped TiO₂ for the Photocatalytic Destruction of the Cyanobacterial Toxin Microcystin-LR under Visible Light Irradiation. *Environ. Sci. Technol.* **2007**, *41* (21), 7530–7535. <https://doi.org/10.1021/es0709122>.
- (15) Mishra, S.; Du, D.; Jeanneau, E.; Dappozze, F.; Guillard, C.; Zhang, J.; Daniele, S. A Facile Molecular Precursor-Based Synthesis of Ag₂Se Nanoparticles and Its Composites with TiO₂ for Enhanced Photocatalytic Activity. *Chemistry – An Asian Journal* **2016**, *11* (11), 1658–1663. <https://doi.org/10.1002/asia.201600157>.
- (16) Lin, J.; Yu, J. C. An Investigation on Photocatalytic Activities of Mixed TiO₂-Rare Earth Oxides for the Oxidation of Acetone in Air. *Journal of Photochemistry and Photobiology A: Chemistry* **1998**, *116* (1), 63–67. [https://doi.org/10.1016/S1010-6030\(98\)00289-5](https://doi.org/10.1016/S1010-6030(98)00289-5).
- (17) Du, P.; Bueno-López, A.; Verbaas, M.; Almeida, A. R.; Makkee, M.; Moulijn, J. A.; Mul, G. The Effect of Surface OH-Population on the Photocatalytic Activity of Rare Earth-Doped P25-TiO₂ in Methylene Blue Degradation. *Journal of Catalysis* **2008**, *260* (1), 75–80. <https://doi.org/10.1016/j.jcat.2008.09.005>.

- (18) Fan, C.; Xue, P.; Sun, Y. Preparation of Nano-TiO₂ Doped with Cerium and Its Photocatalytic Activity. *Journal of Rare Earths* **2006**, *24* (3), 309–313. [https://doi.org/10.1016/S1002-0721\(06\)60115-4](https://doi.org/10.1016/S1002-0721(06)60115-4).
- (19) Ranjit, K. T.; Cohen, H.; Willner, I.; Bossmann, S.; Braun, A. M. Lanthanide Oxide-Doped Titanium Dioxide: Effective Photocatalysts for the Degradation of Organic Pollutants. *Journal of Materials Science* **1999**, *34* (21), 5273–5280. <https://doi.org/10.1023/A:1004780401030>.
- (20) Bloembergen, N. Solid State Infrared Quantum Counters. *Phys. Rev. Lett.* **1959**, *2* (3), 84–85. <https://doi.org/10.1103/PhysRevLett.2.84>.
- (21) Auzel, F. History of Upconversion Discovery and Its Evolution. *Journal of Luminescence* **2020**, *223*, 116900. <https://doi.org/10.1016/j.jlumin.2019.116900>.
- (22) Parker, C. A.; Hatchard, C. G. Sensitised Anti-Stokes Delayed Fluorescence. *Proc. Chem. Soc.* **1962**, 386–387.
- (23) Schulze, T. F.; Schmidt, T. W. Photochemical Upconversion: Present Status and Prospects for Its Application to Solar Energy Conversion. *Energy Environ. Sci.* **2014**, *8* (1), 103–125. <https://doi.org/10.1039/C4EE02481H>.
- (24) Balushev, S.; Miteva, T.; Yakutkin, V.; Nelles, G.; Yasuda, A.; Wegner, G. Up-Conversion Fluorescence: Noncoherent Excitation by Sunlight. *Phys. Rev. Lett.* **2006**, *97* (14), 143903. <https://doi.org/10.1103/PhysRevLett.97.143903>.
- (25) Frazer, L.; Gallaher, J. K.; Schmidt, T. W. Optimizing the Efficiency of Solar Photon Upconversion. *ACS Energy Lett.* **2017**, *2* (6), 1346–1354. <https://doi.org/10.1021/acsenergylett.7b00237>.
- (26) Schulze, T. F.; Czolk, J.; Cheng, Y.-Y.; Fückel, B.; MacQueen, R. W.; Khoury, T.; Crossley, M. J.; Stannowski, B.; Lips, K.; Lemmer, U.; Colsmann, A.; Schmidt, T. W. Efficiency Enhancement of Organic and Thin-Film Silicon Solar Cells with Photochemical Upconversion. *J. Phys. Chem. C* **2012**, *116* (43), 22794–22801. <https://doi.org/10.1021/jp309636m>.
- (27) Khnayzer, R. S.; Blumhoff, J.; Harrington, J. A.; Haefele, A.; Deng, F.; Castellano, F. N. Upconversion-Powered Photoelectrochemistry. *Chem. Commun.* **2011**, *48* (2), 209–211. <https://doi.org/10.1039/C1CC16015J>.

- (28) Kim, J.-H.; Kim, J.-H. Encapsulated Triplet–Triplet Annihilation-Based Upconversion in the Aqueous Phase for Sub-Band-Gap Semiconductor Photocatalysis. *J. Am. Chem. Soc.* **2012**, *134* (42), 17478–17481. <https://doi.org/10.1021/ja308789u>.
- (29) Kim, H.; Kwon, O. S.; Kim, S.; Choi, W.; Kim, J.-H. Harnessing Low Energy Photons (635 nm) for the Production of H₂O₂ Using Upconversion nanohybrid photocatalysts. *Energy Environ. Sci.* **2016**, *9* (3), 1063–1073. <https://doi.org/10.1039/C5EE03115J>.
- (30) Kwon, O. S.; Kim, J.-H.; Cho, J. K.; Kim, J.-H. Triplet–Triplet Annihilation Upconversion in CdS-Decorated SiO₂ Nanocapsules for Sub-Bandgap Photocatalysis. *ACS Appl. Mater. Interfaces* **2015**, *7* (1), 318–325. <https://doi.org/10.1021/am506233h>.
- (31) Pedrini, J.; Monguzzi, A. Recent Advances in the Application Triplet–Triplet Annihilation-Based Photon Upconversion Systems to Solar Technologies. *JPE* **2017**, *8* (2), 022005. <https://doi.org/10.1117/1.JPE.8.022005>.
- (32) Aebischer, A.; Heer, S.; Biner, D.; Krämer, K.; Haase, M.; Güdel, H. U. Visible Light Emission upon Near-Infrared Excitation in a Transparent Solution of Nanocrystalline β -NaGdF₄: Yb³⁺, Er³⁺. *Chemical Physics Letters* **2005**, *407* (1), 124–128. <https://doi.org/10.1016/j.cplett.2005.03.053>.
- (33) Krämer, K. W.; Biner, D.; Frei, G.; Güdel, H. U.; Hehlen, M. P.; Lüthi, S. R. Hexagonal Sodium Yttrium Fluoride Based Green and Blue Emitting Upconversion Phosphors. *Chem. Mater.* **2004**, *16* (7), 1244–1251. <https://doi.org/10.1021/cm031124o>.
- (34) Schäfer, H.; Ptacek, P.; Kömpe, K.; Haase, M. Lanthanide-Doped NaYF₄ Nanocrystals in Aqueous Solution Displaying Strong Up-Conversion Emission. *Chem. Mater.* **2007**, *19* (6), 1396–1400. <https://doi.org/10.1021/cm062385b>.
- (35) Wang, F.; Deng, R.; Wang, J.; Wang, Q.; Han, Y.; Zhu, H.; Chen, X.; Liu, X. Tuning Upconversion through Energy Migration in Core-Shell Nanoparticles. *Nature Materials* **2011**, *10* (12), 968–973. <https://doi.org/10.1038/nmat3149>.
- (36) Ledoux, G.; Joubert, M. F.; Mishra, S. Upconversion Phenomena in Nanofluorides. In *Photonic and Electronic Properties of Fluoride Materials*; Tressaud, A., Poeppelmeier, K., Eds.; Elsevier: Boston, **2016**; pp 35–63. <https://doi.org/10.1016/B978-0-12-801639-8.00003-9>.

- (37) Hewes, R. A.; Sarver, J. F. Infrared Excitation Processes for the Visible Luminescence of Er³⁺, Ho³⁺, and Tm³⁺ in Yb³⁺-Sensitized Rare-Earth Trifluorides. *Phys. Rev.* **1969**, *182* (2), 427–436. <https://doi.org/10.1103/PhysRev.182.427>.
- (38) Auzel, F.; Pecile, D. Comparison and Efficiency of Materials for Summation of Photons Assisted by Energy Transfer. *Journal of Luminescence* **1973**, *8* (1), 32–43. [https://doi.org/10.1016/0022-2313\(73\)90033-1](https://doi.org/10.1016/0022-2313(73)90033-1).
- (39) Zhou, J.; Wu, Z.; Zhang, Z.; Liu, W.; Dang, H. Study on an Antiwear and Extreme Pressure Additive of Surface Coated LaF₃ Nanoparticles in Liquid Paraffin. *Wear* **2001**, *249* (5), 333–337. [https://doi.org/10.1016/S0043-1648\(00\)00547-0](https://doi.org/10.1016/S0043-1648(00)00547-0).
- (40) Stouwdam, J. W.; van Veggel, F. C. J. M. Near-Infrared Emission of Redispersible Er³⁺, Nd³⁺, and Ho³⁺ Doped LaF₃ Nanoparticles. *Nano Lett.* **2002**, *2* (7), 733–737. <https://doi.org/10.1021/nl025562q>.
- (41) Yi, G.-S.; Chow, G.-M. Colloidal LaF₃: Yb, Er, LaF₃: Yb, Ho and LaF₃: Yb, Tm Nanocrystals with Multicolor Upconversion Fluorescence. *J. Mater. Chem.* **2005**, *15* (41), 4460–4464. <https://doi.org/10.1039/B508240D>.
- (42) Yan, R. X.; Li, Y. D. Down/Up-Conversion in Ln³⁺-Doped YF₃ Nanocrystals. *Advanced Functional Materials* **2005**, *15* (5), 763–770. <https://doi.org/10.1002/adfm.200305044>.
- (43) Wang, X.; Zhuang, J.; Peng, Q.; Li, Y. A General Strategy for Nanocrystal Synthesis. *Nature* **2005**, *437* (7055), 121–124. <https://doi.org/10.1038/nature03968>.
- (44) Tsujiuchi, K.; Okada, A.; Matssuura, D.; Soga, K. Development of Flexible and Transparent Upconversion Display by Using Polymer-Ceramics Composite. *J. Photopol. Sci. Technol.* **2009**, *22* (4), 541–546. <https://doi.org/10.2494/photopolymer.22.541>.
- (45) Zhang, Y.-W.; Sun, X.; Si, R.; You, L.-P.; Yan, C.-H. Single-Crystalline and Monodisperse LaF₃ Triangular Nanoplates from a Single-Source Precursor. *J. Am. Chem. Soc.* **2005**, *127* (10), 3260–3261. <https://doi.org/10.1021/ja042801y>.
- (46) Menyuk, N.; Dwight, K.; Pierce, J. W. NaYF₄: Yb, Er—an Efficient Upconversion Phosphor. *Appl. Phys. Lett.* **1972**, *21* (4), 159–161. <https://doi.org/10.1063/1.1654325>.
- (47) Heer, S.; Kömpe, K.; Güdel, H.-U.; Haase, M. Highly Efficient Multicolour Upconversion Emission in Transparent Colloids of Lanthanide-Doped NaYF₄ Nanocrystals. *Advanced Materials* **2004**, *16* (23–24), 2102–2105. <https://doi.org/10.1002/adma.200400772>.

- (48) Yi, G.; Lu, H.; Zhao, S.; Ge, Y.; Yang, W.; Chen, D.; Guo, L.-H. Synthesis, Characterization, and Biological Application of Size-Controlled Nanocrystalline NaYF₄: Yb, Er Infrared-to-Visible Up-Conversion Phosphors. *Nano Lett.* **2004**, *4* (11), 2191–2196. <https://doi.org/10.1021/nl048680h>.
- (49) Zeng, J.-H.; Su, J.; Li, Z.-H.; Yan, R.-X.; Li, Y.-D. Synthesis and Upconversion Luminescence of Hexagonal-Phase NaYF₄: Yb³⁺, Er³⁺ Phosphors of Controlled Size and Morphology. *Advanced Materials* **2005**, *17* (17), 2119–2123. <https://doi.org/10.1002/adma.200402046>.
- (50) Yi, G. S.; Chow, G. M. Synthesis of Hexagonal-Phase NaYF₄: Yb, Er and NaYF₄: Yb, Tm Nanocrystals with Efficient Up-Conversion Fluorescence. *Advanced Functional Materials* **2006**, *16* (18), 2324–2329. <https://doi.org/10.1002/adfm.200600053>.
- (51) Boyer, J.-C.; Cuccia, L. A.; Capobianco, J. A. Synthesis of Colloidal Upconverting NaYF₄: Er³⁺/Yb³⁺ and Tm³⁺/Yb³⁺ Monodisperse Nanocrystals. *Nano Lett.* **2007**, *7* (3), 847–852. <https://doi.org/10.1021/nl070235+>.
- (52) Zhang, Y. Y.; Yang, L. W.; Han, H. L.; Zhong, J. X. Excitation Power Controlled Luminescence Switching in Yb³⁺–Tm³⁺ Co-Doped Hexagonal NaYF₄ Nanorods. *Optics Communications* **2009**, *282* (14), 2857–2860. <https://doi.org/10.1016/j.optcom.2009.04.027>.
- (53) Mishra, S.; Daniele, S.; Ledoux, G.; Jeanneau, E.; Joubert, M.-F. Heterometallic Na–Y(Ln) Trifluoroacetate Diglyme Complexes as Novel Single-Source Precursors for Upconverting NaYF₄ Nanocrystals Co-Doped with Yb and Er/Tm Ions. *Chem. Commun.* **2010**, *46* (21), 3756–3758. <https://doi.org/10.1039/B921474G>.
- (54) Mishra, S.; Ledoux, G.; Jeanneau, E.; Daniele, S.; Joubert, M.-F. Novel Heterometal-Organic Complexes as First Single Source Precursors for Up-Converting NaY(Ln)F₄ (Ln = Yb, Er, Tm) Nanomaterials. *Dalton Trans.* **2012**, *41* (5), 1490–1502. <https://doi.org/10.1039/C1DT11070E>.
- (55) Chen, Y.; Mishra, S.; Ledoux, G.; Jeanneau, E.; Daniel, M.; Zhang, J.; Daniele, S. Direct Synthesis of Hexagonal NaGdF₄ Nanocrystals from a Single-Source Precursor: Upconverting NaGdF₄:Yb³⁺, Tm³⁺ and Its Composites with TiO₂ for Near-IR-Driven Photocatalysis. *Chemistry – An Asian Journal* **2014**, *9* (9), 2415–2421. <https://doi.org/10.1002/asia.201402347>.
- (56) Wang, X.; Zhuang, J.; Peng, Q.; Li, Y. Hydrothermal Synthesis of Rare-Earth Fluoride Nanocrystals. *Inorg. Chem.* **2006**, *45* (17), 6661–6665. <https://doi.org/10.1021/ic051683s>.

- (57) Wang, H.-Q.; Nann, T. Monodisperse Upconverting Nanocrystals by Microwave-Assisted Synthesis. *ACS Nano* **2009**, *3* (11), 3804–3808. <https://doi.org/10.1021/nn9012093>.
- (58) Wang, H.-Q.; Tilley, R. D.; Nann, T. Size and Shape Evolution of Upconverting Nanoparticles Using Microwave-Assisted Synthesis. *CrystEngComm* **2010**, *12* (7), 1993–1996. <https://doi.org/10.1039/B927225A>.
- (59) Niu, W.; Wu, S.; Zhang, S.; Li, L. Synthesis of Colour Tunable Lanthanide-Ion Doped NaYF₄ Upconversion Nanoparticles by Controlling Temperature. *Chem. Commun.* **2010**, *46* (22), 3908–3910. <https://doi.org/10.1039/C002615H>.
- (60) Shan, J.; Ju, Y. Controlled Synthesis of Lanthanide-Doped NaYF₄ Upconversion Nanocrystals via Ligand Induced Crystal Phase Transition and Silica Coating. *Appl. Phys. Lett.* **2007**, *91* (12), 123103. <https://doi.org/10.1063/1.2783476>.
- (61) Yi, G. S.; Lee, W. B.; Chow, G. M. Synthesis of LiYF₄, BaYF₅, and NaLaF₄ Optical Nanocrystals. *Journal of Nanoscience and Nanotechnology* **2007**, *7* (8), 2790–2794. <https://doi.org/10.1166/jnn.2007.638>.
- (62) Mahalingam, V.; Vetrone, F.; Naccache, R.; Speghini, A.; Capobianco, J. A. Colloidal Tm³⁺/Yb³⁺-Doped LiYF₄ Nanocrystals: Multiple Luminescence Spanning the UV to NIR Regions via Low-Energy Excitation. *Advanced Materials* **2009**, *21* (40), 4025–4028. <https://doi.org/10.1002/adma.200901174>.
- (63) Secu, M.; Secu, C. E. Up-Conversion Luminescence of Er³⁺/Yb³⁺ Co-Doped LiYF₄ Nanocrystals in Sol-Gel Derived Oxyfluoride Glass-Ceramics. *Journal of Non-Crystalline Solids* **2015**, *426*, 78–82. <https://doi.org/10.1016/j.jnoncrysol.2015.07.010>.
- (64) Chan, S. H. S.; Wu, T. Y.; Juan, J. C.; Teh, C. Y. Recent Developments of Metal Oxide Semiconductors as Photocatalysts in Advanced Oxidation Processes (AOPs) for Treatment of Dye Waste-Water. *Journal of Chemical Technology & Biotechnology* **2011**, *86* (9), 1130–1158. <https://doi.org/10.1002/jctb.2636>.
- (65) Pasternak, S.; Paz, Y. On the Similarity and Dissimilarity between Photocatalytic Water Splitting and Photocatalytic Degradation of Pollutants. *ChemPhysChem* **2013**, *14* (10), 2059–2070. <https://doi.org/10.1002/cphc.201300247>.

- (66) Zhang, Y.; Hong, Z. Synthesis of Lanthanide-Doped NaYF₄@TiO₂ Core-Shell Composites with Highly Crystalline and Tunable TiO₂ Shells under Mild Conditions and Their Upconversion-Based Photocatalysis. *Nanoscale* **2013**, 5 (19), 8930–8933. <https://doi.org/10.1039/C3NR03051B>.
- (67) Tang, Y.; Di, W.; Zhai, X.; Yang, R.; Qin, W. NIR-Responsive Photocatalytic Activity and Mechanism of NaYF₄: Yb, Tm@TiO₂ Core-Shell Nanoparticles. *ACS Catal.* **2013**, 3 (3), 405–412. <https://doi.org/10.1021/cs300808r>.
- (68) Wang, W.; Ding, M.; Lu, C.; Ni, Y.; Xu, Z. A Study on Upconversion UV–Vis–NIR Responsive Photocatalytic Activity and Mechanisms of Hexagonal Phase NaYF₄: Yb³⁺, Tm³⁺@TiO₂ Core-Shell Structured Photocatalyst. *Applied Catalysis B: Environmental* **2014**, 144, 379–385. <https://doi.org/10.1016/j.apcatb.2013.07.035>.
- (69) Xu, D.-X.; Lian, Z.-W.; Fu, M.-L.; Yuan, B.; Shi, J.-W.; Cui, H.-J. Advanced Near-Infrared-Driven Photocatalyst: Fabrication, Characterization, and Photocatalytic Performance of β-NaYF₄:Yb³⁺, Tm³⁺@TiO₂ Core@shell Microcrystals. *Applied Catalysis B: Environmental* **2013**, 142–143, 377–386. <https://doi.org/10.1016/j.apcatb.2013.05.062>.
- (70) Chatti, M.; Adusumalli, V. N. K. B.; Ganguli, S.; Mahalingam, V. Near-Infrared Light Triggered Superior Photocatalytic Activity from MoS₂–NaYF₄:Yb³⁺/Er³⁺ Nanocomposites. *Dalton Trans.* **2016**, 45 (31), 12384–12392. <https://doi.org/10.1039/C6DT02548J>.
- (71) Su, W.; Zheng, M.; Li, L.; Wang, K.; Qiao, R.; Zhong, Y.; Hu, Y.; Li, Z. Directly Coat TiO₂ on Hydrophobic NaYF₄:Yb, Tm Nanoplates and Regulate Their Photocatalytic Activities with the Core Size. *J. Mater. Chem. A* **2014**, 2 (33), 13486–13491. <https://doi.org/10.1039/C4TA02756F>.

Chapter 2 Synthesis and upconversion studies of NaGdF₄:Yb³⁺, Tm³⁺ nanoparticles: A comparison of anhydrous versus hydrous synthesis

2.1. Introduction

Lanthanide-doped up-converting nanocrystals are proven to be very efficient luminescent materials primarily because of their narrow and sharp emission bands along with a longer lifetime of excited states. These properties give them a distinct advantage over conventional organic fluorophores and quantum dots for their potential applications in solar cells,^{1,2} biological imaging labelling and sensing,³⁻⁷ photodynamic therapy (PDT),^{4,8,9} theranostic¹⁰⁻¹⁴ and photo catalysis¹⁵⁻²⁰ etc. In this regard, the enhancement of the optical output of these lanthanide-doped luminescent materials is of utmost priority. General criteria for achieving this goal include i) selection of a suitable host matrix with low phonon energy (e.g., metal fluoride), ii) selection of an efficient crystal phase and iii) optimization of the concentration of doping lanthanide ions.²¹ But compared to conventional phosphors, the quantum yields of these lanthanide-based UC nanoparticles are extremely low (typically <1%) and, in general, an order of magnitude lower than those of the corresponding upconversion bulk materials.²² The insufficient emission intensity (due to weak absorption of excitation light by lanthanide ions) and transfer of energy *via* a non-radiative energy route (due to complex arrangement of energy levels), which are considered as a major cause for the low quantum yield of nanoparticles can be mitigated by carefully choosing the synthetic strategy for these UC nanomaterials, hence allowing better control over particle size, shape, dispersion and surface properties, which influence all upconversion emission properties.²³⁻²⁵ Bottom-up synthesis of nanomaterials using a precursor that contains all the constituent elements in the required ratio (single-source precursor), facilitates better control over the composition, structure and morphology of nanomaterials.²⁶⁻³² The enhancement in the functionality of these nanoparticles does not come just by taking care of these aforementioned parameters but rather by avoiding the surface defects which might be induced due to the presence of ligands or solvents around the nanoparticles. One of the primary cause of luminescence quenching is -OH defects.³³ So the absence of water during the synthesis of upconverting nanoparticles is highly desirable to obtain nanoparticles with high emission luminescence. It is generally accepted that the construction of a shell of silica or undoped matrix (e.g., NaYF₄, NaGdF₄, etc.) around the upconverting core is an effective way to improve the upconversion luminescence of the UCNPs by confining Ln³⁺ dopant ions to the inner core, thus reducing non-radiative transitions.³⁴⁻³⁷ However, this strategy

cannot be used universally for all types of applications, especially for those requiring construction of additional layers of another material or necessitating short distances given specific interactions with grafted species, e.g., in photocatalysis.³⁸ Since our interest in lanthanide-based UC materials is motivated by the potential application of TiO₂@UCNPs type core-shell structure for IR-induced photocatalysis,¹⁵ we have focused on the synthesis of smaller UC particles with strong emission without having a silica surface passivation layer or an undoped matrix.

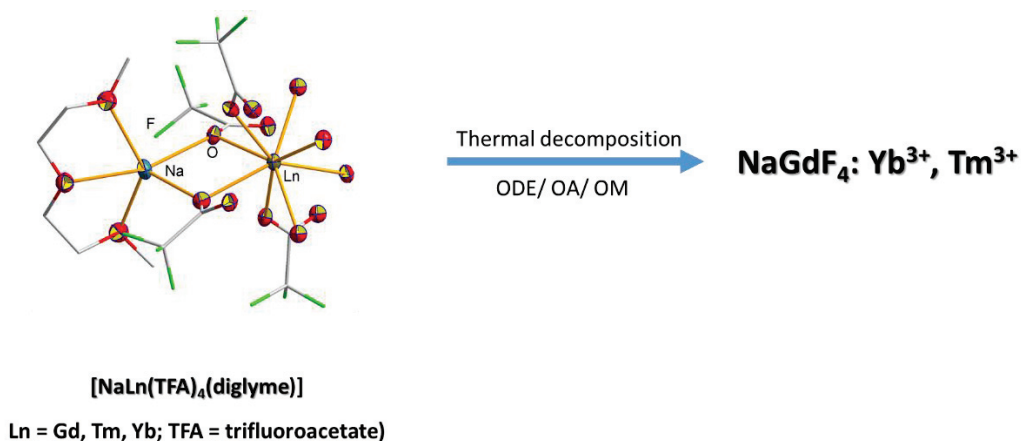
The previous work from the laboratory has used anhydrous molecular precursors as a synthetic strategy to minimize -OH functionality at the surface of lanthanide-based UCNPs,^{39–43} although no effort has been made to compare their up-conversion efficiency with UC materials produced through hydrous synthesis. Literature on the anhydrous synthesis of UC nanomaterials and its influence on upconversion intensity is scarce.⁴⁴

In this chapter, we report the synthesis of upconverting (UC) NaGdF₄: Yb³⁺, Tm³⁺ NPs by two different methods: thermal decomposition of anhydrous metal-organic single-source precursors [NaLn(TFA)₄(diglyme)] (Ln = Gd, Tm, Yb) and room temperature co-precipitation using hydrated inorganic salts Ln(NO₃)₃·5H₂O, NaNO₃ and NH₄F in ethylene glycol. After a detailed study of the influence of the solvents and the dopant percentage on the crystalline phase of the NPs obtained and their complete characterization, the UCNPs synthesized by these two strategies were studied for their upconversion efficiency. These results reveal that uniform nanospheres with an average size of 13 nm obtained from anhydrous single-source precursors (SSPs) had a higher upconversion intensity than agglomerated nanorods (~197 in length and ~95 nm in width) produced from hydrated inorganic salts.

2.2. Results and discussion

2.2.1. Anhydrous synthesis of NaGdF₄: Yb³⁺, Tm³⁺ nanoparticles from thermal decomposition of designed precursors [NaLn(TFA)₄(diglyme)] (Ln = Gd, Tm, Yb): influence of solvents and dopant percentage on the crystal phase of up-converting NPs

The isostructural anhydrous precursors [NaGd(TFA)₄(diglyme)], [NaYb(TFA)₄(diglyme)] and [NaTm(TFA)₄(diglyme)] were prepared following the method as described in the articles from this laboratory.^{39,40} To prepare NaGdF₄: Yb³⁺, Tm³⁺ nanoparticles, these precursors were taken in appropriate amounts and simultaneously decomposed in the mixture of 1-octadecene and oleic acid or 1-octadecene and oleylamine (Scheme 2.1). The details concerning the synthesis procedure, amount of reactants, solvents, etc. are summarized in Table 6.2 and Table 6.3 in Chapter 6.



Scheme 2.1: Synthesis of NaGdF₄: Yb³⁺, Tm³⁺ nanoparticles using anhydrous precursors.

2.2.1.1. Influence of solvents

The decomposition of the precursor [NaGd(TFA)₄(diglyme)] in a non-coordinating solvent 1-octadecene (ODE) at 290 °C, which afforded the β-phase of the NaGdF₄ NPs (ICDD # 04-018-8795), has been described by our group.¹⁵ Although this precursor provides *in situ* the coordinating diglyme ligand, which acts as a surfactant for the NaGdF₄ NPs, but it is less effective than widely used capping ligands such as oleic acid (OA) and oleylamine (OM) in controlling the nanoparticle size and dispersing them in the organic medium. We have, therefore, carried out here a systematic study on the thermal decomposition of this precursor in the mixed reaction medium containing different ratios of ODE, OM and OA. As observed for 1-octadecene, the decomposition of the Na-Gd heterometallic precursor in a 1:1 mixture of ODE + OA resulted in the β-phase of NaGdF₄ (bottom curve in Figure 2.1), although a small percentage of GdF₃ NPs was also present, probably due to the partial destruction of the Na-Gd heterometallic into homometallic components by the possible replacement of the diglyme/TFA groups with oleate ligands. *In situ* substitution of the acetate group by the oleate ligand has previously been observed.³¹ However, the presence of GdF₃ could be suppressed if the decomposition was carried out in the presence of NaTFA (up to 0.25 equivalent). On the other hand, the bottom curve in Figure 2.2 shows that the Na-Gd precursor decomposed in a 1:1 mixture of ODE + OM to give the pure α-phase of the NaGdF₄ NPs (ICDD # 04-019-0931). This result is in contrast with the previous observation where the addition of OM promoted the formation of the β-phase over the α-phase for NaYbF₄ UCNPs.⁴⁵

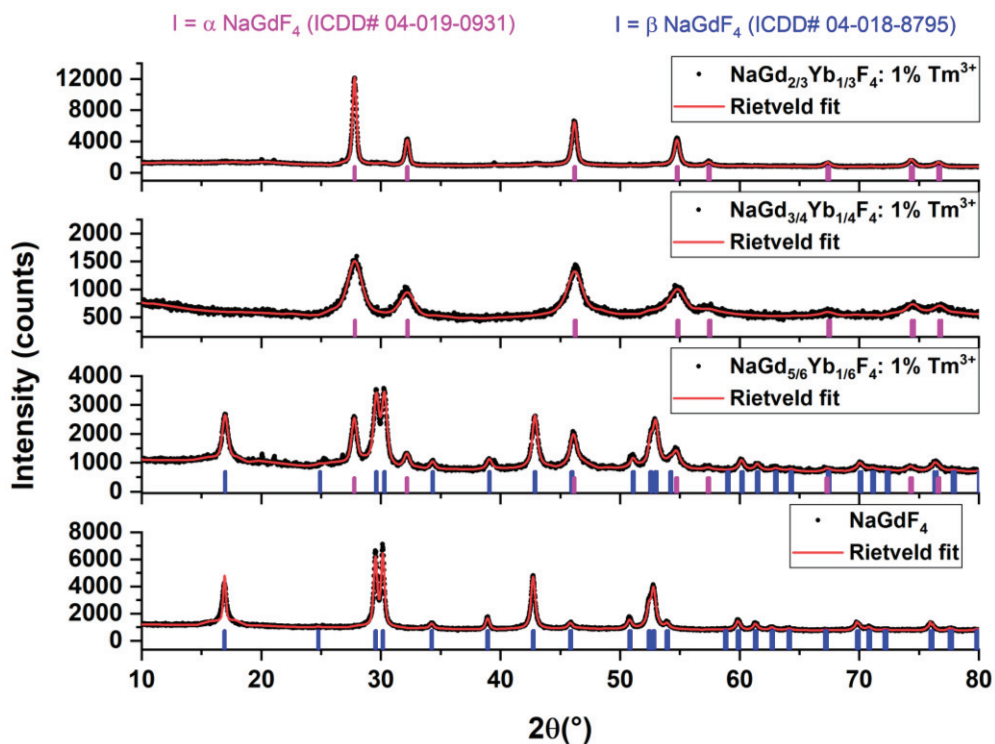


Figure 2.1: Powder XRD of $\text{NaGdF}_4: \text{Yb}^{3+}, \text{Tm}^{3+}$ NPs obtained from the thermal decomposition of SSPs in a 1:1 mixture of ODE + OA (a).

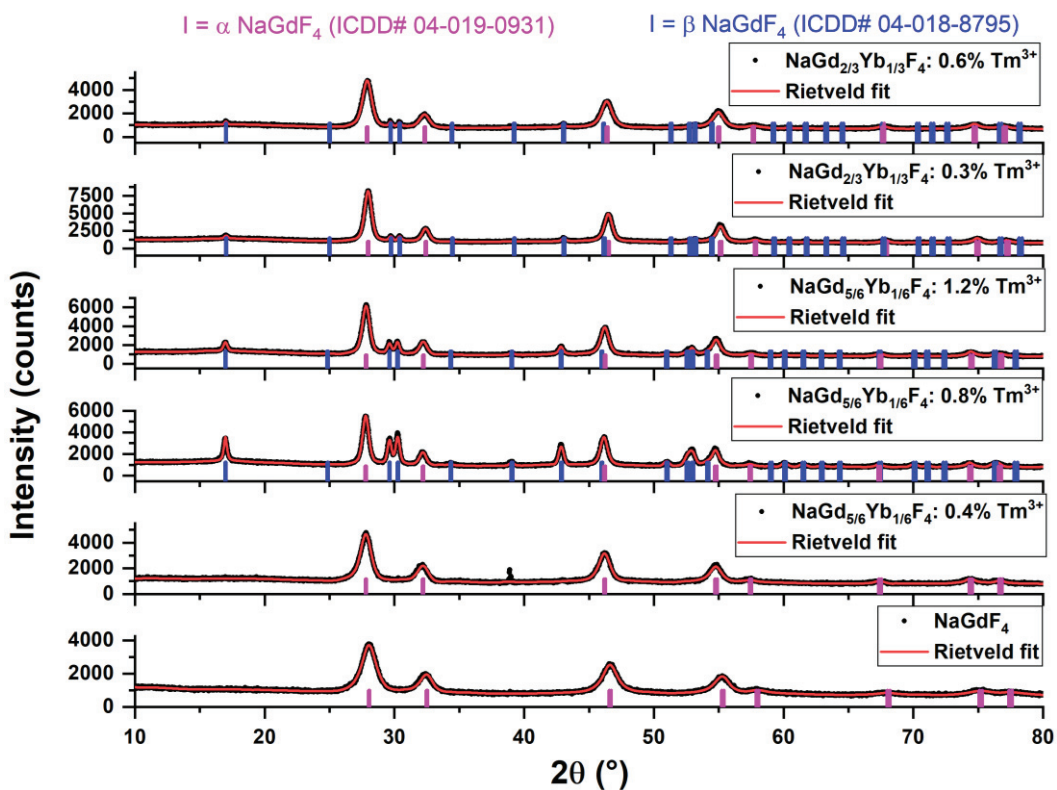


Figure 2.2: Powder XRD of $\text{NaGdF}_4: \text{Yb}^{3+}, \text{Tm}^{3+}$ NPs obtained from the thermal decomposition of SSPs in a 1:1 mixture of ODE + OM (b).

2.2.1.2. Influence of doping ratio of co-doped lanthanide ions (sensitizer and activator)

2.2.1.2.1. Effect on crystalline phase and surface properties

Another critical criterion that influences the UC efficiency is the doping ratio of co-doped lanthanide ions (sensitizer and activator), which needs to be optimized to maximize energy transfer but, at the same time, to minimize the loss of cross-relaxation energy.⁴⁶ To obtain the host matrix NaGdF₄ NPs co-doped with different percentages of Yb³⁺ and Tm³⁺ cations, the precursors [NaLn(TFA)₄(diglyme)] (Ln = Gd, Tm, Yb) were taken in appropriate amounts and then simultaneously decomposed in suitable mixture of solvents. These sets of up-converting nanoparticles obtained under strictly anhydrous conditions are collectively abbreviated as UC_anhyd NPs. In general, while the increase in the percentage of Yb³⁺ favours the formation of the α phase, no clear trend was obtained in the case of thulium. Thus, the mixed α and β -phases obtained for NaGd_{5/6}Yb_{1/6}F₄: 1% Tm³⁺ in the reaction medium ODE + OA are converted into pure α -phase when increasing the amount of Yb to 25% and more. The previous work from our laboratory has already reported that the tendency to get the α phase increases for late lanthanides with smaller radii.^{15,39,40} On the other hand, for a low percentage of Yb (17%), increasing the content of Tm³⁺ ions increases the percentage of the β phase of the matrix. Thus, while a pure α phase is obtained for NaGd_{5/6}Yb_{1/6}F₄: 0.4% Tm³⁺ in ODE + OM reaction medium, increasing the content of Tm³⁺ to 0.8% introduces about 27% of the β phase, which further increases to 37% by raising the amount of Tm³⁺ to 1.2% (Figure 2.2). However, no such influence of Tm³⁺ ions was present on doubling the amount of ytterbium in the matrix, as exemplified by NaGd_{2/3}Yb_{1/3}F₄: 0.3% Tm³⁺ and NaGd_{2/3}Yb_{1/3}F₄: 0.6% Tm³⁺ NPs which display about the same amount of the β -phase (~9%). In short, the use of single-source precursors under different reaction media provides a robust and reproducible strategy for synthesizing a set of lanthanide-doped NaGdF₄ UCNPs in pure α or mixed α + β phases with defined ratios, the latter can be converted easily to pure β -phase by calcination at ~350 °C, with a slight agglomeration but without any significant change in the particle size (Figure 2.3). Getting lanthanide-doped NaGdF₄ UCNPs in pure α , pure β or mixed α + β phases is important given the different potential applications of the different polymorphs.⁴⁷ summarizes the relative ratio of α and/or β -crystalline phases, calculated after Rietveld refinement, and the crystallite size of the NaGdF₄: Yb³⁺, Tm³⁺_anhyd NPs obtained in different reaction media.

The surface property of these nanoparticles is analysed using FT-IR spectroscopic studies as shown in Figure 2.4. The peak around 3400cm⁻¹, which corresponds to the characteristic vibration of N-H bonds, confirms the presence of oleylamine as a capping ligand on these nanoparticles. Also, other

characteristic peaks concerning C-H and C-N vibrational energy levels are present at around 2900 cm^{-1} and 1450 cm^{-1} , respectively.

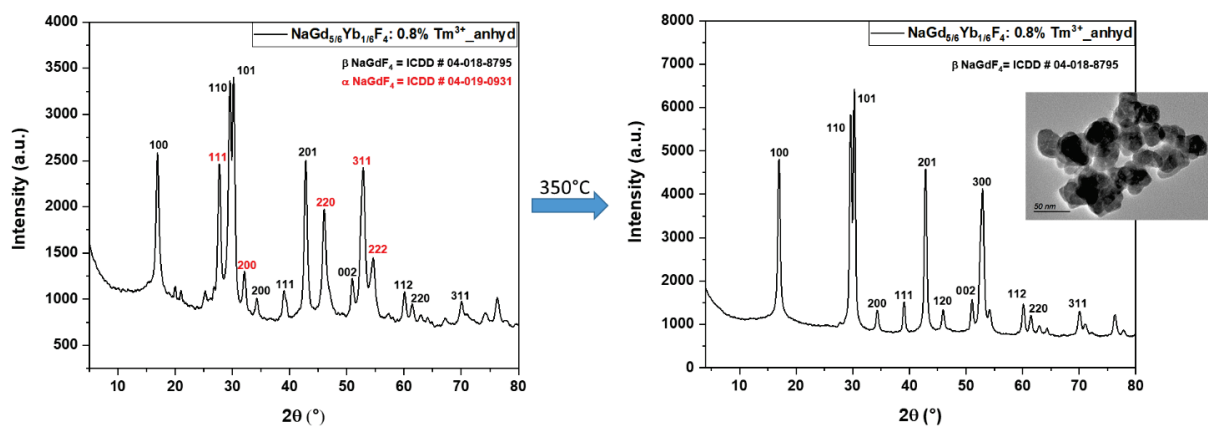


Figure 2.3: Conversion of as-prepared mixed-phase $\text{NaGd}_{5/6}\text{Yb}_{1/6}\text{F}_4: 0.8\% \text{Tm}^{3+}$ NPs ($13\% \alpha + 87\% \beta$) to pure β -phase after calcination at $350\text{ }^\circ\text{C}$.

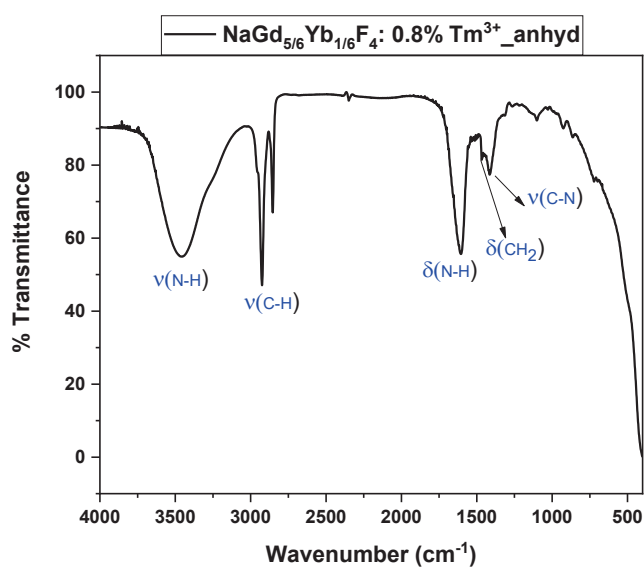


Figure 2.4: FT-IR spectra of $\text{NaGd}_{5/6}\text{Yb}_{1/6}\text{F}_4: 0.8\% \text{Tm}^{3+}$ NPs obtained from a) thermal decomposition of the single-source precursors $[\text{NaLn}(\text{TFA})_4(\text{diglyme})]$ ($\text{Ln} = \text{Gd}, \text{Yb}, \text{Tm}$) at $290\text{ }^\circ\text{C}$ in a 1:1 mixture of 1-octadecene + oleylamine.

Table 2.1: Different crystalline phases and crystallite size of the NaGdF₄: Yb³⁺, Tm³⁺ NPs obtained from the thermal decomposition of SSPs [NaLn(TFA)₃(diglyme)] (Ln = Gd, Yb, Tm) at 290 °C in 1:1 mixture of 1-Octadecene + Oleic acid or 1-Octadecene + Oleylamine.

Composition, crystalline phase and crystallite size (from Scherrer equation) of UCNPs	
ODE + OA	ODE + OM
NaGdF ₄ β (~19 nm)	NaGdF ₄ α (~7 nm)
–	NaGd _{5/6} Yb _{1/6} F ₄ : 0.4% Tm ³⁺ α (~16 nm)
NaGd _{5/6} Yb _{1/6} F ₄ : 1% Tm ³⁺ α (13%) + β (87%) (~13 nm)	NaGd _{5/6} Yb _{1/6} F ₄ : 0.8% Tm ³⁺ α (73%) + β (27%) (~18 nm)
–	NaGd _{5/6} Yb _{1/6} F ₄ : 1.2% Tm ³⁺ α (63%) + β (37%) (~16 nm)
NaGd _{3/4} Yb _{1/4} F ₄ : 1% Tm ³⁺ α (~6 nm)	–
–	NaGd _{2/3} Yb _{1/3} F ₄ : 0.3% Tm ³⁺ α (91%) + β (9%) (~19 nm)
NaGd _{2/3} Yb _{1/3} F ₄ : 1% Tm ³⁺ α (~18 nm)	NaGd _{2/3} Yb _{1/3} F ₄ : 0.6% Tm ³⁺ α (92%) + β (8%) (~9 nm)

2.2.1.2.2. Effect on size, shape and morphology

TEM images of these nanoparticles produced by the thermal decomposition method show that they are almost spherical and less than 20 nm in size {Figure 2.5 and Figure 2.6 (decomposed in the mixture of 1-octadecene and oleylamine) whereas Figure 2.7 (decomposed in the mixture of 1-octadecene and oleic acid)}. These figures correspond to the TEM, HR-TEM and associated FFT of the sample NaGd_{5/6}Yb_{1/6}F₄: 0.8% Tm³⁺ containing the two phases α and β. These images exhibit nearly spherical morphology and controlled size distribution (13.7 ± 3.5 nm) for these nanoparticles (Figure 2.5 (f)). The observed morphology is comparable to that of NaGdF₄ reported by the microwave-assisted decomposition of [Ln(TFA)₃], although the particle size in this study was smaller due to a short reaction time (10 min in the microwave-assisted decomposition vs. 1 h in the thermal decomposition).³¹ The presence of a mixture of phases (α + β), as shown by the XRD, was confirmed by HR-TEM analysis. The HR-TEM image in Figure 2.5 (b) shows two particles with α and β phase, respectively. While the central

particle with an interreticular spacing of 0.302 nm is related to the β phase (Figure 2.5(c)), the FFT of the second particle displayed in Figure 2.5 (d) shows the diffraction pattern of a cubic crystal structure (α -phase) in the zone axis [011] ((e)). The spots corresponding to the {111} planes with an interreticular spacing of 0.318 nm (zone axis [011]) confirm the presence of the α -phase. The spots corresponding to other plane families such as {200}, {022}, {222}, {311}, etc. are also observed.

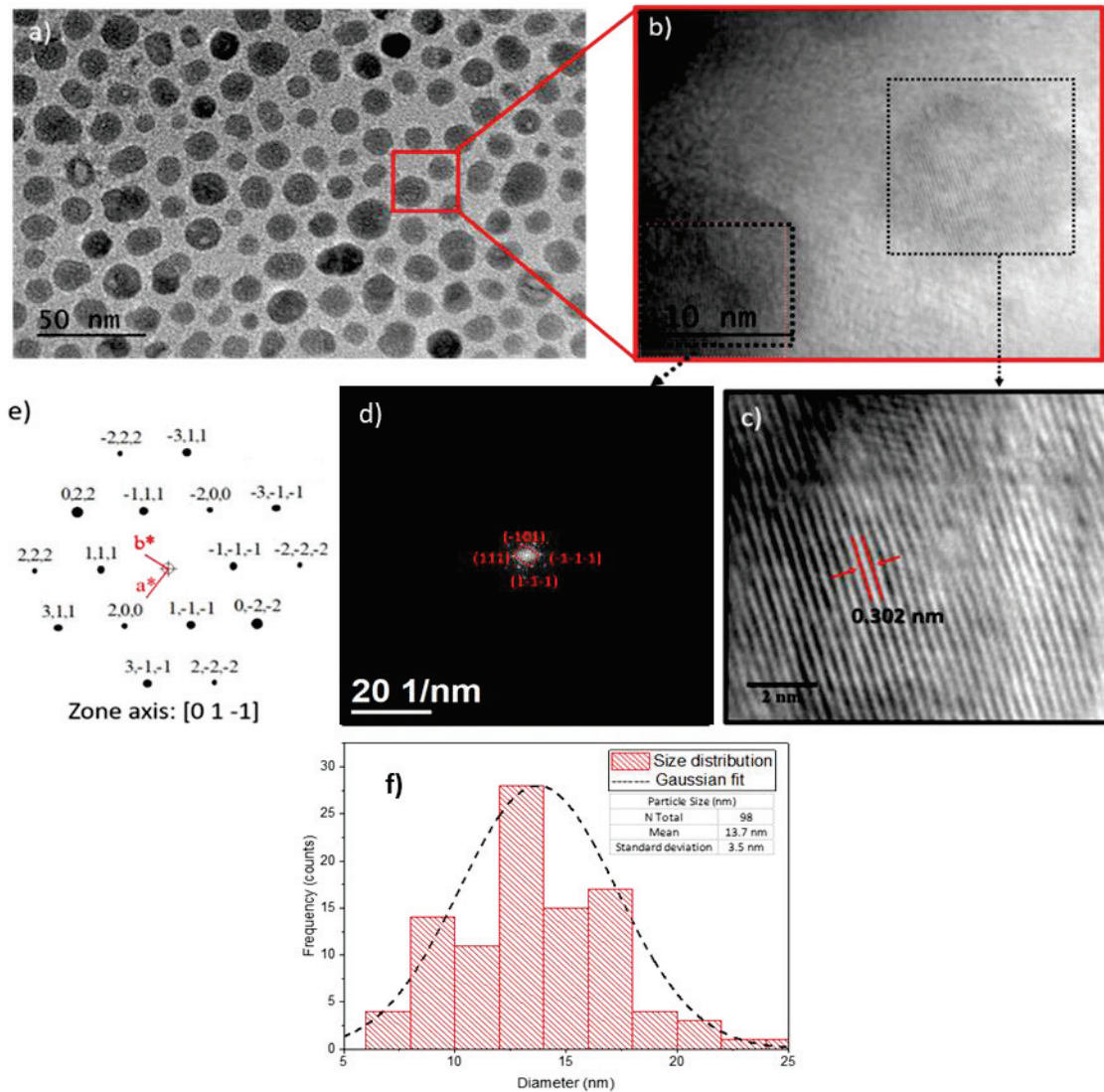


Figure 2.5: TEM, HR-TEM and associated FFT of the NaGd_{5/6}Yb_{1/6}F₄: 0.8% Tm³⁺ NPs obtained from the thermal decomposition of the single source precursors (SSP) [NaLn(TFA)₄(diglyme)] (Ln = Gd, Yb, Tm) at 290°C in a 1:1 mixture of 1-octadecene + oleylamine. The HR-TEM image in (c) shows an interreticular spacing of 0.302 nm related to the β -phase, whereas the FFT of the second particle in (d) corresponds to the diffraction pattern of a cubic crystal structure (α -phase) in the zone axis [01-1] (e). Size distribution of these nanoparticles (f).

Figure 2.6 shows TEM (a) and HRTEM (b) of hexagonal particles obtained by the decomposition of anhydrous precursors in the mixture of 1-octadecene and oleylamine. Figure 2.6 b) showing the high-resolution TEM presents the lattice planes (0.318 nm) corresponding to (111) planes of cubic NaGdF₄ (ICDD# 04-019-0931) also justified by FFT in Figure 2.6 c). Figure 2.7 shows the cubic NaGdF₄ (ICDD# 04-019) synthesized in the mixture of 1- octadecene and oleic acid.

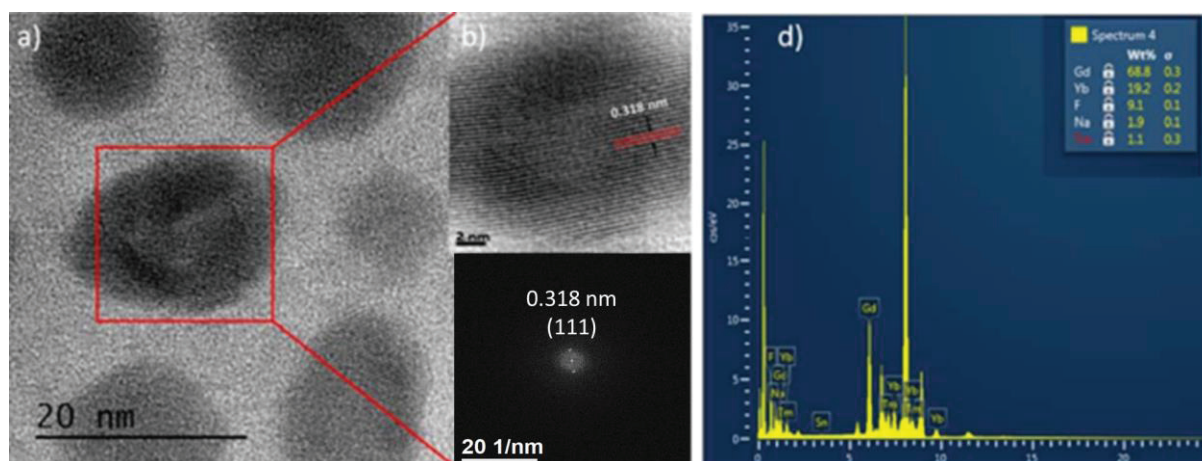


Figure 2.6: TEM (a), HRTEM (b) FFT analysis (c) and EDX analysis (d) of NaGd_{5/6}Yb_{1/6}F₄: 0.8% Tm³⁺ NPs obtained from high temperature decomposition of NaLn(TFA)₄(diglyme) (Ln = Gd, Tm, Yb) in the mixture of 1-octadecene and oleylamine. The crystal structure corresponds to cubic NaGdF₄ (ICDD file # 04-019-0931).

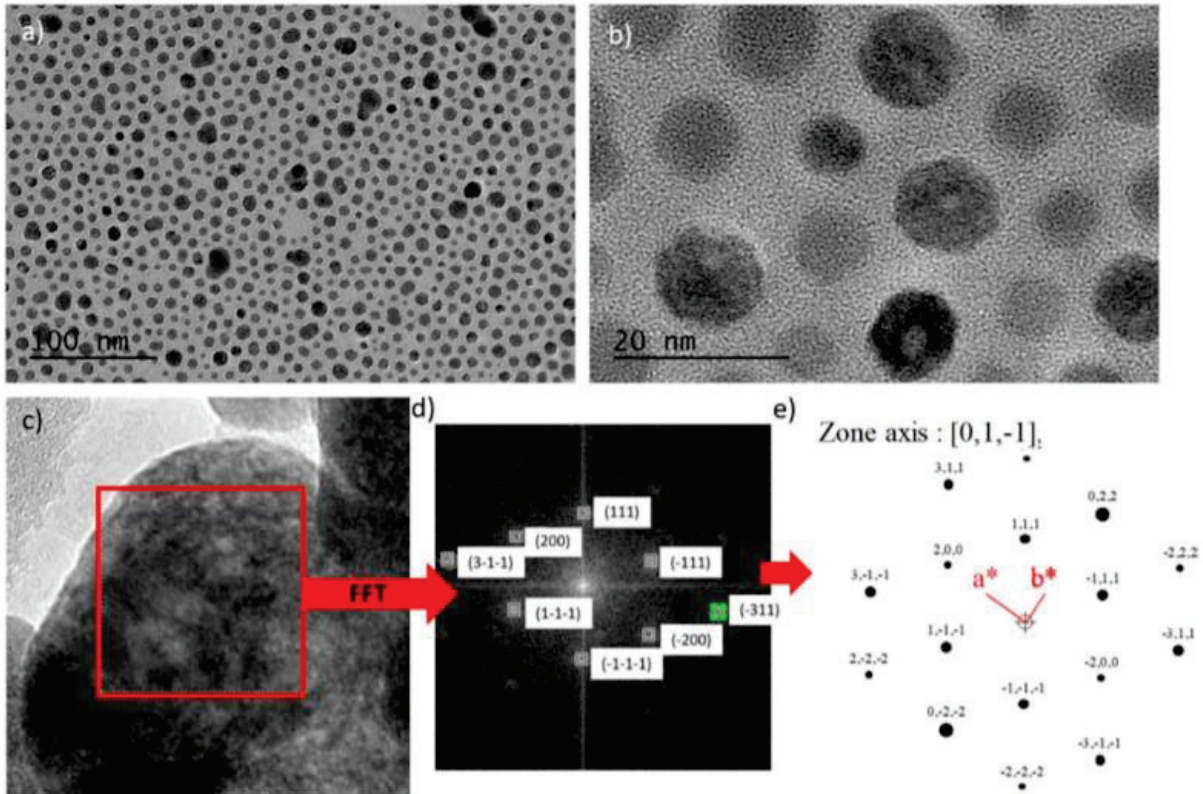
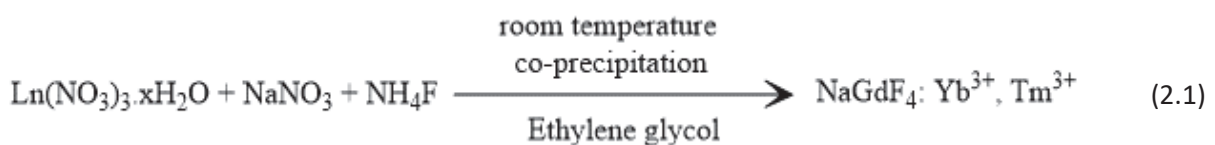


Figure 2.7: TEM (a, b), HRTEM (c) and corresponding FFT analysis (d, e) of $\text{NaGd}_{2/3}\text{Yb}_{1/3}\text{F}_4$: 1% Tm^{3+} NPs obtained from the high temperature decomposition of $\text{NaLn}(\text{TFA})_4(\text{diglyme})$ ($\text{Ln} = \text{Gd}, \text{Tm}, \text{Yb}$) in the mixture of 1- octadecene and oleic acid. The crystal structure corresponds to cubic NaGdF_4 (ICDD file # 04-019-0931).

2.2.2. Hydrous synthesis of NaGdF_4 : Yb^{3+} , Tm^{3+} NPs from the co-precipitation reaction of hydrated inorganic salts at room temperature

To understand the relationship between the synthetic conditions and the structure and morphology of the nanoparticles and their influence over up-conversion efficiency, we have also synthesized the NaGdF_4 : Yb^{3+} , Tm^{3+} NPs from a modified co-precipitation method by reacting $\text{Ln}(\text{NO}_3)_3 \cdot 5\text{H}_2\text{O}$ ($\text{Ln} = \text{Gd}, \text{Tm}, \text{Yb}$), NaNO_3 and NH_4F at room temperature in ethylene glycol.⁴⁸ The synthesis of NaGdF_4 nanoparticles using hydrated inorganic salts like $\text{Ln}(\text{NO}_3)_3 \cdot 5\text{H}_2\text{O}$, NaNO_3 and NH_4F are progressed through co-precipitation of these inorganic salts in ethylene glycol at room temperature. The synthetic procedure and details of precursors used for the synthesis of NaGdF_4 NPs doped with different amount of Yb^{3+} and Tm^{3+} ions are summarized in Table 6.4 in Chapter 6. The reaction followed is presented as follows.



2.2.2.1. Effect on the crystalline phase

In the powder XRD of the as-prepared powder, abbreviated as UC_hyd NPs, all peaks could be indexed with the b-phase of NaGdF₄ (ICDD # 04-018-8795, Figure 2.8). Usually, nanostructures synthesized at low temperature are more likely to contain a higher amount of surface defects.⁴⁹ Since the synthesis was carried out at room temperature, the crystallinity of the as-obtained powders was slightly lower than that of the UC_anhyd NPs which were obtained by decomposition at elevated temperature. In contrast to the thermal decomposition method, the different dopant percentages did not affect the crystalline phase of the UC_hyd NPs in the co-precipitation method (Figure 2.8).

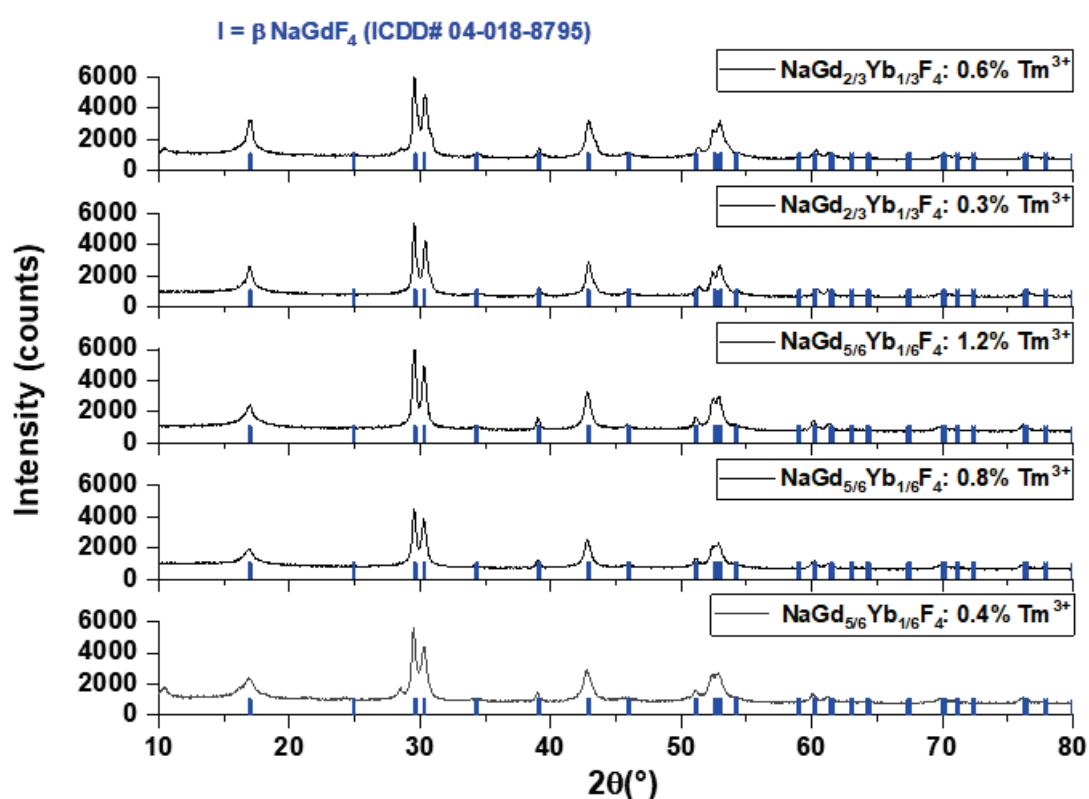


Figure 2.8: Powder XRD of NaGdF₄: Yb³⁺, Tm³⁺ NPs obtained from co-precipitation reaction of hydrated inorganic salts at room temperature

2.2.2.2. Effect on size, shape and morphology

The TEM images show a very different shape, size and morphology of the UC_hyd NPs (agglomerated nanorods with an average size of 197 ± 29 nm in length and 85 ± 10 nm in width vs. uniform spherical anhydrous NPs of less than 15 nm, (Figure 2.9, Figure 2.10, Figure 2.11)). This agglomeration and formation of large particle size can be attributed to the absence of any effective capping ligand during the room temperature synthesis. Although the presence of ethylene glycol ligand

on the surface of the NPs has been confirmed by IR spectra and TG-DTG studies (Figure 2.12 and Figure 2.13), it is less efficient in controlling the nanoparticle size than the capping ligands such as oleic acid (OA) or oleylamine (OM) used in the thermal decomposition method. In Figure 2.9 (d), the FFT pattern of a representative sample i.e. $\text{NaGd}_{5/6}\text{Yb}_{1/6}\text{F}_4: 0.8\% \text{Tm}^{3+}$ shows the diffraction pattern of a hexagonal crystal structure (β -phase) in the zone axis $[001]$. The spots correspond to the $\{110\}$ plane family with an interreticular distance of 0.29 nm and confirm the β -phase.

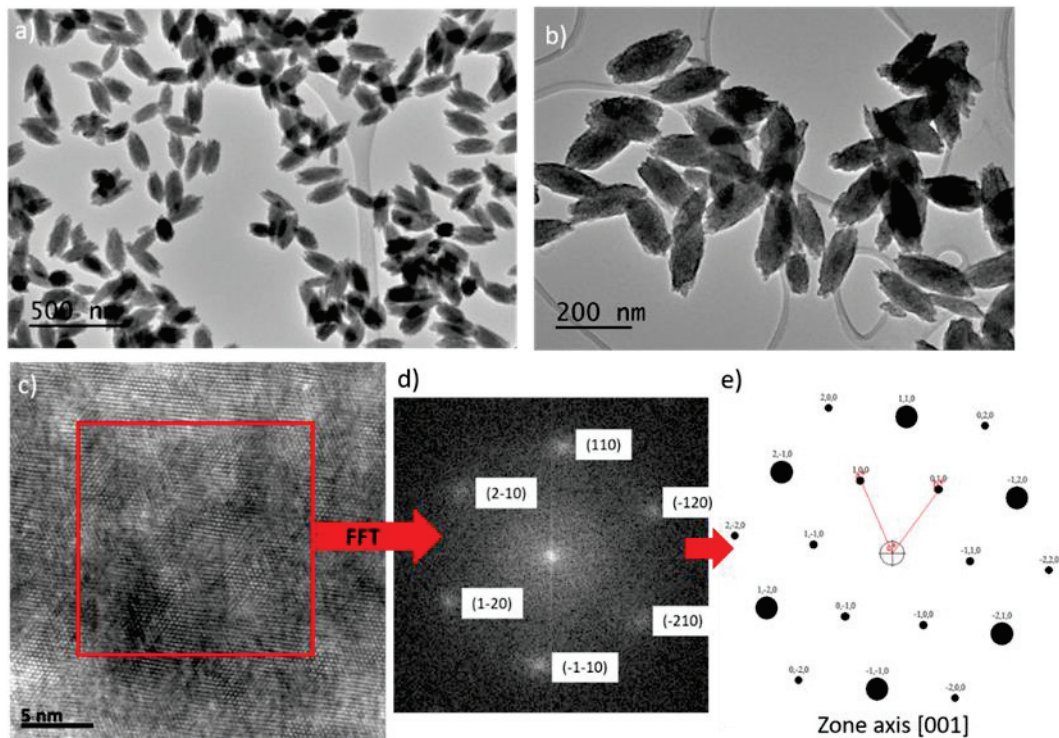


Figure 2.9: TEM images of $\text{NaGd}_{5/6}\text{Yb}_{1/6}\text{F}_4: 1.2\% \text{Tm}^{3+}$ (a) and $\text{NaGd}_{5/6}\text{Yb}_{1/6}\text{F}_4: 0.8\% \text{Tm}^{3+}$ (b) NPs obtained from room temperature co-precipitation using hydrated inorganic salts $\text{Ln}(\text{NO}_3)_3 \cdot x\text{H}_2\text{O}$ ($\text{Ln} = \text{Gd}, \text{Tm}, \text{Yb}$), NaNO_3 and NH_4F in ethylene glycol. HR-TEM (c) and associated FFT analysis (d) of β - $\text{NaGd}_{5/6}\text{Yb}_{1/6}\text{F}_4: 0.8\% \text{Tm}^{3+}$ NPs. The FFT corresponds to the diffraction pattern of a hexagonal crystal structure (β -phase) in the zone axis $[001]$ (e)

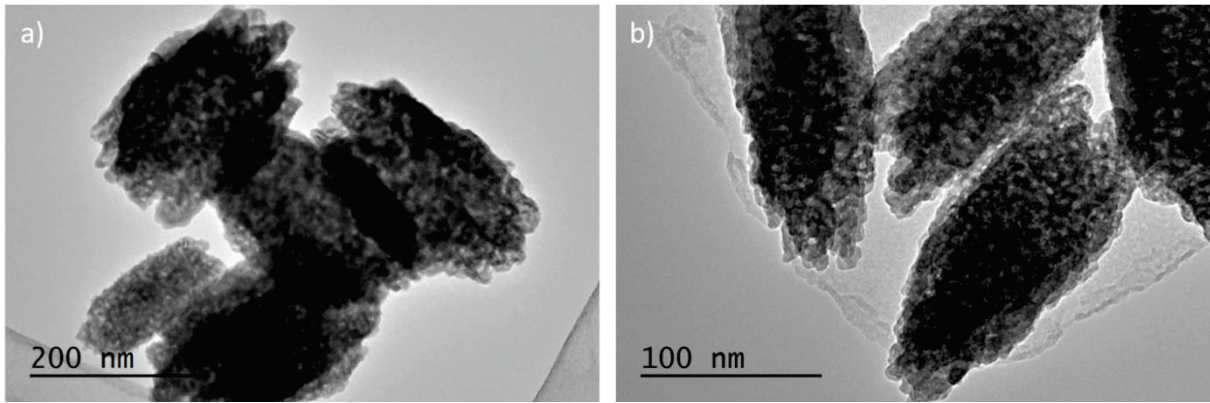


Figure 2.10: TEM images of $\text{NaGd}_{2/3}\text{Yb}_{1/3}\text{F}_4: 0.3\% \text{Tm}^{3+}$ (a) and $\text{NaGd}_{5/6}\text{Yb}_{1/6}\text{F}_4: 1.2\% \text{Tm}^{3+}$ (b) NPs obtained from room temperature co-precipitation using hydrated inorganic salts $\text{Ln}(\text{NO}_3)_3 \cdot x\text{H}_2\text{O}$ ($\text{Ln} = \text{Gd}, \text{Tm}, \text{Yb}$), NaNO_3 and NH_4F in ethylene glycol.

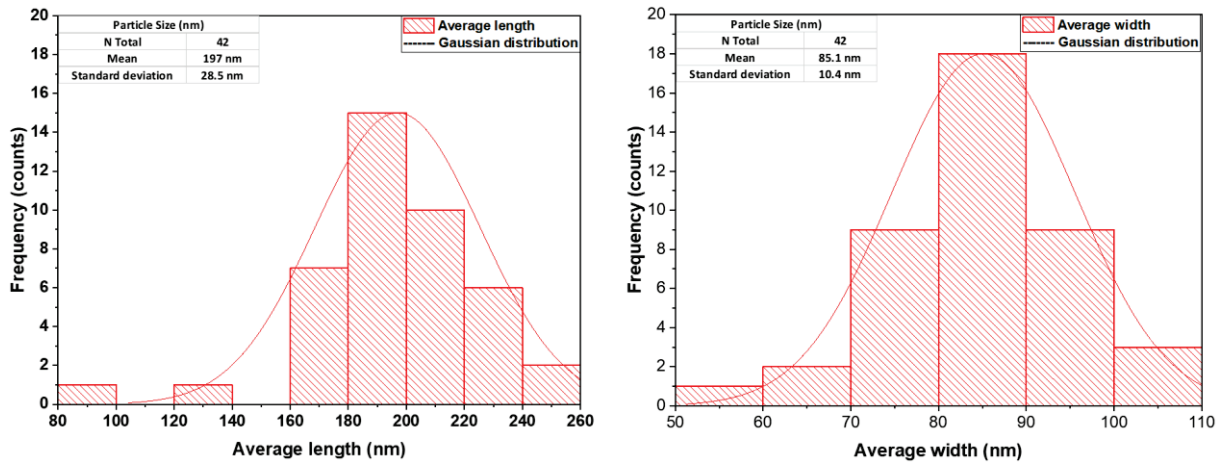


Figure 2.11: Size distribution curves along with the length (a) and width (b) of $\text{NaGd}_{5/6}\text{Yb}_{1/6}\text{F}_4: 1.2\% \text{Tm}^{3+}$ nanorods obtained from room temperature co-precipitation using hydrated inorganic salts $\text{Ln}(\text{NO}_3)_3 \cdot 5\text{H}_2\text{O}$ ($\text{Ln} = \text{Gd}, \text{Tm}, \text{Yb}$), NaNO_3 and NH_4F in ethylene glycol.

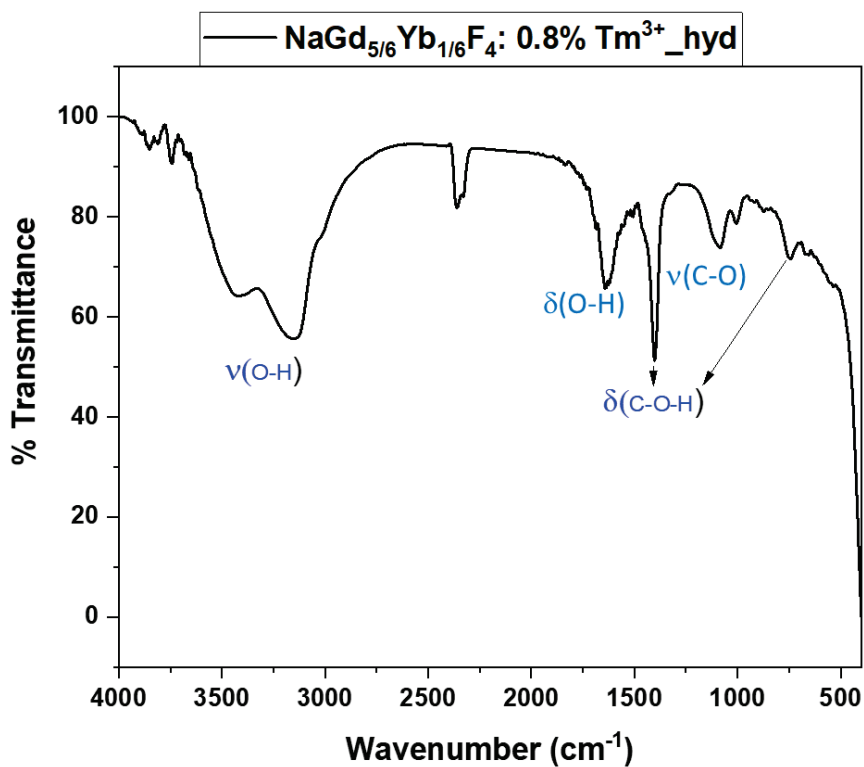


Figure 2.12: FT-IR spectrum of NaGd_{5/6}Yb_{1/6}F₄: 0.8% Tm³⁺ nanorods obtained from room temperature co-precipitation using hydrated inorganic salts Ln(NO₃)₃·5H₂O (Ln = Gd, Tm, Yb), NaNO₃ and NH₄F in ethylene glycol.

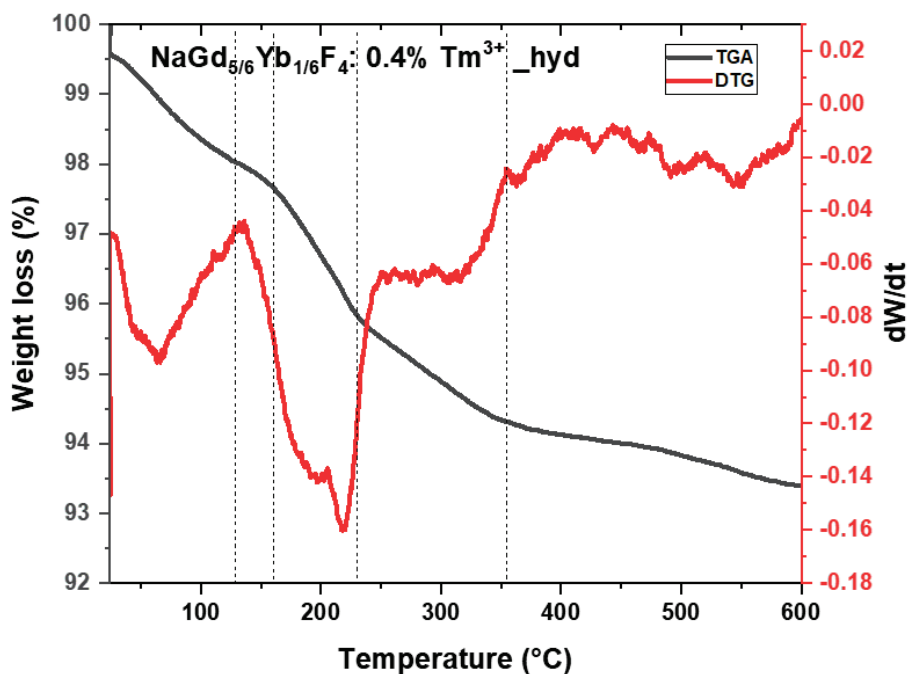


Figure 2.13: Thermogravimetric analysis (TGA) and derivative thermogravimetry (DTG) analysis of NaGd_{5/6}Yb_{1/6}F₄: 0.4%Tm³⁺ NPs obtained from the room temperature co-precipitation using hydrated inorganic salts Ln(NO₃)₃·5H₂O (Ln = Gd, Tm, Yb), NaNO₃ and NH₄F in ethylene glycol.

2.2.3. Comparative upconversion studies

A detailed and systematic study of up-conversion was performed on UC_anhyd and UC_hyd NPs obtained by thermal decomposition of anhydrous precursors in the mixture of 1-octadecene + oleylamine as well co-precipitation method using hydrated inorganic salts in ethylene glycol, respectively (Figure 2.14, Figure 2.15). We observed varying emission intensity profiles for different concentration of doping lanthanide ions (both sensitizer and activator). As up-conversion emission is highly geometry (phase) dependent,⁵⁰⁻⁵³ we tried to observe a variation in the photoluminescence emission profiles and found a trend in the emission profiles by changing the composition of the nanoparticles one by one. From Figure 2.14, it is clear that doubling the doping amount of the sensitizer Yb³⁺ quenches the overall up-conversion, probably because of energy transfer within the sensitizer ions themselves. At the same time, the increase in the concentration of activator Tm³⁺ ions from 0.4% to 1.2% (in both NaGd_{5/6}Yb_{1/6}F₄ and NaGd_{2/3}Yb_{1/3}F₄ series) plays a role in the final up-conversion emission profile. It is, therefore, crucial to obtain an optimal ratio of dopant ions to achieve the highest upconversion efficiency.⁵⁴ A careful analysis of Figure 2.14 reveals that ~17% Yb³⁺ and 0.8% Tm³⁺ is the optimal ratio of sensitizer and activator to obtain the best up-conversion efficiency in the UC_anhyd NPs studied here. Therefore, this ratio was chosen to compare up-conversion emission for anhydrous and hydrous samples. It should be noted that spectra of all the anhydrous samples given in Figure 2.14 were measured under similar conditions, and hence are comparable. The same is true for spectra of the hydrous samples given in Figure 2.15. However, the spectra given in Figure 2.14 and Figure 2.15 should not be compared with each other without taking into account the experimental details, notably the slit width.

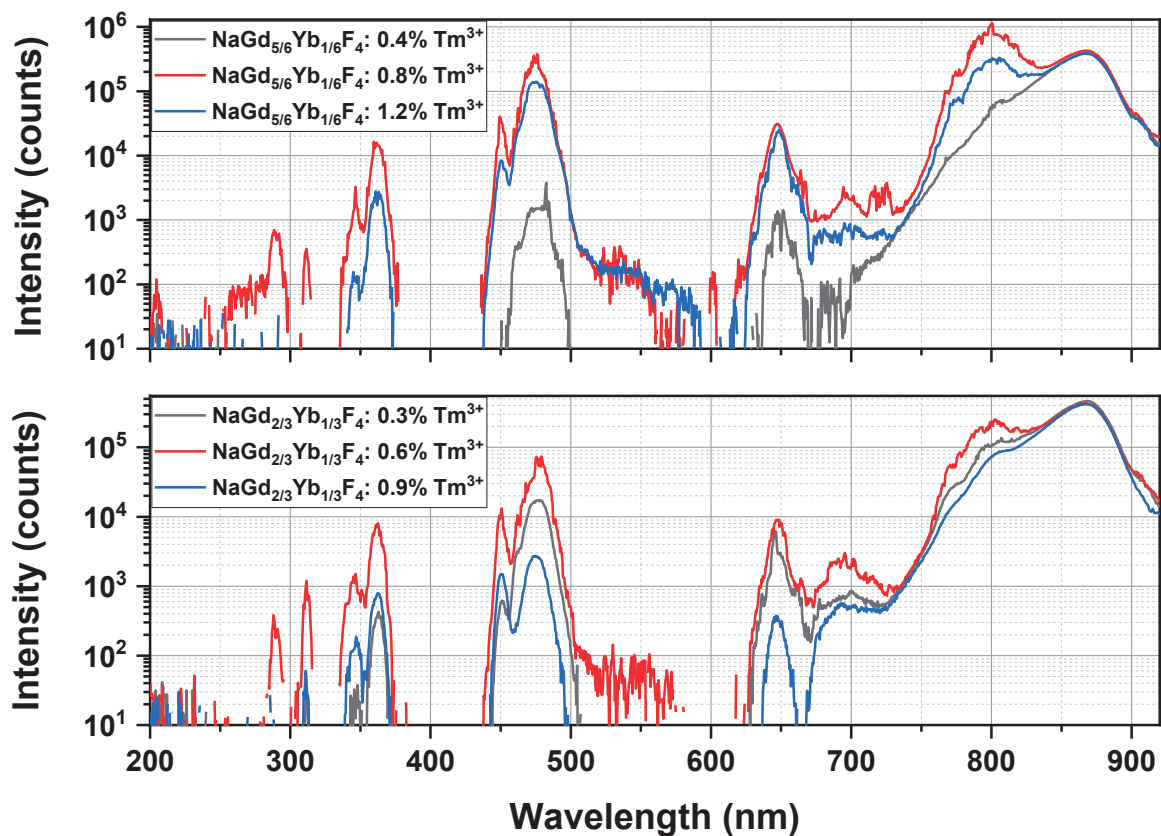


Figure 2.14: Up-conversion studies ($\lambda_{exc} = 972$ nm CW Laser, and slit width = 0.5 mm for entry and exit) of $\text{NaGdF}_4: \text{Yb}^{3+}, \text{Tm}^{3+}$ NPs obtained from the thermal decomposition method.

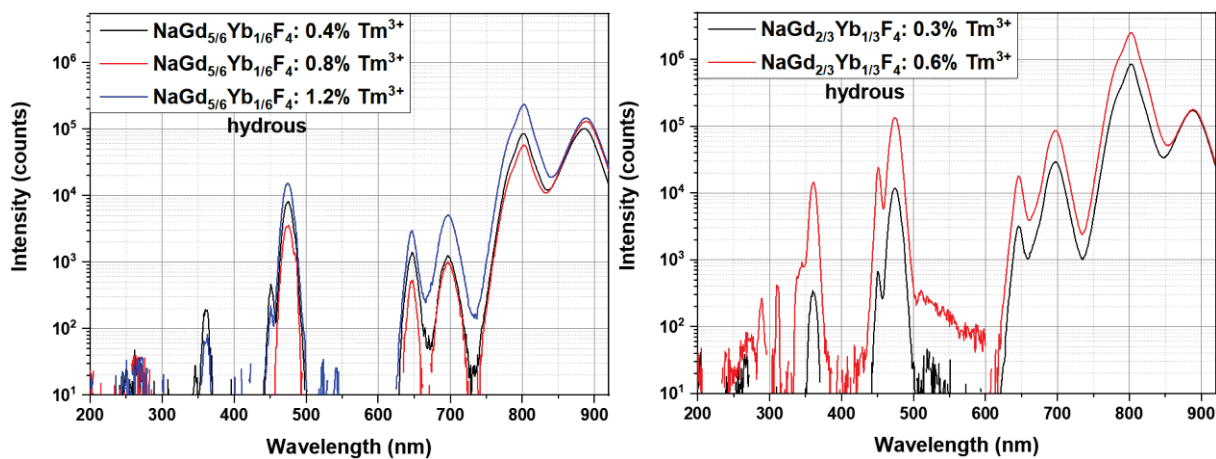


Figure 2.15: Upconversion emission spectra for $\text{NaGdF}_4: \text{Yb}^{3+}, \text{Tm}^{3+}_{\text{hyd}}$ synthesized using hydrated inorganic salts $\text{Ln}(\text{NO}_3)_3 \cdot 5\text{H}_2\text{O}$ ($\text{Ln} = \text{Gd}, \text{Tm}, \text{Yb}$) with 972 nm CW laser excitation (slit width = 2 mm for both entry and exit), showing classical Tm^{3+} emission for samples with different ratio of sensitizers and activators.

Up-conversion emission spectra of $\text{NaGd}_{5/6}\text{Yb}_{1/6}\text{F}_4: 0.8\% \text{Tm}^{3+}$ NPs synthesized under anhydrous and hydrous conditions were measured in the solid-state under 972 nm CW laser excitation (power density = 16.5 W/cm²). Usually, at high laser intensities, the up-conversion response of the material changes. The local photothermal heating causes modulation in the crystal

structure and hence changes the up-conversion emission response.⁵⁵ In our study also, we observed that the hydrous samples started decomposing at moderately higher intensities (>20 W/cm²) while the anhydrous nanoparticles were quite stable even at high laser intensities. The less stability of the hydrous samples may be attributed to their significantly low quantum yield, which would convert most of the energy to heat and, therefore, overheat the samples and decompose them. The peaks in the spectra of Figure 2.16 can be ascribed to the different transitions that occur in the 4f energy levels of the lanthanide ions in the NaGdF₄ matrix.¹⁵ It can be seen that these two samples, NaGd_{5/6}Yb_{1/6}F₄: 0.8% Tm³⁺_anhyd and NaGd_{5/6}Yb_{1/6}F₄: 0.8% Tm³⁺_hyd, exhibit emission peaks of significantly different intensity but at exactly similar positions centred around 362 nm in the UV region which is governed by the ¹D₂ → ³H₆ transition, around 475 nm corresponding to the ¹G₄ → ³H₆ transition and at longer wavelength such as around 650, 698 and 802 nm, representing the ¹G₄ → ³F₄, ¹D₂ → ³H₄ (or ³F₃ → ³H₆) and ³H₄ → ³H₆ transitions, respectively, from the Tm³⁺ ions. Apart from these strong emission peaks, a few peaks were observed in the deep UV region. The peaks at 290 nm and 348 nm are due to electronic transitions in the Tm NaGd_{5/6}Yb_{1/6}F₄: 0.8% Tm³⁺ ions from ¹I₆ to ³H₆ and ³F₄, respectively. These peaks were absent in the NaGd_{5/6}Yb_{1/6}F₄: 0.8% Tm³⁺_hyd sample. In addition, a very sharp emission at 312 nm corresponding to ⁶P_{7/2} → ⁸S_{7/2} of the Gd³⁺ ions is present only in the NaGd_{5/6}Yb_{1/6}F₄: 0.8% Tm³⁺_anhyd sample. As shown in , the upconversion emission for the NaGd_{5/6}Yb_{1/6}F₄: 0.8% Tm³⁺_anhyd sample, even with its unfavourable characteristics such as mixed α and β-phase of the matrix and smaller particle size, is much higher than that of the NaGd_{5/6}Yb_{1/6}F₄: 0.8% Tm³⁺_hyd sample. It is well known that the UC emission intensity of β-NaLnF₄ is about an order of magnitude stronger as compared to the α-NaLnF₄ host lattice due to longer Ln-F distances and a higher coordination number⁵⁶ and the smaller particles usually have lesser up-conversion efficiency owing to their high surface/volume ratio.³¹ Compared to the UC_anhyd spherical nanoparticles, the significant reduction in the emission intensity for UC_hyd nanorods can be attributed to a) irregular surface that results in the generation of defect energy levels next to the Tm³⁺ energy levels,⁵¹⁻⁵³ and b) the presence of a significant amount of OH ions on the surface, as confirmed by the FT-IR and TG-DTG curves (Figure 2.12 and Figure 2.13), competing with the emission of sensitizer Yb³⁺ ions.^{57,58}

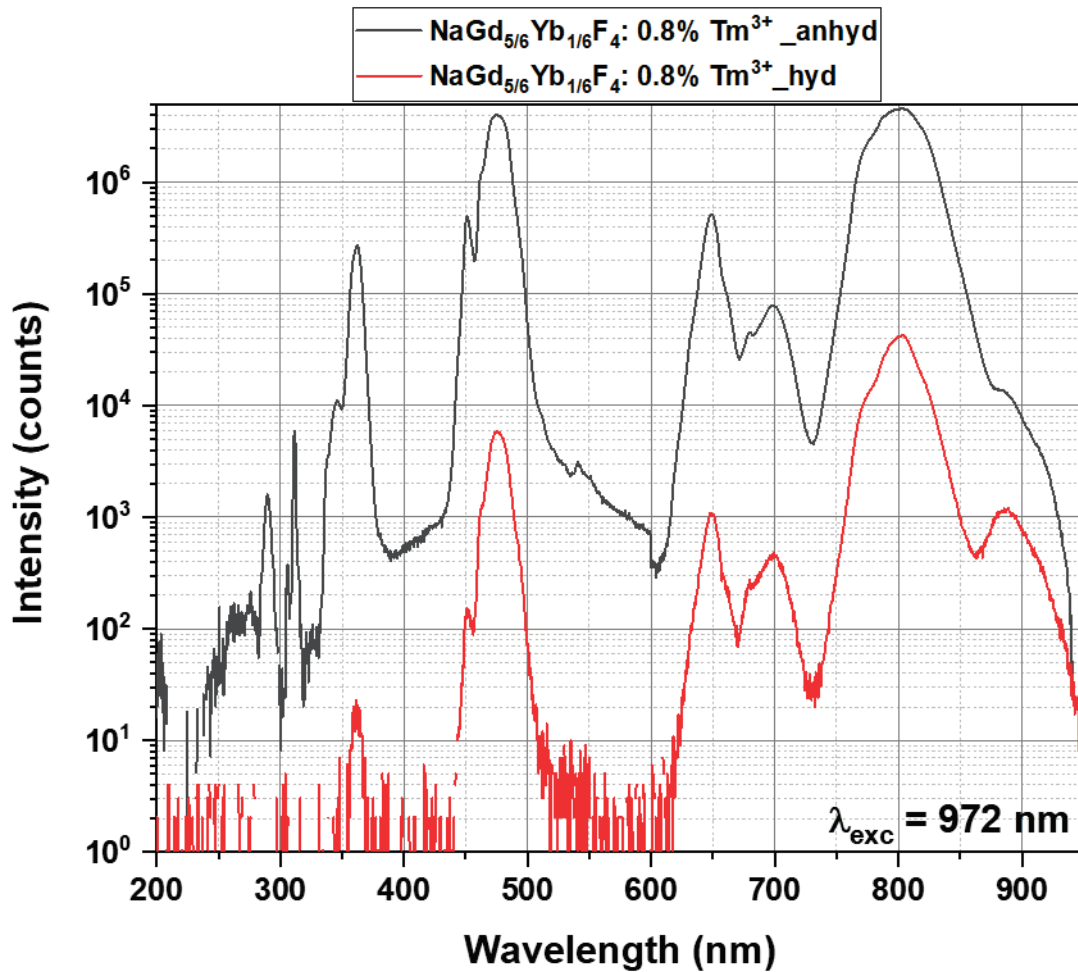


Figure 2.16: Up-conversion studies comparing the emission intensity of $\text{NaGd}_{5/6}\text{Yb}_{1/6}\text{F}_4: 0.8\% \text{Tm}^{3+}_{\text{anhyd}}$ and $\text{NaGd}_{5/6}\text{Yb}_{1/6}\text{F}_4: 0.8\% \text{Tm}^{3+}_{\text{hyd}}$ samples.

Following the qualitative evaluation of the up-conversion emission measurement, we also attempted to quantitatively measure the quantum yield of $\text{NaGd}_{5/6}\text{Yb}_{1/6}\text{F}_4: 0.8\% \text{Tm}^{3+}_{\text{anhyd}}$ and $\text{NaGd}_{5/6}\text{Yb}_{1/6}\text{F}_4: 0.8\% \text{Tm}^{3+}_{\text{hyd}}$ samples with different excitation power densities under otherwise identical conditions to obtain optimal performance. The up-conversion quantum yield was measured using the method originally described by Boyer *et al.*⁵⁹ with a slight modification (described in detail in section 6.2.1). Measurements were made at three different intensities for each sample, which are summarized in Table 2.2 and Table 2.3. While the term quantum yield (ϕ) refers to the ratio of the number of photons emitted to the total number of photons absorbed (Eq. (2.2)), the energy conversion efficiency (ECE) at a particular wavelength is the measure of how much of the input energy (absorbed by the sensitizers) is converted to the output energy (emitted by the activators) (Eq. (2.3)).⁶⁰

$$\phi_{\lambda} = \frac{\text{number of photons emitted}}{\text{number of photons absorbed}} \quad (2.2)$$

Where λ is the wavelength of the photons at which the quantum yield is measured

$$\eta_{\lambda} (ECE_{\lambda}) = \frac{\text{output energy}}{\text{input energy}} \quad (2.3)$$

The power-dependent up-conversion quantum yield (ϕ total) values for the NaGd_{5/6}Yb_{1/6}F₄: 0.8% Tm³⁺_anhyd sample, which range from 0.6% to 1.8% for the power density varying from 4.2 W/cm² to 26.9 W/cm², are superior to those of NaGd_{5/6}Yb_{1/6}F₄: 0.8% Tm³⁺_hyd sample by a factor of 100 (NIR-to-visible light conversion) or more (NIR/visible-to-UV conversion). As noted before, this can mainly be attributed to the presence of a significantly fewer amount of hydroxyl groups on the surface of the former sample. These up-converting NPs respond differently at higher power densities, particularly the hydrous ones, which show a considerable quenching of the up-conversion emission due to local heating of the sample.⁵⁵ Usually, the small size of nanoparticles has a very low quantum yield compared to their bulk counterpart.⁶¹ So ideally, surface passivation via core-shell formation⁶² or use of bulk counterparts is the key strategy to enhance the quantum efficiency, although it might limit their applications. This approach of synthesizing UC materials using anhydrous precursors thus enables the use of even smaller up-converting NPs for many applications like photocatalysis¹⁵ where their use previously was highly limited.

Table 2.2: Upconversion quantum yield (QY) and energy conversion efficiency (ECE) of NaGd_{5/6}Yb_{1/6}F₄: 0.8% Tm³⁺_anhyd at different power densities of the IR laser for different spectral regions: the under-script UV represents the region between 250 and 375nm, 475 corresponds to the region 430-530 nm, 648 corresponds to 635-665 nm, 700 corresponds to 670-720 nm, 802 corresponds to 730-870 nm. Finally, the total stands for the whole 250-900 nm region.

Intensity (W/cm ²)	Φ_{total} ECE _{total}	Φ_{UV} ECE _{UV}	Φ_{475} ECE ₄₇₅	Φ_{648} ECE ₆₄₈	Φ_{700} ECE ₇₀₀	Φ_{802} ECE ₈₀₂
26.9	0.018(3)	1.3(2) x 10 ⁻⁵	3.4(7) x 10 ⁻⁴	1.1(2) x 10 ⁻⁴	1.5(3) x 10 ⁻⁴	0.017(3)
	0.023(4)	3.5(7) x 10 ⁻⁵	7(14) x 10 ⁻⁴	1.7(3) x 10 ⁻⁴	2.1(4) x 10 ⁻⁴	0.021(4)
10.3	0.011(2)	2.7(5) x 10 ⁻⁶	2.2(4) x 10 ⁻⁴	5.9(12) x 10 ⁻⁵	2.5(5) x 10 ⁻⁵	0.010(2)
	0.013(2)	7.3(14) x 10 ⁻⁶	4.6(9) x 10 ⁻⁴	8.9(18) x 10 ⁻⁵	3.6(7) x 10 ⁻⁵	0.013(2)
4.2	0.005(1)	2.9(6) x 10 ⁻⁷	5.4(10) x 10 ⁻⁵	1.6(3) x 10 ⁻⁵	8.2(16) x 10 ⁻⁶	0.005(1)
	0.006(1)	8.1(16) x 10 ⁻⁷	1.1(2) x 10 ⁻⁴	2.4(5) x 10 ⁻⁵	1.1(2) x 10 ⁻⁵	0.006(1)

Table 2.3: Upconversion quantum yield (QY) and energy conversion efficiency (ECE) of NaGd_{5/6}Yb_{1/6}F₄: 0.8% Tm³⁺_hyd at different power densities of the IR laser for different spectral regions: the under-script UV represents the region between 250 and 375nm, 475 corresponds to the region 430-530 nm, 648 corresponds to 635-665 nm, 700 corresponds to 670-720 nm, 802 corresponds to 730-870 nm. Finally, the total stands for the whole 250-900 nm region.

Intensity (W/cm ²)	Φ_{total} ECE _{total}	Φ_{UV} ECE _{UV}	Φ_{475} ECE ₄₇₅	Φ_{648} ECE ₆₄₈	Φ_{700} ECE ₇₀₀	Φ_{802} ECE ₈₀₂
29.4	0.0004(1)	9.0(18) x 10 ⁻⁹	4.1(8) x 10 ⁻⁷	6.4(12) x 10 ⁻⁷	1.8(4) x 10 ⁻⁵	0.00034 (7)
	0.00049(10)	2.4(5) x 10 ⁻⁸	8.5(17) x 10 ⁻⁷	9.5(20) x 10 ⁻⁷	2.5(5) x 10 ⁻⁵	0.00040 (8)
10.9	0.00073(15)	4.2(8) x 10 ⁻⁹	7.0(14) x 10 ⁻⁷	5.2(10) x 10 ⁻⁷	6.2(12) x 10 ⁻⁶	0.00070 (14)
	0.00089(18)	1.1(2) x 10 ⁻⁸	1.4(3) x 10 ⁻⁶	7.8(16) x 10 ⁻⁷	8.7(17) x 10 ⁻⁶	0.00085 (17)
4.2	0.00085(17)	2.4(5) x 10 ⁻⁹	7.4(15) x 10 ⁻⁷	4.6(9) x 10 ⁻⁷	2.0(4) x 10 ⁻⁶	0.00083 (17)
	0.00103(2)	7.1(14) x 10 ⁻⁹	1.5(3) x 10 ⁻⁶	6.9(14) x 10 ⁻⁷	2.9(6) x 10 ⁻⁶	0.10

2.3. Conclusions and perspectives

In this chapter, we reported the synthesis of upconverting NaGdF₄ nanoparticles containing variable ratios of Yb³⁺ and Tm³⁺ ions by two different methods (thermal decomposition of anhydrous single source precursors and co-precipitation at room temperature using hydrated inorganic salts) and the influence of synthetic conditions on the structure and morphology of the nanoparticles as well as the comparative study of up-conversion efficiency. Bottom-up synthesis using anhydrous molecular precursors in appropriate ratio and suitable solvent(s) not only allows better control of the composition, structure and morphology of NaGdF₄: Yb³⁺, Tm³⁺ nanoparticles, including selective access to pure α -, pure β - or mixed $\alpha + \beta$ crystalline phases with defined ratios, but the anhydrous conditions also reduce -OH functionality on the surface to significantly enhance their up-conversion efficiency. This study validates the anhydrous precursor approach as a strategy to obtain small but highly emitting up-converting particles without requiring silica or undoped matrix surface passivation layer, which would be beneficial for the applications that require the construction of additional layers of another material, e.g. TiO₂@UC NPs type shell-core structure for IR-induced photocatalysis.

2.4. References

- (1) Gibart, P.; Auzel, F.; Guillaume, J.-C.; Zahraman, K. Below Band-Gap IR Response of Substrate-Free GaAs Solar Cells Using Two-Photon Up-Conversion. *Jpn. J. Appl. Phys.* **1996**, *35* (Part 1, No. 8), 4401–4402. <https://doi.org/10.1143/JJAP.35.4401>.
- (2) Trupke, T.; Shalav, A.; Richards, B. S.; Würfel, P.; Green, M. A. Efficiency Enhancement of Solar Cells by Luminescent Up-Conversion of Sunlight. *Solar Energy Materials and Solar Cells* **2006**, *90* (18), 3327–3338. <https://doi.org/10.1016/j.solmat.2005.09.021>.
- (3) Jin, Y.; Wang, H.; Li, X.; Zhu, H.; Sun, D.; Sun, X.; Liu, H.; Zhang, Z.; Cao, L.; Gao, C.; Wang, H.; Liang, X.-J.; Zhang, J.; Yang, X. A Multifunctional DNA Polymer Assisted Upconversion Therapeutic Nanoplatfrom for Enhanced Photodynamic Therapy. *ACS Appl. Mater. Interfaces* **2020**, *acsami.0c03274*. <https://doi.org/10.1021/acsami.0c03274>.
- (4) Wang, S.; Wei, Z.; Li, L.; Ning, X.; Liu, Y. Luminescence Imaging-Guided Triple-Collaboratively Enhanced Photodynamic Therapy by Bioresponsive Lanthanide-Based Nanomedicine. *Nanomedicine: Nanotechnology, Biology and Medicine* **2020**, 102265. <https://doi.org/10.1016/j.nano.2020.102265>.
- (5) Wang, Y.; Pan, M.; Yu, X.; Xu, L. The Recent Advances of Fluorescent Sensors Based on Molecularly Imprinted Fluorescent Nanoparticles for Pharmaceutical Analysis. *CURR MED SCI* **2020**, *40* (3), 407–421. <https://doi.org/10.1007/s11596-020-2195-z>.
- (6) Näreoja, T.; Deguchi, T.; Christ, S.; Peltomaa, R.; Prabhakar, N.; Fazeli, E.; Perälä, N.; Rosenholm, J. M.; Arppe, R.; Soukka, T.; Schäferling, M. Ratiometric Sensing and Imaging of Intracellular PH Using Polyethylenimine-Coated Photon Upconversion Nanoprobes. *Anal. Chem.* **2017**, *89* (3), 1501–1508. <https://doi.org/10.1021/acs.analchem.6b03223>.
- (7) Guo, Y.; Zou, R.; Si, F.; Liang, W.; Zhang, T.; Chang, Y.; Qiao, X.; Zhao, J. A Sensitive Immunoassay Based on Fluorescence Resonance Energy Transfer from Up-Converting Nanoparticles and Graphene Oxide for One-Step Detection of Imidacloprid. *Food Chemistry* **2020**, 127609. <https://doi.org/10.1016/j.foodchem.2020.127609>.
- (8) Samhadaneh, D. M.; Mandl, G. A.; Han, Z.; Mahjoob, M.; Weber, S. C.; Tuznik, M.; Rudko, D. A.; Capobianco, J. A.; Stochaj, U. Evaluation of Lanthanide-Doped Upconverting Nanoparticles for in Vitro and in Vivo Applications. *ACS Appl. Bio Mater.* **2020**. <https://doi.org/10.1021/acsabm.0c00381>.

- (9) Zhou, K.; Qiu, X.; Xu, L.; Li, G.; Rao, B.; Guo, B.; Pei, D.; Li, A.; He, G. Poly(Selenoviologen) Assembled Upconversion Nanoparticles for Low Power Single NIR Light Triggered Synergistic Photodynamic and Photothermal Antibacterial Therapy. *ACS Appl. Mater. Interfaces* **2020**, acsami.0c04506. <https://doi.org/10.1021/acsami.0c04506>.
- (10) Dramićanin, M. D. Trends in Luminescence Thermometry. *Journal of Applied Physics* **2020**, *128* (4), 040902. <https://doi.org/10.1063/5.0014825>.
- (11) Tang, J.; Du, P.; Li, W.; Luo, L. Boosted Thermometric Performance in NaGdF₄:Er³⁺/Yb³⁺ Upconverting Nanorods by Fe³⁺ Ions Doping for Contactless nanothermometer Based on Thermally and Non-Thermally Coupled Levels. *Journal of Luminescence* **2020**, *224*, 117296. <https://doi.org/10.1016/j.jlumin.2020.117296>.
- (12) Cao, B.; Bao, Y.; Liu, Y.; Shang, J.; Zhang, Z.; He, Y.; Feng, Z.; Dong, B. Wide-Range and Highly-Sensitive Optical Thermometers Based on the Temperature-Dependent Energy Transfer from Er to Nd in Er/Yb/Nd Codoped NaYF₄ Upconversion Nanocrystals. *Chemical Engineering Journal* **2020**, *385*, 123906. <https://doi.org/10.1016/j.cej.2019.123906>.
- (13) Zhao, Y.; Wang, X.; Zhang, Y.; Li, Y.; Yao, X. Winning Wide-Temperature-Range and High-Sensitive Thermometry by a Multichannel Strategy of Dual-Lanthanides in the New Tungstate Phosphors. *Journal of Alloys and Compounds* **2020**, 154998. <https://doi.org/10.1016/j.jallcom.2020.154998>.
- (14) Liu, Y.; Bai, G.; Pan, E.; Hua, Y.; Chen, L.; Xu, S. Upconversion Fluorescence Property of Er³⁺/Yb³⁺ Codoped Lanthanum Titanate Microcrystals for Optical Thermometry. *Journal of Alloys and Compounds* **2020**, *822*, 153449. <https://doi.org/10.1016/j.jallcom.2019.153449>.
- (15) Chen, Y.; Mishra, S.; Ledoux, G.; Jeanneau, E.; Daniel, M.; Zhang, J.; Daniele, S. Direct Synthesis of Hexagonal NaGdF₄ Nanocrystals from a Single-Source Precursor: Upconverting NaGdF₄:Yb³⁺, Tm³⁺ and Its Composites with TiO₂ for Near-IR-Driven Photocatalysis. *Chemistry – An Asian Journal* **2014**, *9* (9), 2415–2421. <https://doi.org/10.1002/asia.201402347>.
- (16) Jiang, Q.; Xie, X.; Riley, D. J.; Xie, F. Harvesting the Lost Photon by Plasmonic Enhanced Hematite-Upconversion Nanocomposite for Water Splitting. *J. Chem. Phys.* **2020**, *153* (1), 011102. <https://doi.org/10.1063/5.0013060>.
- (17) Habibi-Yangjeh, A.; Asadzadeh-Khaneghah, S.; Vadivel, S. Integration of C-Dots with g-C₃N₄ Nanosheet/Ag₂CO₃ Nanocomposites as Effective Z-Scheme Visible-Light Photocatalysts for Removal of

Hazardous Organic and Inorganic Contaminates. *J Mater Sci: Mater Electron* **2020**.
<https://doi.org/10.1007/s10854-020-03894-7>.

(18) Zhao, J.; Xu, J.; Jian, X.; Xu, J.; Gao, Z.; Song, Y.-Y. NIR-Light Driven Photocatalysis on Amphiphilic TiO₂ Nanotubes for Controllable Drug Release. *ACS Appl. Mater. Interfaces* **2020**, acsami.0c04260.
<https://doi.org/10.1021/acsami.0c04260>.

(19) Wu, S.; Wang, F.; Li, Q.; Wang, J.; Zhou, Y.; Duan, N.; Niazi, S.; Wang, Z. Photocatalysis and Degradation Products Identification of Deoxynivalenol in Wheat Using Upconversion Nanoparticles@TiO₂ Composite. *Food Chemistry* **2020**, 126823.
<https://doi.org/10.1016/j.foodchem.2020.126823>.

(20) Rao, Z.; Shi, G.; Wang, Z.; Mahmood, A.; Xie, X.; Sun, J. Photocatalytic Degradation of Gaseous VOCs over Tm³⁺-TiO₂: Revealing the Activity Enhancement Mechanism and Different Reaction Paths. *Chemical Engineering Journal* **2020**, 395, 125078. <https://doi.org/10.1016/j.cej.2020.125078>.

(21) Ledoux, G.; Joubert, M. F.; Mishra, S. Upconversion Phenomena in Nanofluorides. In *Photonic and Electronic Properties of Fluoride Materials*; Tressaud, A., Poeppelmeier, K., Eds.; Elsevier: Boston, 2016; pp 35–63. <https://doi.org/10.1016/B978-0-12-801639-8.00003-9>.

(22) Tessitore, G.; Mandl, G. A.; Brik, M. G.; Park, W.; Capobianco, J. A. Recent Insights into Upconverting Nanoparticles: Spectroscopy, Modeling, and Routes to Improved Luminescence. *Nanoscale* **2019**, 11 (25), 12015–12029. <https://doi.org/10.1039/C9NR02291K>.

(23) Li, Z.; Zhang, Y. An Efficient and User-Friendly Method for the Synthesis of Hexagonal-Phase NaYF₄:Yb, Er/Tm Nanocrystals with Controllable Shape and Upconversion Fluorescence. *Nanotechnology* **2008**, 19 (34), 345606. <https://doi.org/10.1088/0957-4484/19/34/345606>.

(24) Shi, F.; Wang, J.; Zhang, D.; Qin, G.; Qin, W. Greatly Enhanced Size-Tunable Ultraviolet Upconversion Luminescence of Monodisperse β-NaYF₄: Yb, Tm Nanocrystals. *J. Mater. Chem.* **2011**, 21 (35), 13413–13421. <https://doi.org/10.1039/C1JM11480H>.

(25) Zhao, J.; Lu, Z.; Yin, Y.; McRae, C.; Piper, J. A.; Dawes, J. M.; Jin, D.; Goldys, E. M. Upconversion Luminescence with Tunable Lifetime in NaYF₄: Yb, Er Nanocrystals: Role of Nanocrystal Size. *Nanoscale* **2013**, 5 (3), 944–952. <https://doi.org/10.1039/C2NR32482B>.

- (26) Mishra, S.; Daniele, S. Molecular Engineering of Metal Alkoxides for Solution Phase Synthesis of High-Tech Metal Oxide Nanomaterials. *Chem. Eur. J.* **2020**, *26* (42), 9292–9303. <https://doi.org/10.1002/chem.202000534>.
- (27) Mishra, S.; Daniele, S. Metal-Organic Derivatives with Fluorinated Ligands as Precursors for Inorganic Nanomaterials. *Chem. Rev.* **2015**, *115* (16), 8379–8448. <https://doi.org/10.1021/cr400637c>.
- (28) Gahlot, S.; Jeanneau, E.; Singh, D.; Panda, P. K.; Mishra, Y. K.; Ahuja, R.; Ledoux, G.; Mishra, S. Molecules versus Nanoparticles: Identifying a Reactive Molecular Intermediate in the Synthesis of Ternary Coinage Metal Chalcogenides. *Inorg. Chem.* **2020**, *59* (11), 7727–7738. <https://doi.org/10.1021/acs.inorgchem.0c00758>.
- (29) Mishra, S.; Jeanneau, E.; Berger, M.-H.; Hocheplied, J.-F.; Daniele, S. Novel Heteroleptic Heterobimetallic Alkoxide Complexes as Facile Single-Source Precursors for Ta⁵⁺ Doped TiO₂–SnO₂ Nanoparticles. *Inorg. Chem.* **2010**, *49* (23), 11184–11189. <https://doi.org/10.1021/ic102134w>.
- (30) Mishra, S.; Jeanneau, E.; Daniele, S.; Mendez, V. Aminoalkoxo-Supported Heteroleptic Hexanuclear Gallium(III) Wheel as a Synthron for Group 13 Heterometallics: A Rare Sol-Gel Precursor for Mixed Al–Ga Oxide as Support for Gold Catalysts. *Dalton Trans.* **2010**, *39* (32), 7440–7443. <https://doi.org/10.1039/C0DT00485E>.
- (31) Halimi, I.; Rodrigues, E. M.; Maurizio, S. L.; Sun, H.-Q. T.; Grewal, M.; Boase, E. M.; Liu, N.; Marin, R.; Hemmer, E. Pick Your Precursor! Tailoring the Size and Crystal Phase of Microwave-Synthesized Sub-10 nm Upconverting Nanoparticles. *J. Mater. Chem. C* **2019**, *7* (48), 15364–15374. <https://doi.org/10.1039/C9TC04817K>.
- (32) Mishra, S.; Mendez, V.; Jeanneau, E.; Caps, V.; Daniele, S. A Single Source Precursor Route to Group 13 Homo- and Heterometallic Oxides as Highly Active Supports for Gold-Catalyzed Aerobic Epoxidation of Trans-Stilbene. *European Journal of Inorganic Chemistry* **2013**, *2013* (4), 500–510. <https://doi.org/10.1002/ejic.201201191>.
- (33) Wang, Z.; Meijerink, A. Concentration Quenching in Upconversion Nanocrystals. *J. Phys. Chem. C* **2018**, *122* (45), 26298–26306. <https://doi.org/10.1021/acs.jpcc.8b09371>.
- (34) Cao, C.; Liu, Q.; Shi, M.; Feng, W.; Li, F. Lanthanide-Doped Nanoparticles with Upconversion and Downshifting Near-Infrared Luminescence for Bioimaging. *Inorg. Chem.* **2019**, *58* (14), 9351–9357. <https://doi.org/10.1021/acs.inorgchem.9b01071>.

- (35) Chen, X.; Peng, D.; Ju, Q.; Wang, F. Photon Upconversion in Core-Shell Nanoparticles. *Chem. Soc. Rev.* **2015**, *44* (6), 1318–1330. <https://doi.org/10.1039/C4CS00151F>.
- (36) Li, X.; Shen, D.; Yang, J.; Yao, C.; Che, R.; Zhang, F.; Zhao, D. Successive Layer-by-Layer Strategy for Multi-Shell Epitaxial Growth: Shell Thickness and Doping Position Dependence in Upconverting Optical Properties. *Chem. Mater.* **2013**, *25* (1), 106–112. <https://doi.org/10.1021/cm3033498>.
- (37) Vetrone, F.; Naccache, R.; Mahalingam, V.; Morgan, C. G.; Capobianco, J. A. The Active-Core/Active-Shell Approach: A Strategy to Enhance the Upconversion Luminescence in Lanthanide-Doped Nanoparticles. *Advanced Functional Materials* **2009**, *19* (18), 2924–2929. <https://doi.org/10.1002/adfm.200900234>.
- (38) Zhang, Q.; Yang, F.; Xu, Z.; Chaker, M.; Ma, D. Are Lanthanide-Doped Upconversion Materials Good Candidates for Photocatalysis? *Nanoscale Horiz.* **2019**, *4* (3), 579–591. <https://doi.org/10.1039/C8NH00373D>.
- (39) Mishra, S.; Daniele, S.; Ledoux, G.; Jeanneau, E.; Joubert, M.-F. Heterometallic Na–Y(Ln) Trifluoroacetate Diglyme Complexes as Novel Single-Source Precursors for Upconverting NaYF₄ Nanocrystals Co-Doped with Yb and Er/Tm Ions. *Chem. Commun.* **2010**, *46* (21), 3756–3758. <https://doi.org/10.1039/B921474G>.
- (40) Mishra, S.; Ledoux, G.; Jeanneau, E.; Daniele, S.; Joubert, M.-F. Novel Heterometal–Organic Complexes as First Single Source Precursors for Up-Converting NaY(Ln)F₄ (Ln = Yb, Er, Tm) Nanomaterials. *Dalton Trans.* **2012**, *41* (5), 1490–1502. <https://doi.org/10.1039/C1DT11070E>.
- (41) Chen, Y.; Mishra, S.; Ledoux, G.; Jeanneau, E.; Daniel, M.; Zhang, J.; Daniele, S. Direct Synthesis of Hexagonal NaGdF₄ Nanocrystals from a Single-Source Precursor: Upconverting NaGdF₄: Yb³⁺, Tm³⁺ and Its Composites with TiO₂ for Near-IR-Driven Photocatalysis. *Chemistry – An Asian Journal* **2014**, *9* (9), 2415–2421. <https://doi.org/10.1002/asia.201402347>.
- (42) Ayadi, H.; Fang, W.; Mishra, S.; Jeanneau, E.; Ledoux, G.; Zhang, J.; Daniele, S. Influence of Na⁺ Ion Doping on the Phase Change and Upconversion Emissions of the GdF₃: Yb³⁺, Tm³⁺ Nanocrystals Obtained from the Designed Molecular Precursors. *RSC Adv.* **2015**, *5* (122), 100535–100545. <https://doi.org/10.1039/C5RA20781A>.
- (43) Mishra, S.; Morfin, F.; Mendez, V.; Swamy, P. N.; Rousset, J.-L.; Daniele, S. Nanometric NaYF₄ as an Unconventional Support for Gold Catalysts for Oxidation Reactions. *ACS Omega* **2019**, *4* (3), 5852–5861. <https://doi.org/10.1021/acsomega.9b00173>.

- (44) Tessitore, G.; Mudring, A.-V.; Krämer, K. W. Upconversion Luminescence in Sub-10 nm β -NaGdF₄: Yb³⁺, Er³⁺ Nanoparticles: An Improved Synthesis in Anhydrous Ionic Liquids. *RSC Adv.* **2019**, *9* (60), 34784–34792. <https://doi.org/10.1039/C9RA05950D>.
- (45) Chen, B.; Kong, W.; Wang, N.; Zhu, G.; Wang, F. Oleylamine-Mediated Synthesis of Small NaYbF₄ Nanoparticles with Tunable Size. *Chem. Mater.* **2019**, *31* (13), 4779–4786. <https://doi.org/10.1021/acs.chemmater.9b01050>.
- (46) Chen, B.; Wang, F. Combating Concentration Quenching in Upconversion Nanoparticles. *Acc. Chem. Res.* **2020**, *53* (2), 358–367. <https://doi.org/10.1021/acs.accounts.9b00453>.
- (47) Liu, N.; Marin, R.; Mazouzi, Y.; Cron, G. O.; Shuhendler, A.; Hemmer, E. Cubic versus Hexagonal – Effect of Host Crystallinity on the T1 Shortening Behaviour of NaGdF₄ Nanoparticles. *Nanoscale* **2019**, *11* (14), 6794–6801. <https://doi.org/10.1039/C9NR00241C>.
- (48) Du, P.; Ran, W.; Hou, Y.; Luo, L.; Li, W. Eu³⁺-Activated NaGdF₄ Nanorods for Near-Ultraviolet Light-Triggered Indoor Illumination. *ACS Appl. Nano Mater.* **2019**, *2* (7), 4275–4285. <https://doi.org/10.1021/acsanm.9b00743>.
- (49) Niu, W.; Wu, S.; Zhang, S.; Li, L. Synthesis of Colour Tunable Lanthanide-Ion Doped NaYF₄ Upconversion Nanoparticles by Controlling Temperature. *Chem. Commun.* **2010**, *46* (22), 3908–3910. <https://doi.org/10.1039/C002615H>.
- (50) Sun, Y.; Chen, Y.; Tian, L.; Yu, Y.; Kong, X.; Zeng, Q.; Zhang, Y.; Zhang, H. Morphology-Dependent Upconversion Luminescence of ZnO: Er³⁺ Nanocrystals. *Journal of Luminescence* **2008**, *128* (1), 15–21. <https://doi.org/10.1016/j.jlumin.2007.04.011>.
- (51) Wang, F.; Wang, J.; Liu, X. Direct Evidence of a Surface Quenching Effect on Size-Dependent Luminescence of Upconversion Nanoparticles. *Angewandte Chemie International Edition* **2010**, *49* (41), 7456–7460. <https://doi.org/10.1002/anie.201003959>.
- (52) Bian, W.; Lin, Y.; Wang, T.; Yu, X.; Qiu, J.; Zhou, M.; Luo, H.; Yu, S. F.; Xu, X. Direct Identification of Surface Defects and Their Influence on the Optical Characteristics of Upconversion Nanoparticles. *ACS Nano* **2018**, *12* (4), 3623–3628. <https://doi.org/10.1021/acsnano.8b00741>.
- (53) Mai, H.-X.; Zhang, Y.-W.; Sun, L.-D.; Yan, C.-H. Highly Efficient Multicolor Up-Conversion Emissions and Their Mechanisms of Monodisperse NaYF₄: Yb, Er Core and Core/Shell-Structured Nanocrystals. *J. Phys. Chem. C* **2007**, *111* (37), 13721–13729. <https://doi.org/10.1021/jp073920d>.

- (54) Kraft, M.; Würth, C.; Palo, E.; Soukka, T.; Resch-Genger, U. Colour-Optimized Quantum Yields of Yb, Tm Co-Doped Upconversion Nanocrystals. *Methods Appl. Fluoresc.* **2019**, *7* (2), 024001. <https://doi.org/10.1088/2050-6120/ab023b>.
- (55) Min, Q.; Lei, J.; Guo, X.; Wang, T.; Yang, Q.; Zhou, D.; Yu, X.; Yu, S. F.; Qiu, J.; Zhan, Q.; Xu, X. Atomic-Level Passivation of Individual Upconversion Nanocrystal for Single Particle Microscopic Imaging. *Advanced Functional Materials* **2020**, *30* (6), 1906137. <https://doi.org/10.1002/adfm.201906137>.
- (56) Aebischer, A.; Hostettler, M.; Hauser, J.; Krämer, K.; Weber, T.; Güdel, H. U.; Bürgi, H.-B. Structural and Spectroscopic Characterization of Active Sites in a Family of Light-Emitting Sodium Lanthanide Tetrafluorides. *Angewandte Chemie International Edition* **2006**, *45* (17), 2802–2806. <https://doi.org/10.1002/anie.200503966>.
- (57) Wilhelm, S.; Kaiser, M.; Würth, C.; Heiland, J.; Carrillo-Carrion, C.; Muhr, V.; Wolfbeis, O. S.; Parak, W. J.; Resch-Genger, U.; Hirsch, T. Water Dispersible Upconverting Nanoparticles: Effects of Surface Modification on Their Luminescence and Colloidal Stability. *Nanoscale* **2015**, *7* (4), 1403–1410. <https://doi.org/10.1039/C4NR05954A>.
- (58) Mai, H.-X.; Zhang, Y.-W.; Si, R.; Yan, Z.-G.; Sun, L.; You, L.-P.; Yan, C.-H. High-Quality Sodium Rare-Earth Fluoride Nanocrystals: Controlled Synthesis and Optical Properties. *J. Am. Chem. Soc.* **2006**, *128* (19), 6426–6436. <https://doi.org/10.1021/ja060212h>.
- (59) Boyer, J.-C.; Veggel, F. C. J. M. van. Absolute Quantum Yield Measurements of Colloidal NaYF₄: Er³⁺, Yb³⁺ Upconverting Nanoparticles. *Nanoscale* **2010**, *2* (8), 1417–1419. <https://doi.org/10.1039/C0NR00253D>.
- (60) Wong, K.-L.; Bünzli, J.-C. G.; Tanner, P. A. Quantum Yield and Brightness. *Journal of Luminescence* **2020**, *224*, 117256. <https://doi.org/10.1016/j.jlumin.2020.117256>.
- (61) Kaiser, M.; Würth, C.; Kraft, M.; Hyppänen, I.; Soukka, T.; Resch-Genger, U. Power-Dependent Upconversion Quantum Yield of NaYF₄:Yb³⁺, Er³⁺ Nano- and Micrometer-Sized Particles – Measurements and Simulations. *Nanoscale* **2017**, *9* (28), 10051–10058. <https://doi.org/10.1039/C7NR02449E>.
- (62) Würth, C.; Fischer, S.; Grauel, B.; Alivisatos, A. P.; Resch-Genger, U. Quantum Yields, Surface Quenching, and Passivation Efficiency for Ultrasmall Core/Shell Upconverting Nanoparticles. *J. Am. Chem. Soc.* **2018**, *140* (14), 4922–4928. <https://doi.org/10.1021/jacs.8b01458>.

Chapter 3 Precursor-guided synthesis of $\text{LiYF}_4:\text{Yb}^{3+}$, Tm^{3+} nanoparticles having comparable efficiency with single crystals

3.1. Introduction

The unconventional energy conversion properties (from low energy photons to high energy photons) of upconverting nanomaterials make them versatile for a variety of applications such as optical biosensors,^{1,2} photocatalysis,³⁻⁵ photodynamic therapy⁶ etc. Among the commonly used host matrices such as oxides (Y_2O_3 , YVO_4), sulphides (ZnS , MoS_2), and fluorides (NaGdF_4 , YF_3 , LiYF_4) based matrix, the fluoride-based matrices enjoy the advantage of having relatively low phonon energy ($<400\text{ cm}^{-1}$) and therefore, serve as an ideal host for lanthanide dopants like Yb^{3+} and Tm^{3+} . In particular, the LiYF_4 matrix, being optically inactive (in the spectral range of interest) and also due to their ability to provide very large anti-stokes emission ranging from deep UV (265 nm) up to NIR (800 nm) region, could be used to overcome many challenges including undesirable non-radiative energy transfer, cross relaxations etc.

The availability of defect-free, less strained and anhydrous surface of these nanoparticles is of prime importance. As we know that getting UV emission from upconverting is very difficult and has a unique mechanism that is not very clear but it somehow requires sequential absorption of at least three or more photons which is highly unlikely. So the hindrance in energy transformation between lanthanide ions due to surface deactivations has adverse effects on the spectral conversion of NIR to UV photons. Literature on the anhydrous synthesis of upconverting nanomaterials and its influence on up-conversion intensity is limited.⁷ As the major focus of our research is based on the premise of using these nanoparticles for IR induced photocatalytic applications, especially using the classical titania (TiO_2) approach, which essentially requires UV radiation for their active participation in the photocatalytic process, the necessity of defect-free and surface OH^- devoid upconverting nanoparticles is necessary. Therefore, our attempt to produce well crystalline, surface defect-free nanocrystals includes the use of anhydrous molecular precursors. As discussed in the previous chapter that the use of anhydrous molecular precursors has a definite edge towards the synthesis of brighter upconverting nanoparticles which have minimal availability of surface OH^- groups. The inclusion of additional defect levels and competition with various energy level transitions in between lanthanide ions is the major drawback offered by surface $-\text{OH}$ groups. The minimisation of $-\text{OH}$ functionality on the surface can be achieved by surface passivation either using the core-shell strategy or by incorporating hydrophobic

ligands on the nanocrystal's surface. The use of later strategy has been developed by our group and described to be very efficient for obtaining very luminescent upconverting nanomaterials.^{5,8}

This chapter reports the synthesis of novel anhydrous molecular precursors and their properties which are then further used for the preparation of high-quality upconverting nanoparticles. These anhydrous precursors are prepared by a one-step process starting from oxides which is an improvement over previously reported anhydrous precursors in terms of the number of steps required for their synthesis. Further, these precursors are thermally decomposed in different conditions by varying temperature, concentration, solvents, time etc. Once the best performing upconverting nanoparticle configuration is chosen, we compare its upconversion emission performance with bulk single crystal with similar composition under similar excitation conditions.

3.2. Results and discussion

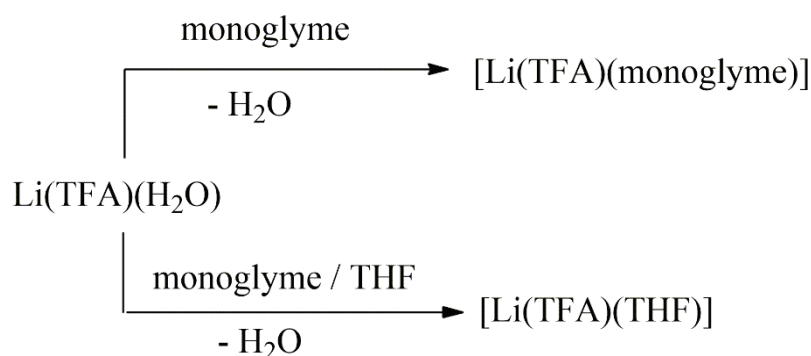
3.2.1. Synthesis and characterization of novel anhydrous molecular precursors

3.2.1.1. Synthesis

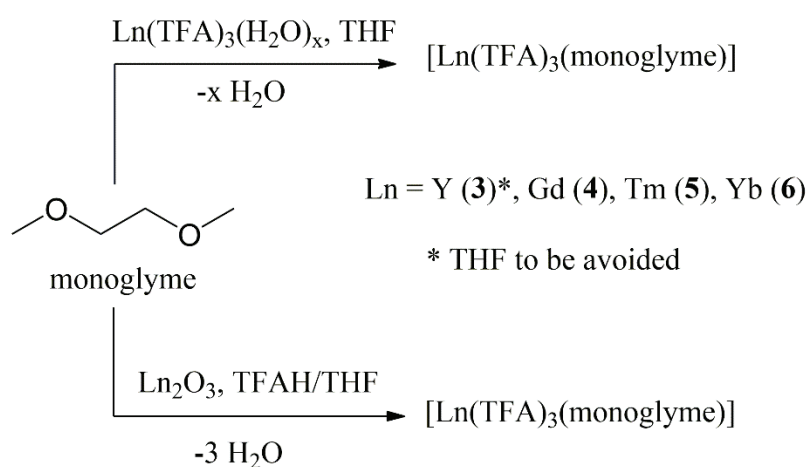
As mentioned in the Introduction section, there is a clear void in the literature for the well-characterized molecular precursors for LiLnF₄-based up-converting nanomaterials. Metal trifluoroacetate complexes are the most easily available and the cheapest source for the metal fluoride/oxofluoride nanomaterials.⁹ The hydrated Li(TFA)(H₂O) and Ln(TFA)₃(H₂O)_x are commercially available, but can also be synthesized easily by reacting LiOH or Ln₂O₃ with trifluoroacetic acid under reflux. However, the presence of water molecules is detrimental to the luminescent properties of UC nanomaterials.¹⁰ As thermal dehydration of these hydrated complexes have proved difficult,¹¹ the use of an ancillary co-ligand seems to be a preferred strategy to make them anhydrous. We and some other groups have previously demonstrated that the acyclic polyether glyme ligands, CH₃O(CH₂CH₂O)_xCH₃ [x = 1 (monoglyme), 2 (diglyme), 3 (triglyme), 4 (tetraglyme)], not only replace the water molecules of hydrated metal trifluoroacetates to afford anhydrous precursors, but also stabilize metal complexes by wrapping/shielding the metal cations efficiently and saturating their coordination spheres.^{5,8,12-15} Using this strategy, anhydrous glyme adducts of metal trifluoroacetates, such as [Li₃(TFA)₃(diglyme)₂],¹² [Li₅(TFA)₅(tetraglyme)₂],¹³ [Ln(TFA)₃(diglyme)] (Ln = Gd, Tm, Yb),¹⁴ [NaLn(TFA)₄(diglyme)] (Ln = Y, Gd)^{5,8,15} and [Na₂Y(TFA)₅(tetraglyme)]⁸ have been synthesized and characterized structurally. These glyme ligands also act as a surfactant during decomposition and, therefore, help to get nanoparticles with controlled size and desired dispersibility in organic media. In this work, we describe new anhydrous adducts of lithium and lanthanide trifluoroacetates with monoglyme and THF ligands as potential precursors for LiLnF₄-based up-converting nanoparticles. As compared to the high boiling di-, tri- and tetraglyme (162-275 °C), employing a low boiling monoglyme

(b. p. 85 °C) here has allowed us to use it both as a solvent and an ancillary co-ligand in a straightforward one-pot synthesis of the anhydrous precursors. This has important implication in terms of producing these precursors on large scale for industrial applications.

A simple stirring of $\text{Li}(\text{TFA})(\text{H}_2\text{O})$ in monoglyme affords a new anhydrous precursor $[\text{Li}(\text{TFA})(\text{monoglyme})]$ (**1**) in good yield. When the reaction medium was a 1:1 mixture of THF and monoglyme, it afforded anhydrous THF adduct $[\text{Li}(\text{TFA})(\text{THF})]$ (**2**). We also synthesized new anhydrous lanthanide monoglyme adducts $[\text{Ln}(\text{TFA})_3(\text{monoglyme})]$ [$\text{Ln} = \text{Y}$ (**3**), Gd (**4**), Tm (**5**), Yb (**6**)] by refluxing Ln_2O_3 with trifluoroacetic acid in THF in the presence of monoglyme (Scheme 2). Alternatively, the derivatives (**3**)–(**6**) could also be synthesized by stirring $\text{Ln}(\text{TFA})_3(\text{H}_2\text{O})_x$ with monoglyme in the presence of THF. Only, in the case of yttrium, it was necessary to avoid THF which promoted the formation of $[\text{Y}(\text{TFA})_3(\text{THF})_2]$. The details regarding their formation are mentioned in section 6.3. These air-sensitive complexes (**1**) - (**6**) were isolated as colourless crystals. They are readily soluble in THF, mildly soluble in monoglyme and sparingly soluble in Et_2O , hexane and pentane.



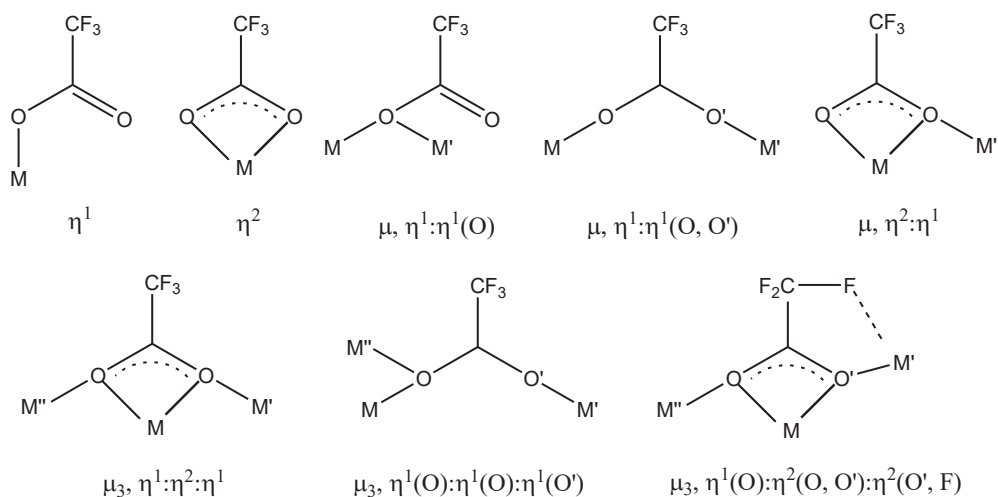
Scheme 3.1: Synthesis of anhydrous lithium precursors **1** and **2**.



Scheme 3.2: Synthesis of anhydrous lanthanide precursors **3-6**.

3.2.1.2. Structural characterization

Structural characterization of the precursors is critical to understand molecule-to-material transformation and, therefore, to optimize the properties of the final materials. Since the trifluoroacetate ligand can bind to a metal centre in a variety of fashions (Scheme 3.3), it is difficult to predict the structure of metal trifluoroacetate complexes. Therefore, we have carried out single-crystal X-ray structural studies on some representative compounds among newly synthesized **1-6**.



Scheme 3.3: Common bonding modes observed for the trifluoroacetate ligand in metal complexes.

The THF adduct $[\text{Li}(\text{TFA})(\text{THF})]_{\infty}$ (**2**) crystallizes in the triclinic space group $P\bar{1}$ and forms a straight 1D polymeric chain along the a -axis. Each TFA ligand bridges three lithium atoms in a $\mu_3, \eta^1(\text{O}):\eta^1(\text{O}):\eta^1(\text{O})$ manner (Figure 3.1 (a)). Each lithium atom bears a THF molecule to attain a 4-coordination number, which is further supplemented by secondary $\text{Li}\cdots\text{Li}$ [2.827(7)-3.795(4) Å] and $\text{Li}\cdots\text{F}$ [2.921(8)-4.633(8) Å] interactions. The overall structure can be seen as the $[\text{Li}(\mu, \eta^1(\text{O}):\eta^1(\text{O})-\text{TFA})(\text{THF})]_2$ dimers being joined *via* four-membered Li_2O_2 rings, thus forming 8- and 4-membered rings in an alternate manner (Figure 3.1 (b)). The $\text{Li}-\text{O}$ bond lengths range from 1.887(4) to 1.975(4) Å, which are consistent with those observed in the related $[\text{Li}_3(\text{TFA})_3(\text{diglyme})_2]^{12}$ and $[\text{Li}_5(\text{TFA})_5(\text{tetraglyme})_2]^{13}$. As expected, the $\text{Li}\cdots\text{Li}$ distance is significantly shorter in the 4-membered ring [2.827(7) Å] than in the 8-membered ring [3.795(4) Å]. Some selected bond lengths (Å) and angles ($^\circ$) for **2** are given in Table 3.1.

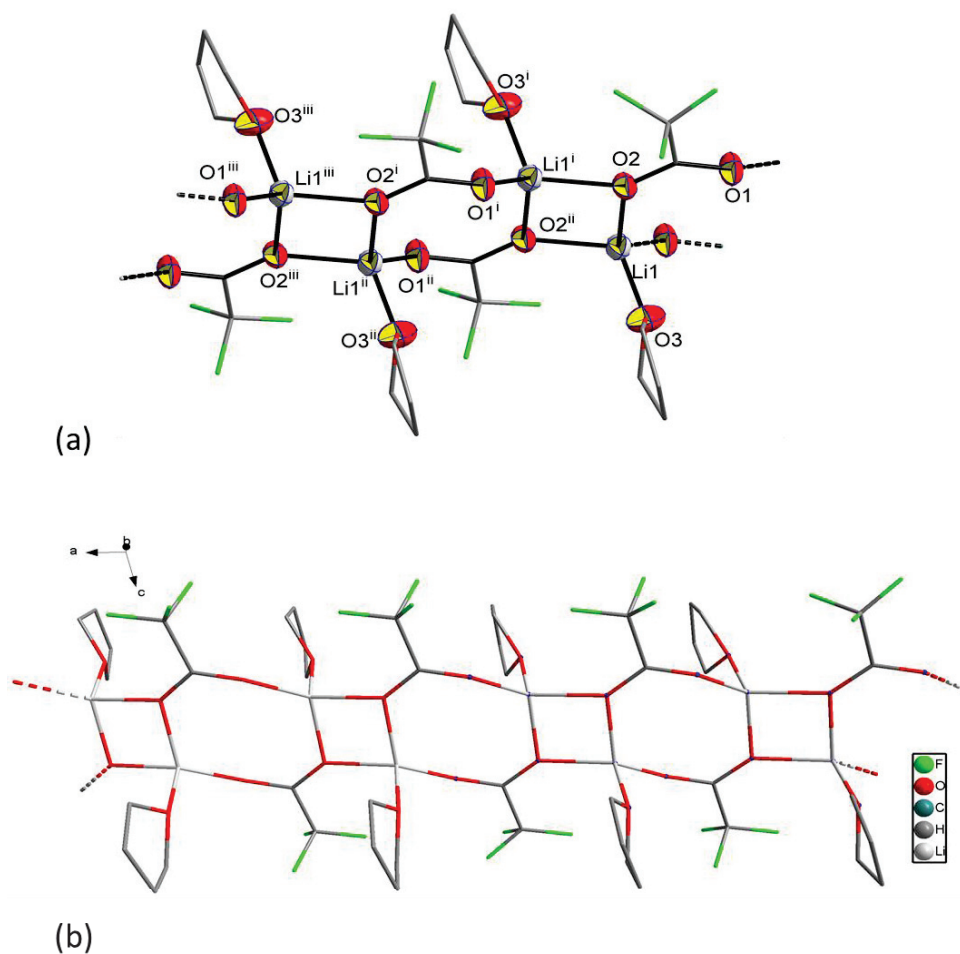


Figure 3.1: (a) Perspective view of $[\text{Li}(\text{TFA})(\text{THF})]_{\infty}$ (**2**) with displacement ellipsoids drawn at the 30% probability level. (b) One-dimensional structure of **2**. H-atoms on the THF ligand have been omitted for clarity. Symmetry codes: (i) $2-x, 1-y, -z$; (ii) $2+x, -1+y, z$;

Table 3.1: Selected bond lengths (Å) and angles (°) for **2**.

Bond length			
O1 ⁱ -Li1 ⁱ	1.887(4)	O2-Li1 ⁱ	1.956(4)
O2-Li1	1.975(4)	O3-Li1	1.927(5)
Li1---Li1 ⁱ	2.827(7)		
Bond angle			
O1 ⁱⁱ -Li1 ⁱⁱ -O2 ⁱ	121.4(2)	O1 ⁱⁱ -Li1 ⁱⁱ -O3 ⁱⁱ	107.2(2)
O2 ⁱⁱⁱ -Li1 ⁱⁱ -O2 ⁱ	88.0(1)	O3 ⁱⁱ -Li1 ⁱⁱ -O2 ⁱⁱⁱ	110.3(2)

Symmetry codes: (i) $2-x, 1-y, -z$; (ii) $2+x, -1+y, z$; (iii) $3-x, 1-y, -z$.

The lanthanide complexes $[\text{Ln}(\text{TFA})_3(\text{monoglyme})]_{\infty}$ [$\text{Ln} = \text{Gd}$ (**4**) and Yb (**6**)] are isostructural, which crystallize in the monoclinic space group $C2/c$ and form 1D zig-zag polymer. The perspective and extended structures of **4** and **6** are shown in Figure 3.2 and Figure 3.3, respectively, whereas Table 3.2

and Table 3.3 summarize their selected bond lengths (Å) and angles (°). For the sake of brevity, only the gadolinium(III) complex (**4**) is described in detail here.

The gadolinium centres in **4** are bridged by two and four TFA ligands alternatively, all bonded in $\mu, \eta^1: \eta^1$ fashion. The Gd...Gd distance [5.5644(10) Å] is significantly longer when bridged by only two TFA ligands, as against 4.4526(7) Å for Gd atoms bridged by four TFA ligands. Each Gd atom bears one bidentate monoglyme ligand to attain an 8-coordination number, the geometry being square antiprismatic. The Gd–O (η^2 -monoglyme) and Gd–O (μ -TFA) bond lengths range from 2.316(5) to 2.501(5) Å. As expected, the Gd–O (η^2 -monoglyme) bonds (av. 2.50 Å) are longer than the corresponding Gd–O ($\mu, \eta^1: \eta^1$ -TFA) ones (av. 2.357 Å). The structure of **4** and **6** can be related to that of $[\text{Y}(\text{TFA})_3(\text{THF})(\text{H}_2\text{O})]_\infty$, where the metals are bridged by four and two $\mu, \eta^1: \eta^1$ -TFA ligands alternatively.¹¹

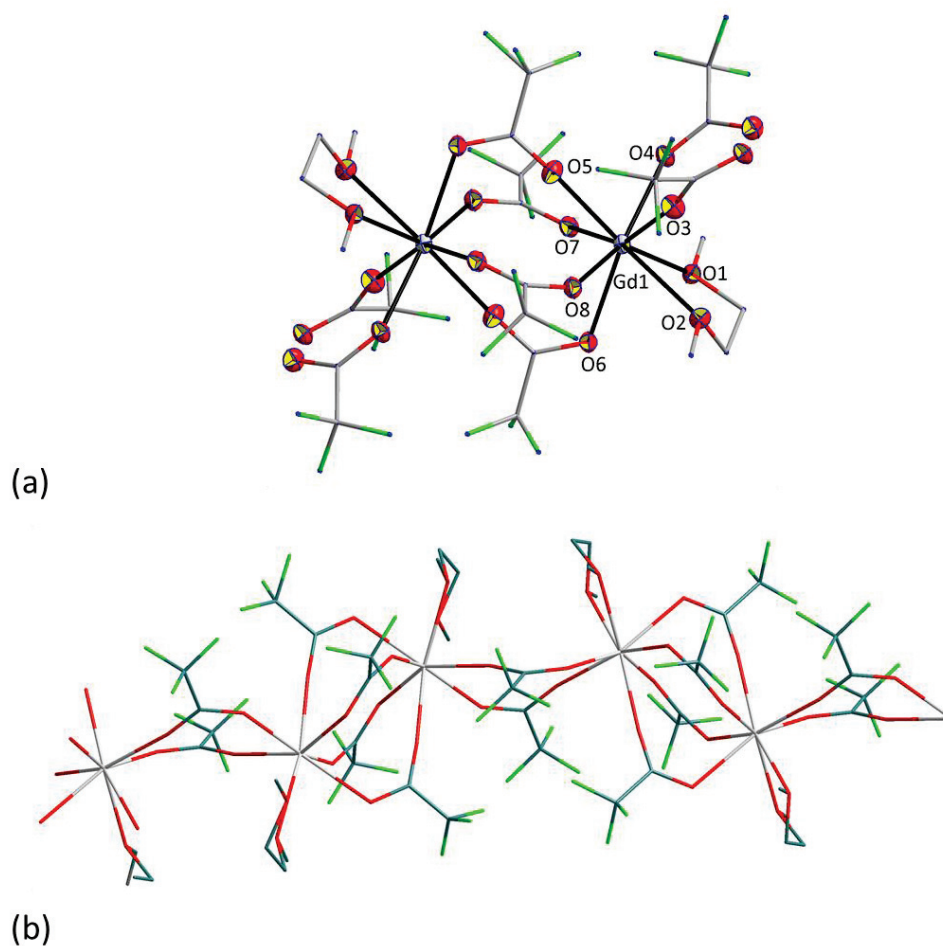


Figure 3.2: (a) Perspective view of $[\text{Gd}(\text{TFA})_3(\text{monoglyme})]$ (**4**) with displacement ellipsoids drawn at the 50% probability level. (b) One-dimensional structure of **4**. H-atoms on monoglyme ligand have been omitted for clarity. Atom colour scheme same as shown in Figure 3.1.

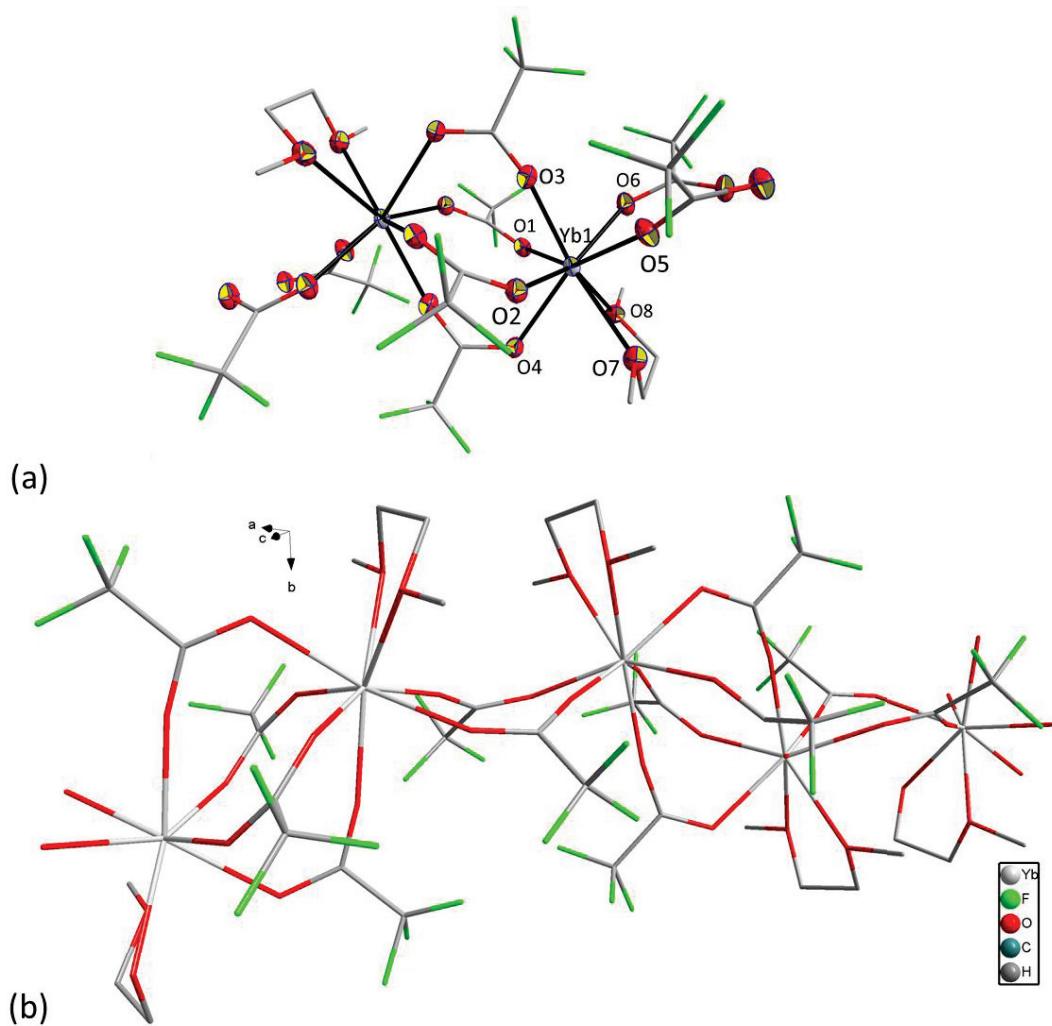


Figure 3.3: (a) Perspective view of $[\text{Yb}(\text{TFA})_3(\text{monoglyme})]$ (**6**) with displacement ellipsoids drawn at the 50% probability level. (b) One-dimensional structure of **6**. H-atoms on monoglyme ligand have been omitted for clarity.

Table 3.2: Selected bond lengths (\AA) and angles ($^\circ$) for **4**.

Bond length			
Gd1-O2	2.499(5)	Gd1-O1	2.501(5)
Gd1-O3	2.316(5)	Gd1-O4	2.347(5)
Gd1-O5	2.325(5)	Gd1-O6	2.421(5)
Gd1-O7	2.358(5)	Gd1-O8	2.376(5)
Bond angle			
O2-Gd1-O1	65.04(16)	O3-Gd1-O2	71.67(18)
O3-Gd1-O1	111.60(18)	O5-Gd1-O2	149.81(17)
O5-Gd1-O6	119.32(18)	O5-Gd1-O1	142.58(18)
O7-Gd1-O2	133.25(17)	O5-Gd1-O4	77.75(19)

Table 3.3: Selected bond lengths (Å) and angles (°) for **6**.

Bond length			
Yb1-O1	2.282(4)	Yb1-O2	2.301(5)
Yb1-O3	2.251(4)	Yb1-O4	2.324(4)
Yb1-O5	2.251(4)	Yb1-O6	2.271(4)
Yb1-O7	2.428(5)	Yb1-O8	2.440(5)
Bond angle			
O1-Yb1-O2	118.81(15)	O1-Yb1-O7	134.31(15)
O1-Yb1-O8	74.39(15)	O3-Yb1-O1	76.67(16)
O3-Yb1-O5	81.83(17)	O3-Yb1-O7	148.48(15)
O5-Yb1-O8	112.56(16)	O7-Yb1-O8	66.42(15)

3.2.1.3. Spectroscopic characterization

The FT-IR spectra of **1-6** account for anhydrous species (absence of νOH absorptions in the region $3000\text{-}3500\text{ cm}^{-1}$). The asymmetric and symmetric vibrations of the $\nu(\text{CO}_2)$ group are indicative of binding modes of a carboxylate ligand (Scheme 3.3). The stretching frequency of the C=O bond differs for solely bridging, chelating or both bridging and chelating TFA ligand. The position of this frequency is affected also by the number and type of donating atoms of the coordinating ligand on the metal centre. The appearance of a single but relatively broad peak in the region $1550\text{-}1800\text{ cm}^{-1}$ for the monoglyme complexes **1-6** is consistent with only one type of TFA ligand present in these precursors (Figure 3.4). The frequencies around $1110\text{-}1210\text{ cm}^{-1}$ confirm the presence of C-F and C-O bonds. Some low-frequency peaks around $410\text{-}650\text{ cm}^{-1}$ are characteristic vibration peaks for $\nu\text{M-O}$ bonds.

The ^1H NMR spectra of the diamagnetic complexes **1** and **3** show peaks of the coordinated monoglyme moiety at δ 3.28 and 3.46 ppm for CH_3 and CH_2 protons, respectively, whereas in the spectrum of **2**, the coordinated THF appears as two triplets at δ 1.81–1.89 and 3.66–3.70 ppm for the β - and α -hydrogens, respectively. A single peak at δ – 76.9–77.0 ppm in the ^{19}F NMR spectra of **1-3** confirmed the presence of TFA groups. These spectroscopic results, along with the elemental analysis data, indicate that the bulk powders of **1-6** are consistent with the single-crystal structures described in the previous subsection.

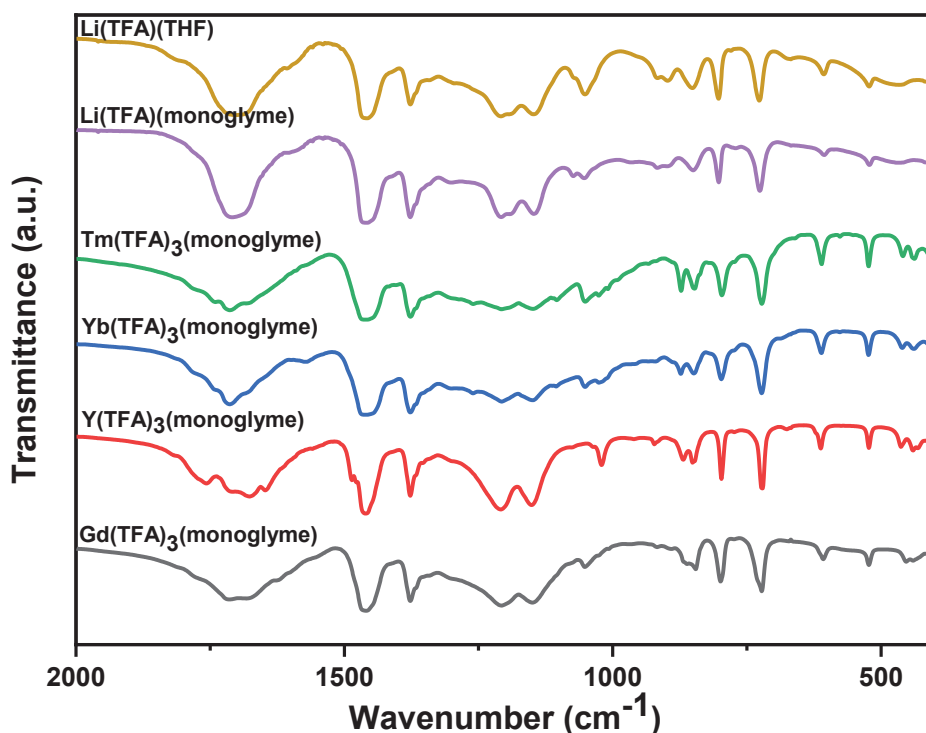


Figure 3.4: FT-IR spectra of 1-6.

3.2.1.4. Thermogravimetric analysis

The thermal behaviour of the new anhydrous lithium and lanthanide trifluoroacetate monoglyme precursors was investigated under an argon atmosphere in the 20-600 °C temperature range by thermogravimetric analysis (TGA) (Figure 3.5). The TGA curves of the lanthanide precursors ($\text{Ln}(\text{TFA})_3(\text{monoglyme})$) show predominantly one-step decomposition, as indicated by a prominent endothermic DTG peak at ~300 °C. The remaining weight of the residues (37.2-37.7% at 350 °C) is consistent with the formation of LnF_3 (theoretical values ~36.5 - 38.2%) as the end product. The lithium derivative **1** also shows a similar 1-step decomposition, with an endothermic peak at 300 °C. The remaining residue weight (~18% at 350 °C) accounts for a little more than the expected yield of LiF materials (12.4%), indicating an incomplete decomposition due to the presence of argon atmosphere. As compared to the starting hydrated complexes $\text{Li}(\text{TFA})(\text{H}_2\text{O})$ and $\text{Y}(\text{TFA})_3(\text{H}_2\text{O})_x$, the newly synthesized monoglyme complexes not only show a better-defined decomposition pattern but also require a slightly lower temperature to decompose. These monoglyme complexes are also better than the THF adduct $[\text{Y}(\text{TFA})_3(\text{THF})_2]$ which shows a clear 2-step decomposition.¹¹ More importantly, the good compatibility in the thermal behaviour of $[\text{Li}(\text{TFA})(\text{monoglyme})]$ and $[\text{Ln}(\text{TFA})_3(\text{monoglyme})]$ suggests that these precursors can be decomposed simultaneously to afford the LiLnF_4 matrix.

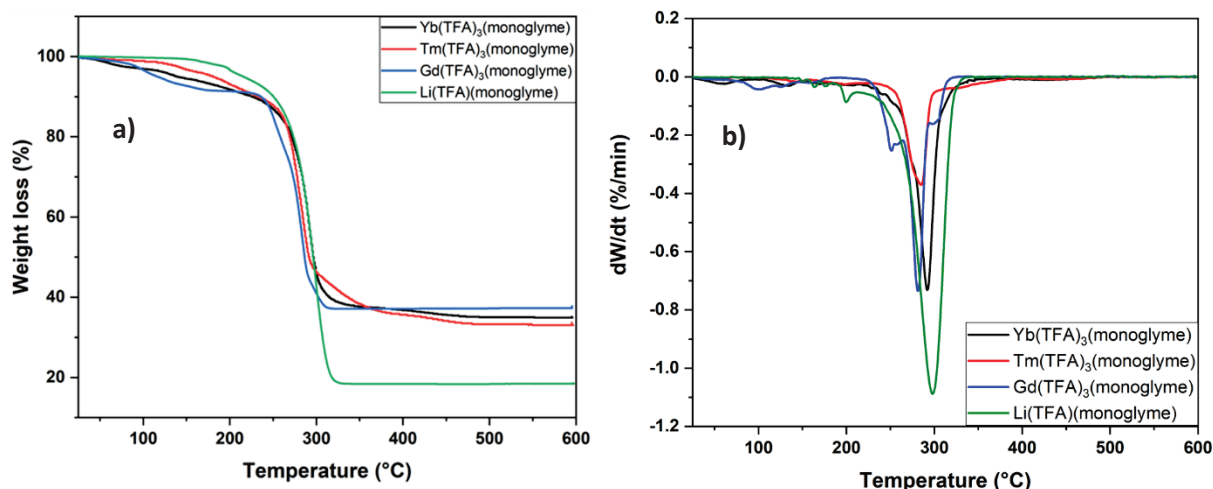


Figure 3.5: TGA (a) and DTG (b) curves of anhydrous monoglyme complex of metal trifluoroacetate.

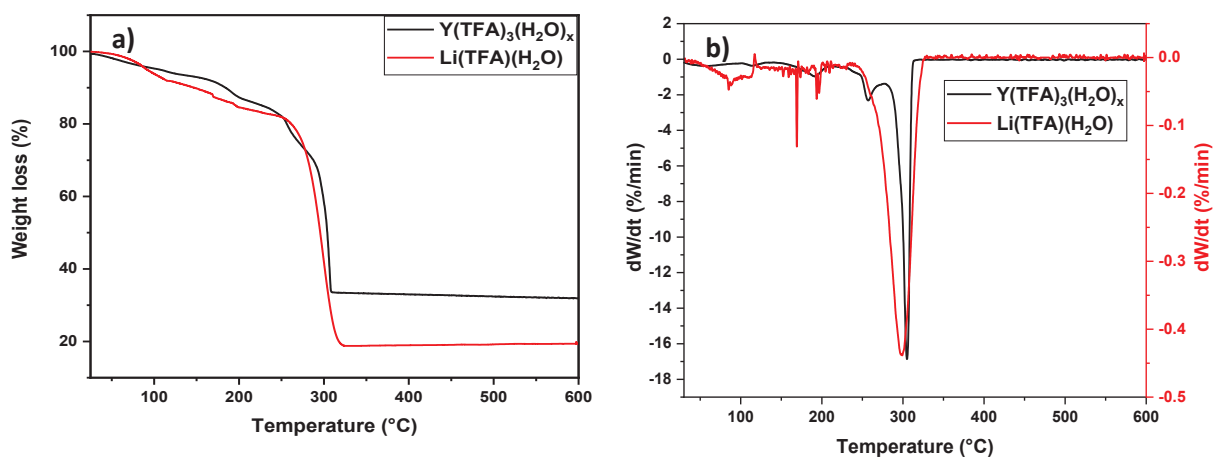


Figure 3.6: TGA (a) and DTG (b) curves of hydrated trifluoroacetate of lithium and yttrium.

3.2.2. Synthesis of undoped and Yb^{3+} , Tm^{3+} co-doped LiYF_4 nanoparticles from the thermal decomposition of anhydrous precursors

3.2.2.1. Synthesis of undoped LiLnF_4 matrices

The upconversion process is significantly dependent on the choice of host matrix, as it can exert a crystal field around the dopant ions and modify the excitation energy of dopant through lattice vibrations.¹⁶ Hence, it is necessary to choose a perfect host matrix that promises very low phonon energy and non-radiative relaxation emission. Many studies show the importance of fluoride matrices for obtaining high upconversion emission.¹⁷

As noted in the introduction of this chapter, the lithium-based matrix LiLnF_4 ($\text{Ln} = \text{Y}, \text{Gd}$) are promising host matrices for NIR to UV upconversion. As reported by Mahalingam et al.¹⁷ and Panov et al.,¹⁸ the main advantage of the LiYF_4 matrix is that due to the absence of any optically active ions, they

are completely devoid of any internal energy transfer between them, which can otherwise affect the upconversion efficiency or alter the upconversion mechanisms. Therefore, we synthesized LiYF_4 by simultaneous thermal decomposition of a 1:1 mixture of $[\text{Y}(\text{TFA})_3(\text{monoglyme})]$ and $[\text{Li}(\text{TFA})(\text{monoglyme})]$ anhydrous precursors in the mixture of 1-octadecene (ODE) and oleic acid (OA). This decomposition results in the formation of phase pure and well crystalline tetragonal LiYF_4 nanoparticles as indicated by its powder XRD pattern that corresponds to ICDD# 04-007-5501 (Figure 3.7 (a)).

On the other hand, a similar reaction of $[\text{Gd}(\text{TFA})_3(\text{monoglyme})]$ and $[\text{Li}(\text{TFA})(\text{monoglyme})]$ under identical synthetic conditions afforded a mixture of LiF and GdF_3 instead of LiGdF_4 (Figure 3.7 (b)). The possible reason for the non-formation of LiGdF_4 via this method may be that the thermodynamic barrier for the formation of tetragonal LiGdF_4 is high compared to LiYF_4 and therefore orthorhombic GdF_3 which has a lower energetic barrier is readily formed.¹⁹ Ya-Ping Du et al,²⁰ reported previously that heavier lanthanides (Dy to Lu including Y) tend to arrange themselves stoichiometrically into tetragonal LiLnF_4 phase whereas a mixture of LiF and LnF_3 is formed for lighter lanthanides (La to Gd).

To verify this hypothesis, we performed subsequently the reaction of $[\text{Yb}(\text{TFA})_3(\text{monoglyme})]$ and $[\text{Li}(\text{TFA})(\text{monoglyme})]$ under similar synthetic conditions and we obtained well crystalline LiYbF_4 indexed with ICDD# 04-010-3625 (Figure 3.7 (c)) nanoparticles. Although the LiYbF_4 matrix is isostructural to LiYF_4 , unlike the Y^{3+} ion, the Yb^{3+} ion could act as the sensitizer ion to transfer energy to the other active centres to enhance the luminescence of the upconverting nanoparticles. Hence, we can eliminate the limit of adding a small amount of sensitizer, which due to concentration quenching, reduces the upconversion luminescence. That is why they are considered as one of the brightest host matrices.²¹

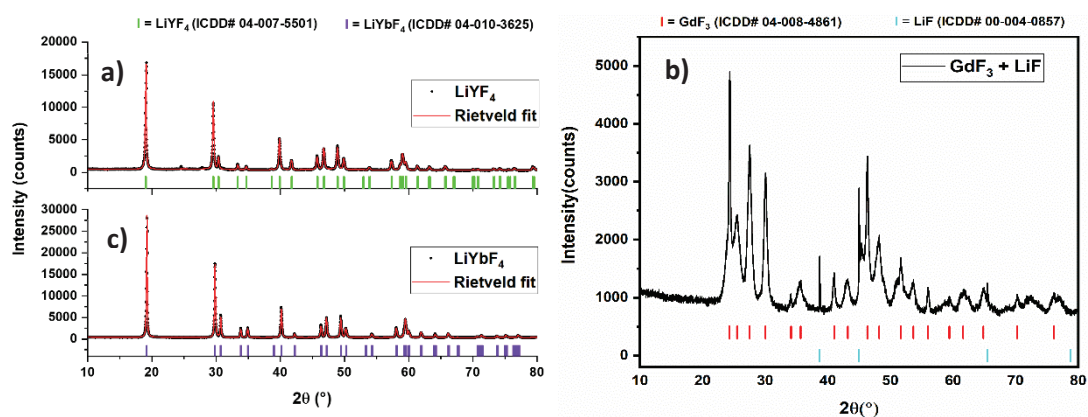


Figure 3.7: powder x-ray diffraction pattern of undoped LiLnF_4 ($\text{Ln} = \text{Y}$ (a), Yb (c)) prepared by thermal decomposition of anhydrous molecular precursors in 1:1 ratio of ODE and OA. The synthesis using the Gd precursors yielded in the mixture of GdF_3 and LiF (b) instead of LiGdF_4 . The ticks below the plot indicate the respective positions of the reflection for that particular phase.

The TEM images presented show that both the LiYF_4 and LiYbF_4 matrices have similar crystallographic tetragonal phase and also there is no big difference in their morphology. In Figure 3.8(a) we see that LiYF_4 nanosheets are stacked over each other whereas Figure 3.8(b) shows more nanoplate like morphology of LiYbF_4 . These nanostructures are well-crystalline as also observed from their higher X-ray diffraction intensities.

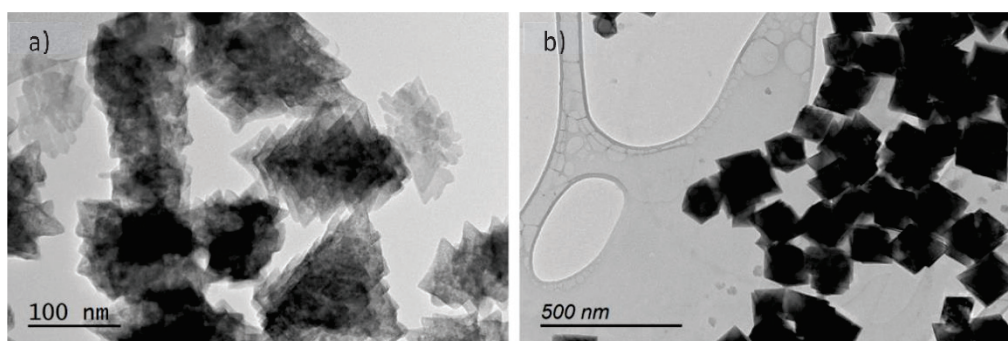


Figure 3.8: Transmission electron microscopy images of a) undoped LiYF_4 and b) undoped LiYbF_4 prepared by thermal decomposition of anhydrous molecular precursors.

3.2.2.2. Synthesis of Yb^{3+} , Tm^{3+} doped LiYF_4 nanoparticles under different synthetic conditions

3.2.2.2.1. Influence of ratio of activator ions

The ratio of both sensitizer and activator ions play an important role in the final upconversion emission. In a codoped system like $\text{LiY}_x\text{Yb}_z\text{F}_4: \text{Tm}^{3+}$, if the amount of dopants ($\text{Yb}^{3+}/\text{Tm}^{3+}$) is less than the full potential of these nanoparticles cannot be observed, but on the other hand, a slight excess in the concentration of these dopant ions can reduce the upconversion emission to a great extent due to the phenomenon called concentration quenching.^{21,22} So, a very well balance of concentration of both dopants (sensitizer Yb^{3+} and activator Tm^{3+}) is needed to maximize the upconversion emission. The optimum amount of the sensitizer is necessary to both absorb and transfer as much light as we can

before we start to observe quenching of upconversion due to a higher concentration of these ions. Similarly, the amount of activator thulium ions is also a key factor to get higher upconversion emission. From our previous chapter, we learnt that for efficient absorption and transfer of the infrared light the ideal concentration of sensitizer should be ~20%. Beyond that, due to the concentration quenching effect, we started losing the upconversion intensity.^{21,22} Hence, on this basis we decided to fix the concentration of Yb³⁺ ions to be ~20% for our study and in this section, we will study the effect of change of activator ion's concentration.

To find the optimum concentration of dopant activator ions for efficient upconversion, we conducted our study on the effect of activator ion (Tm³⁺) with fixed sensitizer (Yb³⁺) concentration. We kept the doping concentration of sensitizer (Yb³⁺) to be 20 mol% of the host matrix and varied the concentration of activator (Tm³⁺) as 0.4%, 0.8% and 1.2%. Generally, going beyond 2% of activator concentration leads to reduced upconversion emission due to cross-relaxation between different transitions.²¹ The synthesis of these nanoparticles was achieved by thermal decomposition of appropriate amounts of [Ln(TFA)₃(monoglyme)] (Ln = Y, Yb, Tm) and [Li(TFA)(monoglyme)] anhydrous molecular precursors in a 1:1 mixture of ODE and OA.

a) Effect on the crystalline phase

The effect of varying the concentration of activator on the crystalline phase of LiYF₄ nanoparticles was studied by powder X-ray diffraction. Figure 3.9 shows the Rietveld refinement of a series of samples prepared by varying the doping ratio of activator ions while keeping the concentration of sensitizer (Yb³⁺) fixed at 20 mol%. All these samples are well-crystalline and there is no major change in their crystal phase. They are phase-pure tetragonal LiYF₄ and are indexed with ICDD database file # 04-004-5501.

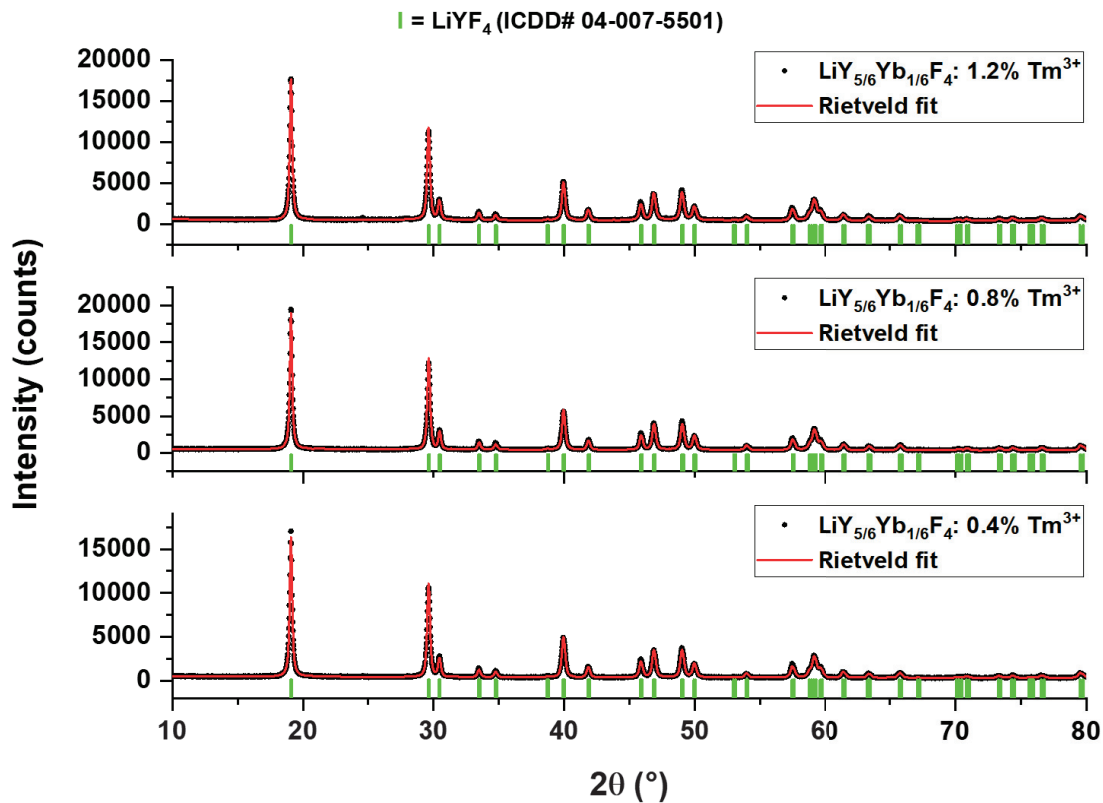


Figure 3.9: Rietveld refinement performed on X-ray diffraction pattern of a series of doped LiYF_4 with fixed ratio of sensitizer (Yb^{3+}) but different ratio of activators (Tm^{3+}) ($\text{Yb} = \sim 20\%$; $\text{Tm} = 0.4\%, 0.8\%, 1.2\%$). The ticks below the plot indicate the respective positions of the reflection for that particular phase.

b) Effect on morphology/shape of nanoparticles

The morphology of these nanoparticles was studied by transmission electron microscopic studies. The TEM images, as shown in Figure 3.10, show that these nanoparticles tend to be arranged in a diamond shape. We performed TEM studies on samples doped with 20% of sensitizer ytterbium (Yb^{3+}) with a different ratio such as 0.4%, 0.8% and 1.2% of activator thulium (Tm^{3+}). In all these images (Figure 3.10 (a-c)), these diamond-shaped, plate-like nanoparticles are stacked over each other. These diamond-shaped nanoparticles then stack in a way to form star-shaped agglomerated nanoparticles.

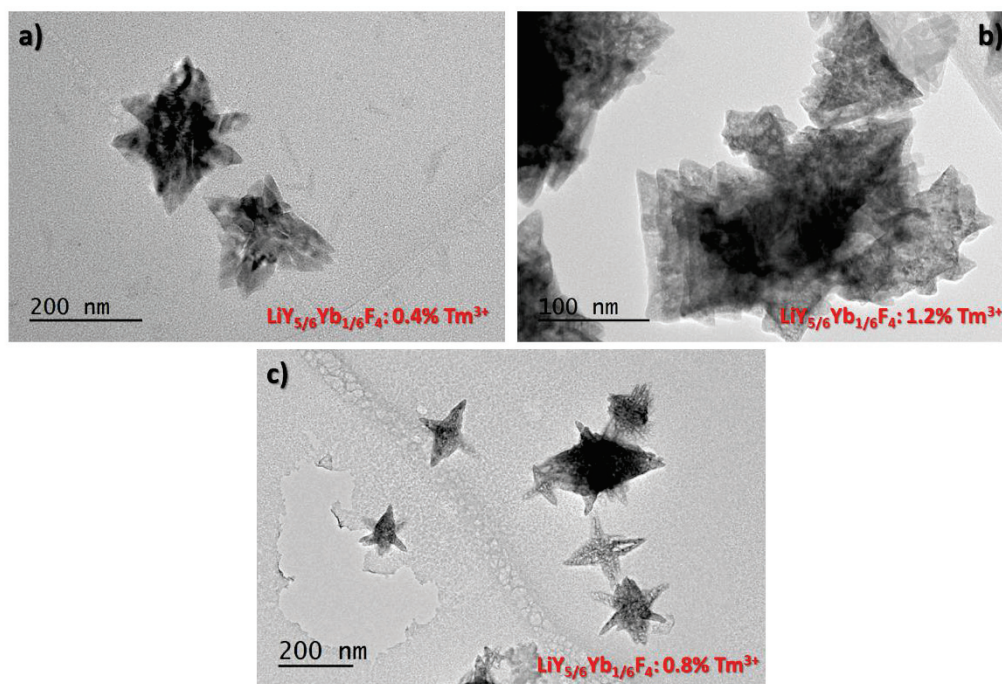


Figure 3.10: Transmission electron microscopy images of $\text{LiY}_{5/6}\text{Yb}_{1/6}\text{F}_4: 0.4\% \text{Tm}^{3+}$ (a), $\text{LiY}_{5/6}\text{Yb}_{1/6}\text{F}_4: 1.2\% \text{Tm}^{3+}$ (b) and $\text{LiY}_{5/6}\text{Yb}_{1/6}\text{F}_4: 0.8\% \text{Tm}^{3+}$ (c).

c) Effect on upconversion efficiency

We performed upconversion studies on all these samples to find out the best concentration of dopant lanthanide ions at a power density of $\sim 5 \text{ W/cm}^2$. As reported, at a higher concentration of dopant ions, the average dopant-dopant separations become smaller, therefore increasing the rates and efficiencies of a variety of energy-transfer processes.²¹ These processes not only include various essential energy transfer processes to achieve upconversion, but also undesired energy-loss pathways such as cross-relaxation and energy migration to the nanoparticle surface. The doping per cent of sensitizer (Yb^{3+}) and activator ions (Tm^{3+}) can range from 0-60% and 0.5-8%, respectively, before concentration quenching takes place.²¹

On exciting these samples with 973 nm CW laser, we observed a very clear trend in the upconversion emission (Figure 3.11). All the characteristic Tm^{3+} transitions can be observed. The spectra are dominated by NIR ${}^3\text{H}_4 \rightarrow {}^3\text{H}_6$ transitions centred at 794 nm. Other transitions corresponding to 475 nm (${}^1\text{G}_4 \rightarrow {}^3\text{H}_6$) and 364 nm (${}^1\text{D}_2 \rightarrow {}^3\text{H}_6$) are also prominent in nearly all the samples. The only difference is their intensity values. At a 20% doping concentration of the sensitizer (Yb^{3+}) ions, we observed some deep UV emission arising from ${}^1\text{I}_6$ to the ground levels. This particular transition is very prominent in the sample doped with 0.4% of Tm^{3+} ions. Out of all these samples, the highest upconversion emission we observed is for this particular sample. Also, all the other transitions are

very efficient at this doping percentage of Tm^{3+} . This suggests that to obtain high upconversion emission intensities from this series of nanoparticles doped with different amount of lanthanide ions, the optimum concentration of sensitizer Yb^{3+} and activator Tm^{3+} would be 20% and 0.4%, respectively.

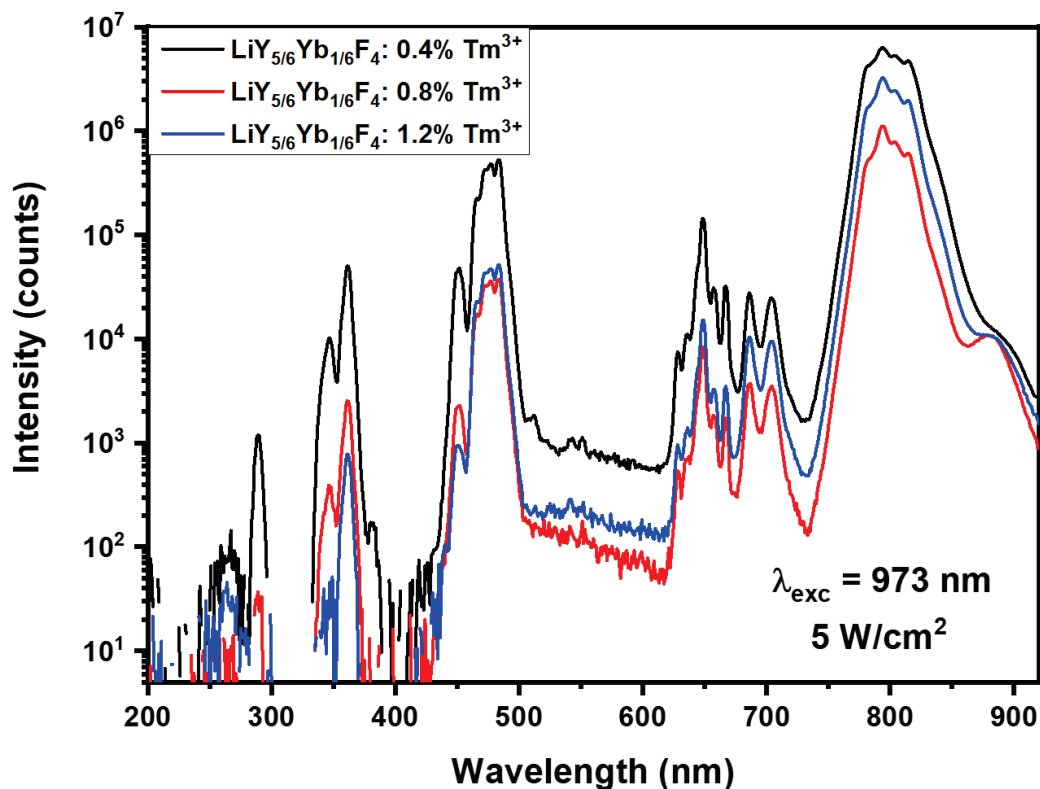


Figure 3.11: Difference in the upconversion emission intensities of the samples prepared with a different doping concentration of activator ions (Tm^{3+}) while keeping sensitizer (Yb^{3+}) at a fixed concentration. These spectra were measured from dry powder under similar excitation condition for all the samples.

d) Response to temperature and its effect on upconversion emission intensities

The thermal response of these nanoparticles was studied by thermogravimetric analysis performed in the air in the range of 25 °C to 600 °C. The heat ramping rate was fixed as 5 °C/min. TGA curve (Figure 3.12) shows that these nanoparticles are quite stable at high temperature. There is a major weight loss of 1.5% starting after 225 °C, which corresponds to the loss of capped oleic acid ligands on the nanoparticle's surface.

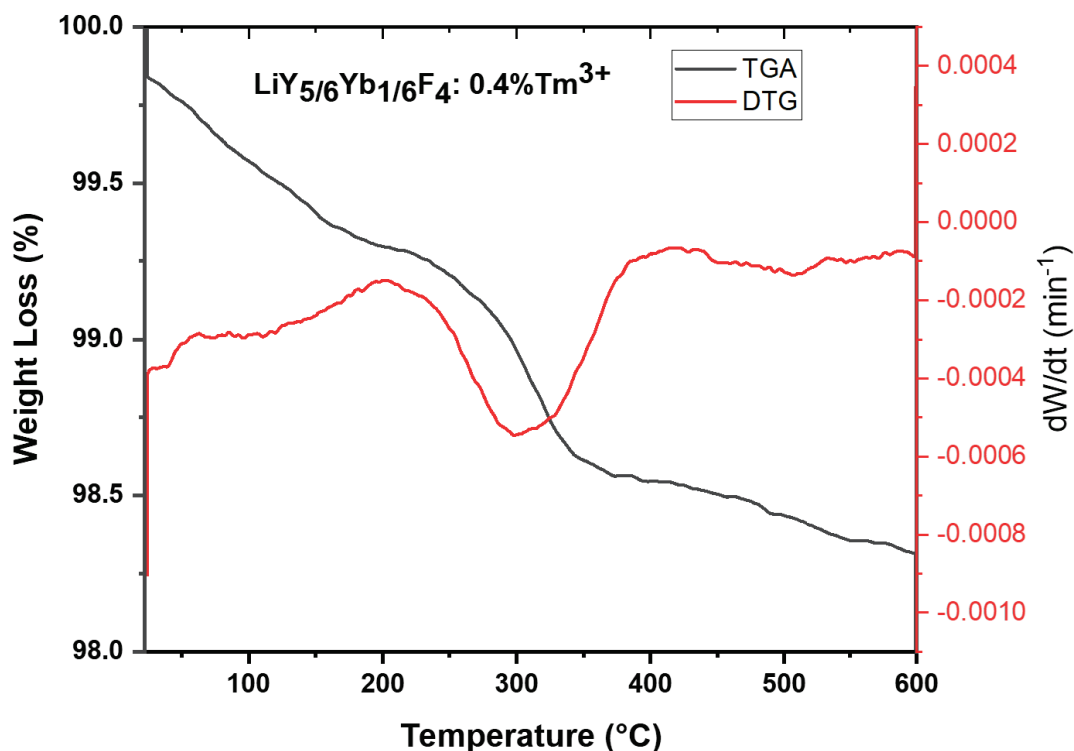


Figure 3.12: TGA and DTG curves of LiYF_4 doped with 20% Yb^{3+} and 0.4% Tm^{3+}

Since we found these nanoparticles to be quite stable at the higher temperature, and from the literature, we understand that the upconversion luminescence is highly dependent on the surrounding temperature,²³ therefore, we conducted a temperature-dependent upconversion response for the $\text{LiY}_{5/6}\text{Yb}_{1/6}\text{F}_4: 0.4\% \text{Tm}^{3+}$ nanoparticles, as we observed highest upconversion emission from this particular combination of dopant ions. The samples were placed on a DSC600 heating/cooling stage from Linkam Corporation equipped with a sapphire window. We recorded the response in the temperature range of -180 °C to 210 °C (Figure 3.13). As expected, with the increase in temperature, we observed a decrease in the upconversion emission from $^1\text{I}_6$, $^1\text{D}_2$, and $^1\text{G}_4$ energy levels. On the contrary, we see a clear switch in the emission behaviour of the sample where the increase in the emission intensity is observed for the transitions from $^3\text{F}_i$ and $^3\text{H}_4$ energy levels to the ground state (> 670 nm). This might be because cross-relaxation and non-radiative recombination steps may not necessarily lead to irreversible energy loss, but the energy may be used in the next energy-transfer upconversion step.²² These results show the potential of these nanoparticles for their use in temperature sensing applications as well.

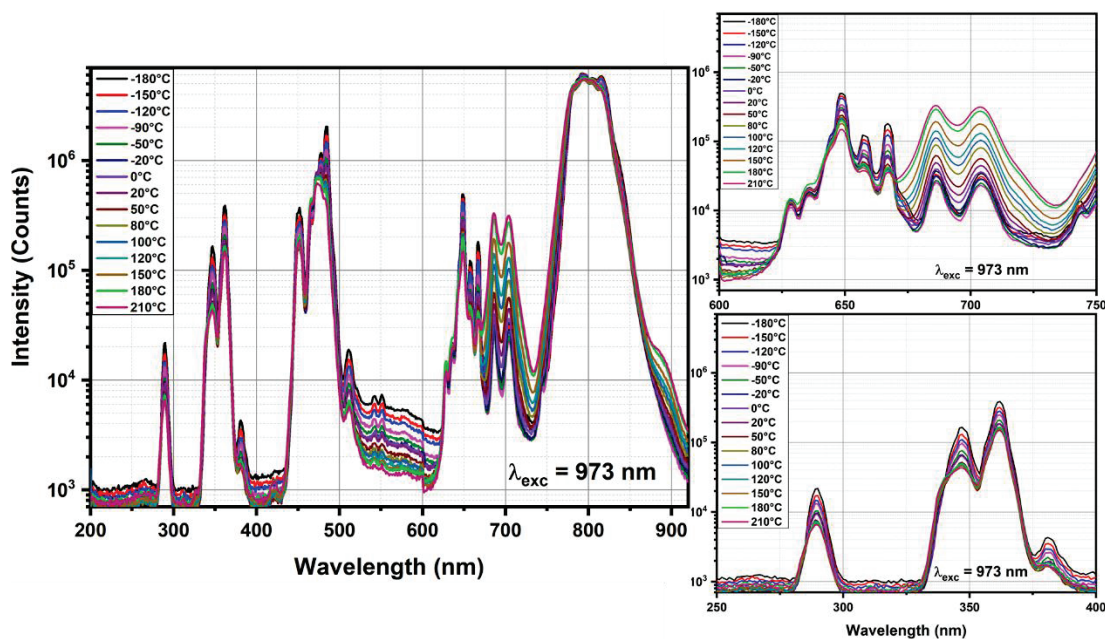


Figure 3.13: Temperature-dependent upconversion response of $\text{LiY}_{5/6}\text{Yb}_{1/6}\text{F}_4: 0.4\% \text{Tm}^{3+}$.

3.2.2.2.2. Influence of ratios of ODE and OA

a) Effect on crystalline phase and composition

The ratio of solvents during the decomposition of anhydrous precursors greatly affects the shape and size of $\text{LiY}_{5/6}\text{Yb}_{1/6}\text{F}_4: 0.4\% \text{Tm}^{3+}$ upconverting nanoparticles. To understand the effect of varying the ratio of solvent during the thermal decomposition, we chose three different samples having a nearly similar concentration of lithium (0.03 g/ml) or Yttrium (0.11 g/ml), but the different ratio of solvent (1-octadecene and oleic acid = 1:1, 1:3 and 3:1). The decomposition performed with these different conditions results in highly crystalline nanoparticles which show no major change in their phase, but a few extra peaks of YF_3 and LiF were observed in the cases of 1:3 and 3:1 ratio of 1-octadecene (ODE) and oleic acid (OA), respectively. All the indexed peaks from powder XRD can be associated with the tetragonal arrangement of LiYF_4 (ICDD # 04-007-5501), cubic LiF (ICDD # 00-004-0857) and orthorhombic YF_3 (ICDD # 00-032-1431) (Figure 3.14). On assessing the composition of these nanoparticles using Rietveld analysis (Table 3.4), we found that when the ratio of solvents is not 1:1 then apart from LiYF_4 , we also observe a small amount of either YF_3 (5.2%), if the ratio of ODE and OA is 1:3 or LiF (5.6%) when this ratio is reversed to 3:1. From the careful analysis of the presence of a small amount of LiF and YF_3 in the powder, it can be concluded that the formation of LiYF_4 nanoparticles is achieved by the interaction of individual LiF and YF_3 at high temperature. In bulk, LiF and YF_3 binary systems usually result in a eutectic mixture of LiF-YF_3 , followed by the formation of single-crystal LiYF_4 ;²⁴⁻²⁷ whereas in nanoparticles they either form well crystalline LiYF_4 single-crystal nanoparticles

or a part of them may remain in the forms of LiF and YF_3 depending upon the reaction conditions (temperature, duration and solvent ratio).^{16,28} In our study, we found that when the amount of OA in the decomposition solvent is more than ODE (3:1; $\text{OA} > \text{ODE}$), it favours the formation of thermodynamically stable orthorhombic YF_3 first, (due to feeble competition between Li^+ and Y^{3+} ions to interact with F^- ions in the solution) and then depending on the reaction conditions (high temperature, long reaction time, etc.) the slow diffusion of Li^+ ions causes the phase transformation from orthorhombic YF_3 into tetragonal LiYF_4 . On the contrary, when the amount of OA is less than ODE (1:3; $\text{OA} < \text{ODE}$), then the solubility of F^- ions in the solution reduces and super saturation of Li^+ increases, resulting in LiF crystals. These already precipitated LiF crystals then react with Y^{3+} and F^- present in the solution to yield LiYF_4 nanocrystals. With a longer reaction time, we can completely transform these LiF crystals and get pure LiYF_4 nanocrystals. These findings are consistent with the detailed study on the impact of pH on the formation of YF_3 nanoparticles by Ye et al.²⁹ Supported by these, our findings further demonstrate that the formation of LiYF_4 nanoparticles does not involve the formation of LiYF_4 seeds and their growth further on but, instead, it is governed by the formation of YF_3 (or LiF) nanoseeds and then its growth into subsequent LiYF_4 crystals.¹⁸

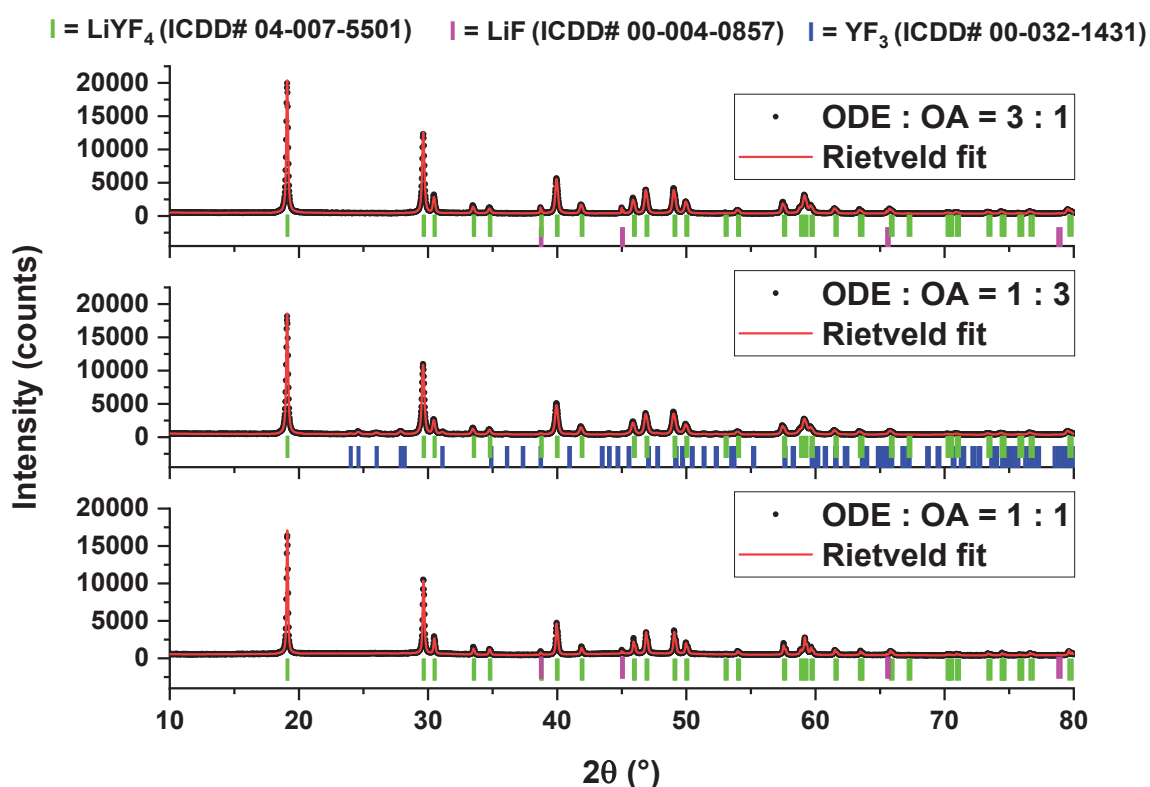


Figure 3.14: Rietveld refinement performed on X-ray diffraction pattern of three different samples prepared using different ratios of ODE and OA. The ticks below the plot indicate the respective positions of the reflection for that particular phase.

Table 3.4: Rietveld refinement parameters of powder X-ray diffraction pattern of different samples prepared with different ratio of solvents during thermal decomposition.

Parameters		ODE : OA = 1 : 3	ODE : OA = 3 : 1	ODE : OA = 1 : 1
Phase (%)	LiYF ₄	94.7	94.9	95.9
	YF ₃	5.1	-	-
	LiF	0.2	5.1	4.1
Chi square		1.6	1.8	1.7
R _{wp} (%)		8.0	8.0	9.6

b) Effect on morphology

From the TEM images (Figure 3.15), it is quite evident that the composition of solvents for the thermal decomposition of anhydrous precursors has a great impact on not only the morphology (size and shape) but also the phase of nanoparticles prepared. When the volumetric ratio of ODE and OA is kept at either 1:3 or 3:1, we observed agglomerated, unevenly distributed non-uniform nanoparticles, whereas well-crystalline diamond-shaped nanoparticles are observed for the ratio 1:1. The use of an optimum ratio of these solvents is of prime importance for the synthesis of these upconverting nanoparticles as it is one of the major factor deciding the morphology and composition of these upconverting nanoparticles. The fact that oleic acid becomes more sensitive towards the water at higher pH,²⁹ underline the importance of our upconverting nanoparticles synthesis approach using anhydrous precursors.

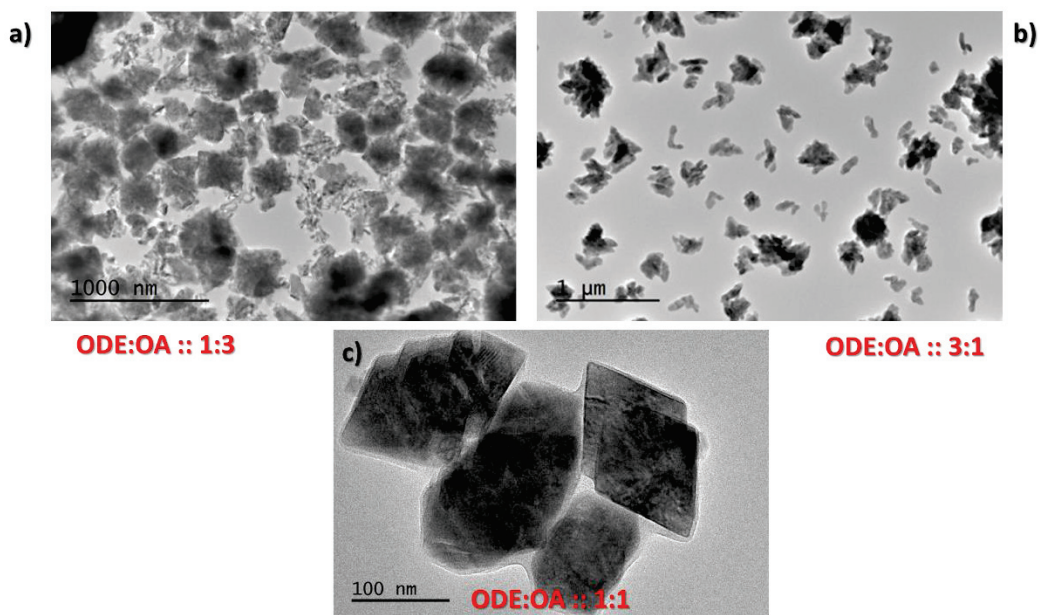


Figure 3.15: Transmission electron microscopy images of different $\text{LiY}_{5/6}\text{Yb}_{1/6}\text{F}_4: 0.4\% \text{Tm}^{3+}$ samples prepared by varying the ratio of ODE to OA as a) 1:3, b) 3:1, and c) 1:1

c) Effect on upconversion efficiency

This agglomeration and uneven distribution of nanoparticles might result in higher surface defects on the nanoparticle surface, which can also be assessed by observing the intensity of upconversion. Under similar excitation conditions ($\lambda_{\text{exc}} = 972 \text{ nm}$; power density = 10.9 W/cm^2), the samples prepared using different ratios of the solvents show varied photoluminescence emission profile. In Figure 3.16, for the nanoparticles prepared using 1:1 ratio, we can easily observe sharp and strong UV emission starting from 265 nm (${}^3\text{P}_2 \rightarrow {}^3\text{H}_6$) up to 362 nm (${}^1\text{D}_2 \rightarrow {}^3\text{H}_6$) including 290 nm (${}^1\text{I}_6 \rightarrow {}^3\text{H}_6$), 312 nm (${}^3\text{P}_2 \rightarrow {}^3\text{F}_4$), 347 nm (${}^1\text{I}_6 \rightarrow {}^3\text{F}_4$). The emission intensity for the same transitions shows a strong reduction for the samples prepared using 1:3 and 3:1 ratio of solvents. The dip in the upconversion emission intensity can be attributed to the combination of the following factors - lower crystallinity, higher cross-relaxation due to the phase transformation from orthorhombic YF_3 to the tetragonal LiYF_4 ^{16,28}, or higher surface defects.³⁰⁻³³ Usually, the presence of $-\text{OH}$ groups^{34,35} on the surface is the major cause of upconversion intensity quenching. However, since all these syntheses were carefully carried out in the inert atmosphere under schlenk lines, so the probability of the presence of $-\text{OH}$ groups on their surface is significantly lower. The important aspect of this study is that the UV component of the upconversion intensity is high and comparable to the near-infrared region, which is usually not observed in the case of small nanoparticles because of higher surface energies and defects.^{36,37} This can be attributed to the high crystallinity of the nanoparticles prepared using thermal decomposition of anhydrous precursors (as discussed in the previous chapter 2).

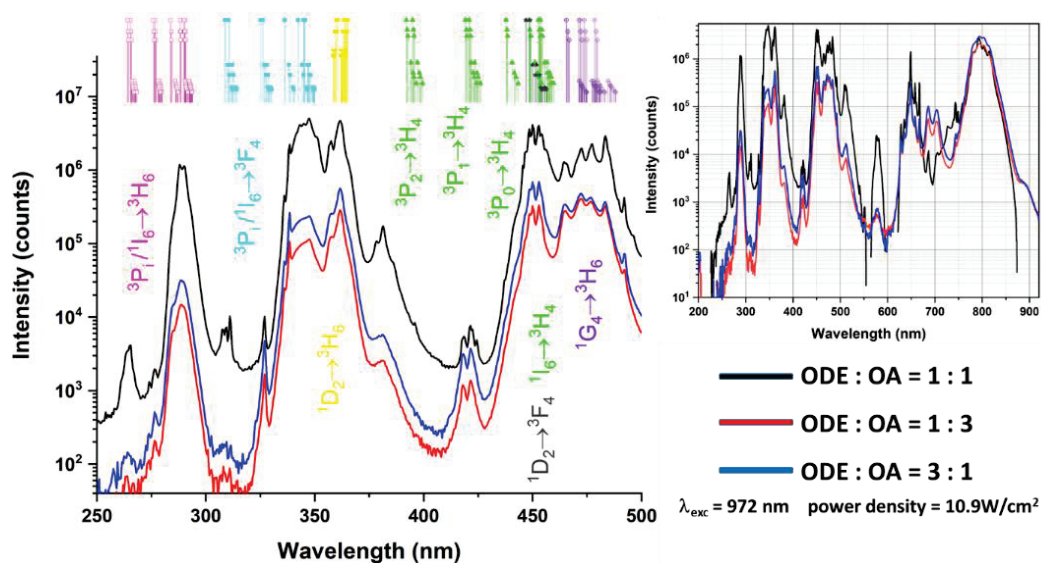


Figure 3.16: Difference in the upconversion emission intensities of the samples prepared using three different ratios of solvents (ODE and OA). These spectra were measured from dry powder in the same excitation condition for all three samples.

3.2.2.2.3. Influence of precursor's concentration

a) Effect on crystalline phase and composition

In the previous section, we summarized how the formation of LiYF_4 is progressed by the formation of YF_3 seeds, followed by the intercalation of Li^+ into the YF_3 crystal lattice. The study of variation of concentration of precursors further enhances our understanding of the formation of LiYF_4 nanoparticles. Here, we prepared two different precursor solutions, one having a concentration of Li (or Y) equal to 0.520 mmol/ml and another with a concentration of 0.175 mmol/ml. These solutions were then decomposed separately in the mixture of 1:1 ODE and OA at 290 °C for 1h under an inert atmosphere. The powder XRD patterns confirm the presence of phase-pure LiYF_4 for lower concentration (0.175 mmol/ml) and a mixture of LiYF_4 and YF_3 nanoparticles for higher concentration (0.520 mmol/ml) of precursors (Figure 3.17). The composition of different phases was then analysed using Rietveld refinement. The decomposition performed with a higher concentration of precursors results in a mixed-phase of ~19% orthorhombic YF_3 and ~81% tetragonal LiYF_4 , whereas for a lower concentration of precursors, we obtained ~100% tetragonal LiYF_4 . The complete refinement data is provided in Table 3.5. During the thermal decomposition process, we mix all the precursors in the mixture of ODE and OA and homogenize the solution by heating it to 120°C for about an hour (as discussed in chapter 6 experimental). From the previously discussed section and available literature, we can say that formation of LiYF_4 is achieved by the synthesis of YF_3 nuclei seeds first and then incorporation of Li^+ ions into the crystal matrix leads to the formation of tetragonal LiYF_4 .^{16,28,38} However, at a higher concentration of precursors in the decomposition solution the diffusion of Li^+ ions

(being already slow) into the YF_3 seeds now become more hindered (due to the presence of longer alkyl chains, which results in steric repulsion, therefore, keeping these particles well separated in the solutions) leading to precipitation of YF_3 . But if the reaction conditions are modified (e.g. prolonged reaction time), this problem of slow diffusion could be overcome. In other words, at higher concentration of these precursors, due to steric hindrance, the preferential growth of initial orthorhombic YF_3 nuclei into tetragonal LiYF_4 via Li^+ intercalation is limited, hence, leading to the mixture of tetragonal LiYF_4 and some non-transformed orthorhombic YF_3 .

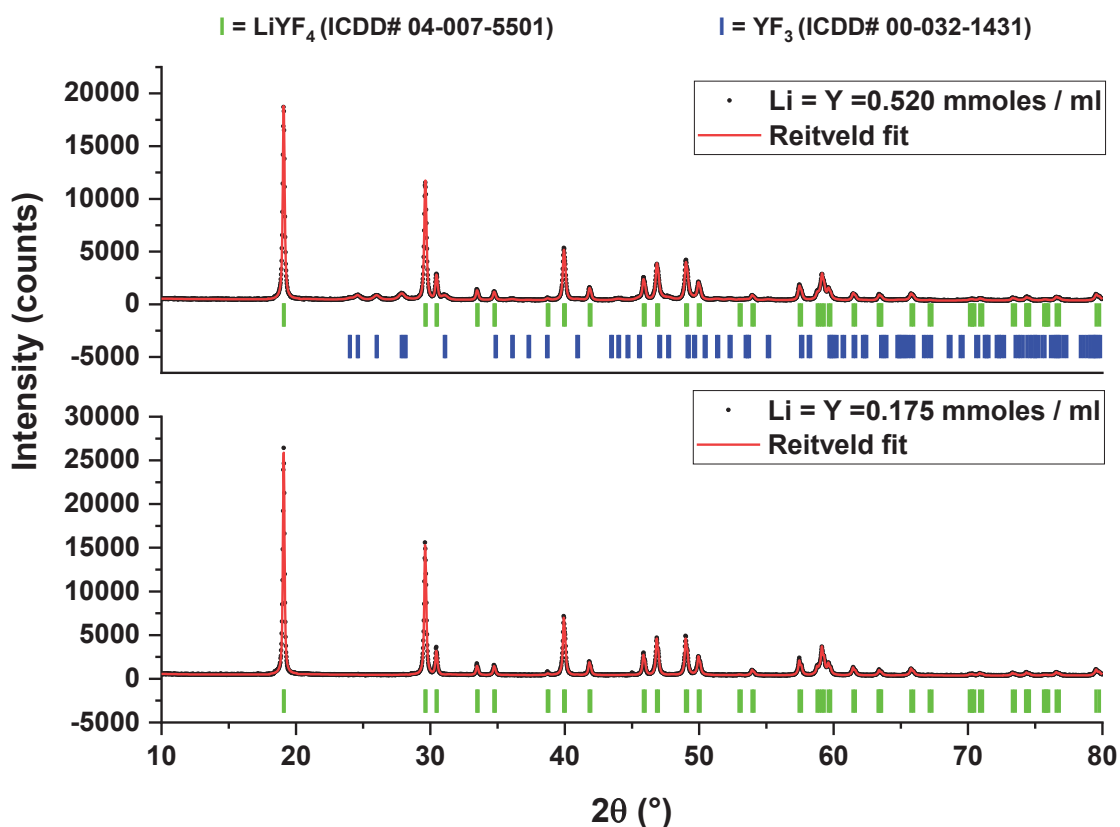


Figure 3.17: Rietveld refinement performed on X-ray diffraction pattern of three different samples prepared by taking different concentrations of precursors. The ticks below the plot indicate the respective positions of the reflection for that particular phase

Table 3.5: Rietveld refinement parameters of powder X-ray diffraction pattern of different samples prepared with different concentration of precursors during thermal decomposition.

Parameters		Li = Y = 0.175 mmol/ml	Li = Y = 0.520 mmol/ml
Phase (%)	LiYF ₄	100	81.5
	YF ₃	-	18.5
	LiF	-	-
Chi square		1.6	1.6
R _{wp} (%)		8.0	8.9

b) Effect on morphology

The concentration of precursors during the synthesis of nanoparticles has a great impact on the morphology of these nanoparticles. From the transmission electron microscopy data (Figure 3.18), we observe that the more the concentration of precursors is, the more non-uniformity in their shape is observed. Also, the higher concentration of precursors leads to spherical nanoparticles (~15 nm), whereas at lower concentrations, we observe diamond-shaped (of varied sizes) nanoparticles. From the HRTEM analysis, we found that these particles are well-crystalline.

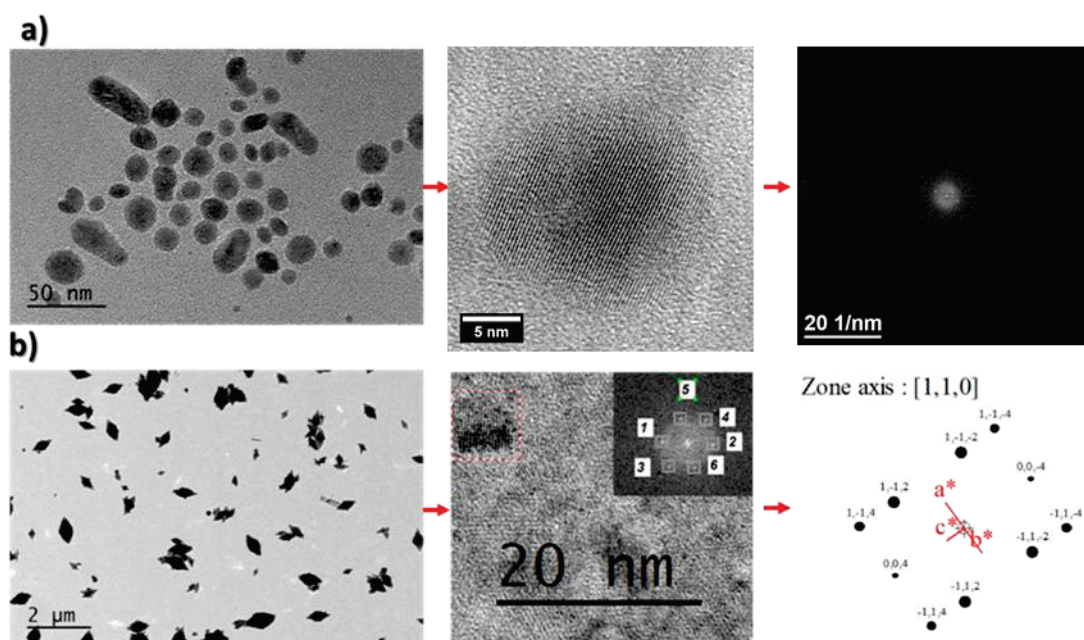


Figure 3.18: Transmission electron microscopy images of different LiY_{5/6}Yb_{1/6}F₄: 0.4% Tm³⁺ samples prepared by varying the concentration of precursors and their size distribution. a) 0.520 mmol/ml; b) 0.175 mmol/ml.

c) Effect on upconversion efficiency

The upconversion emission intensity observed for the doped $\text{LiY}_{5/6}\text{Yb}_{1/6}\text{F}_4$: 0.4% Tm^{3+} nanocrystals, prepared by varying the concentration of precursors, are quite different (Figure 3.19). Under similar excitation conditions ($\lambda_{\text{exc}} = 972 \text{ nm}$; power density = 10.9 W/cm^2), the decrease in the intensity by almost 1 order of magnitude can be accounted for differently shaped nanoparticles. The difference in the lattice energies of upconverting nanoparticles can lead to the different way the phonons are relaxed in the lattice.³⁹ Intense and very sharp UV and visible emissions are observed for both samples. These emissions justify that the prepared nanoparticles are of very good quality (high crystallinity, lower phonons cross relaxations) because these emissions require a transfer of at least 3 or more photons to the higher excited states, which is not usual for the particles synthesized in hydrated precursors using similar decomposition techniques. The absence of OH^- ions during decomposition and optimum ratio of solvents during decomposition, helps us to analyse the effect of shape and morphology on the upconversion luminescence. Hence we can conclude that the optical properties of the nanoparticles can be tailored not only by changing the size of nanoparticles but also by varying their morphology.

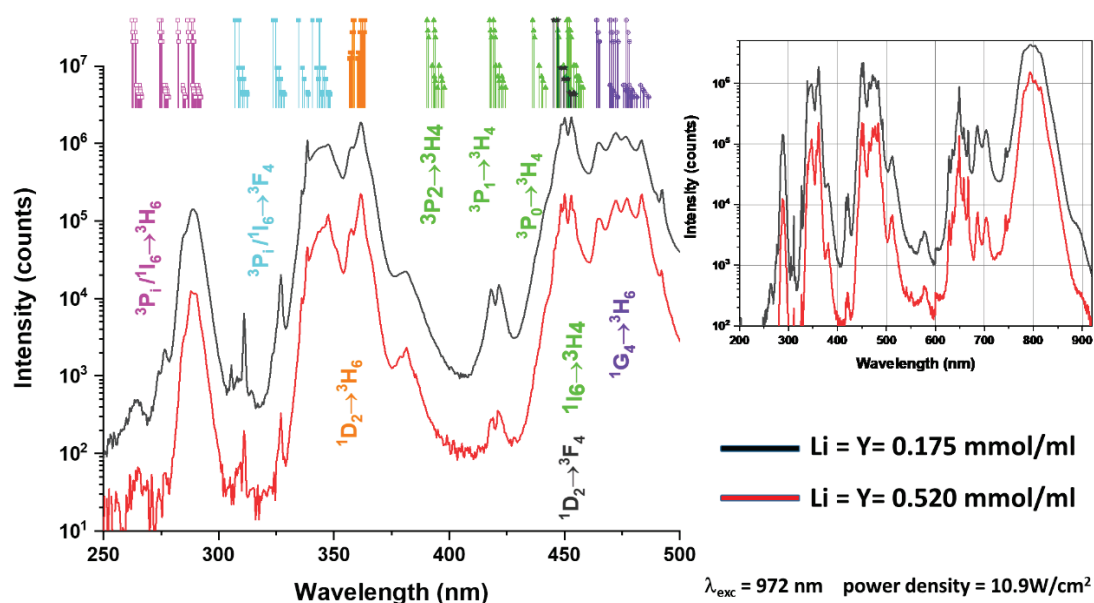


Figure 3.19: Difference in the upconversion emission intensities of the samples prepared using different concentration of precursors. These spectra were measured from dry powder in the same excitation condition for all three samples

3.2.2.2.4. Influence of decomposition temperature

This section primarily focuses on how the decomposition temperature plays a role in understanding the evolution of upconverting LiYF_4 nanoparticles. We investigate the transformation of anhydrous molecular precursors into desired LiYF_4 nanoparticles by decomposing them at different temperatures because temperature provides sufficient threshold energy for LiYF_4 formation and, therefore, it plays a crucial role in understanding the growth mechanism of LiYF_4 nanoparticles.

a) Effect on crystalline phase and composition

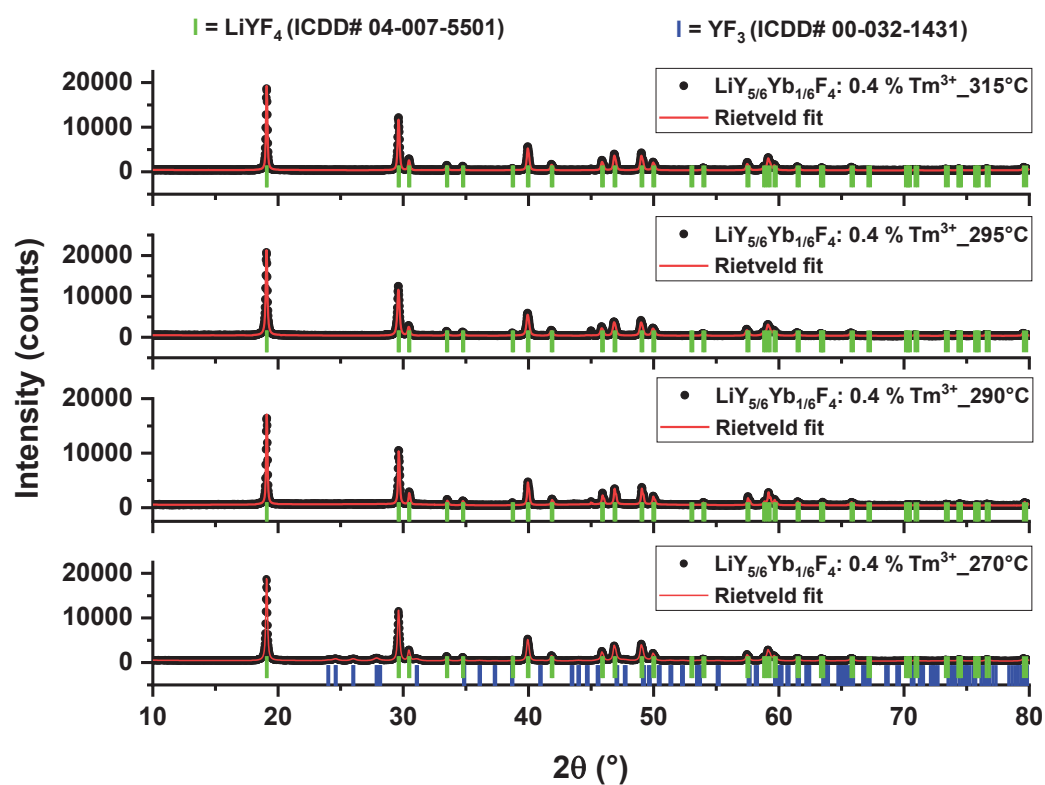


Figure 3.20: Rietveld refinement of powder X-ray diffraction pattern of different samples prepared by decomposition of anhydrous precursors at varied temperatures (from 270°C - 315°C). These peaks have been indexed with tetragonal LiYF_4 and orthorhombic YF_3 .

As we already discussed in section 3.2.1.4) about the properties of anhydrous monoglyme precursors that their decomposition starts at 270°C and completes at around 300°C. As we can see in Figure 3.20, that when the precursors are decomposed at 270°C, the composition of the resulting powder is not pure tetragonal LiYF_4 but a small per cent of YF_3 is also present. So, their decomposition and the formation of LiYF_4 is not simultaneous. This further justifies that the formation of LiYF_4 does

not occur directly via the nuclei formation of LiYF_4 and its growth further. Instead, it is formed by the interaction of LiF and YF_3 individually at elevated temperature (section 3.2.2.2.2).¹⁸ The absence of LiF in powder XRD can be justified due to its loss during the final step of washing with ethanol. However, at higher decomposition temperatures (290°C and onwards), we did not observe any impurity of YF_3 or LiF . Hence, we can state that the formation of LiYF_4 using these precursors is completed at 290°C and after. The size of these nanocrystals is also increased with the increase in decomposition temperature due to Ostwald ripening or to an arrangement of smaller nanoparticles in directions particularly favourable for the reduction in the surface energy and subsequent aggregation.

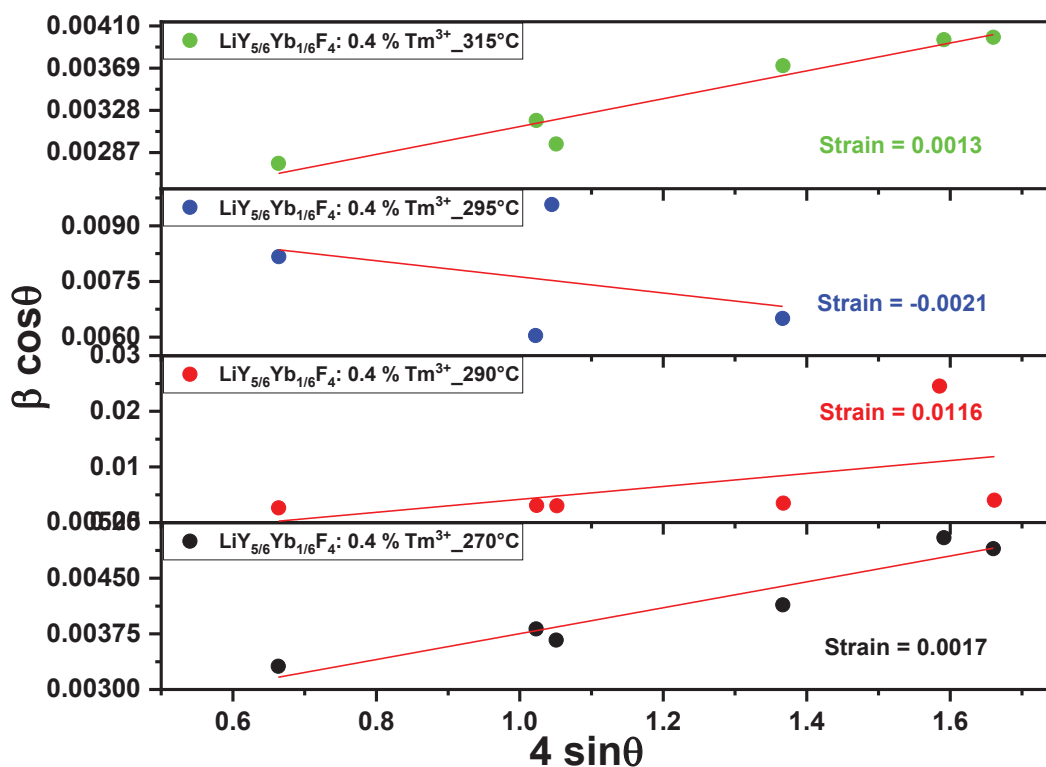


Figure 3.21: Williamson-Hall (W-H) plot derived from powder X-ray diffraction data of different samples prepared by decomposition of anhydrous precursors at varied temperatures (from 270°C – 315°C). The sample decomposed at 295°C has negative strain (compression) whereas other samples have positive values of strain (tensile strain).

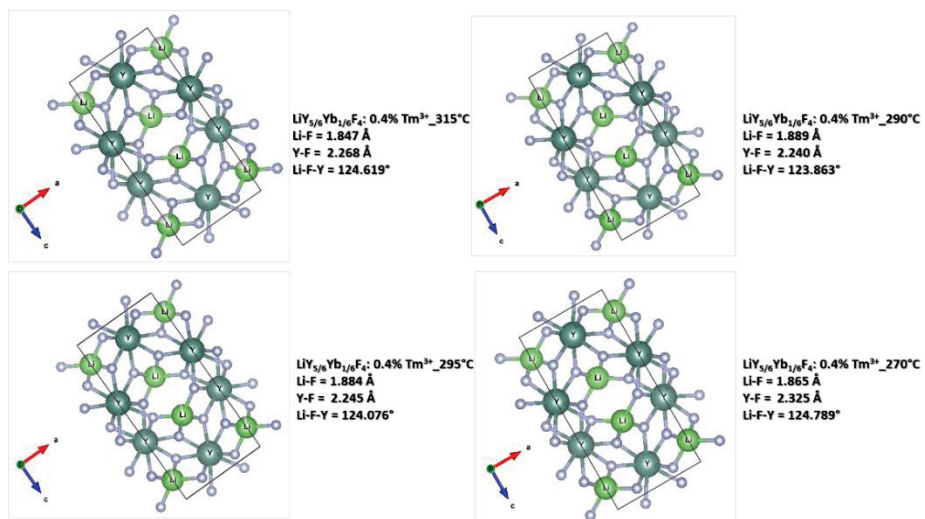


Figure 3.22: Unit cell, bond length and bond angle values for the crystal structure of different samples decomposed at different temperature (270 °C-315 °C).

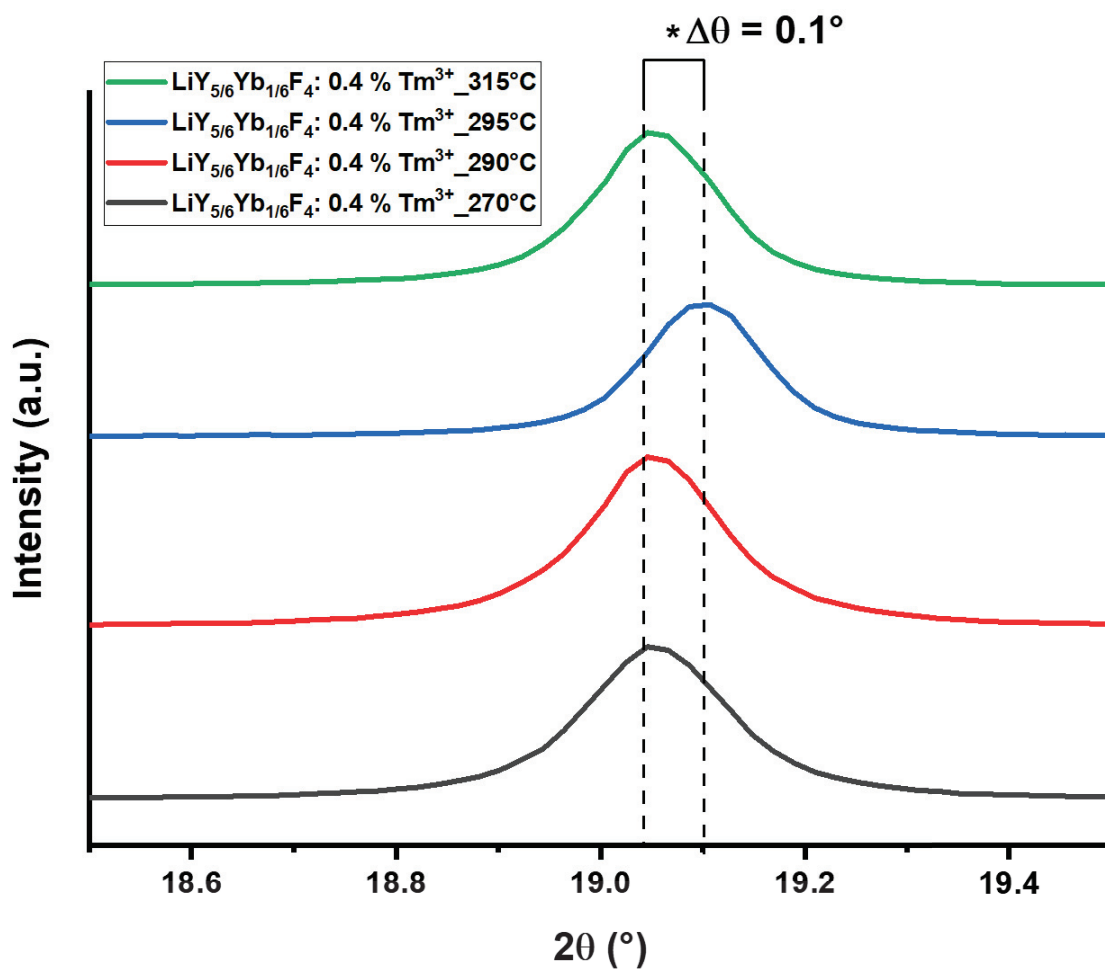


Figure 3.23: Powder diffraction pattern showing a shift in the peak position for one sample decomposed at 295 °C.

During one particular synthesis at 295 °C, we observed a lot of temperature fluctuations (due to surrounding conditions) and we were not able to maintain the exact temperature. The fluctuation was ± 5 °C. This variation in the synthesis conditions might have induced strain in the resulting nanoparticle system. As reported by A. Kar et al. that strain in any nanoparticle system varies with the temperature of heating and morphology of nanocrystals.⁴⁰ Supposedly, due to which we observe a shift of 0.1° in all the peaks of the powder diffraction pattern (Figure 3.23) for this particular sample. The W-H plot (Figure 3.21) also justifies our assumption of the addition of macro strain in the sample with its negative slope. We also calculated different unit cell parameters to understand more about the effect of decomposition temperature on the crystalline phase and the arrangement of ions within the unit cells. In Figure 3.22, we can see the arrangement of ions within the matrix. The packing within the system is consistent and we did not see any major difference in the unit cell parameters such as bond length (Li-F; Y-F) and bond angle (Li-F-Y) values of these systems.

However, the change in their morphology is significant at elevated decomposition temperature, which we will study in the following section.

b) Effect on morphology

The transmission electron microscopic studies of $\text{LiY}_{5/6}\text{Yb}_{1/6}\text{F}_4$: 0.4% Tm^{3+} prepared at different temperatures helps us to understand the key mechanism of formation of diamond-shaped upconverting tetragonal LiYF_4 nanoparticles. On combining our understanding about the formation of LiYF_4 nanoparticles from previous sections (Section 3.2.2.2) and the from Figure 3.24, we can say that at lower decomposition temperature (270°C) the spherical YF_3 and LiF nuclei are formed first which arrange/ organize themselves in a particular thermodynamically favourable direction to get transformed into tetragonal LiYF_4 nanoparticles. The inter-planer spacing values (d-values) calculated by HRTEM analysis (Figure 3.15) of these spherical nanoparticles reveals that they are indeed orthorhombic YF_3 which act as an intermediate product during the formation of LiYF_4 nanoparticles. At 290 °C we do see some small spherical YF_3 nanoparticles but their number is not high enough to be detected by powder X-ray diffraction. At temperatures higher than 290 °C, we observe that the transformation of spherical nanoparticles into diamond-shaped particles is favoured and even smaller diamond-shaped nanoparticles arrange in a way to grow into larger particles (as shown in Figure 3.24). The sample decomposed at 295 °C has a very uneven surface. Such surface can induce defects at molecular levels of the nanoparticle system which can affect their optical performance. At 315°C, the decomposition leads to very high crystalline nanocrystals. The average size of these diamond-shaped nanocrystals is ~ 100 nm (length) and ~ 60 nm (width).

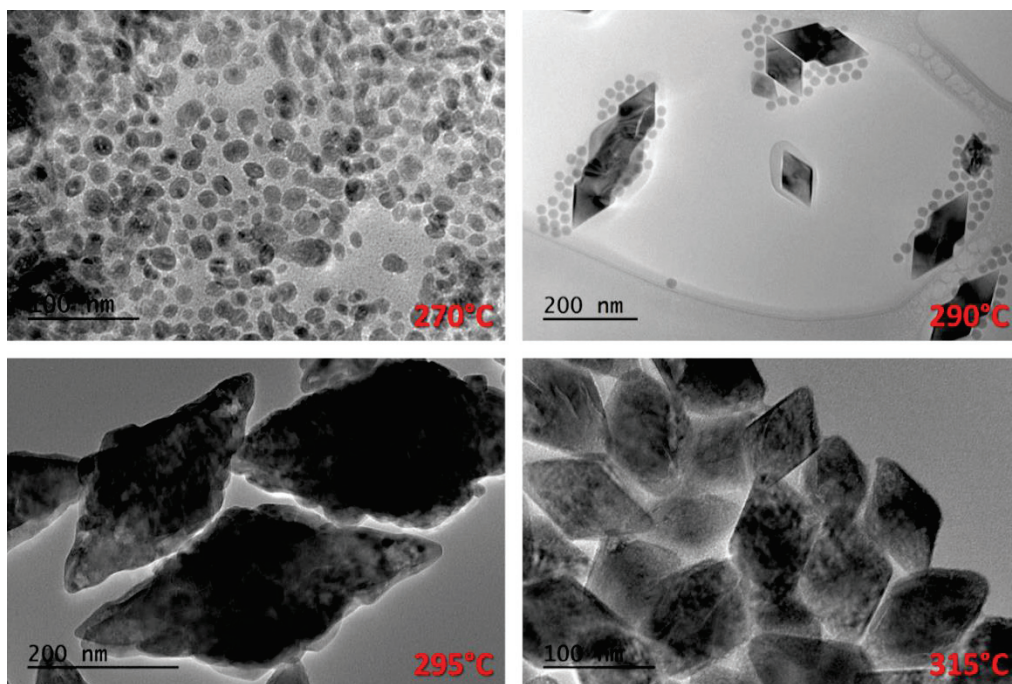


Figure 3.24: Transmission electron microscopy images of $\text{LiY}_{5/6}\text{Yb}_{1/6}\text{F}_4: 0.4\% \text{Tm}^{3+}$ samples prepared by decomposing anhydrous precursors at different temperature (from 270 °C – 315 °C).

c) Effect on upconversion properties

The upconversion phenomenon is very much dependent on the crystalline nature of nanoparticles.⁴¹ The upconversion properties of the samples synthesized at different temperature shows how the crystallinity of the sample affects the upconversion emission. At lower decomposition temperature, the crystallinity of the upconverting nanoparticles is lower. In our results, we also observed variation in the upconversion emission intensity of nanoparticles. The assessment of the difference in upconversion emission intensity can be done based on the crystallinity of the powder sample. As we know that if the sample is more crystalline then there would be fewer defects levels induced into the matrix. The defect energy levels always compete with the intrinsic energy levels of material, leading to loss of energy as heat and unnecessary radiative losses.⁴² As seen in Figure 3.25, the variation in the upconversion emission is consistent with the change in crystallinity of the sample. As seen from the powder diffraction pattern (Figure 3.20), the peak width of the samples decomposed at higher temperature (315 °C) is slightly narrower than the samples decomposed at a lower temperature (270 °C) and, therefore, the upconversion emission of this sample is also higher than all the other samples. The effect on the upconversion intensity, however, is not only governed by the crystallinity but by other aspects also such as different morphology of nanoparticles or defects induced due to lattice strain. The interplay of many factors simultaneously increases the non-linearity of the sample. As we discuss in section 3.2.2.2.5 LiYF_4 can exist in different shapes such as spherical and diamonds like morphologies. This can also be one of the factors for the varied upconversion emission

of nanoparticles. Finally, the strain in the sample can significantly modify how the sample behaves optically. The strain induces more defect energy levels and thus alters the upconversion intensities. These defect levels can be both beneficial or detrimental for upconversion, depending on the upconverting nanoparticle system. As mentioned by A. Kar et al (Figure 3.26), the upconversion intensity can be significantly enhanced if the tensile (positive) strain is decreased. However, if the compressive strain increases (towards more negative values), then also the upconversion intensity can be significantly enhanced.⁴⁰ Here in our $\text{LiY}_{5/6}\text{Yb}_{1/6}\text{F}_4: 0.4\% \text{ Tm}^{3+}$ upconverting system, we observed strange behaviour of the sample having compressive (negative) strain values. We plotted the normalized upconversion intensity (at laser excitation, 973 nm) on the y-axis and the corresponding wavelength on the x-axis. At low excitation densities (0.5 W/cm^2) (Figure 3.25), this sample does only show weak Tm^{3+} emission corresponding to $^1\text{G}_4 \rightarrow ^3\text{H}_6$ transitions. Similar behaviour is observed for the less crystalline and slightly impure sample prepared at 270°C . For the sample prepared at 315°C , we observe Tm^{3+} emission corresponding to the transitions from $^1\text{D}_2 \rightarrow ^3\text{H}_6$ even at this low excitation density. At higher excitation power density (29 W/cm^2) (Figure 3.25 (d)), the trend of increase in upconversion emission with an increase in decomposition temperature is very clear (except for one particular sample prepared at 295°C).

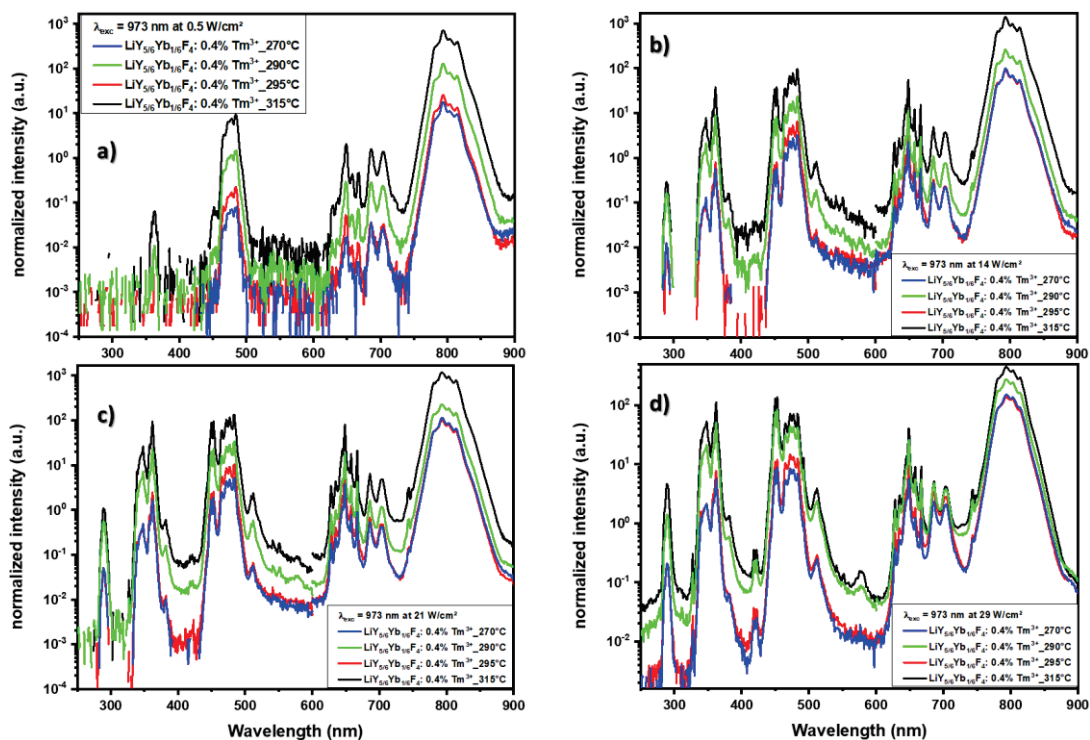


Figure 3.25: Variation of upconversion emission intensity of samples prepared at different temperatures (270°C - 315°C).

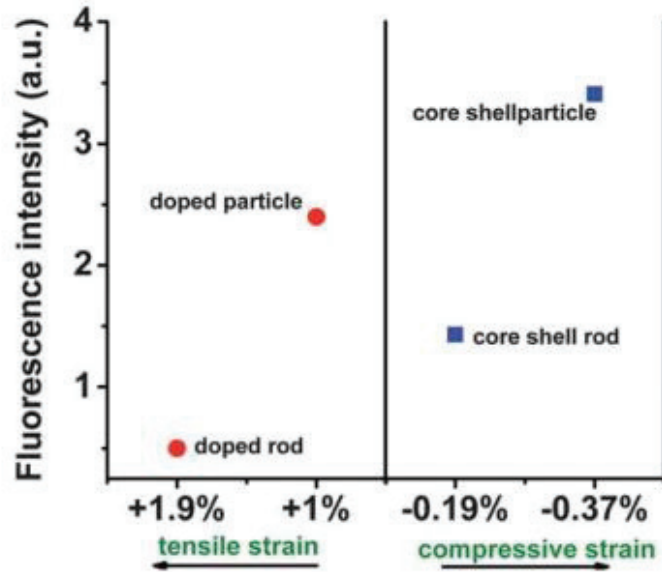


Figure 3.26: A plot of upconversion fluorescence peak intensity (green) against lattice strain of doped particle/ rod and core-shell particle/rod and Yb doped LaPO_4 nanorod (reported by P. Ghosh et al and A. Kar et al).^{40,43}

A power-dependent upconversion study of these samples is shown in Figure 3.27 where except for the sample prepared at 295 °C, all other samples show a uniform trend of increase of upconversion emission with incident laser power. This laser power-dependent study shows that even at low excitation power densities, we can observe the UV emission from our upconverting nanoparticles. This shows that this $\text{LiY}_{5/6}\text{Yb}_{1/6}\text{F}_4: 0.4\% \text{Tm}^{3+}$ upconverting system if combined with an efficient UV photocatalyst (such as TiO_2), can result in NIR based photocatalysis.

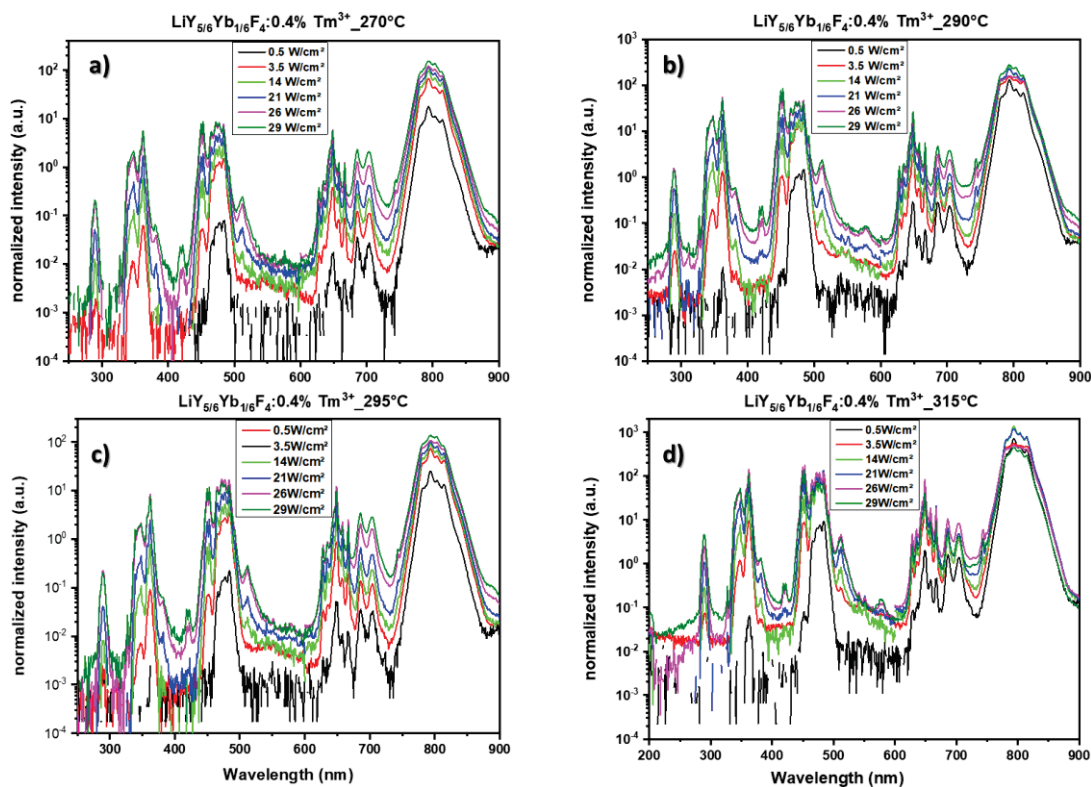


Figure 3.27: Incident power-dependent upconversion studies of $\text{LiY}_{5/6}\text{Yb}_{1/6}\text{F}_4:0.4\% \text{Tm}^{3+}$ prepared by decomposing anhydrous molecular precursors at different temperatures (270 °C, 290 °C, 295 °C, and 315 °C). These samples are excited by a 973 nm CW laser.

3.2.2.2.5. Influence of reaction time

a) Effect on morphology and suggested mechanism

The main objective of this study was to understand the growth mechanism of different morphology of $\text{LiY}_{5/6}\text{Yb}_{1/6}\text{F}_4:0.4\% \text{Tm}^{3+}$. During decomposition with a 1:1 ratio of solvent ODE and OA at 290 °C, we isolated different samples at different time (from 30 min to 2 h) intervals so that we can analyse the growth mechanism and formation of different morphology among these nanoparticles. Interestingly, we found that the diamond-like morphology^{17,44–46} is not the only possibility while decomposing the anhydrous precursors at high temperature. It varies very much on the surrounding conditions of the nanoseeds. During 2 hours, starting from spherical seeds these nanoparticles grow in size, guided by the surface energy of a particular lattice plane into specific morphology of nanoparticles. It is well-known that understanding of surface energy (or ratio of surface-area-to-volume) of the growing nanoparticles is very crucial in determining the shape and morphology of nanoparticles.^{28,29,36,38,39} In the initial 30 min of reaction (Figure 3.28 (a)) we observe the formation of very small nanoparticles (< 5 nm), which tend to grow into bigger size nanoparticles retaining a similar spherical shape (Figure 3.28 (b)) until 60 min of the reaction (Figure 3.28 (c)). These nanoparticles then

start to grow/arrange themselves (Figure 3.28 (d)) into a particular (011) direction, leading to the formation of tetragonal diamond-shaped morphology of LiYF_4 nanoparticles. After 2 h, the reaction was stopped and two samples were collected; One just after the reaction is completed, and the second when it was naturally cooled down at room temperature. The transformation from spherical-shaped nanoparticles to diamond-shaped nanoparticles is visible in Figure 3.28 (d). After two hours of decomposition, most of these nanoparticles are diamond-shaped.

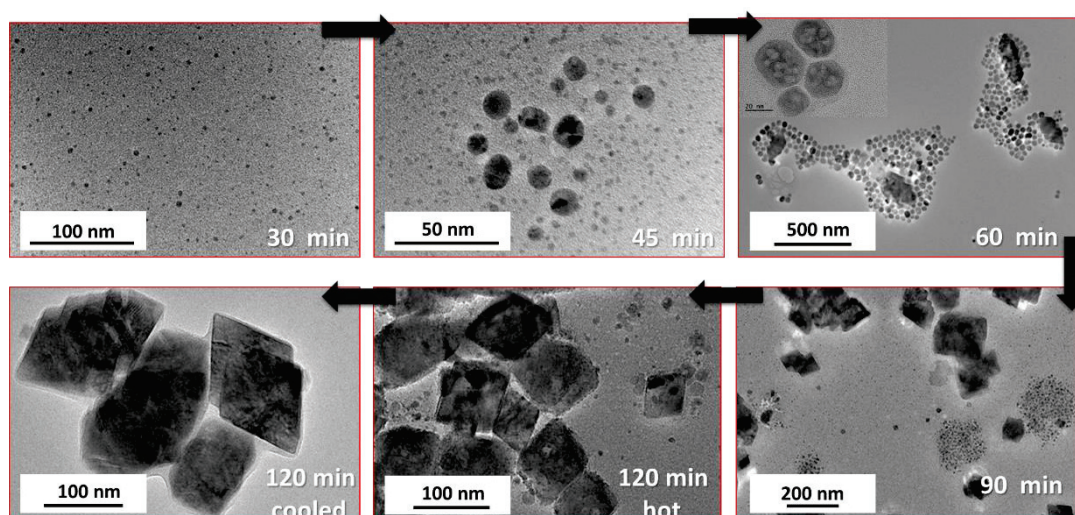


Figure 3.28: Transmission electron microscopy images of $\text{LiY}_{5/6}\text{Yb}_{1/6}\text{F}_4: 0.4\% \text{Tm}^{3+}$ samples taken at a different course of reaction from 30 min to 2 h. These images clearly show the formation of diamond morphology of nanoparticles is guided through small spherical seeds which align themselves in accordance to their minimum surface energy to get the most thermodynamic stable phase and morphology.

3.2.3. Comparative upconversion study of $\text{LiYF}_4:\text{Yb}^{3+}, \text{Tm}^{3+}$ nanoparticles and bulk single crystals

The process of upconversion luminescence in lanthanides originates from the intra 4f transitions, due to the availability of a large number of intermediate energy levels. Although, the process of upconversion itself is independent of any external factor such as particle size, surrounding ligands, solvent etc. but the overall emission luminescence (brightness of inorganic particles) depends very much on these external factors. It is quite evident from the previously reported results⁴⁷ that the quantum yield of the particles decreases drastically with lowering the size of particles. This is primarily due to the increase of surface area on reducing the size of particles. This exposes more number of dopants ions on the surface, leading to enhancement of non-radiative relaxations of emitting and intermediate levels. The increased surface area of smaller particles also increases the number of surface defects which could create additional defect levels, therefore leading to upconversion quenching. That justifies the use of bulk materials as an ideal material for quantitative measurement of the upconversion luminescence. But in many daily life applications such as biological imaging,

photodynamic therapy, etc..^{2,48,49} the use of bulk materials is highly restricted. So there is a very big demand for highly bright and stable nanoparticles with nearly similar properties to that of bulk materials. In this work, we compared the upconversion efficiency of the nanoparticles prepared using anhydrous precursors with the bulk single crystal prepared using the modified Bridgman technique of nearly similar dopant concentration.

The upconversion intensities of these bulk and nanocrystals were then studied under similar excitation conditions. The intensity of upconversion has been compared to that of a single crystal of similar composition (see Figure 3.29). The overall intensity of the nanoparticles under the same excitation intensity and collection geometry corresponds to 78% of the one measured on the single crystal. Upconversion photoluminescence quantum yield (UC-QY) and energy conversion efficiencies (ECE) have also been measured and are reported in Table 3.6. While less intense (by a factor of ~ 2) than the one reported by the ref,⁵⁰ our nanoparticles are about 6 times smaller than theirs. The larger surface-to-volume ratio in our case suggests that our particles have only a small quenching at the surface, while they are well-crystallized and devoid of volume defects.

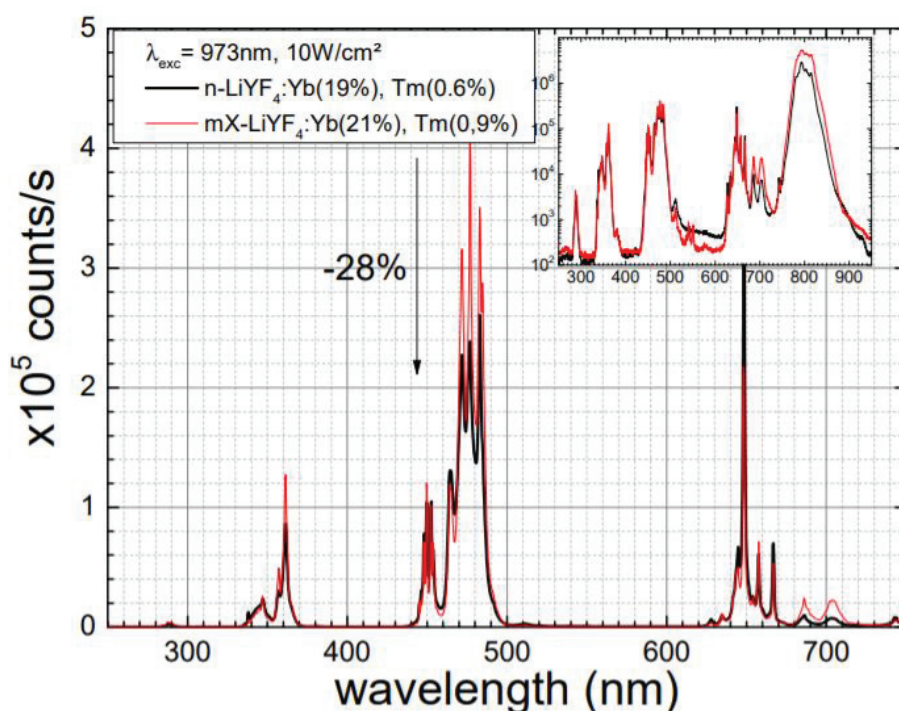


Figure 3.29: Upconversion emission spectra obtained under 10 W/cm^2 for the nanocrystals studied (black line) and for a single crystal (red) of the similar composition obtained by a modified Bridgman method. The doping concentrations have been measured by EDS

The quantitative analysis of upconversion emission was performed by measuring upconversion quantum yield using the method described by Boyer and Van Veggel et al..⁴⁷ An undoped

LiYF₄ sample prepared under similar conditions was used as a reference sample to estimate the absorption of the laser. The sample under study and the reference sample are placed alternatively in an integrating sphere (IS200-4 from Thorlabs). One port of the sphere is connected to the detection system described in the manuscript. This detection system has been calibrated thanks to a NIST traceable Oriel QT 63358 tungsten lamp over the range 250-1000 nm to obtain its absolute response at each wavelength. Thus, absolute emission from the sample and diffusion of the laser can be measured. The absorption of the laser by the sample is estimated by the difference between the diffusion by the undoped sample and the diffusion from the doped sample. Thus, an absolute number of absorbed photons (resp. energy absorbed), as well as an absolute number of emitted photons (resp. emitted energy) at each wavelength range, is given. The UCQY (resp. energy conversion efficiency (ECE)) is then simply the ratio between these two values. The measurements are performed under five excitation intensities and reported in following Table 3.6.

Table 3.6: upconversion Quantum yield (QY) and energy conversion efficiency(ECE) at different intensities of the IR laser for different spectral regions: the under-script UV represents the region between 250 and 375nm, 451 corresponds to the region 440-460 nm, 480 to the region 461-507 nm, 649 to the region 620-732 nm, 794 to the region 733-880 nm. Finally, the total stands for the whole 250-900 nm region.

Intensity (W/cm ²)	Φ_{total} ECE _{total}	Φ_{UV} ECE _{UV}	Φ_{451} ECE ₄₅₁	Φ_{480} ECE ₄₈₀	Φ_{649} ECE ₆₄₉	Φ_{794} ECE ₇₉₄
26.9	0.015(5) ^a	4.0(1) × 10 ⁻⁶	7.0(3) × 10 ⁻⁶	4.7(14) × 10 ⁻⁵	1.7(5) × 10 ⁻⁴	0.015(5)
	0.019(6)	1.0(4) × 10 ⁻⁵	1.5(5) × 10 ⁻⁵	1.0(3) × 10 ⁻⁴	2.4(8) × 10 ⁻⁴	0.018(6)
10.3	0.014(5)	1.1(4) × 10 ⁻⁶	1.8(6) × 10 ⁻⁶	4.0(2) × 10 ⁻⁵	5.0(2) × 10 ⁻⁵	0.014(5)
	0.017(6)	3.0(1) × 10 ⁻⁶	4.0(1) × 10 ⁻⁶	9.0(2) × 10 ⁻⁵	7.0(2) × 10 ⁻⁵	0.017(6)
4.2	0.008(3)	1.5(5) × 10 ⁻⁷	1.9(6) × 10 ⁻⁷	1.2(4) × 10 ⁻⁵	1.4(5) × 10 ⁻⁵	0.008(3)
	0.010(3)	5.0(2) × 10 ⁻⁷	4.0(1) × 10 ⁻⁷	2.4(8) × 10 ⁻⁵	2.1(7) × 10 ⁻⁵	0.010(3)
1.4	0.004(1)	3.0(1) × 10 ⁻⁸	2.0(1) × 10 ⁻⁸	3.0(1) × 10 ⁻⁶	4.0(1) × 10 ⁻⁶	0.004(1)
	0.050(2)	1.0(3) × 10 ⁻⁷	4.0(3) × 10 ⁻⁸	6.0(2) × 10 ⁻⁶	6.0(2) × 10 ⁻⁶	0.050(2)
0.67	0.0020(6)	u. ^b	u. ^b	8.0(3) × 10 ⁻⁷	2.0(6) × 10 ⁻⁶	0.0020(6)
	0.0030(8)	u.	u.	1.5(5) × 10 ⁻⁶	3.0(1) × 10 ⁻⁶	0.0030(8)

^a uncertainties on the final digit are presented in parentheses

^b u. : undetectable

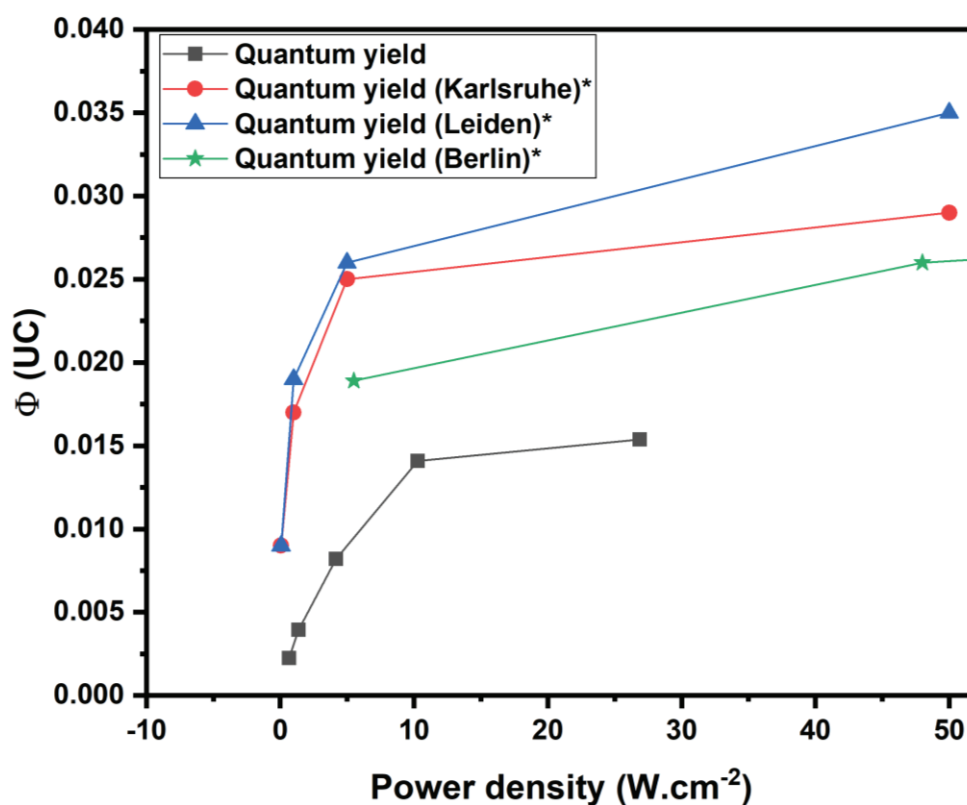


Figure 3.30: Comparative upconversion quantum yield of the sample prepared using anhydrous molecular precursors versus the quantum yield of samples prepared at different laboratories as already reported (*) by Meijer et al.⁵⁰

These measurements show that at a power density of 10 W/cm² the upconversion emission of nanoparticles is quite comparable to that of the bulk single crystal. There is a reduction of 28% of upconversion emission in contrast to a single crystal of similar composition. In Figure 3.30, we present comparative upconversion studies of upconversion efficiencies of nearly similar composition of LiY_{5/6}Yb_{1/6}F₄: 0.4% Tm³⁺ prepared using different methods at different laboratories. In black, the quantum yield of the sample prepared using anhydrous molecular precursors and other samples marked with an asterisk (*) are as reported by Meijer et al.⁵⁰ Considering that the quantum yield measurements were performed on 6-month-old samples and the average size of our nanoparticles (15 ± 5 nm) is smaller compared to the one reported by Meijer et al. (87 ± 9 nm),⁵⁰ the total quantum yield of our sample, which is about 1.5%, can be considered good. In general, the quantum yield for such nanoparticles is expected to be in the range of 0.005% to 0.4%.⁴⁷ Hence, we can say that the strategy employed to prepare nanoparticles is very efficient as the absence of water molecules during synthesis is highly beneficial to avoid the risk of formation of oxyfluoride phases and, therefore, produces high-quality nanocrystals (NCs) with enhanced upconversion intensity.

3.3. Conclusions and perspectives

Precursor-directed synthesis has an edge over other methods of synthesis of upconverting nanoparticles by having better control over many properties of the nanoparticles such as crystalline phase purity, size, morphology etc. In this chapter, we synthesized novel anhydrous molecular precursors for obtaining high performance-oriented upconverting nanoparticles. After their complete characterization using a range of Physico-chemical technique including single-crystal X-ray structure, these anhydrous precursors were decomposed to form upconverting nanostructures in a variety of different conditions. Many parameters have been examined to have a better understanding of LiYF_4 : Yb^{3+} , Tm^{3+} upconverting system, which includes the understanding of the effect of i) varying the ratio of dopant ions, ii) ratio of solvents during thermal decomposition, iii) concentration of precursors and iv) reaction time over crystalline phase, size, shape, morphology and upconverting properties of nanoparticles. In comparison with their bulk counterpart, these nanoparticles have far better performance due to fewer surface defects. While comparing, the overall intensity of the nanoparticles under the similar excitation intensity and the collection geometry corresponds to 78% of the one measured on the single crystal.

3.4. References

- (1) Sheng, W.; Huang, N.; Liu, Y.; Zhang, B.; Zhang, W.; Wang, S. An Ultrasensitive Fluorescence Immunoassay Based on Magnetic Separation and Upconversion Nanoparticles as Labels for the Detection of Chloramphenicol in Animal-Derived Foods. *Food Anal. Methods* **2020**. <https://doi.org/10.1007/s12161-020-01820-5>.
- (2) Näreoja, T.; Deguchi, T.; Christ, S.; Peltomaa, R.; Prabhakar, N.; Fazeli, E.; Perälä, N.; Rosenholm, J. M.; Arppe, R.; Soukka, T.; Schäferling, M. Ratiometric Sensing and Imaging of Intracellular pH Using Polyethylenimine-Coated Photon Upconversion Nanoprobes. *Anal. Chem.* **2017**, *89* (3), 1501–1508. <https://doi.org/10.1021/acs.analchem.6b03223>.
- (3) Zhao, J.; Xu, J.; Jian, X.; Xu, J.; Gao, Z.; Song, Y.-Y. NIR-Light Driven Photocatalysis on Amphiphilic TiO₂ Nanotubes for Controllable Drug Release. *ACS Appl. Mater. Interfaces* **2020**, *acsami.0c04260*. <https://doi.org/10.1021/acsami.0c04260>.
- (4) Wu, S.; Wang, F.; Li, Q.; Wang, J.; Zhou, Y.; Duan, N.; Niazi, S.; Wang, Z. Photocatalysis and Degradation Products Identification of Deoxynivalenol in Wheat Using Upconversion Nanoparticles@TiO₂ Composite. *Food Chemistry* **2020**, 126823. <https://doi.org/10.1016/j.foodchem.2020.126823>.
- (5) Chen, Y.; Mishra, S.; Ledoux, G.; Jeanneau, E.; Daniel, M.; Zhang, J.; Daniele, S. Direct Synthesis of Hexagonal NaGdF₄ Nanocrystals from a Single-Source Precursor: Upconverting NaGdF₄:Yb³⁺, Tm³⁺ and Its Composites with TiO₂ for Near-IR-Driven Photocatalysis. *Chemistry – An Asian Journal* **2014**, *9* (9), 2415–2421. <https://doi.org/10.1002/asia.201402347>.
- (6) Yang, W.; Yang, S.; Jiang, L.; Zhou, Y.; Yang, C.; Deng, C. Tumor Microenvironment Triggered Biodegradation of Inorganic Nanoparticles for Enhanced Tumor Theranostics. *RSC Advances* **2020**, *10* (45), 26742–26751. <https://doi.org/10.1039/D0RA04651E>.
- (7) Tessitore, G.; Mudring, A.-V.; Krämer, K. W. Upconversion Luminescence in Sub-10 nm β-NaGdF₄:Yb³⁺, Er³⁺ Nanoparticles: An Improved Synthesis in Anhydrous Ionic Liquids. *RSC Adv.* **2019**, *9* (60), 34784–34792. <https://doi.org/10.1039/C9RA05950D>.
- (8) Mishra, S.; Ledoux, G.; Jeanneau, E.; Daniele, S.; Joubert, M.-F. Novel Heterometal-Organic Complexes as First Single Source Precursors for Up-Converting NaY(Ln)F₄ (Ln = Yb, Er, Tm) Nanomaterials. *Dalton Trans.* **2012**, *41* (5), 1490–1502. <https://doi.org/10.1039/C1DT11070E>.

- (9) Mishra, S.; Daniele, S. Metal-Organic Derivatives with Fluorinated Ligands as Precursors for Inorganic Nanomaterials. *Chem. Rev.* **2015**, *115* (16), 8379–8448. <https://doi.org/10.1021/cr400637c>.
- (10) Wang, Z.; Meijerink, A. Concentration Quenching in Upconversion Nanocrystals. *J. Phys. Chem. C* **2018**, *122* (45), 26298–26306. <https://doi.org/10.1021/acs.jpcc.8b09371>.
- (11) Mishra, S.; Hubert-Pfalzgraf, L. G.; Daniele, S.; Rolland, M.; Jeanneau, E.; Jouguet, B. Thermal Dehydration of $Y(TFA)_3(H_2O)_3$: Synthesis and Molecular Structures of $[Y(\mu, \eta^1: \eta^1-TFA)_3(THF)(H_2O)]_{1\infty} \cdot THF$ and $[Y_4(\mu_3-OH)_4(\mu, \eta^1: \eta^1-TFA)_6(\eta^1-TFA)(\eta^2-TFA)(THF)_3(DMSO)(H_2O)] \cdot 6THF$ (TFA=trifluoroacetate). *Inorganic Chemistry Communications* **2009**, *12* (2), 97–100. <https://doi.org/10.1016/j.inoche.2008.11.021>.
- (12) Henderson, W. A.; Young, V. G.; Brooks, N. R.; Smyrl, W. H. Li^+ Cation Coordination in $[Li_2(CF_3SO_3)_2(Diglyme)]$ and $[Li_3(C_2F_3O_2)_3(Diglyme)]$. *Acta Crystallogr C Cryst Struct Commun* **2002**, *58* (10), m501–m503. <https://doi.org/10.1107/S0108270102015135>.
- (13) Henderson, W. A.; Brooks, N. R.; Young, V. G. Tetraglyme– Li^+ Cation Solvate Structures: Models for Amorphous Concentrated Liquid and Polymer Electrolytes (II). *Chem. Mater.* **2003**, *15* (24), 4685–4690. <https://doi.org/10.1021/cm034352r>.
- (14) Ayadi, H.; Fang, W.; Mishra, S.; Jeanneau, E.; Ledoux, G.; Zhang, J.; Daniele, S. Influence of Na^+ Ion Doping on the Phase Change and Upconversion Emissions of the $GdF_3: Yb^{3+}, Tm^{3+}$ Nanocrystals Obtained from the Designed Molecular Precursors. *RSC Adv.* **2015**, *5* (122), 100535–100545. <https://doi.org/10.1039/C5RA20781A>.
- (15) Mishra, S.; Daniele, S.; Ledoux, G.; Jeanneau, E.; Joubert, M.-F. Heterometallic $Na-Y(Ln)$ Trifluoroacetate Diglyme Complexes as Novel Single-Source Precursors for Upconverting $NaYF_4$ Nanocrystals Co-Doped with Yb and Er/Tm Ions. *Chem. Commun.* **2010**, *46* (21), 3756–3758. <https://doi.org/10.1039/B921474G>.
- (16) Zhang, X.; Wang, M.; Ding, J.; Gao, D.; Shi, Y.; Song, X. The Novel Upconversion Properties of $LiYbF_4: Er$ Microcrystals Compared to the Na Counterpart. *CrystEngComm* **2012**, *14* (24), 8357–8360. <https://doi.org/10.1039/C2CE26159F>.
- (17) Mahalingam, V.; Vetrone, F.; Naccache, R.; Speghini, A.; Capobianco, J. A. Colloidal Tm^{3+}/Yb^{3+} -Doped $LiYF_4$ Nanocrystals: Multiple Luminescence Spanning the UV to NIR Regions via Low-Energy Excitation. *Advanced Materials* **2009**, *21* (40), 4025–4028. <https://doi.org/10.1002/adma.200901174>.

- (18) Panov, N.; Marin, R.; Hemmer, E. Microwave-Assisted Solvothermal Synthesis of Upconverting and Downshifting Rare-Earth-Doped LiYF₄ Microparticles. *Inorg. Chem.* **2018**, *57* (23), 14920–14929. <https://doi.org/10.1021/acs.inorgchem.8b02697>.
- (19) Na, H.; Jeong, J. S.; Chang, H. J.; Kim, H. Y.; Woo, K.; Lim, K.; Mkhoyan, K. A.; Jang, H. S. Facile Synthesis of Intense Green Light Emitting LiGdF₄: Yb, Er-Based Upconversion Bipyramidal Nanocrystals and Their Polymer Composites. *Nanoscale* **2014**, *6* (13), 7461–7468. <https://doi.org/10.1039/C4NR00857J>.
- (20) Du, Y.-P.; Zhang, Y.-W.; Sun, L.-D.; Yan, C.-H. Optically Active Uniform Potassium and Lithium Rare Earth Fluoride Nanocrystals Derived from Metal Trifluoroacetate Precursors. *Dalton Trans.* **2009**, No. 40, 8574–8581. <https://doi.org/10.1039/B909145A>.
- (21) Ma, C.; Xu, X.; Wang, F.; Zhou, Z.; Liu, D.; Zhao, J.; Guan, M.; Lang, C. I.; Jin, D. Optimal Sensitizer Concentration in Single Upconversion Nanocrystals. *Nano Lett.* **2017**, *17* (5), 2858–2864. <https://doi.org/10.1021/acs.nanolett.6b05331>.
- (22) Rabouw, F. T.; Prins, P. T.; Villanueva-Delgado, P.; Castelijns, M.; Geitenbeek, R. G.; Meijerink, A. Quenching Pathways in NaYF₄: Er³⁺, Yb³⁺ Upconversion Nanocrystals. *ACS Nano* **2018**, *12* (5), 4812–4823. <https://doi.org/10.1021/acs.nano.8b01545>.
- (23) Dramićanin, M. D. Trends in Luminescence Thermometry. *Journal of Applied Physics* **2020**, *128* (4), 040902. <https://doi.org/10.1063/5.0014825>.
- (24) Thoma, R. E.; Brunton, G. D.; Penneman, R. A.; Keenan, T. K. Equilibrium Relations and Crystal Structure of Lithium Fluorolanthanate Phases. *Inorg. Chem.* **1970**, *9* (5), 1096–1101. <https://doi.org/10.1021/ic50087a019>.
- (25) Sui, J.; Yan, J.; Wang, K.; Luo, G. Efficient Synthesis of Lithium Rare-Earth Tetrafluoride Nanocrystals via a Continuous Flow Method. *Nano Res.* **2020**, *13*, 2837–2846. <https://doi.org/10.1007/s12274-020-2938-y>.
- (26) Braud, A.; Girard, S.; Doualan, J. L.; Thuau, M.; Moncorgé, R.; Tkachuk, A. M. Energy-Transfer Processes in Yb: Tm-Doped KY₃F₁₀, LiYF₄, and BaY₂F₈ Single Crystals for Laser Operation at 1.5 and 2.3 μm. *Phys. Rev. B* **2000**, *61* (8), 5280–5292. <https://doi.org/10.1103/PhysRevB.61.5280>.

- (27) Li, C.; Zhang, Y.; Zhang, X.; Zeng, F.; Mauro, T.; Liu, J. Spectral Properties of Tm, Ho: LiYF₄ Laser Crystal. *Journal of Rare Earths* **2011**, *29* (6), 592–595. [https://doi.org/10.1016/S1002-0721\(10\)60503-0](https://doi.org/10.1016/S1002-0721(10)60503-0).
- (28) Zhang, X.; Wang, M.; Ding, J. Shape-Selective Synthesis, Characterization and Upconversion Improvement of Yb³⁺/Er³⁺ Doped LiYF₄ Microphosphors through PH Tuning. *RSC Adv.* **2014**, *4* (55), 29165. <https://doi.org/10.1039/C4RA02538E>.
- (29) Ye, S.; Hu, R.; Jiang, N.; Wang, H.; Wang, D. PH Value Manipulated Phase Transition, Microstructure Evolution and Tunable Upconversion Luminescence in Yb³⁺–Er³⁺ Codoped LiYF₄/YF₃ Nanoparticles. *Dalton Trans.* **2015**, *44* (35), 15583–15590. <https://doi.org/10.1039/C5DT01552A>.
- (30) Bian, W.; Lin, Y.; Wang, T.; Yu, X.; Qiu, J.; Zhou, M.; Luo, H.; Yu, S. F.; Xu, X. Direct Identification of Surface Defects and Their Influence on the Optical Characteristics of Upconversion Nanoparticles. *ACS Nano* **2018**, *12* (4), 3623–3628. <https://doi.org/10.1021/acsnano.8b00741>.
- (31) Wang, F.; Wang, J.; Liu, X. Direct Evidence of a Surface Quenching Effect on Size-Dependent Luminescence of Upconversion Nanoparticles. *Angewandte Chemie International Edition* **2010**, *49* (41), 7456–7460. <https://doi.org/10.1002/anie.201003959>.
- (32) Sun, Y.; Chen, Y.; Tian, L.; Yu, Y.; Kong, X.; Zeng, Q.; Zhang, Y.; Zhang, H. Morphology-Dependent Upconversion Luminescence of ZnO: Er³⁺ Nanocrystals. *Journal of Luminescence* **2008**, *128* (1), 15–21. <https://doi.org/10.1016/j.jlumin.2007.04.011>.
- (33) Mai, H.-X.; Zhang, Y.-W.; Sun, L.-D.; Yan, C.-H. Highly Efficient Multicolor Up-Conversion Emissions and Their Mechanisms of Monodisperse NaYF₄: Yb, Er Core and Core/Shell-Structured Nanocrystals. *J. Phys. Chem. C* **2007**, *111* (37), 13721–13729. <https://doi.org/10.1021/jp073920d>.
- (34) Mai, H.-X.; Zhang, Y.-W.; Si, R.; Yan, Z.-G.; Sun, L.; You, L.-P.; Yan, C.-H. High-Quality Sodium Rare-Earth Fluoride Nanocrystals: Controlled Synthesis and Optical Properties. *J. Am. Chem. Soc.* **2006**, *128* (19), 6426–6436. <https://doi.org/10.1021/ja060212h>.
- (35) Wilhelm, S.; Kaiser, M.; Würth, C.; Heiland, J.; Carrillo-Carrion, C.; Muhr, V.; Wolfbeis, O. S.; Parak, W. J.; Resch-Genger, U.; Hirsch, T. Water Dispersible Upconverting Nanoparticles: Effects of Surface Modification on Their Luminescence and Colloidal Stability. *Nanoscale* **2015**, *7* (4), 1403–1410. <https://doi.org/10.1039/C4NR05954A>.

- (36) Hong, A.-R.; Kim, S. Y.; Cho, S.-H.; Lee, K.; Jang, H. S. Facile Synthesis of Multicolor Tunable Ultrasmall LiYF₄: Yb, Tm, Er/ LiGdF₄ Core/Shell Upconversion Nanophosphors with Sub-10 nm Size. *Dyes and Pigments* **2017**, *139*, 831–838. <https://doi.org/10.1016/j.dyepig.2016.12.048>.
- (37) Cheng, T.; Marin, R.; Skripka, A.; Vetrone, F. Small and Bright Lithium-Based Upconverting Nanoparticles. *J. Am. Chem. Soc.* **2018**, *140* (40), 12890–12899. <https://doi.org/10.1021/jacs.8b07086>.
- (38) Xue, X.; Uechi, S.; Tiwari, R. N.; Duan, Z.; Liao, M.; Yoshimura, M.; Suzuki, T.; Ohishi, Y. Size-Dependent Upconversion Luminescence and Quenching Mechanism of LiYF₄: Er³⁺/Yb³⁺ Nanocrystals with Oleate Ligand Adsorbed. *Opt. Mater. Express* **2013**, *3* (7), 989. <https://doi.org/10.1364/OME.3.000989>.
- (39) Shan, J.; Uddi, M.; Wei, R.; Yao, N.; Ju, Y. The Hidden Effects of Particle Shape and Criteria for Evaluating the Upconversion Luminescence of the Lanthanide Doped Nanophosphors. *J. Phys. Chem. C* **2010**, *114* (6), 2452–2461. <https://doi.org/10.1021/jp908976n>.
- (40) Kar, A.; Patra, A. Impacts of Core-Shell Structures on Properties of Lanthanide-Based Nanocrystals: Crystal Phase, Lattice Strain, Downconversion, Upconversion and Energy Transfer. *Nanoscale* **2012**, *4* (12), 3608–3619. <https://doi.org/10.1039/C2NR30389B>.
- (41) Liu, N.; Marin, R.; Mazouzi, Y.; Cron, G. O.; Shuhendler, A.; Hemmer, E. Cubic versus Hexagonal – Effect of Host Crystallinity on the T1 Shortening Behaviour of NaGdF₄ Nanoparticles. *Nanoscale* **2019**, *11* (14), 6794–6801. <https://doi.org/10.1039/C9NR00241C>.
- (42) Bian, W.; Lin, Y.; Wang, T.; Yu, X.; Qiu, J.; Zhou, M.; Luo, H.; Yu, S. F.; Xu, X. Direct Identification of Surface Defects and Their Influence on the Optical Characteristics of Upconversion Nanoparticles. *ACS Nano* **2018**, *12* (4), 3623–3628. <https://doi.org/10.1021/acsnano.8b00741>.
- (43) Ghosh, P.; Oliva, J.; Rosa, E. D. la; Haldar, K. K.; Solis, D.; Patra, A. Enhancement of Upconversion Emission of LaPO₄: Er@Yb Core–Shell Nanoparticles/Nanorods. *J. Phys. Chem. C* **2008**, *112* (26), 9650–9658. <https://doi.org/10.1021/jp801978b>.
- (44) Li, W.; Xu, J.; He, Q.; Sun, Y.; Sun, S.; Chen, W.; Guzik, M.; Boulon, G.; Hu, L. Highly Stable Green and Red Up-Conversion of LiYF₄: Yb³⁺, Ho³⁺ for Potential Application in Fluorescent Labeling. *Journal of Alloys and Compounds* **2020**, 155820. <https://doi.org/10.1016/j.jallcom.2020.155820>.

- (45) Huang, Q. The Construction of Sublattice Level Energy Cluster for Promoting UV Upconversion Emission in Tetragonal LiYF_4 . *Journal of Alloys and Compounds* **2020**, *821*, 153544. <https://doi.org/10.1016/j.jallcom.2019.153544>.
- (46) Choi, J. E.; Kim, H.-K.; Kim, Y.; Kim, G.; Lee, T. S.; Kim, S.; Kim, D.; Jang, H. S. 800 nm Near-Infrared Light-Excitable Intense Green-Emitting $\text{Li}(\text{Gd}, \text{Y})\text{F}_4:\text{Yb}$, Er-Based Core/Shell/Shell Upconversion Nanophosphors for Efficient Liver Cancer Cell Imaging. *Materials & Design* **2020**, 108941. <https://doi.org/10.1016/j.matdes.2020.108941>.
- (47) Boyer, J.-C.; van Veggel, F. C. J. M. Absolute Quantum Yield Measurements of Colloidal $\text{NaYF}_4:\text{Er}^{3+}, \text{Yb}^{3+}$ Upconverting Nanoparticles. *Nanoscale* **2010**, *2* (8), 1417. <https://doi.org/10.1039/c0nr00253d>.
- (48) Du, H.; Yu, J.; Guo, D.; Yang, W.; Wang, J.; Zhang, B. Improving the MR Imaging Sensitivity of Upconversion Nanoparticles by an Internal and External Incorporation of the Gd^{3+} Strategy for in Vivo Tumor-Targeted Imaging. *Langmuir* **2016**, *32* (4), 1155–1165. <https://doi.org/10.1021/acs.langmuir.5b04186>.
- (49) Jin, Y.; Wang, H.; Li, X.; Zhu, H.; Sun, D.; Sun, X.; Liu, H.; Zhang, Z.; Cao, L.; Gao, C.; Wang, H.; Liang, X.-J.; Zhang, J.; Yang, X. A Multifunctional DNA Polymer Assisted Upconversion Therapeutic Nano platform for Enhanced Photodynamic Therapy. *ACS Appl. Mater. Interfaces* **2020**, acsami.0c03274. <https://doi.org/10.1021/acsami.0c03274>.
- (50) Meijer, M. S.; Rojas-Gutierrez, P. A.; Busko, D.; Howard, I. A.; Frenzel, F.; Würth, C.; Resch-Genger, U.; Richards, B. S.; Turshatov, A.; Capobianco, J. A.; Bonnet, S. Absolute Upconversion Quantum Yields of Blue-Emitting $\text{LiYF}_4:\text{Yb}^{3+}, \text{Tm}^{3+}$ Upconverting Nanoparticles. *Phys. Chem. Chem. Phys.* **2018**, *20* (35), 22556–22562. <https://doi.org/10.1039/C8CP03935F>.

Chapter 4 Synergistic UV upconversion mechanism in LiYF₄: Yb³⁺, Tm³⁺ nanocrystals (Dual Laser Excitation/ Excited-state absorption spectroscopic studies and sun-like excitation)

4.1. Introduction

As we already discussed in detail in chapter 1 that solar-driven photocatalysis is a steadily growing market and it has reached \$2 billion in 2014.¹ Most of the applications are based on titania, but other inorganic compounds (ZnO, CeO₂, etc.), metal complexes (tetrabutylammonium decatungstate, chromium carbenes, etc.), or organic compounds (acetone, etc.) are also used.¹ A common trend of these photocatalysts is that they are efficient mainly under UV excitation. Therefore, only a very small amount of solar spectrum photons is useful. For instance, only 1.5% of solar spectrum photons are exploited in the case of titania. Using upconversion materials to convert many more solar spectrum photons into useful ones could greatly enhance the production rate, provided that they demonstrate the ability to produce UV photons. Considering the nonlinearity of this effect, upconversion-enhanced photocatalysis has only been demonstrated with a relatively high excitation provided by an infrared laser.²⁻⁸ It is generally considered that for the Yb³⁺-Tm³⁺ codoped system (see Figure 4.1 for reference) the successive energy transfers by three NIR photons, which promotes the electrons to the ³H₅, ³F₂ and ¹G₄ energy is the key mechanism for upconversion in such a system.² As it is difficult to directly populate the ¹D₂ energy level by the absorption of the fourth photon, due to large energy mismatch between them,⁹ cross-relaxation in between the Tm³⁺ ions promotes the population of ¹D₂ and higher energy levels. Nevertheless, our group previously demonstrated that upconverting NaGdF₄:Yb³⁺, Tm³⁺ nanocrystals can also enhance photocatalysis under solar irradiation.¹⁰ This last result was counterintuitive if one considers that the addition of the energy of at least 3 photons in the IR is required to obtain one excitation in the UV. In this chapter, we demonstrate that at low power densities excitation this process of IR to UV conversion under broadband excitation is not a third-order process but it becomes a first-order process by a subtle intermix of energy transfer and excited-state absorption using the blue part of the solar spectrum, which also makes this process entirely comparable with natural light excitation.

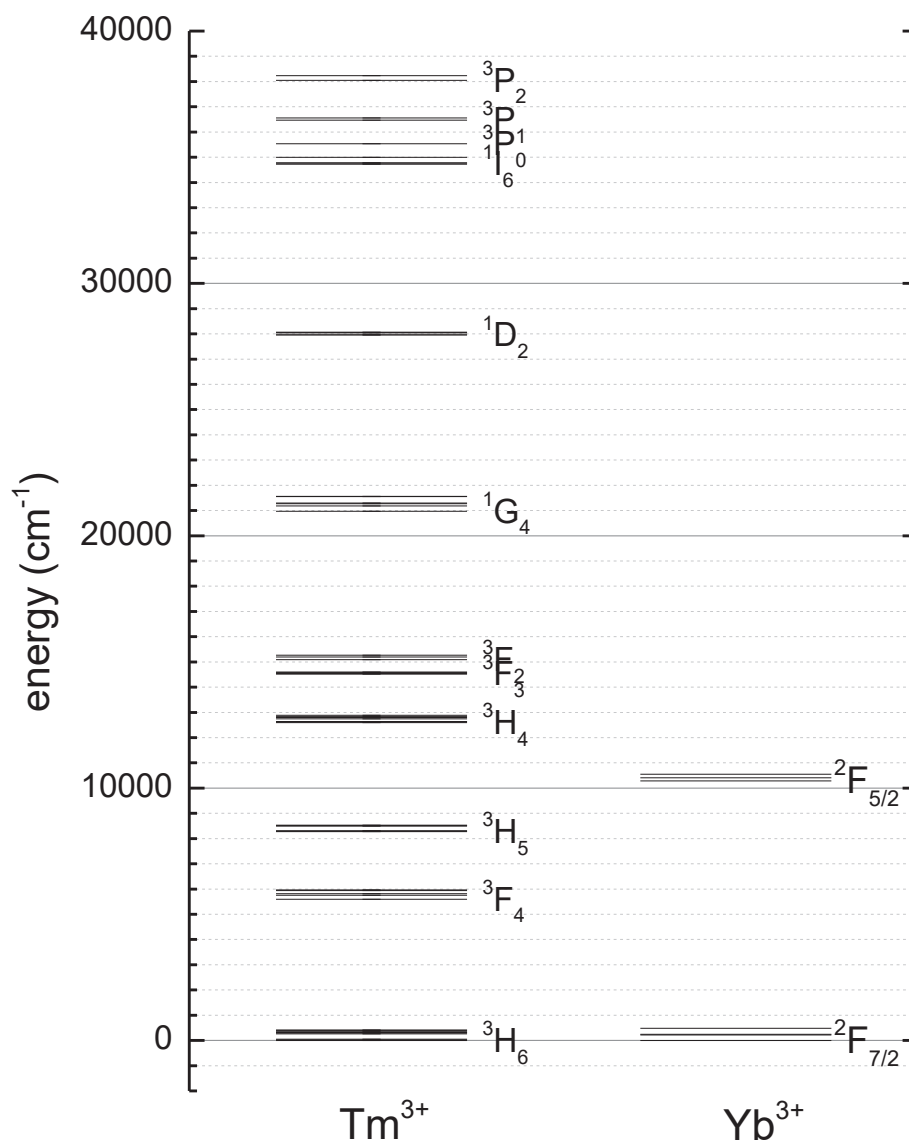


Figure 4.1: Energy level diagram for Tm^{3+} and Yb^{3+} as reported by Dulick and collaborators¹¹ and also by Bensalah et al.¹².

4.2. Results and discussion

4.2.1. Synthesis and characterization (structural and morphological) of upconverting nanoparticles

The $LiY_{5/6}Yb_{1/6}F_4: 0.4\% Tm^{3+}$ nanocrystals were synthesized via thermal decomposition of anhydrous metal trifluoroacetate derivatives $[Ln(TFA)_3(\text{monoglyme})]$ ($Ln = Y, Tm, Yb$) and $Li(TFA)(\text{monoglyme})$ (where TFA = trifluoroacetate) as molecular precursors at high temperature in high boiling solvents like 1-octadecene (ODE) and Oleic acid (OA). The detailed procedure is discussed in chapter 6. The crystalline phase and morphology of these nanoparticles have been characterized by an X-ray diffraction pattern (Figure 4.2) of the dried powder showing that they crystallize in the Scheelite structure space group $I 41/a$, and transmission electron microscopy images (Figure 4.3) in

both low and high resolution showing a reasonably broad size distribution centred around 15 nm diameter of well-crystallized nanoparticles.

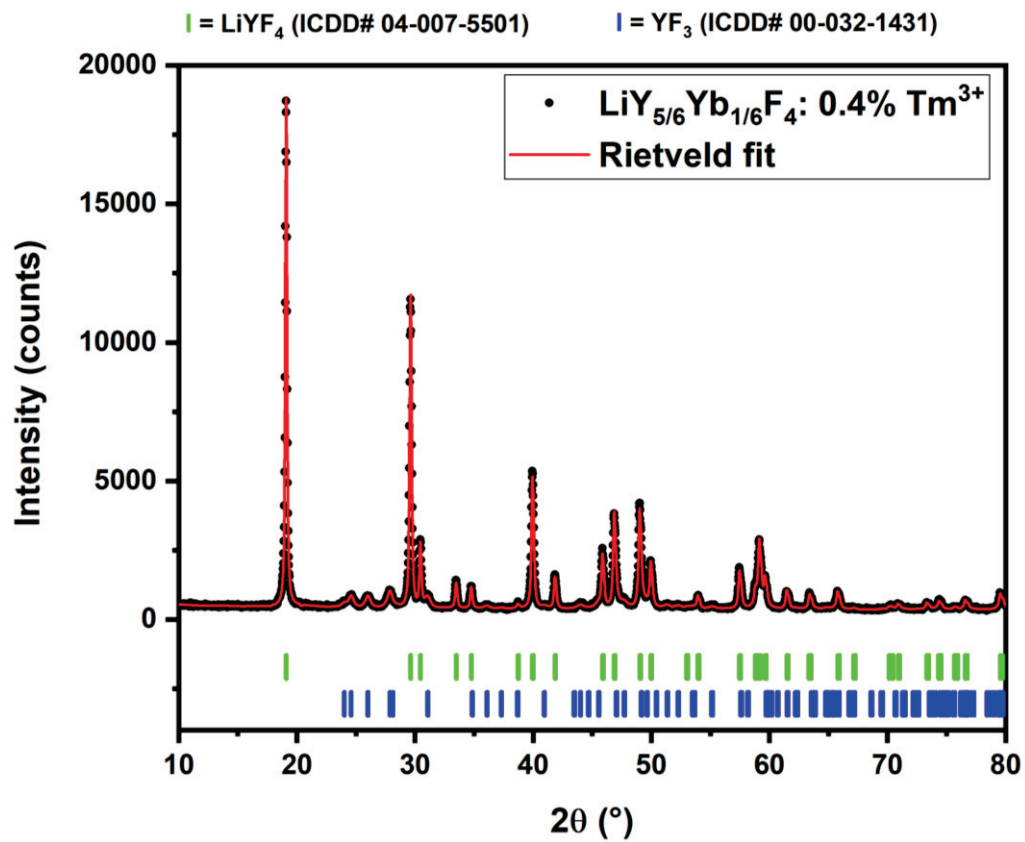


Figure 4.2: Powder XRD spectrum of $\text{LiY}_{5/6}\text{Yb}_{1/6}\text{F}_4: 0.4\% \text{Tm}^{3+}$ nanocrystals

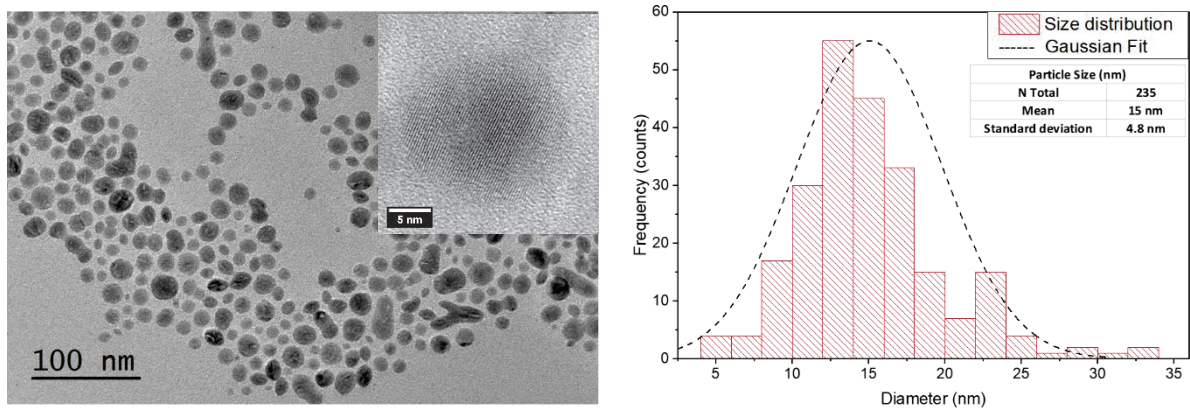


Figure 4.3: TEM and HR-TEM (inset) images of $\text{LiY}_{5/6}\text{Yb}_{1/6}\text{F}_4: 0.4\% \text{Tm}^{3+}$ nanocrystals as well as the size distribution deduced from the analysis of 235 particles.

4.2.2. Experimental setup

The samples are placed on a DSC600 heating/cooling stage from Linkam Corporation equipped with a sapphire window. They are therefore maintained at 25 °C at all times. The first laser with continuous wave (CW) excitation at 973 nm and with a power of 2 W is focused to a square spot of $1 \times 1 \text{ mm}^2$ on the sample with quasi-top-hat energy distribution. Its power can be varied thanks to a set of neutral density filters allowing a variation of the intensity from 200 W/cm^2 down to $8.4 \text{ }\mu\text{W/cm}^2$. A second laser, an optical parametric oscillator (OPO) from EKSPLA (model NT230-50-SH) with a fixed repetition rate of 50 Hz and a pulse width of 3 ns, is also shone on the sample. Its emission wavelength can be tuned from 211 nm up to $2.5 \text{ }\mu\text{m}$. The spot size has a 5 mm diameter on the sample with a Gaussian intensity distribution. The two lasers are collinear at the sample surface. Therefore, in the central $1 \times 1 \text{ mm}^2$ square spot both laser excitations are almost homogeneous (meaning less than 10% variation over the central $1 \times 1 \text{ mm}^2$ area for both lasers). The light emitted from this central spot is collected by an optical fibre placed as close as possible to the sample and fed to a monochromator from Jobin-Yvon (TRIAX 320) equipped with automatic order removing filters and coupled to an EMCCD (Newton 920U from Andor) or a cooled photomultiplier (Hamamatsu R943-02). The signal from the photomultiplier is sent to an SR400 counting module from Stanford Research Systems. A simple LED (M455L1 from Thorlabs) can be focused on the sample over a surface of 0.6 cm^2 , as an alternative to the OPO laser source excitation. The wavelength of the peak intensity of the LED has been measured to be 460 nm with a full width at half-maximum (FWHM) of 30 nm. Its intensity can be varied continuously from 0 to 15 mW/cm^2 . The emission can also be excited by an EQ99 Xe laser-driven light source from ENERGETIQ together with a YG12 coloured long-pass filter to mimic solar irradiation without its UV component. The schematic diagram (Figure 4.4) of the experimental setup is as follows:

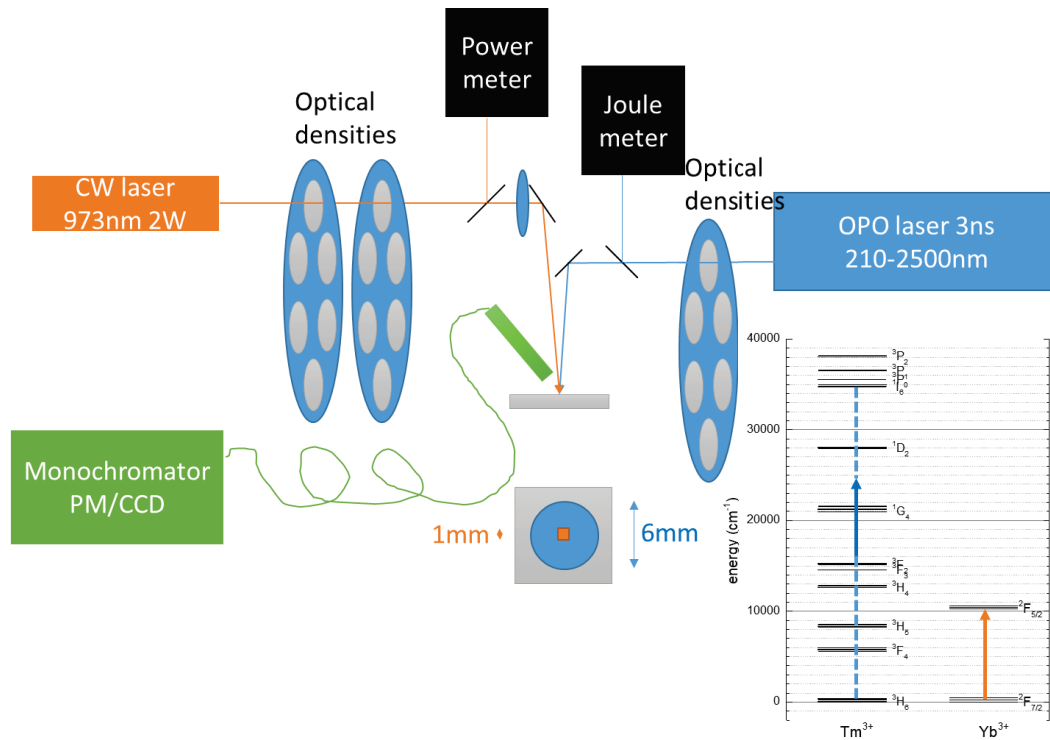


Figure 4.4: Experimental setup for excited state emission spectroscopic measurements.

4.2.3. Upconversion studies

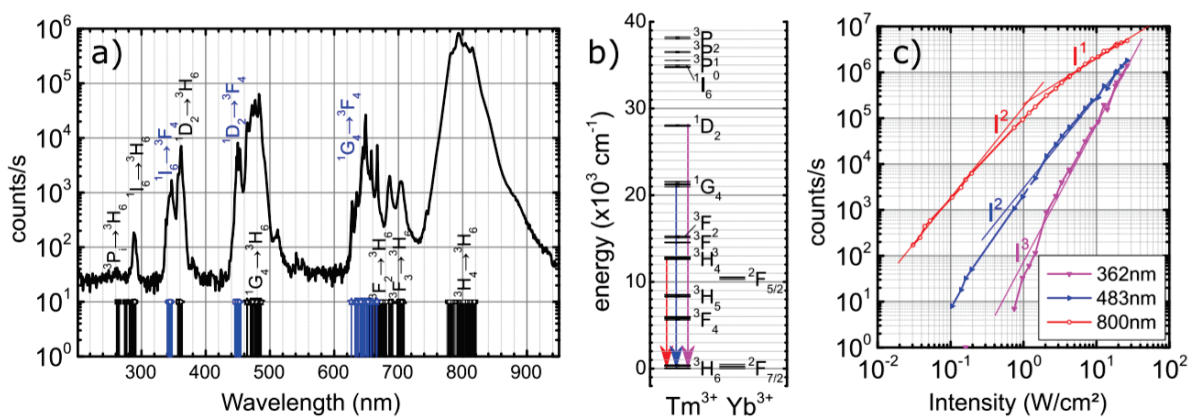


Figure 4.5: Upconversion spectra of $\text{LiY}_{5/6}\text{Yb}_{1/6}\text{F}_4$: 0.4% Tm^{3+} nanocrystals under a 973 nm excitation wavelength with an incidence power density of 4.32 W/cm^2 (a). Energy level diagram for Yb^{3+} - Tm^{3+} codoped system (b). The luminescence intensity variations of the principal emission components for the excitation intensity of the IR laser (c).

We performed upconversion studies on $\text{LiY}_{5/6}\text{Yb}_{1/6}\text{F}_4$: 0.4% Tm^{3+} nanocrystals under a 973 nm excitation wavelength with an incidence power density of 4.32 W/cm^2 . As observed in Figure 4.5, this process is nonlinear; Figure 4.5(a) shows, in a semilog scale, a characteristic upconversion emission

spectrum of LiYF₄ nanoparticles with a doping concentration measured by EDS of 19 ± 1% Yb³⁺ and 0.6 ± 0.5% Tm³⁺ ions under a moderate density of excitation (4.32 W/cm² at 973 nm). The different emission lines can be easily ascribed to the *f-f* intra-configurational transitions of thulium as reported by Dulick and collaborators¹¹ and also by Bensalah et al.¹² for which the energy level diagram is presented in Figure 4.5(b). The spectrum is dominated by the emission around 800 nm coming from the ³H₄ → ³H₆ transition from Tm³⁺ ions. At a shorter wavelength, the blue emission around 480 nm arises mainly from ¹G₄ → ³H₆ and the UV region is dominated by the ¹D₂ → ³H₆ transition at 360 nm. Here in Figure 4.5 (a) the black lines show the emission transitions going down to the ground level of Tm³⁺ (³H₆), while the blue lines represent the transitions going down to the first excited multiplet of Tm³⁺ (³F₄). The arrows in Figure 4.5(b) indicate the three transitions presented in panel (c) with the same colour code.

Figure 4.5(c) presents the evolution of luminescence intensity of the three main emissions as a function of the excitation source intensity. From a few tens of mW/cm² up to 30 W/cm², the blue emission shows an almost quadratic behaviour, the UV emission depends on the third power of the excitation density, while the 800 nm emission is quadratic up to about 1 W/cm² and becomes linear afterwards.

The full description of the upconversion process in co-doped thulium–ytterbium systems is still a matter of debate, and essentially two different scenarios have been considered, both using Yb³⁺ for each excitation step: either a sequential transfer or a cooperative sensitization by several Yb³⁺ ions. In the first hypothesis,^{13,14} a Yb³⁺ ion transfers its excitation to a Tm³⁺ into its ³H₅ and/or ³F₄ level. Then a second transfer promotes Tm³⁺ in a higher excited state (³F₂ or even ¹G₄), and the process is repeated as long as the excited Yb³⁺ ions can transfer some excitation. In the second hypothesis^{15,16} two excited Yb³⁺ ions that are sufficiently close to a single Tm³⁺ ion transfer simultaneously by cooperative sensitization of their excitation to the Tm³⁺ ion, promoting it directly to its ¹G₄ excited state. Then some additional excitation from another excited Yb³⁺ ion brings the Tm³⁺ to a higher excited state.

To provide deeper insight into these two potential processes, we have performed excited state excitation spectroscopy.

4.2.4. Excited-state excitation spectroscopic studies

4.2.4.1. Dual Laser [Continuous wave (CW) + optical parametric oscillator (OPO)] Excitation

A CW IR laser at a low enough excitation density (13 mW/cm²) is used to populate the excited state of the Yb³⁺ ions without any detectable upconversion emission. Under this excitation, we expect to have a significant amount of Yb³⁺ ions in the excited state (~2.2 × 10¹⁵ cm⁻³) at all times and a small

amount of Tm^{3+} in the lower-lying excited states ($^3\text{F}_4$ and $^3\text{H}_5$) excited through energy transfer from $\text{Yb}^{3+} \ ^2\text{F}_{5/2}$ at all times. Thus, when the Tm^{3+} ions are brought to one of the $^3\text{F}_4$ or $^3\text{H}_5$ excited states by a second tunable laser, through energy transfer, the excited Tm^{3+} ions can be brought to higher excited states if the correct conditions exist. The $^3\text{H}_4 \rightarrow ^3\text{H}_6$ upconversion emission at 800 nm is thus monitored as a function of the wavelength of the tunable excitation laser.

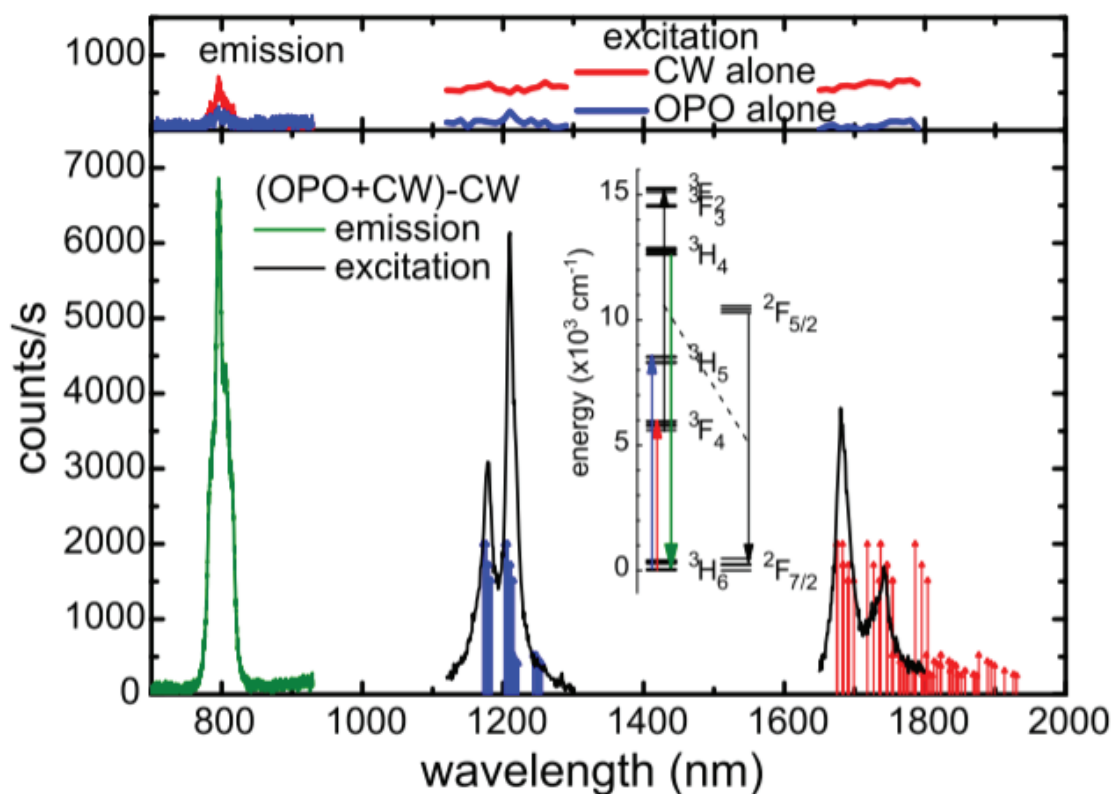


Figure 4.6: Various Tm^{3+} transitions under different excitation conditions.

Description: Upper panel: In blue, excitation (right) and emission (left) of the $^3\text{H}_4 \rightarrow ^3\text{H}_6$ transition of Tm^{3+} ions in LiYF_4 nanocrystals at 805 nm with the OPO laser alone. In red, excitation (right) and emission (left) of the same transition with the CW laser alone. Lower panel: for the same transition in black, excitation spectra under a combined excitation of a CW laser at 973 nm with an intensity of 13 mW/cm^2 and a variable-wavelength OPO pulsed laser after subtraction of the IR laser contribution. On the left, in green, the corresponding emission spectra with the OPO centred at 1210 nm.

As can be seen in Figure 4.6, the 800 nm emission is hardly detected when the two lasers are used as separate excitation sources, while a series of peaks appear around 1680 and 1210 nm when the two lasers are used simultaneously. These two excitation lines perfectly match the $^3\text{H}_6 \rightarrow ^3\text{F}_4$ and $^3\text{H}_6 \rightarrow ^3\text{H}_5$ transitions, respectively. This indicates that when the $^3\text{F}_4$ level is populated since the $^3\text{F}_4$ to $^3\text{F}_2$ energy difference is almost resonant with the ytterbium $^2\text{F}_{5/2}$ to $^2\text{F}_{7/2}$ energy difference, it is an

extremely efficient means of obtaining the emission from the 3H_4 level. To confirm this hypothesis, lifetimes in the excited state have been determined with either a single excitation of Yb^{3+} or a double excitation with a CW laser at 973 nm and a pulsed laser tuned at 1210 nm corresponding to the $^3H_6 \rightarrow ^3H_5$ transition. These data are presented in Figure 4.7 and confirms the process described above.

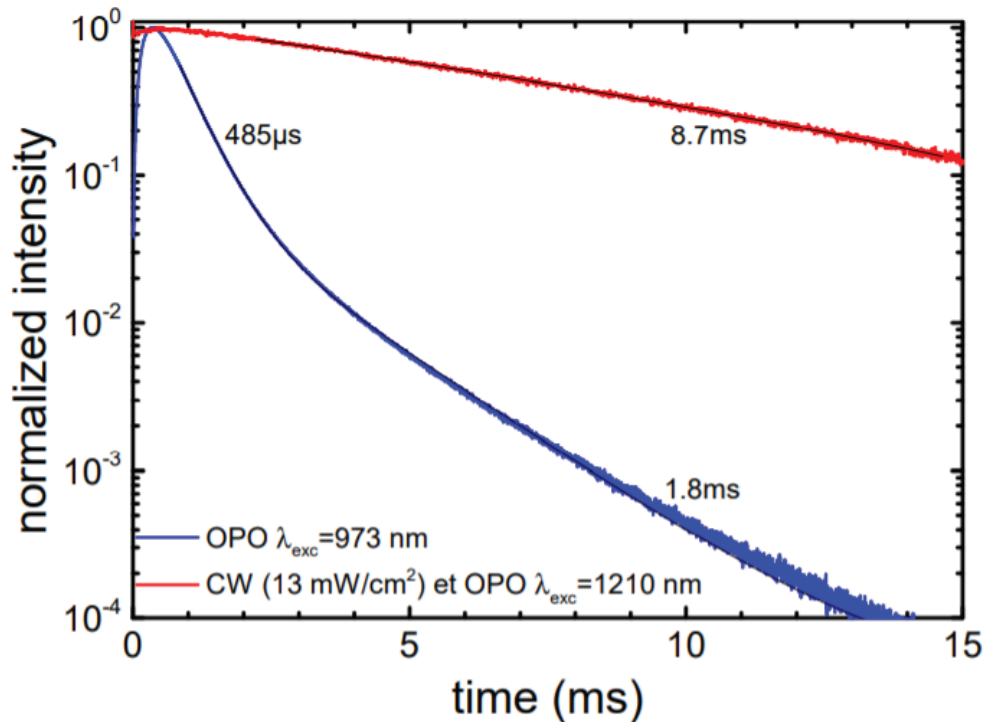


Figure 4.7: lifetime in the excited state $^3H_4 \rightarrow ^3H_6$ under different excitation schemes (continuous wave and pulsed laser).

Figure 4.7 presents lifetime in the excited state measurements of the $^3H_4 \rightarrow ^3H_6$ (805 nm) under two different excitation schemes. The first one, in blue, is under excitation of the Yb^{3+} ions, in a classical upconversion scheme. A build-up time appears at short time scales followed by a bi-exponential decay. The two components of the decay probably come from the lifetime of the emitting level (3H_4 with 1.8 ms) as well as from the 3F_3 (with 485 μs) level just above, from which part of the excitation passes through. The second measure, in red, is performed under double excitation of a continuous wave (W) IR laser at 973 nm with low power intensity (13 mW/cm^2) and a pulsed laser (3 ns) at 1210 nm corresponding to the $^3H_6 \rightarrow ^3H_5$ absorption of Tm^{3+} . In this second case, a very weak build-up time is observed and the lifetime is dominated by a very long single monoexponential decay of 8.7 ms close to the lifetime of the 3F_4 level.¹⁷ i. e. the pulsed laser populates the 3H_4 level that rapidly decays to the 3F_4 level. Because the other laser is continuous it populates, following the lifetime of the 3F_4 , the 3F_2 level by cross-relaxation of excited Yb^{3+} ions giving rise to the $^3H_4 \rightarrow ^3H_6$ emission. Similar behaviour is observed if exciting directly in the 3F_4 level with the OPO laser.

A similar study has been performed on the ${}^1G_4 \rightarrow {}^3H_6$ emission of Tm^{3+} , and the results are presented in Figure 4.8. The main result is that the most efficient way to excite this level is by cooperative sensitization. Indeed, the sequential excitation would involve a transition from the 3H_5 to 1G_4 levels of Tm^{3+} , which is most unlikely since its energy corresponds to 125% of the ${}^2F_{5/2} \rightarrow {}^2F_{7/2}$ transition in Yb^{3+} .

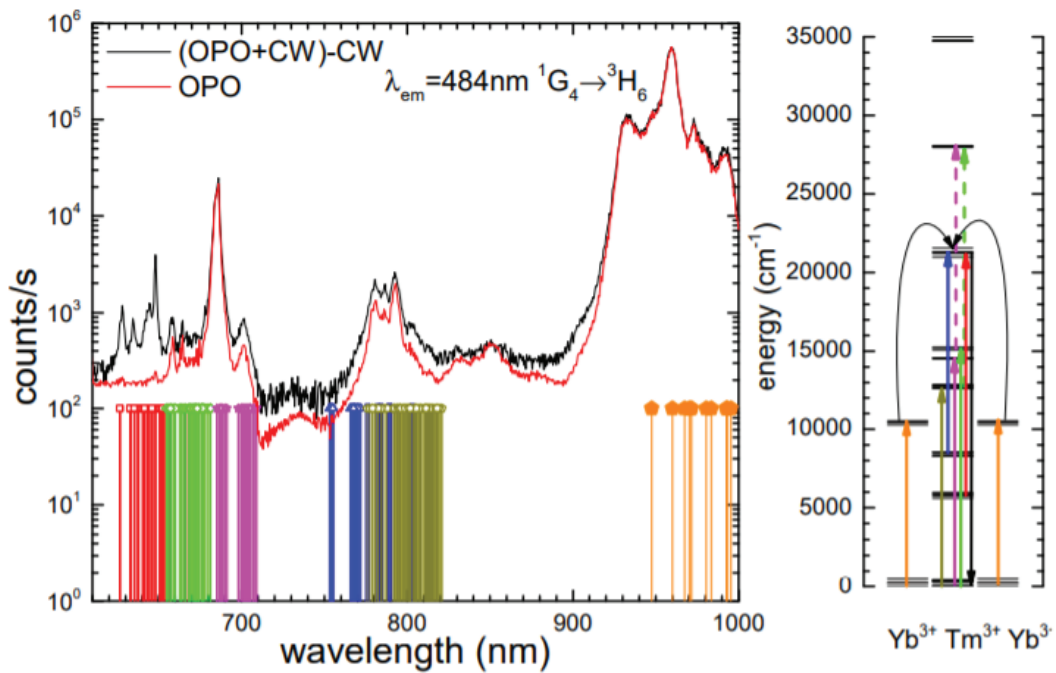


Figure 4.8: Excitation spectra of the ${}^1G_4 \rightarrow {}^3H_6$ transition with (black) or without (red) the CW IR laser at 100 mW/cm^2 .

Description: Below have presented the different transitions in Tm^{3+} and Yb^{3+} ions. In orange, the ${}^2F_{7/2} \rightarrow {}^2F_{5/2}$ absorption of Ytterbium can generate blue emission of Tm^{3+} by sensitive cooperation. In dark green the ${}^3H_6 \rightarrow {}^3H_4$ transition is almost resonant with the ${}^3H_5 \rightarrow {}^1G_4$ (in blue) transition allowing a two-photon upconversion up to the 1G_4 manifold. In magenta, the ${}^3H_6 \rightarrow {}^3F_3$ transition is in close resonance with the ${}^3F_3 \rightarrow {}^1D_2$ transition (dotted magenta arrow) allowing to populate the 1D_2 levels by upconversion. In green the ${}^3H_6 \rightarrow {}^3F_2$ transition in resonance with the ${}^3H_4 \rightarrow {}^1D_2$ transition also allowing to populate the 1D_2 level by upconversion. For all these transitions the emission is similar with or without CW laser at 973 nm. On the contrary, the ${}^3H_4 \rightarrow {}^1G_4$ transition in red only appears when the IR laser is present.

More interesting is the study of the 1D_2 to 3H_6 transition around 360 nm. As shown in Figure 4.9, increasing the IR laser excitation density up to 100 mW/cm^2 results in weak emission from the 3H_4 and the 1G_4 and undetectable emission from 1D_2 . When excited at about 450 nm with a pulsed laser fluence of 50 mJ/cm^2 , this emission cannot be detected either. When the lasers are combined, a strong synergetic effect is demonstrated with an increase by more than 2 orders of magnitude of the ${}^1D_2 \rightarrow {}^3H_6$ emission at 360 nm.

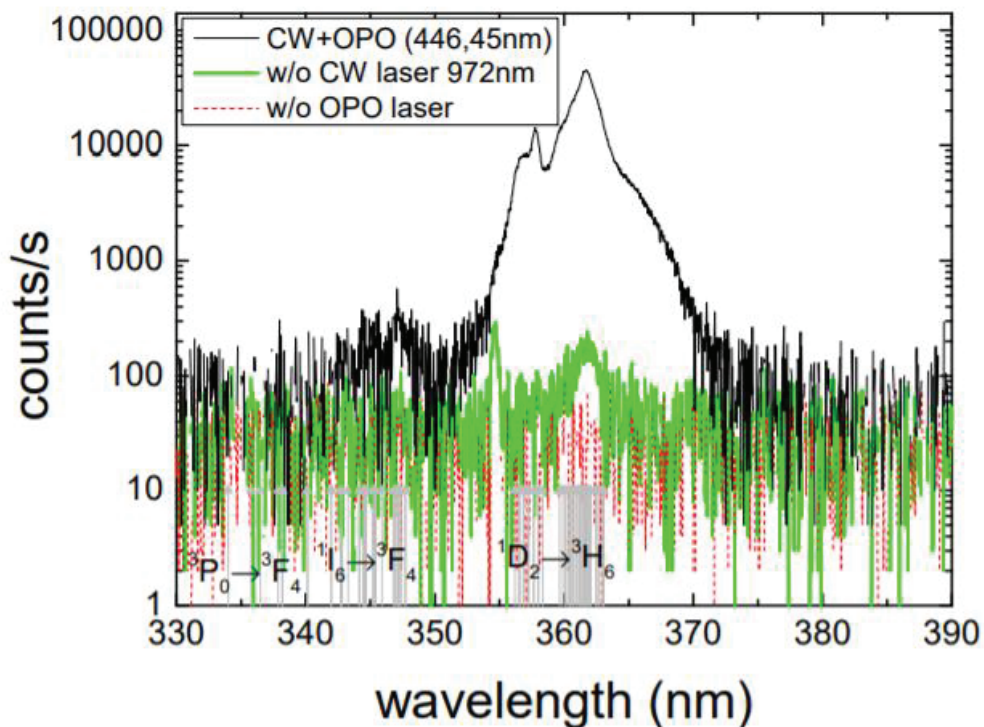


Figure 4.9: Emission spectra of Tm^{3+} ions in $LiYF_4:Yb^{3+}$, Tm^{3+} nanocrystals under dual excitation (black line) of a CW IR laser ($\sim 1 \text{ W/cm}^2$) at 973 nm and an OPO laser at 446.45 nm or simple excitation with the IR laser (dashed red line) or with the OPO laser (thick green line).

The excitation spectrum of this phenomenon is presented in Figure 4.10, where the different transitions can be assigned. It demonstrates that excited state absorption from the 3F_4 to the 1D_2 or from the 3H_4 level to the 1I_6 or 3P_1 levels is a very efficient process, leading to a drastic increase of the emission of the 1D_2 level when the IR source helps to populate the 3F_4 level thanks to an energy transfer from the $^2F_{5/2}$ level of Yb^{3+} . On the other hand, there is no effect on the 1D_2 emission with the addition of the IR source when the OPO source leads to a population of the 1G_4 level (direct excitation from the 3H_6). This means that an energy transfer from the $^2F_{5/2}$ level of Yb^{3+} is not efficient for populating the 1D_2 level from the 1G_4 level. These results allow us to state that the most efficient processes leading to the excitation of the 1D_2 by classical upconversion are the sequential mechanisms involving a first step that populates the 3F_4 level and then the second step of cooperative sensitization from two excited Yb^{3+} ions to generate a 1D_2 excited Tm^{3+} ion. This result is consistent with the calculations of Carnall et al.,¹⁸ who showed that the $^3F_4 \rightarrow ^1D_2$ transition is hypersensitive ($\Delta J = 2$) and its squared U(2) matrix element is 0.5689, therefore one of the strongest absorptions of the Tm^{3+} ions. Again lifetime in the

excited state has been measured under single or dual excitation, and the results are presented in Figure 4.11. As before, this confirms the above-described process with the appearance of a single monoexponential decay for the $^1D_2 \rightarrow ^3H_6$ emission once the second laser is present, corresponding only to the lifetime of the 1D_2 level.

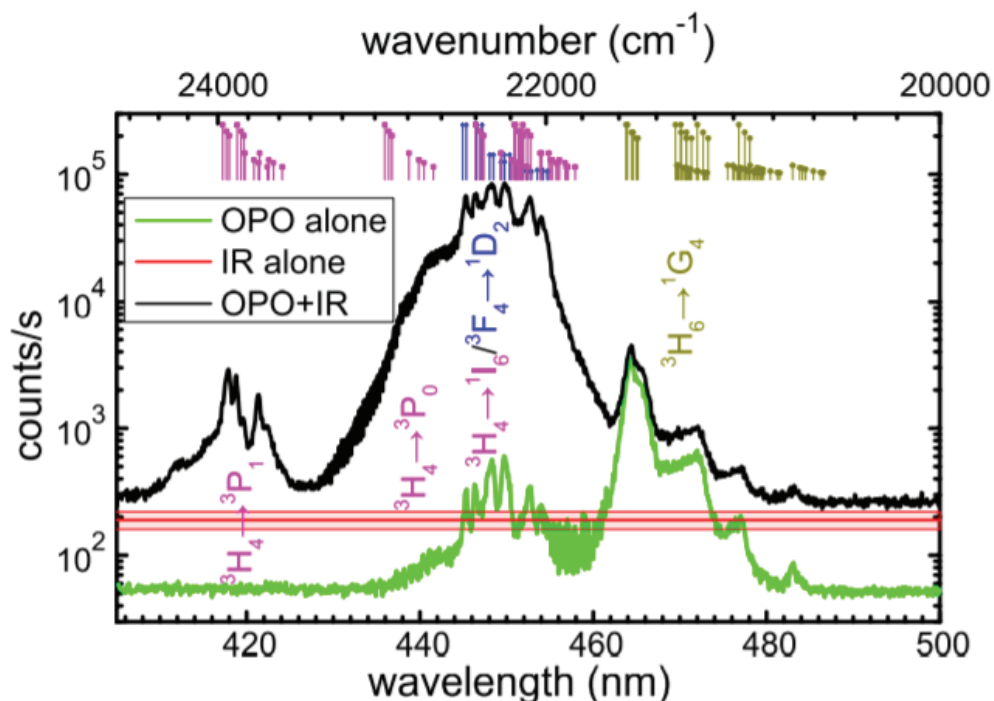


Figure 4.10: Excitation spectra of the $^1D_2 \rightarrow ^3H_6$ transition of Tm^{3+} ions in $LiYF_4: Yb^{3+}, Tm^{3+}$ nanocrystals.

Description: The black curve corresponds to the dual excitation with a CW IR laser at 973 nm and the OPO laser of varying wavelength. The green curve corresponds to the excitation spectrum using only the OPO laser source. The red curve corresponds to the average emission intensity when using only the IR excitation (the clear red band being the $\pm 2\sigma$ intensity fluctuation over time). In the upper part, the different possible transitions for thulium ions¹¹ are plotted with their intensities normalized to their expected relative population from the starting levels according to a simple Boltzmann distribution at room temperature. The colours of the transition are the text tag colours of the bottom figure.

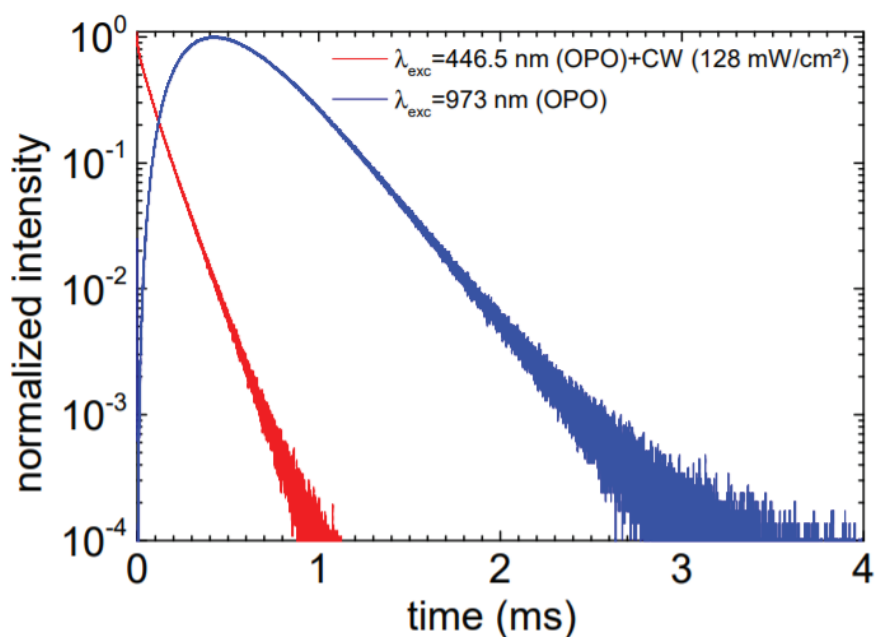


Figure 4.11: lifetime in the excited state of the emission at 360 nm ($^1D_2 \rightarrow ^3H_6$) under two different excitation schemes.

Figure 4.11 presents lifetime in the excited state measurements of the $^1D_2 \rightarrow ^3H_6$ under two different excitation schemes. The first one, in blue, is under excitation of the Yb^{3+} ions, in a classical upconversion scheme. A build-up time appears at short time scales followed by an exponential decay corresponding to the filling of the high excited level of Tm^{3+} as classically observed in Yb^{3+} , Tm^{3+} co-doped systems (see for instance¹⁹). The second one, in red, is performed under double excitation of a CW IR laser at 973 nm with middle power intensity (128 mW/cm^2) and a pulsed laser (3 ns) at 446.5 nm corresponding to the $^3F_4 \rightarrow ^1D_2$ absorption of Tm^{3+} . In this second case, no build-up time is observed and the lifetime is dominated by a single monoexponential decay of $103 \mu\text{s}$, the lifetime of the 1D_2 level.²⁰ The pulsed laser pump directly from the 3F_4 level that is permanently being fed by the continuous wave laser through cross-relaxation of excited Yb^{3+} ions.

4.2.4.2. Continuous wave (CW) + LED excitation

The above results were obtained with relatively high excitation densities far from daylight excitation. It allows an understanding of the different steps that can take place in the upconversion phenomena and for us to sort out which wavelength domains play a role in a broadband excitation scheme. However, by our admission, it is far from real-life applications such as a solar photocatalysis plant. In the following section, we aim to demonstrate that this process still occurs under continuous moderate sunlight-type excitation conditions. The OPO laser is replaced by a standard LED, as described before, that has its maximum in the range of the $^3F_4 \rightarrow ^1D_2$ excitation. Figure 4.12 presents

spectra in the range of the $^1D_2 \rightarrow ^3H_6$ emission under separate and simultaneous blue and IR excitations, highlighting the same synergetic phenomena. These excitations correspond to a typical sun irradiance on the earth for these two ranges of wavelengths as described by the standard AM1.5.²¹ As can be seen in this figure, as soon as the IR intensity is decreased below a few W/cm^2 , no UV light can be detected if no blue excitation is present. On the contrary, if the blue LED is turned on with rather low excitation intensities ($9\text{ mW}/cm^2$), UV emission can be detected even for very low intensities of the IR laser.

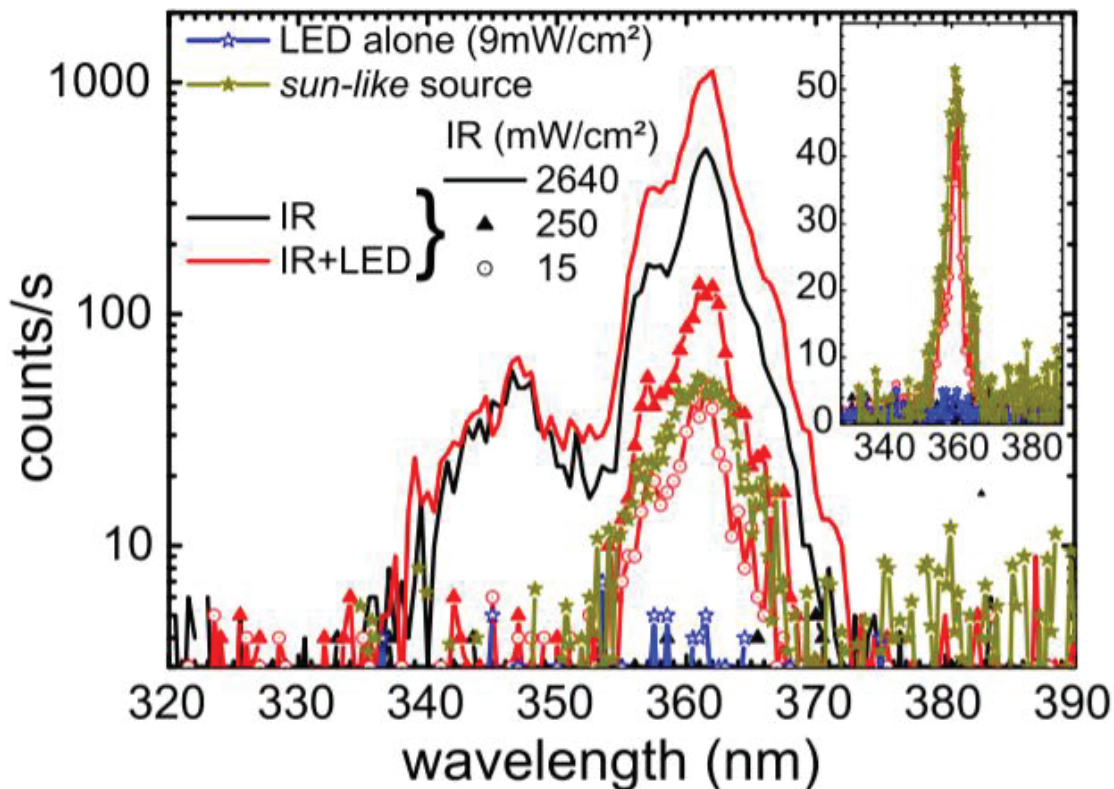


Figure 4.12: Emission spectra of Tm^{3+} ions in $LiYF_4:Yb, Tm$ nanocrystals under dual excitation.

Description: The red lines represent the dual excitation of an SCW IR laser at 973 nm and the LED or by the LED alone is shown by blue stars and black lines represent the IR laser alone. The brown stars correspond to excitation with sun-like excitation (lamp + filter). The inset is a close-up in a linear scale of the weaker spectra. The noise of the detector is around 3 counts/s.

To demonstrate the impact of the discussed mechanisms on the change of the power-law regime for the 1D_2 emission, we compared the UV intensity as a function of the IR laser intensity with or without the blue LED ($3\text{ mW}/cm^2$). The results presented in Figure 4.13 with IR excitation alone follow a third-order dependence as expected and already presented. When the LED is turned on, the power-law shape is radically modified and becomes linear up to $1\text{ W}/cm^2$, indicating that the IR excitation switches from a three-photon to a single IR photon process. As described above, by energy transfer, the IR absorption of a single photon in Yb^{3+} allows the excitation of the 3F_4 of Tm^{3+} , and the

blue excitation promotes Tm^{3+} to the $^1\text{D}_2$ state. At higher excitation density, the third-order process is, as expected, dominant. Similarly, when varying the power of the LED while keeping the IR laser power constant, a linear behaviour is observed, as evidenced in Figure 4.14. It demonstrates that the overall mechanism involves 1 photon in the blue and 1 photon in the IR, which satisfies the energy conservation law to obtain UV light at 360 nm.

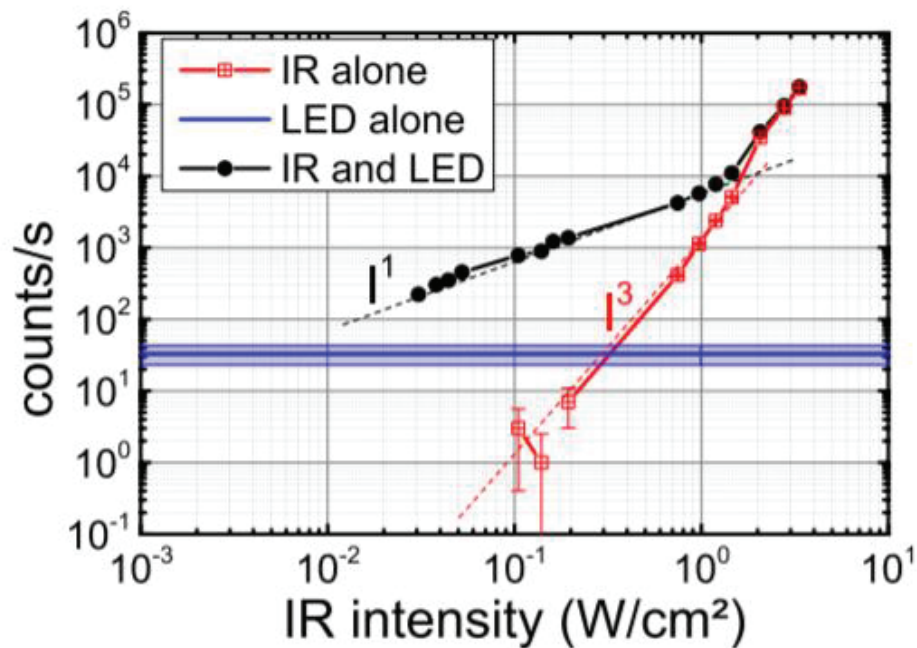


Figure 4.13: Emission intensity of the $^1\text{D}_2 \rightarrow ^3\text{H}_6$ of Tm^{3+} ions in $\text{LiYF}_4:\text{Yb}^{3+}, \text{Tm}^{3+}$ nanocrystals under dual excitation (black line) of a CW IR laser at 973 nm and an LED centred at 460 nm.

Description: The red line represents the excitation of the CW IR laser alone and the blue line represents the excitation from LED alone (together with its $\pm 2\sigma$ variation) as a function of the IR intensity. The black line represents the total emission of Tm^{3+} ions in $\text{LiYF}_4:\text{Yb}^{3+}, \text{Tm}^{3+}$ nanocrystals in the range of 360-370 nm ($^1\text{D}_2 \rightarrow ^3\text{H}_6$ of Tm^{3+} ions) under dual excitation (IR + LED). The LED is kept at $3 \text{ mW}/\text{cm}^2$. The dashed lines are a guide for the eyes showing a variation following a linear relation with intensity (black) or following a power law with a factor of 3 (red).

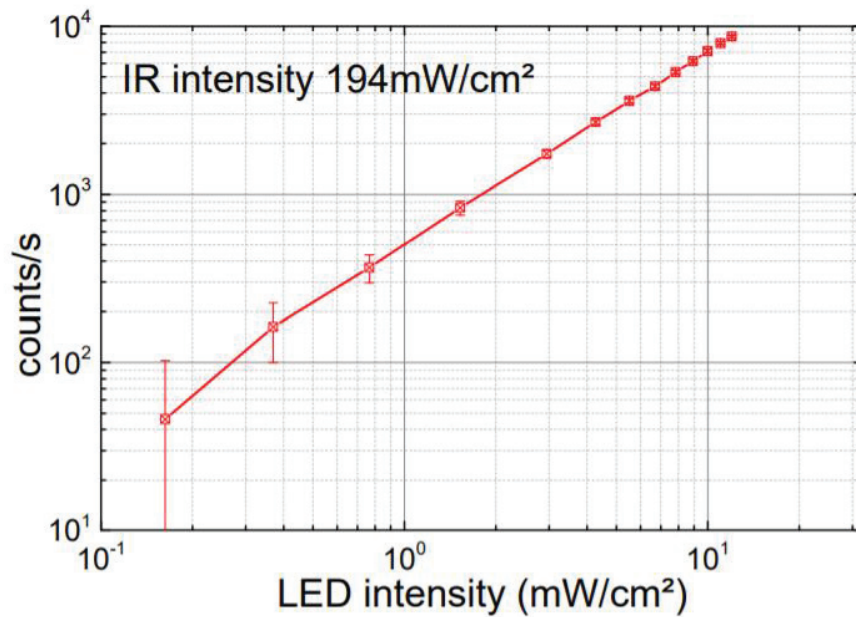


Figure 4.14: Total emission in the range 360-370 nm Tm^{3+} ions in $LiYF_4:Yb, Tm$ nanocrystals ($^1D_2 \rightarrow ^3H_6$) under dual excitation of a CW IR laser at 973 nm and a LED centred at 460 nm (M455L1 from Thorlabs) with varying intensity.

4.2.4.3. Mimicking solar excitation

As the last demonstration, we simulated a solar illumination using a filtered Xe lamp with a spectrum shown in Figure 4.15. UV emission under such excitation is presented in Figure 4.12 as brown stars compared to the IR excitation through upconversion mechanisms or with the combination of LED and an IR laser. A clear band is obtained at 360 nm, and the band is slightly broader because the system resolution, in this case, was 2.5 nm instead of 1 nm.

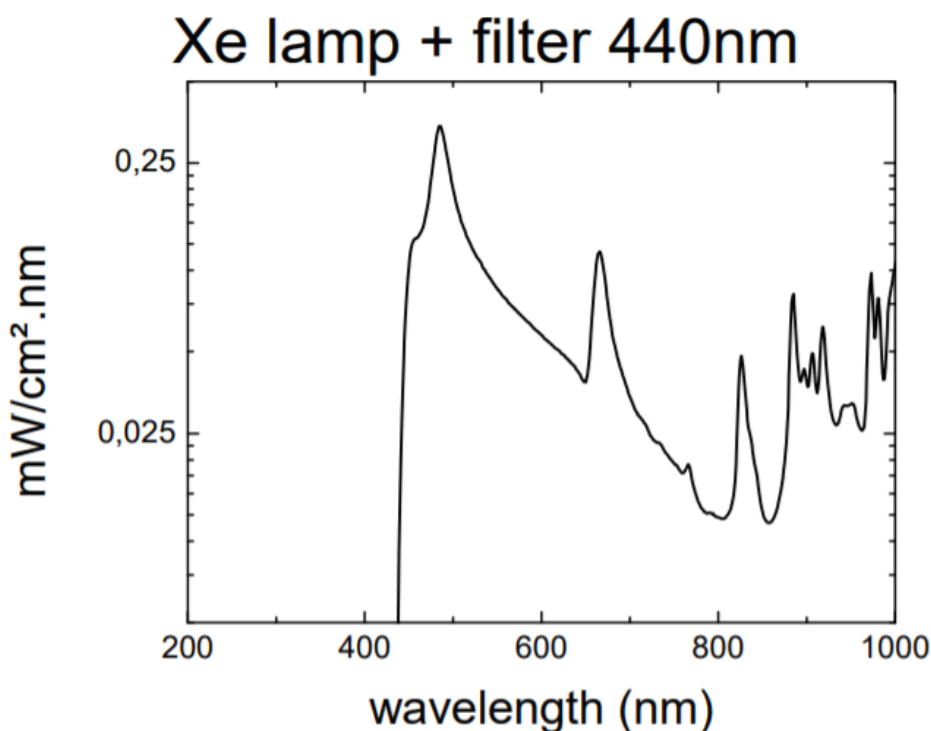


Figure 4.15: Measured spectra of the Xe lamp and filter used to excite the nanoparticles under sun-like excitation.

This excitation, similar to the sun, can promote high energy excitations in Yb^{3+} , Tm^{3+} co-doped LiYF_4 . It would enable the generation, by energy transfer, of electron-hole pairs compatible with standard photocatalysts. Combining upconverter and photocatalyst, a significant part of the solar spectrum that is unused can stimulate photocatalysis, which, after optimization and use of efficient energy transfer ions²²⁻²⁴, has the potential to improve the overall photocatalysis efficiency by a factor of 3, as we have shown in a previous work¹⁰. Such an approach would allow a significant decrease in the time of reaction that currently takes between hours and weeks in solar photocatalysis plants¹ and could also allow the use of photocatalysts that have been discarded since they need photons with an energy that is too high.

This exciting result comes from the simple addition of the energy of an IR and a visible photon, thus reducing the nonlinearity of the UV upconversion phenomena, which in part originates from the idea behind Auzel's original publication in 1966 to make a "quantum counter by energy transfer from Yb^{3+} to Tm^{3+} ".²⁵

4.3. Conclusions and perspectives

In this chapter, we presented a detailed analysis of the multicolour excitation of $\text{LiY}_{5/6}\text{Yb}_{1/6}\text{F}_4$: 0.4% Tm^{3+} nanocrystals which leads to UV emission through upconversion. We demonstrated in particular that the combination of blue and IR light for generating upconversion UV emission is a linear mechanism that occurs at a rather low density of excitation (a few mW/cm^2). This upconversion efficiency is fully compatible with the broadband excitation from the sun, with a comparable density similar to daylight excitation. These results demonstrate that an appropriate design, combining photocatalyst and a dedicated upconverter could lead to drastic improvement of the photocatalytic effect.

4.4. References

- (1) Spasiano, D.; Marotta, R.; Malato, S.; Fernandez-Ibañez, P.; Di Somma, I. Solar Photocatalysis: Materials, Reactors, Some Commercial, and Pre-Industrialized Applications. A Comprehensive Approach. *Applied Catalysis B: Environmental* **2015**, *170–171*, 90–123. <https://doi.org/10.1016/j.apcatb.2014.12.050>.
- (2) Tang, Y.; Di, W.; Zhai, X.; Yang, R.; Qin, W. NIR-Responsive Photocatalytic Activity and Mechanism of NaYF₄: Yb, Tm@TiO₂ Core-Shell Nanoparticles. *ACS Catal.* **2013**, *3* (3), 405–412. <https://doi.org/10.1021/cs300808r>.
- (3) Zhang, Y.; Hong, Z. Synthesis of Lanthanide-Doped NaYF₄@TiO₂ Core-Shell Composites with Highly Crystalline and Tunable TiO₂ Shells under Mild Conditions and Their Upconversion-Based Photocatalysis. *Nanoscale* **2013**, *5* (19), 8930. <https://doi.org/10.1039/c3nr03051b>.
- (4) Wang, W.; Ding, M.; Lu, C.; Ni, Y.; Xu, Z. A Study on Upconversion UV–Vis–NIR Responsive Photocatalytic Activity and Mechanisms of Hexagonal Phase NaYF₄:Yb³⁺, Tm³⁺@TiO₂ Core-Shell Structured Photocatalyst. *Applied Catalysis B: Environmental* **2014**, *144*, 379–385. <https://doi.org/10.1016/j.apcatb.2013.07.035>.
- (5) Wang, W.; Li, Y.; Kang, Z.; Wang, F.; Yu, J. C. A NIR-Driven Photocatalyst Based on α-NaYF₄: Yb, Tm@TiO₂ Core-Shell Structure Supported on Reduced Graphene Oxide. *Applied Catalysis B: Environmental* **2016**, *182*, 184–192. <https://doi.org/10.1016/j.apcatb.2015.09.022>.
- (6) Ullah, S.; Hazra, C.; Ferreira-Neto, E. P.; Silva, T. C.; Rodrigues-Filho, U. P.; Ribeiro, S. J. L. Microwave-Assisted Synthesis of NaYF₄: Yb³⁺/Tm³⁺ Upconversion Particles with Tailored Morphology and Phase for the Design of UV/NIR-Active NaYF₄: Yb³⁺/Tm³⁺@TiO₂ Core@shell Photocatalysts. *CrystEngComm* **2017**, *19* (25), 3465–3475. <https://doi.org/10.1039/C7CE00809K>.
- (7) Su, W.; Zheng, M.; Li, L.; Wang, K.; Qiao, R.; Zhong, Y.; Hu, Y.; Li, Z. Directly Coat TiO₂ on Hydrophobic NaYF₄: Yb, Tm Nanoplates and Regulate Their Photocatalytic Activities with the Core Size. *J. Mater. Chem. A* **2014**, *2* (33), 13486–13491. <https://doi.org/10.1039/C4TA02756F>.
- (8) Yin, D.; Zhang, L.; Cao, X.; Tang, J.; Huang, W.; Han, Y.; Liu, Y.; Zhang, T.; Wu, M. Improving Photocatalytic Activity by Combining Upconversion Nanocrystals and Mo-Doping: A Case Study on β-NaLuF₄: Gd, Yb, Tm@SiO₂ @TiO₂: Mo. *RSC Advances* **2015**, *5* (106), 87251–87258. <https://doi.org/10.1039/C5RA12852H>.

- (9) Qin, G.; Qin, W.; Wu, C.; Huang, S.; Zhang, J.; Lu, S.; Zhao, D.; Liu, H. Enhancement of Ultraviolet Upconversion in Yb³⁺ and Tm³⁺ Codoped Amorphous Fluoride Film Prepared by Pulsed Laser Deposition. *Journal of Applied Physics* **2003**, *93* (7), 4328–4330. <https://doi.org/10.1063/1.1557775>.
- (10) Chen, Y.; Mishra, S.; Ledoux, G.; Jeanneau, E.; Daniel, M.; Zhang, J.; Daniele, S. Direct Synthesis of Hexagonal NaGdF₄ Nanocrystals from a Single-Source Precursor: Upconverting NaGdF₄: Yb³⁺, Tm³⁺ and Its Composites with TiO₂ for Near-IR-Driven Photocatalysis. *Chemistry – An Asian Journal* **2014**, *9* (9), 2415–2421. <https://doi.org/10.1002/asia.201402347>.
- (11) Dulick, M.; Faulkner, G. E.; Cockroft, N. J.; Nguyen, D. C. Spectroscopy and Dynamics of Upconversion in Tm³⁺: YLiF₄. *Journal of Luminescence* **1991**, *48–49*, 517–521. [https://doi.org/10.1016/0022-2313\(91\)90183-V](https://doi.org/10.1016/0022-2313(91)90183-V).
- (12) Bensalah, A.; Guyot, Y.; Ito, M.; Brenier, A.; Sato, H.; Fukuda, T.; Boulon, G. Growth of Yb³⁺-Doped YLiF₄ Laser Crystal by the Czochralski Method. Attempt of Yb³⁺ Energy Level Assignment and Estimation of the Laser Potentiality. *Optical Materials* **2004**, *26* (4), 375–383. <https://doi.org/10.1016/j.optmat.2003.09.015>.
- (13) Peretti, R.; Jurdyc, A.-M.; Jacquier, B.; Gonnet, C.; Pastouret, A.; Cavani, O. How Do Traces of Thulium Explain Photodarkening in Yb Doped Fibers? **2010**, *6*.
- (14) Guy, S.; Jurdyc, A. M.; Jacquier, B.; Meffre, W. M. Excited States Tm Spectroscopy in ZBLAN Glass for S-Band Amplifier. *Optics Communications* **2005**, *250* (4–6), 344–354. <https://doi.org/10.1016/j.optcom.2005.02.058>.
- (15) Knüpfer, A.; Ostroumov, V.; Heumann, E.; Huber, G.; Lupei, V. Mechanisms of Up-Conversion Excitation of Blue Emission in YAG: Tm, Yb. *J. Phys. IV France* **1994**, *04* (C4), C4-501–C4-504. <https://doi.org/10.1051/jp4:19944120>.
- (16) Mishra, S.; Ledoux, G.; Jeanneau, E.; Daniele, S.; Joubert, M.-F. Novel Heterometal-Organic Complexes as First Single Source Precursors for Up-Converting NaY(Ln)F₄ (Ln = Yb, Er, Tm) Nanomaterials. *Dalton Trans.* **2012**, *41* (5), 1490–1502. <https://doi.org/10.1039/C1DT11070E>.
- (17) Aleshire, C. E.; Yu, C. X.; Reed, P. A.; Fan, T. Y. Efficient Cryogenic Near-Infrared Tm: YLF Laser. *Opt. Express, OE* **2017**, *25* (12), 13408–13413. <https://doi.org/10.1364/OE.25.013408>.
- (18) Carnall, W. T. [Argonne N. Lab. (ANL), Argonne, IL (United States)]; Crosswhite, H. [Johns H. Univ., Baltimore, MD (United States)]; Crosswhite, H. M. [Johns H. Univ., Baltimore, MD (United

States)]. *Energy Level Structure and Transition Probabilities in the Spectra of the Trivalent Lanthanides in LaF₃*; United States, **1978**. <https://doi.org/10.2172/6417825>.

(19) Villanueva-Delgado, P.; Krämer, K. W.; Valiente, R. Simulating Energy Transfer and Upconversion in β -NaYF₄: Yb³⁺, Tm³⁺. *J. Phys. Chem. C* **2015**, *119* (41), 23648–23657. <https://doi.org/10.1021/acs.jpcc.5b06770>.

(20) Auzel, F. Compteur Quantique Par Transfert d'énergie Entre Deux Ions de Terres Rares Dans Un Tungstate Mixte et Dans Un Verre. *C. R. Acad. Sci. Paris* **1966**, *262*, 1016–1019.

(21) Standard Tables for Reference Solar Spectral Irradiances: Direct Normal and Hemispherical on 37° Tilted Surface. <https://doi.org/10.1520/G0173-03R20>.

(22) Wang, F.; Deng, R.; Wang, J.; Wang, Q.; Han, Y.; Zhu, H.; Chen, X.; Liu, X. Tuning Upconversion through Energy Migration in Core-Shell Nanoparticles. *Nature Materials* **2011**, *10* (12), 968–973. <https://doi.org/10.1038/nmat3149>.

(23) Su, Q.; Han, S.; Xie, X.; Zhu, H.; Chen, H.; Chen, C.-K.; Liu, R.-S.; Chen, X.; Wang, F.; Liu, X. The Effect of Surface Coating on Energy Migration-Mediated Upconversion. *J. Am. Chem. Soc.* **2012**, *134* (51), 20849–20857. <https://doi.org/10.1021/ja3111048>.

(24) Ledoux, G.; Amans, D.; Joubert, M.-F.; Mahler, B.; Mishra, S.; Daniele, S.; Dujardin, C. Modeling Energy Migration for Upconversion Materials. *J. Phys. Chem. C* **2018**, *122* (1), 888–893. <https://doi.org/10.1021/acs.jpcc.7b10113>.

(25) Auzel, F. Compteur Quantique Par Transfert d'énergie de Yb³⁺ à Tm³⁺ Dans Un Tungstate Mixte et Dans Un Verre Germanate. *C. R. Acad. Sci. Paris* **1966**, *263*, 819.

Chapter 5 TiO₂-LiYF₄:Yb³⁺, Tm³⁺ nanocomposites for near-IR driven photocatalysis

5.1. Introduction

Titanium dioxide (TiO₂) as a non-expensive, chemically stable, renewable and non-polluting material, is the most widely used UV photocatalyst which constitutes above 60% of the overall photocatalyst industry.¹ However, it suffers from two major drawbacks: i) it has a bandgap of 3.2 eV (anatase), which limits its applications mostly in the UV region, and ii) a large number of electron-hole pair recombination dissipates energy in the form of heat and light, which reduces its efficiency further. The IR region of the sunlight, which accounts for almost half of the energy of the sunlight radiation (as against only about 5% of the UV radiation), remains largely unused for photocatalysis (see Figure 5.1 for reference). In this context, we² and a few other groups³⁻¹² have previously shown that the nanocomposites of UCNPs with TiO₂ in the form of a core-shell structure could be a very promising approach for near infrared-induced photocatalytic applications. These strategies exploit the ability of the upconverting nanoparticles (UCNPs) to convert IR photons to UV-visible, which in turn could be used by titania for photocatalysis. While the other teams obtained enhancement only under strong laser IR irradiation, we achieved enhancement under solar excitation using migration-assisted energy transfers allowing an efficient transfer from the UC nanoparticle to the photocatalyst.² So far, different surfactant ligands such as PVP, CTAB, etc. have been used majorly to facilitate the formation of TiO₂ shell around UCNPs. However, the obtained core-shell structures lack homogeneity and it is difficult to obtain a sufficiently thick layer of titania. Besides, reproducibility, stability and scalability of these structures are also challenging tasks. These issues can be addressed by alternate strategies to obtain nanocomposites. Among these, the strategy to embed UCNPs in TiO₂-based metallogels could lead to efficient composites with high surface area and intimate mixing of the two components.^{13,14} This strategy could also be useful in introducing a suitable luminescent molecule in these UCNPs-TiO₂ systems. These molecules, due to their antenna effect,¹⁵ may allow a broad absorption and, therefore, further improve the optical properties of the composites. In this chapter, we describe our attempts to i) improve the core-shell synthesis of TiO₂@UCNP by using oleic acid or amino alcohols as surfactants, and ii) prepare transparent UCNPs-embedded TiO₂ metallogels as a precursor to UCNPs-TiO₂ xerogels.

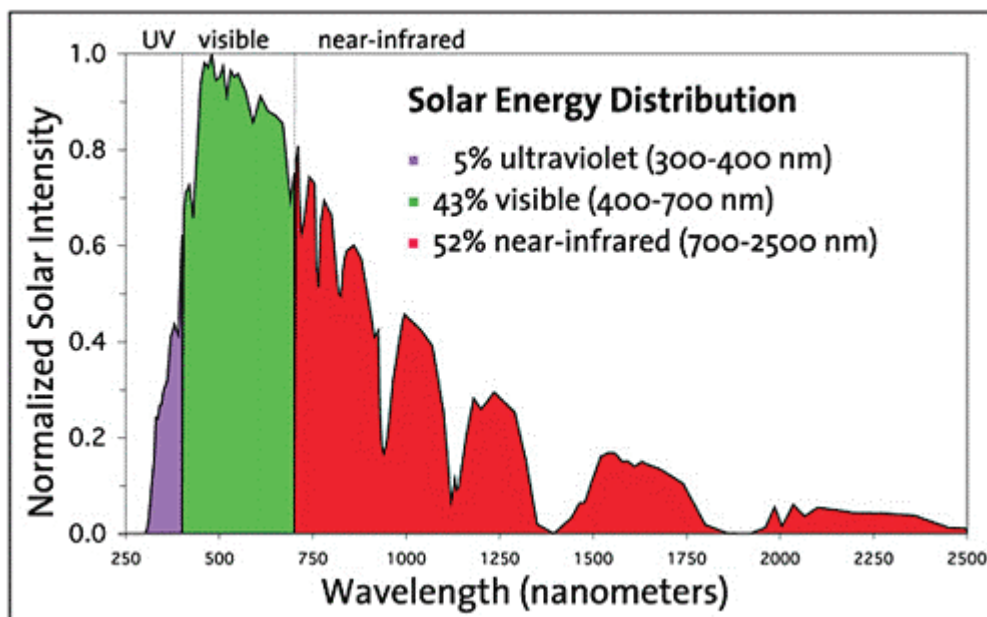


Figure 5.1: Contribution of different radiation in the solar spectrum.¹⁶

5.2. Results and discussion

5.2.1. Synthesis of UCNPs-TiO₂ nanocomposites

5.2.1.1. Synthesis and characterization shell-core TiO₂@UCNPs

As mentioned in the introduction of this chapter, few reports have already appeared on the synthesis of TiO₂@UCNP shell-core structures using different capping ligands.²⁻¹² However, there are some major issues such as lack of homogeneity and sufficient thickness of the shell layer, difficulty in scaling up their synthesis as well as reproducibility and stability of these structures, which make their applications challenging. To prepare efficient TiO₂@UCNP shell-core structures that can be used to harness a substantial amount of solar spectrum, the selection of an appropriate capping ligand is crucial. For this work, we chose LiYF₄: Yb³⁺, Tm³⁺ as core upconverting nanomaterial which is a great host for NIR to UV upconversion. The synthesis, structural, morphological and upconversion properties of oleic acid-capped LiY_{5/6}Yb_{1/6}F₄: 0.4% Tm³⁺ upconverting nanoparticles has been discussed in detail in Chapter 3. The orientation of the oleic acid ligand around the upconverting nanoparticles is such that the hydrophobic tail is extended outward,^{17,18} which makes them dispersible, and therefore manipulative for further functionalization, in the organic medium. Given this orientation of the oleic acid around NPs, we decided to keep this ligand as a surfactant for the core-shell formation. For this, we also modified the Ti(OPri)₄ by reacting it with oleic acid at 120°C for one hour.¹⁹ The formed pale yellow titanium-oleate complex^{20,21} was injected under argon flow into an isopropanol solution containing the as-prepared LiY_{5/6}Yb_{1/6}F₄: 0.4% Tm³⁺ UC NPs in dispersible form. After stirring for a few

minutes, a calculated amount of hydrolysing solution was added to start the hydrolysis and condensation of the titanium precursor. After usual manipulation, the obtained $\text{TiO}_2@ \text{LiY}_{5/6}\text{Yb}_{1/6}\text{F}_4$: 0.4% Tm^{3+} shell-core structures were isolated by centrifugation and characterized by transmission electron microscopy (TEM), which confirmed the formation of TiO_2 shell around UC core nanoparticles (Figure 5.2).

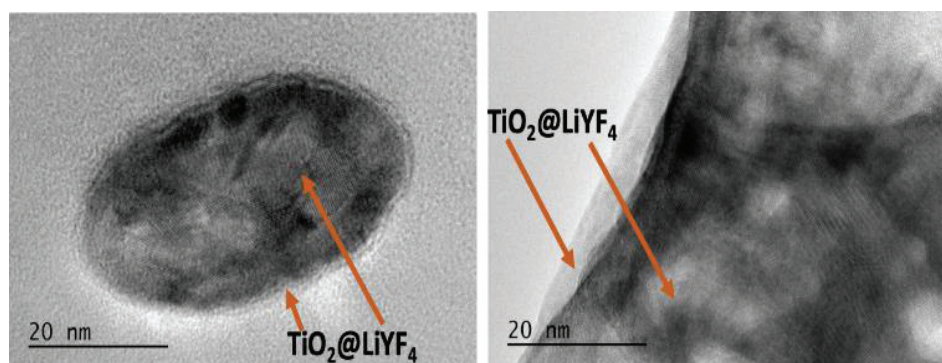


Figure 5.2: TEM images of $\text{TiO}_2@ \text{LiY}_{5/6}\text{Yb}_{1/6}\text{F}_4$: 0.4% Tm^{3+} NPs using oleic acid as a capping ligand.

However, the obtained TiO_2 layer was neither uniform nor sufficiently thick, probably due to weak steric interaction among the long carbon chain of the oleic acid/oleate ligand. As the interaction between the nanoparticles and the titanium precursor through the capping ligand is crucial for the formation of a uniform shell of sufficient thickness around NPs, we replaced oleic acid with sterically less hindered *N*-methyl substituted amino alcohols of different denticity as possible surfactants.

5.2.1.1.1. Use of *N*-methyl substituted amino alcohols as capping ligands:

The *N*-methyl ethanol-based amino alcohols, *N*, *N*-dimethylaminoethanol (dmeaH) and *N*-methyl diethanolamine (mdeaH₂) (Figure 5.3) have previously been shown to be excellent capping ligands which could not only control the size, shape and dispersibility of the NPs but also, due to their variable functionality, facilitate homogeneous shell formation of a metal oxide materials.^{22–24} The general preparation of $\text{TiO}_2@ \text{LiY}_{5/6}\text{Yb}_{1/6}\text{F}_4$: 0.4% Tm^{3+} is demonstrated in Scheme 5.1 and briefly stated as follows: The as-synthesized $\text{LiY}_{5/6}\text{Yb}_{1/6}\text{F}_4$: 0.4% Tm^{3+} UCNPs were dispersed in isopropanol in the presence of either mdeaH₂ or dmeaH ligand, followed by addition of calculated amounts of titanium isopropoxide (TIP) and a hydrolysis mixture of acetic acid and water in isopropanol. The hydrolysis and condensation of TIP lead to the formation of the Ti-O-Ti network around the core UCNPs. The purpose of the amino alcohol was two folds: to modify the titanium precursor by substituting some of the alkoxy groups with amino alkoxide and, therefore, decrease its hydrolytic reactivity,²⁵ and act as a capping ligand to facilitate shell formation around the UC core.^{22–24,26} Acetic acid usually provides stability to

the formed sol.²⁷ After general workup, the core-shell composite powders were isolated by centrifugation.

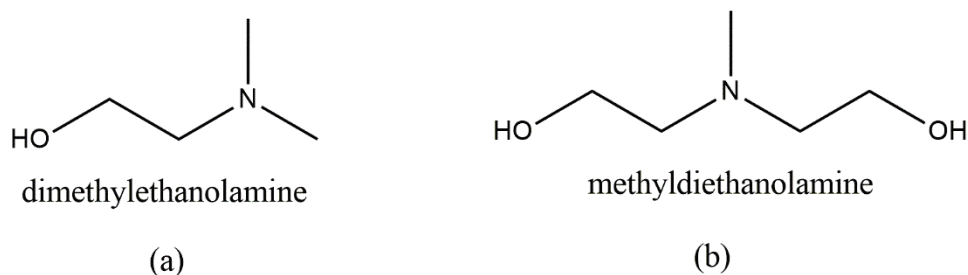
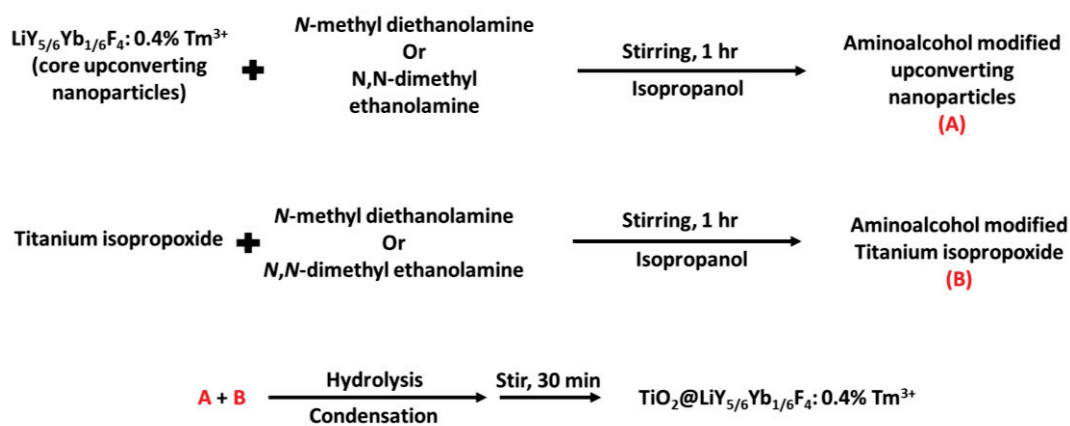


Figure 5.3: *N,N*-dimethylaminoethanol (dmeaH) (a) and *N*-methyl diethanolamine (mdeaH₂) (b) ligands used as capping ligands in the present study.



Scheme 5.1: Different steps for the synthesis of $\text{TiO}_2@\text{UCNPs}$ shell-core structure using amino alcohols as functionalising ligand.

Transmission microscopy is very useful when it comes to determining whether the core-shell is present or not. Figure 5.4 and Figure 5.5 show the TEM images of the as-prepared core-shell particles (before calcination) obtained using the upconverting nanoparticles functionalized by the *N,N*-dimethyl ethanolamine and *N*-methyl diethanolamine as capping ligands, respectively. We observe the presence of an amorphous TiO_2 layer around the upconverting nanoparticles. The line profiling from the HRTEM analysis further confirms the presence of (101) planes of tetragonal LiYF_4 . To further investigate the composition of the amorphous coating around these nanoparticles, we performed STEM analysis and EDX mapping which clearly shows the presence of Ti and O around these nanoparticles.

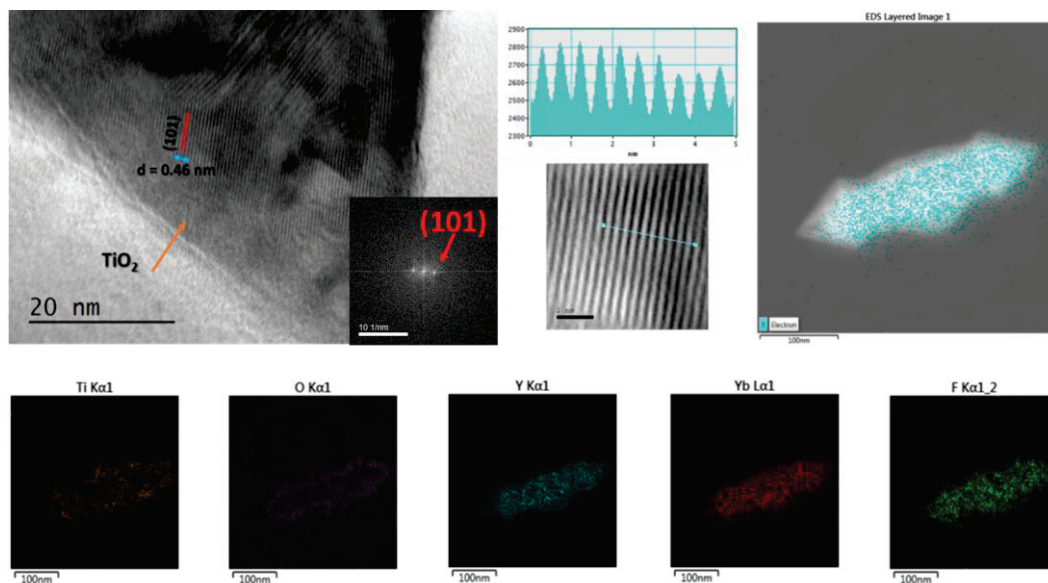


Figure 5.4: Transmission electron microscopy images of TiO_2 coated $\text{LiY}_{5/6}\text{Yb}_{1/6}\text{F}_4: 0.4\% \text{Tm}^{3+}$ samples when *N,N*-dimethyl ethanolamine was used as functionalizing ligand. The top left image clearly shows the coating of amorphous TiO_2 on well crystalline LiYF_4 nanoparticle which is further confirmed by calculating *d* spacing of 0.46 nm corresponding to (101) planes of tetragonal LiYF_4 . The STEM image on the top right and subsequent EDX mapping data show a nearly uniform coating of TiO_2 around LiYF_4 nanocrystals.

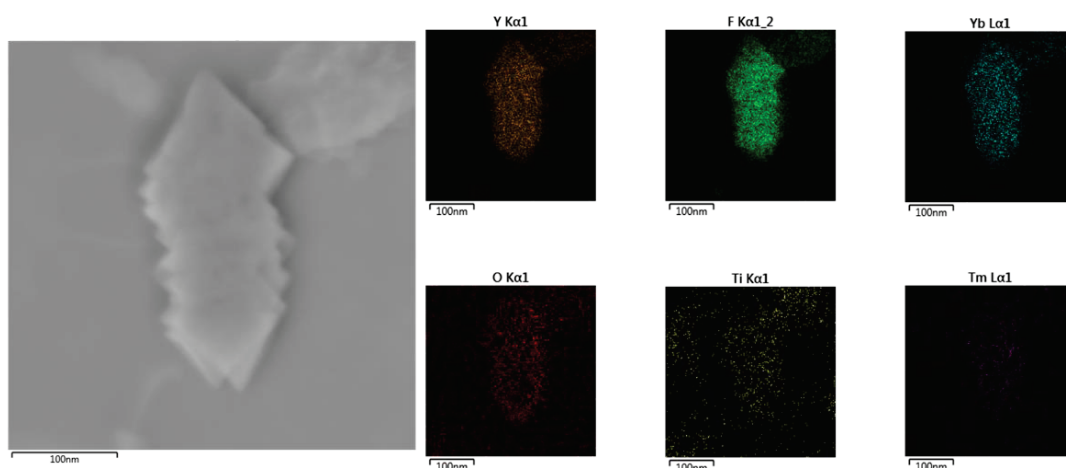


Figure 5.5: STEM imaging and EDX mapping of TiO_2 coated $\text{LiY}_{5/6}\text{Yb}_{1/6}\text{F}_4: 0.4\% \text{Tm}^{3+}$ upconverting nanoparticles using *N*-methyl diethanolamine as a functionalizing ligand.

Although the coating around the nanoparticles is not very uniform, but concept-wise, the use of amino alcohols as a functional ligand could be an easy and efficient way to prepare TiO_2 @UCNPs shell-core nanostructure, provided we optimise certain parameters such as Ti/Y ratio, amount of water during the reaction, etc.

5.2.1.2. UCNPs-embedded transparent TiO₂ metallogels for TiO₂-LiYF₄:Yb³⁺,Tm³⁺ nanocomposites with high surface area

Self-assembled hybrid materials containing both molecules and appropriately functionalized nanoparticles is a new exciting way of fabricating soft materials with significant advantages.^{13,14,28–31} This multi-scale self-assembly strategy makes it possible to obtain synergetic properties and to arrange the various components in a complex hierarchical architecture allowing, for example, the modulation of optical, electronic and mechanical performances. The possibility to enhance the upconversion-induced photocatalysis depends on the material's ability to absorb and transfer as much light as possible. Both of these necessary criteria can be achieved by embedding UCNPs in transparent TiO₂ metallogel, followed by its soft drying. It is not only expected to provide highly homogeneous TiO₂-UCNPs composites with a high specific surface area but may also allow the introduction of appropriate luminescent species in this UCNPs-embedded gel. These species would act as an antenna to boost the NIR absorption of the UCNPs, therefore hold great promise for improving the efficiency of photocatalytic performance of TiO₂ in the visible and infrared region of the solar spectrum. Metallogels are exceptionally versatile, soft materials formed by the cooperation of covalent and self-complementary interactions of the low-molecular-weight species resulting in a self-assembled network capable of immobilizing the solvent, and therefore, yielding a solid-like appearance.³² To achieve robust gels, usually organic ligands with different functionalities are introduced into gel networks. However, the presence of these ligands might be detrimental for photocatalysis. Fortunately, monolithic TiO₂ metallogels can be obtained via the sol-gel process in a controlled acidic medium without using any organic ligand.^{33,34} In the present case, we prepared well-defined transparent TiO₂ monolithic metallogel *via* controlled hydrolysis and polycondensation reactions using an optimized ratio of Ti(OEt)₄ and HCl in EtOH.

The hydrolysis was carried out under controlled conditions using a calculated amount of water (hydrolysis ratio 2). This is crucial for getting the desired phase of the titania (i.e. anatase). It has been shown previously that with the higher water content, the chances of conversion of the anatase to the brookite phase becomes higher.³⁵ Also, if the water content during the reaction is high then due to the faster rate of hydrolysis, the embedding of the nanoparticles won't be effective and uniform. Moreover, the choice of HCl also favours the formation of the anatase phase, which is the most active phase for photocatalysis. Although the presence of the Cl⁻ ions in the gel is undesired, it can be removed by washing the dried gel with water.³⁶ More importantly, we did not use any organic ligand for enhancing the interaction between the titanium precursors and the upconverting nanoparticles, which could be detrimental for photocatalysis. The photocatalytic mechanisms for the

degradation of organic pollutants or water splitting are based on the utilization of UV light^{8,37} and if the photo catalytically generated free radicals are utilized by the organics present around this catalytic system then it will reduce the overall efficiency of the catalytic system.

The incorporation of upconverting $\text{LiY}_{5/6}\text{Yb}_{1/6}\text{F}_4: 0.4\% \text{Tm}^{3+}$ nanoparticles in the solution of $\text{Ti}(\text{OEt})_4$ in EtOH before its controlled hydrolysis leads to the formation of TiO_2 metallogel with the uniform embedding of UCNPs. We chose the different amount of UCNPs to be embedded in the TiO_2 metallogel. The uniform embedding of these UCNPs into the metallogels and their transparency, particularly for the low amounts of NPs, can be seen from the naked eyes (Figure 5.6 a)). Expectedly, the transparency of these TiO_2 metallogels decreases on increasing NPs contents. Figure 5.6 b) shows the digital images of these UCNPs-embedded metallogels being irradiated with the 973 nm laser excitation thus confirming further the even distribution of upconverting nanoparticles.

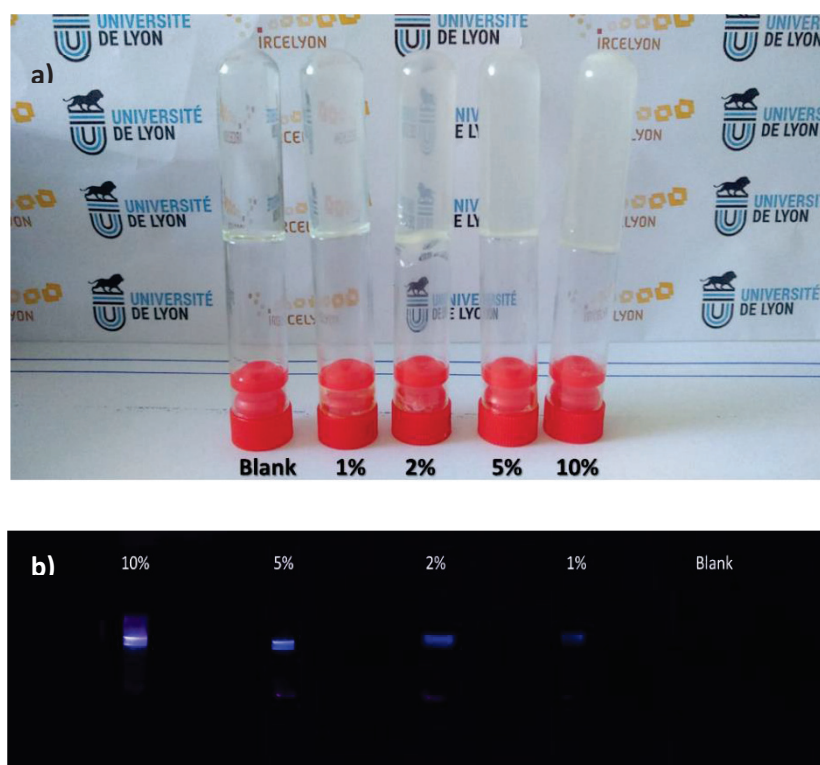


Figure 5.6: Blank and UCNPs-embedded TiO_2 metallogels synthesized using controlled hydrolysis and condensation of $\text{Ti}(\text{OEt})_4$ in the presence of varying amounts of $\text{LiY}_{5/6}\text{Yb}_{1/6}\text{F}_4: 0.4\% \text{Tm}^{3+}$ NPs (a). The varied intensity of Tm^{3+} luminescence with different doping percentage of up-converting $\text{LiY}_{5/6}\text{Yb}_{1/6}\text{F}_4: 0.4\% \text{Tm}^{3+}$ nanoparticles in TiO_2 metallogels (b). The nanoparticles are uniformly embedded in TiO_2 gel as observed from the output blue luminescence.

Characterization and surface properties of dried TiO₂-UCNPs xerogel

The obtained metallogels were dried by leaving them in the open air for 2 days. The as-dried undoped TiO₂ xerogel was amorphous as indicated by its powder XRD (Figure 5.7 a)). Its thermogravimetric analysis, performed in the air in the range of 25°C to 600°C with a heating rate of 5°C/min (Figure 5.7 b)), shows one step dehydration process. This loss in the mass (25.9%) can be attributed to the removal of coordinated/weakly adsorbed surface water and alcohol molecules as well as condensation of the hydroxyl groups to TiO₂. There is no further mass loss observed in the TGA curve after 300°C. The N₂ adsorption-desorption isotherm of this as-dried sample, pre-treated for 24 h at 100 °C under 10⁻³ Torr, is typical of mesoporous materials, with a significantly high BET surface area of 489 m²/g (Figure 5.7 c)). Subsequently, the as-dried undoped powder was calcined at different temperature (with a heating rate of 10°C/ min for 2h, following the natural cooling) to study the effect of calcination temperature on its crystallinity as well as surface properties. The powder XRD studies on these samples show that the powder remains amorphous till 200 °C, starts crystallizing before 300 °C and is completely crystallized at 400 °C. All the XRD peaks are indexed to the ICDD database file number 04-001-7641, which corresponds to the anatase phase of TiO₂. From the BET analysis of the non-calcined sample, it is evident that the amorphous gel network possesses small micro/mesopores, whose average size is found to be less than 4 nm. As expected, the calcined samples show relatively less surface area (336 m²/g and 127 m²/g for the samples calcined at 300°C and 400°C, respectively) due to shrinkage of the amorphous gel network into a well-arranged and dense crystalline arrangement of metal oxide nanoparticles. These changes also result in well-defined isotherms of type IV with the range of hysteresis increasing gradually with the calcination temperature (in the region 0.4 < P/P₀ < 0.8 for the sample calcined at 400 °C). The way the solvent molecules are removed from the TiO₂ molecular gels can significantly change the surface area of the sample. Similar to isotherms, the pore size distribution in the calcined samples also becomes more symmetrical, and shifted towards a larger size (Figure 5.7 d)). Also, some of the micropores observed in the as-dried xerogel are eliminated in the calcined samples.

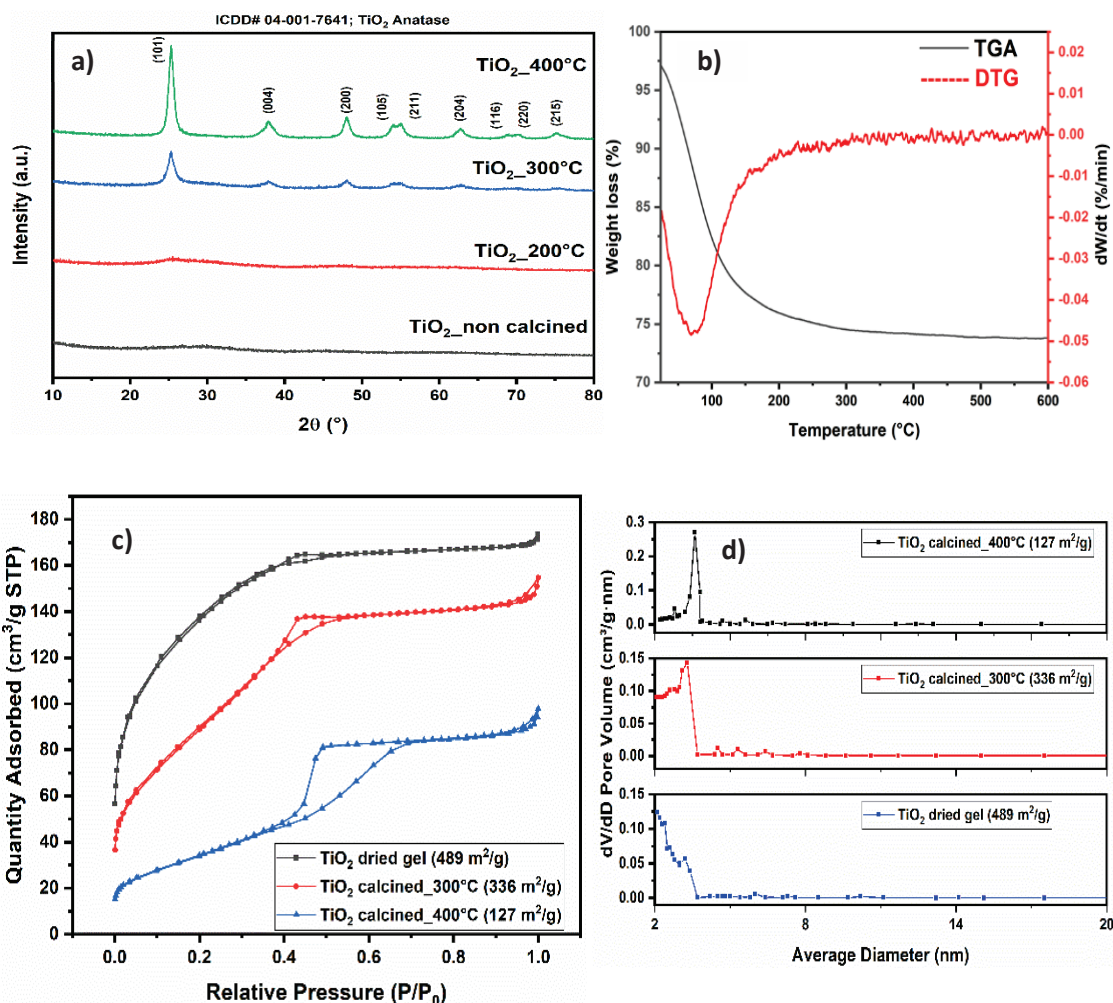


Figure 5.7: Characterization of undoped dried TiO₂ metallogel. Powder X-ray diffraction pattern of dried TiO₂ metallogel with and without heat treatment and evolution of its crystalline anatase form with an increase in calcination temperature from 200°C to 400°C (a). Thermogravimetric analysis (TGA) and differential thermogravimetric (DTG) curve of undoped TiO₂ dried gel (b). N₂ adsorption and desorption isotherms of dried microporous TiO₂ gel both in the calcined and non-calcined state with different surface areas (c), the distribution of pore volume with average pore diameter (d).

Following the above studies on undoped TiO₂ xerogel, we performed a similar characterization on UCNP-containing xerogels obtained by drying different UCNP-embedded metallogels. The powder XRD pattern of the as-dried and calcined xerogel samples containing maximum UCNP (i.e. 10% of LiY_{5/6}Yb_{1/6}F₄: 0.4% Tm³⁺) is given in Figure 5.8 a). As expected, the as-dried sample shows the diffraction peaks only for LiYF₄: Yb³⁺, Tm³⁺ due to the amorphous nature of TiO₂, whereas the sample calcined at 400 °C / 2 h exhibits XRD peaks characteristic of both LiYF₄ and TiO₂. Interestingly, there is a small percentage of YF₃ also in the sample, probably due to partial loss of volatile Lithium ions from the crystal sites. As compared to other alkali metals, lithium has a more covalent character and, therefore, more volatile. This is also one of the reasons why we took the lithium precursor in slight excess during the synthesis of LiY_{5/6}Yb_{1/6}F₄: 0.4% Tm³⁺ nanoparticles at high temperature (see Chapter 6 for experimental details). Interestingly, when the as-prepared LiY_{5/6}Yb_{1/6}F₄:

0.4% Tm^{3+} nanoparticles were calcined alone at 400 °C, they did not yield any YF_3 impurity (Figure 5.8 a)). This underlines the importance of the surrounding environment during the synthesis and treatment of lithium-based upconverting nanoparticles.

The N_2 adsorption-desorption isotherms (Figure 5.8 b)) of these as-dried UC NPs-embedded TiO_2 xerogels are quite similar to the isotherm obtained for the undoped TiO_2 xerogel. Even though the basic features of the obtained type IV isotherms remain unchanged, the BET surface area of these UC NPs-embedded TiO_2 xerogels, particularly for those with a smaller % of NPs, are even higher than that of the undoped TiO_2 sample. Thus, as compared to a surface area of 489 m^2/g obtained for the as-dried undoped TiO_2 , the as-dried TiO_2 xerogels with 1, 2 and 5% of UC NPs show BET surface area of 581, 548 and 564 m^2/g , respectively. The incorporation of the nanoparticles in the metallogel network provide additional surface and the total surface area of the embedded metallogel has a contribution from both the components. Because the gelification happens after the incorporation of UC NPs, there is no significant change in the characteristics of the NPs-embedded metallogels (as compared to undoped TiO_2 metallogel). It also ensures the homogeneous distribution of the upconverting nanoparticles, even though the average particle size of UC NPs is larger than the average pore size in the metallogel. A slightly less surface area of 436 m^2/g for the as-dried TiO_2 xerogel with 10% UC NPs is probably due to partial blocking of the pores of the network.

TEM studies were performed on the as-dried TiO_2 xerogels to understand the nature and stability of the interaction between the upconverting nanoparticles and TiO_2 . (Figure 5.8 c)) shows the TEM analysis and EDX spectroscopic studies on the as-dried 10% UCNP@ TiO_2 dried xerogel. The TEM images show the intimate mixing of amorphous titania and well crystalline upconverting nanoparticles. While the HRTEM image confirms the presence of (112) planes corresponding to tetragonal LiYF_4 , the presence of titanium is further confirmed by the EDX spectrum.

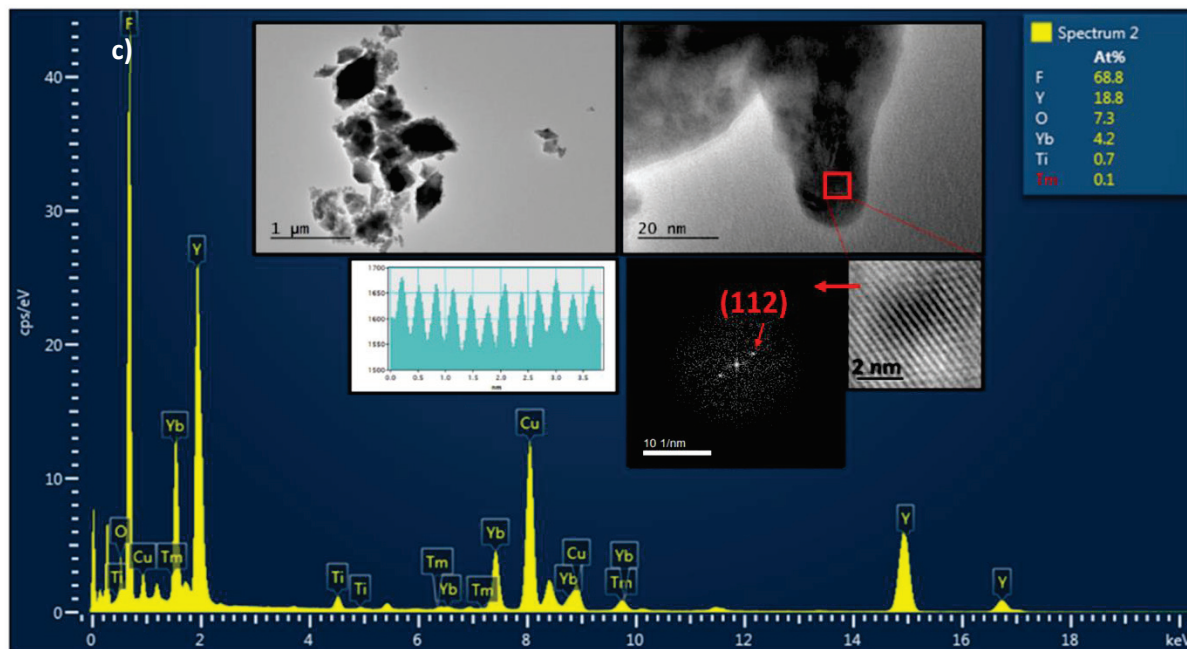
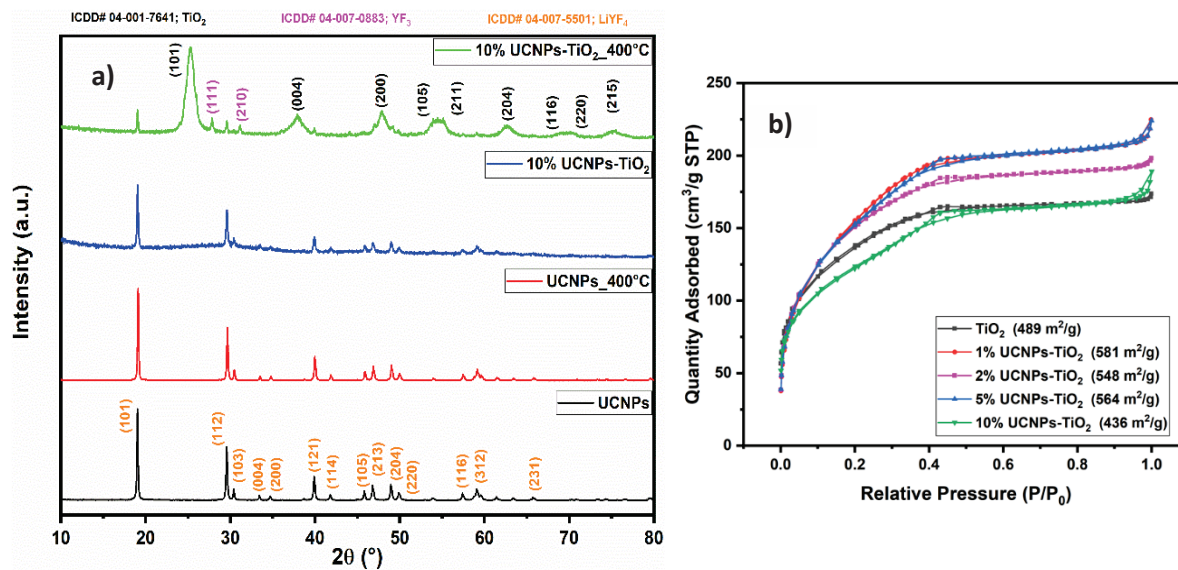


Figure 5.8: Characterization of UCNPs embedded TiO₂ metallogels. Powder X-ray diffraction pattern of Pure LiY_{5/6}Yb_{1/6}F₄: 0.4% Tm³⁺ and its composite with TiO₂ metallogel with and without heat treatment (a). N₂ adsorption and desorption isotherms of undoped TiO₂ dried gel and TiO₂ gels embedded with different percentages of LiY_{5/6}Yb_{1/6}F₄: 0.4% Tm³⁺ (b). TEM and EDX spectroscopic studies of 10% UCNP-TiO₂ sample before calcination of the dried gel. The HRTEM image shows lattice fringes corresponding to the (112) plane of tetragonal LiYF₄ (c).

5.2.2. Upconversion studies

We performed upconversion studies on these UCNPs-TiO₂ nanocomposites to evaluate their performance for their application for photocatalysis. In this regard, we first studied the upconversion properties of shell-core upconverting nanostructures (TiO₂@ LiY_{5/6}Yb_{1/6}F₄: 0.4% Tm³⁺) synthesized using different capping ligands (using CW laser excitation at 973 nm). These composites showed reduced upconversion emission intensity as compared to the non-coated LiY_{5/6}Yb_{1/6}F₄: 0.4% Tm³⁺ in the UV region of the upconversion spectrum. Here in the sample marked (a) was prepared using mdeaH₂ ligand whereas (b) was prepared using dmeaH ligand. The modification of bare upconverting nanoparticles with these ligands has certainly an impact on how the Ti precursor get attached to these nanoparticles. These spectra are normalized for ¹G₄ → ³F₄ transition. All the classical peaks for 4f-4f intra-band Tm³⁺ transitions are observed in the spectra but, the characteristic UV emission from ¹I₆ to ³H₄ (290 nm) was very prominent in the non-coated sample is completely absent in both of the TiO₂-coated samples. Also, the emission intensity at 348 nm, representing ¹I₆ to ³F₄ Tm³⁺ transition has been quenched significantly for both (a) and (b). On careful analysis of the coating of both the ligands (mdeaH₂ (a) and dmeaH (b)), as the distribution of TiO₂ on the surface of nanoparticle is more uniform in the case of coating using dmeaH (b), the probable transfer of energy to the TiO₂ is more efficient and this is evident by 5.1 times reduction in the emission intensity (Figure 5.9) compared to 2.8 times for mdeaH₂ (a). The other major peaks in the UV region (362 nm, concerning ¹D₂ to ³H₆ transition) have also observed reduced emission intensity (around 2.1 times for (a) and 2.4 times for (b)).

The reduction in the upconversion emission depends not only on the presence of titanium dioxide around them but also on the other phenomena such as i) presence of defects on the surface³⁸⁻⁴⁰; ii) presence of competing -OH groups on the surface⁴¹ and hence the quality of the nanoparticles can also be estimated by analysing the relative intensity of upconversion emission between different samples⁴². However, the absence of peaks at around 290 nm and the quenching of upconversion emission in other UV regions (348 nm (¹I₆ → ³F₄) and 362 nm (¹D₂ → ³H₄)) as well in the titania-coated samples justifies i) the relatively uniform presence of titania around the samples, and ii) the systematic non-radiative energy transfer from Tm³⁺ to titania².

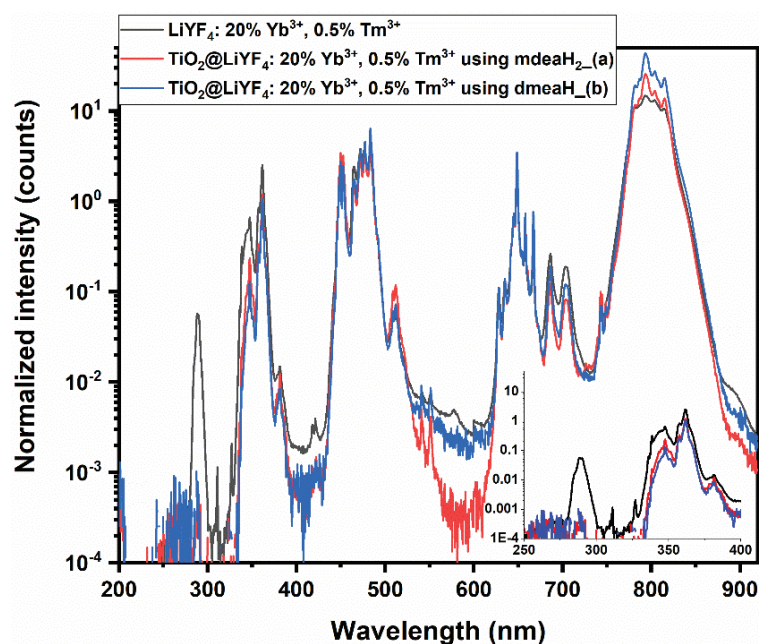


Figure 5.9: Up conversion emission studies for non-coated $\text{LiYF}_4:20\% \text{Yb}^{3+}, 0.5\% \text{Tm}^{3+}$ and titania coated $\text{LiYF}_4:20\% \text{Yb}^{3+}, 0.5\% \text{Tm}^{3+}$ using different ligands for functionalization, upon 972 nm CW laser excitation. These spectra are normalized with respect to ${}^1\text{G}_4 \rightarrow {}^3\text{F}_4 \text{Tm}^{3+}$ transition.

We also performed some quick and preliminary upconversion studies on both undoped TiO_2 dried gel and $\text{LiY}_{5/6}\text{Yb}_{1/6}\text{F}_4: 0.4\% \text{Tm}^{3+}$ doped TiO_2 dried gel. Figure 5.10 shows the upconversion spectra measured at two different excitation power densities of 973 nm CW laser. As the nature of bonding between the upconverting nanoparticles and TiO_2 can be varied after their thermal treatment, we calcined these dried powder *in situ*. At different power, we observe the characteristic thulium emission from UV to IR. At high power (20.8 W/cm^2), we even observe the deep UV emission at 290 nm corresponding to ${}^1\text{I}_6 \rightarrow {}^3\text{H}_6$ transitions of Tm^{3+} ions. We should note that this calcination was done *in situ* on a DSC600 heating/cooling stage from Linkam Corporation equipped with a sapphire window. We performed the initial measurement and then calcined the powder at 300 °C (the maximum temperature that we can reach *in situ* in our system) for 30 min. we then recorded the upconversion of the sample again without disturbing the arrangement of powder to keep uniformity while recording the spectrum for the later comparisons. In these spectra (normalized for ${}^1\text{G}_4 \rightarrow {}^3\text{F}_4$ transition), we noticed the decrease of upconversion emission intensity after the calcination step. At higher power (20.8 W/cm^2), the emission intensity at 348 nm, representing ${}^1\text{I}_6$ to ${}^3\text{F}_4$ of Tm^{3+} transition is reduced 2.9 times after the calcination of the sample. Also for 362 nm (concerning ${}^1\text{D}_2$ to ${}^3\text{H}_6$ of Tm^{3+} transition), the intensity has been lowered by 1.4 times after calcination. We observed a similar trend at lower excitation power also. This reduction in the upconversion emission intensity shows that after the

calcination step the interaction between the UCNP and TiO₂ becomes more efficient for the non-radiative transfer of energy from UCNP to TiO₂.

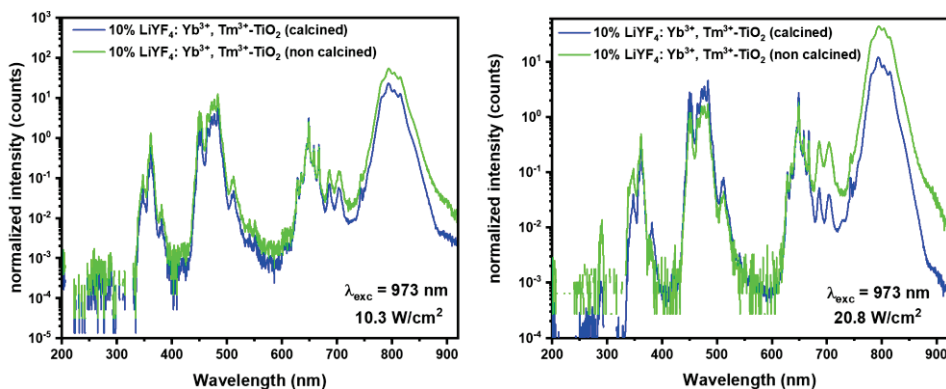


Figure 5.10: power variation upconversion emission studies for undoped TiO₂ dried gel and LiY_{5/6}Yb_{1/6}F₄: 0.4% Tm³⁺ doped TiO₂ samples upon 973 nm CW laser excitation. These spectra are normalized for ¹G₄ → ³F₄ Tm³⁺ transition.

5.2.3. Photocatalytic studies

We chose methylene blue dye as a model pollutant to evaluate the photocatalytic activities of undoped and LiY_{5/6}Yb_{1/6}F₄: 0.4% Tm³⁺ UCNP-doped TiO₂. Figure 5.11 shows the setup used for this photocatalytic test. A detailed description of the photocatalytic measurement is given in Chapter 6 experimental part.

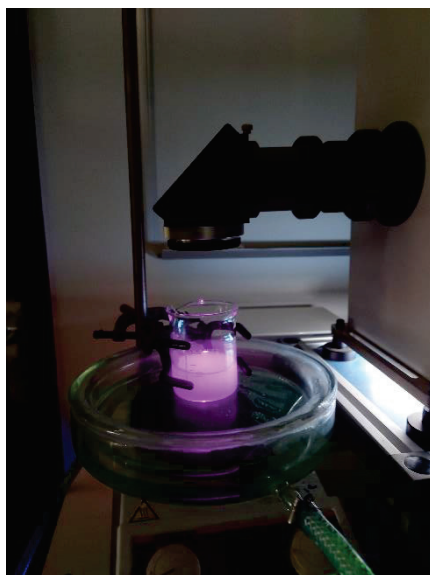


Figure 5.11: Experimental setup for degradation of methylene blue (MB).

For all these measurements, we chose a volume of 60 ml of an aqueous solution of methylene blue (15 mg/L) containing 30 mg of the catalysts (TiO₂ or UCNP-TiO₂ NPs calcined previously at 400 °C)

(0.5 g/L). The solution was first stirred for 12 h in dark to reach an adsorption-desorption equilibrium between the nanoparticles and the solution.⁴³ The extent of degradation of aliquots at different time interval was determined by analysing the UV-Vis spectra by measuring the solution's concentration using Beer-Lambert law.

From Figure 5.12 a), we observe the degradation behaviour of methylene blue aqueous solution under Xe lamp with infrared irradiation band (800 nm -2500 nm) using HWB-800 filter. First, we performed a blank experiment without any catalyst just to see the behaviour of methylene blue under only IR irradiation and, as expected we did not see any decrease in the MB concentration. Then photocatalytic behaviour of TiO₂ alone was observed and unexpectedly, we did see some reduction in MB concentration in the solution. Furthermore, with a different mixing ratio of UCNPs in TiO₂, we observe a significant reduction in the concentration of methylene blue. Figure 5.12(b) shows the relationship between $\ln(C_0/C)$ and time for 5% UCNPs-TiO₂, 10% UCNPs-TiO₂ and pure TiO₂ sample along with the reference MB dye sample, where C_0 is the initial concentration of MB and C is the concentration of the dye at time t . The curve for UCNPs-TiO₂ is nearly linear and the ratio of $\ln(C_0/C)$ increases at a nearly constant rate with increasing time. We can observe faster kinetics for methylene blue dye degradation compared to pure TiO₂. The performance of catalysts towards the degradation of methylene blue dye could be demonstrated by the respective rate constant considering the first-order kinetic degradation of MB. The first-order rate constants were calculated using the following equation:

$$\ln \frac{C_0}{C} = kt \quad (5.1)$$

Figure 5.12(e) shows the rate constant values for different catalysts. The 5% UCNPs-TiO₂ sample has a k value of 0.034 hour⁻¹ which is higher than 10% UCNPs-TiO₂ sample ($k = 0.021$ hour⁻¹). In 12h duration, 5% UCNPs-TiO₂ shows the degradation of nearly 35% of the dye concentration as against ~20% degradation by 10% UCNPs-TiO₂. These values show an enhanced photocatalytic activity for the 5% UCNPs-TiO₂ sample, probably due to its higher surface area (564 m²/g for as-dried sample) than that of the 10% UCNPs-TiO₂ sample (436 m²/g).

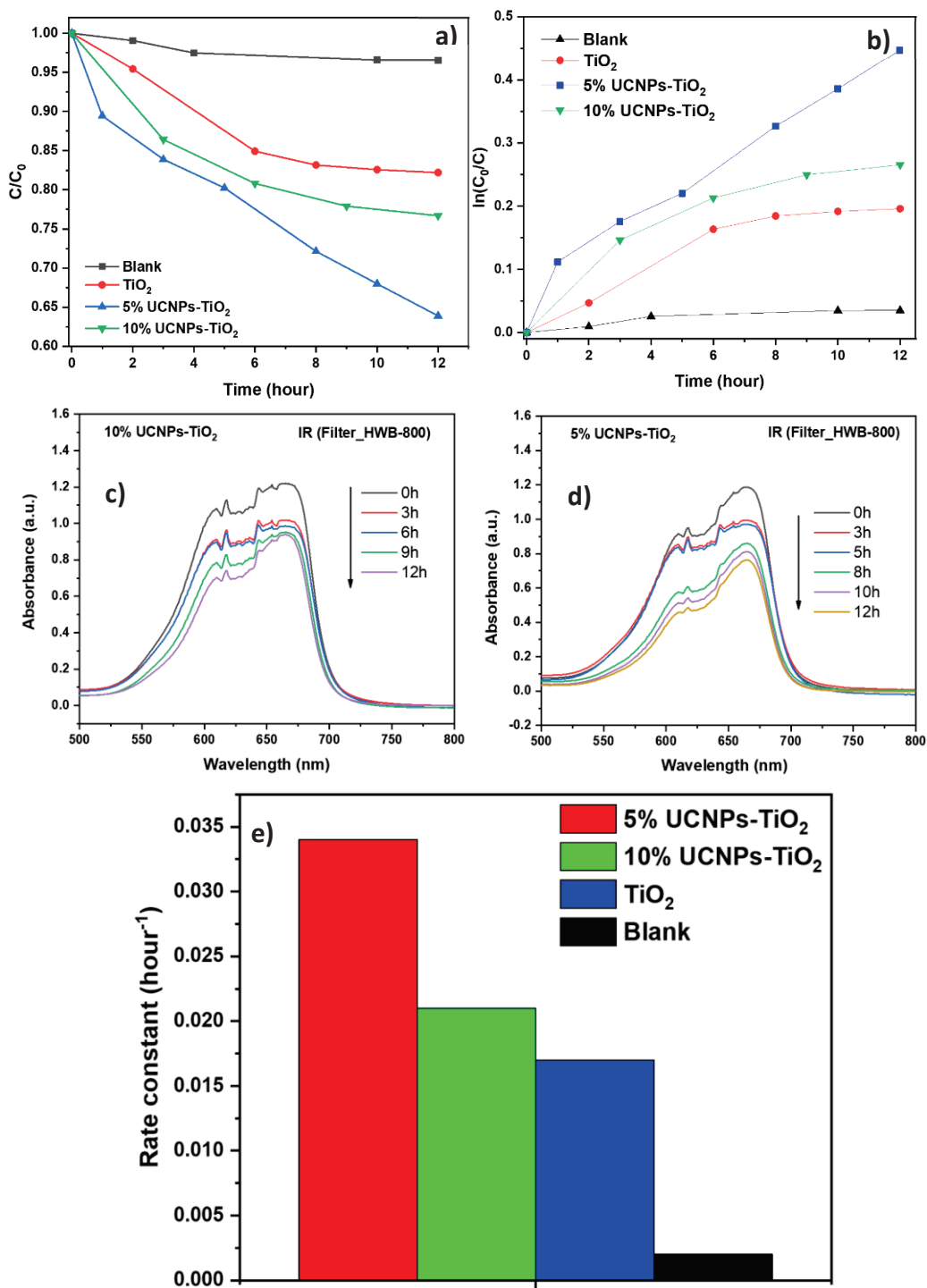


Figure 5.12: Photodegradation study of methylene blue shown by the relative change in concentration using Xe lamp under infrared irradiation band (above 800nm) (a). Natural logarithm of the ratio of initial concentration (C_0) and final concentration (C) for understanding degradation kinetics (b). UV-Vis absorption spectra showing degradation of methylene blue c) 10% UCNPs- TiO_2 and d) 5% UCNPs- TiO_2 nanocomposites. First-order rate constants, k (hour $^{-1}$), of different UCNPs- TiO_2 catalyst for the degradation of MB (e).

5.3. Conclusions and perspectives

These preliminary results show that the metallogel-strategy to obtain UCNPs-TiO₂ composites with high surface area and the desired crystalline phases of the components is an efficient, easy-to-scale up and viable alternative to the core-shell approach to get IR-active photocatalysts. These results also underline that small changes in the gelation conditions have a strong effect in terms of transparency of the metallogels as well as the surface area of the dried xerogels and that a subtle balance in terms of the ratio of the upconverting NPs and TiO₂ must be found to get most efficient photocatalysts. More studies are required for better optimization of these results. Hence, future work will be devoted to strategies to improve further the efficiencies of these photocatalysts by using a wider range of the solar spectrum, for example, by introducing in metallogel a suitable luminescent molecule that absorbs in the IR-region and therefore allows a broad absorption by acting as an antenna.

5.4. References

- (1) Schneider, J.; Matsuoka, M.; Takeuchi, M.; Zhang, J.; Horiuchi, Y.; Anpo, M.; Bahnemann, D. W. Understanding TiO₂ Photocatalysis: Mechanisms and Materials. *Chem. Rev.* **2014**, *114* (19), 9919–9986. <https://doi.org/10.1021/cr5001892>.
- (2) Chen, Y.; Mishra, S.; Ledoux, G.; Jeanneau, E.; Daniel, M.; Zhang, J.; Daniele, S. Direct Synthesis of Hexagonal NaGdF₄ Nanocrystals from a Single-Source Precursor: Upconverting NaGdF₄:Yb³⁺, Tm³⁺ and Its Composites with TiO₂ for Near-IR-Driven Photocatalysis. *Chemistry – An Asian Journal* **2014**, *9* (9), 2415–2421. <https://doi.org/10.1002/asia.201402347>.
- (3) Wang, W.; Ding, M.; Lu, C.; Ni, Y.; Xu, Z. A Study on Upconversion UV–Vis–NIR Responsive Photocatalytic Activity and Mechanisms of Hexagonal Phase NaYF₄: Yb³⁺, Tm³⁺@TiO₂ Core-Shell Structured Photocatalyst. *Applied Catalysis B: Environmental* **2014**, *144*, 379–385. <https://doi.org/10.1016/j.apcatb.2013.07.035>.
- (4) Zhang, Y.; Hong, Z. Synthesis of Lanthanide-Doped NaYF₄@TiO₂ Core-Shell Composites with Highly Crystalline and Tunable TiO₂ Shells under Mild Conditions and Their Upconversion-Based Photocatalysis. *Nanoscale* **2013**, *5* (19), 8930. <https://doi.org/10.1039/c3nr03051b>.
- (5) Tang, Y.; Di, W.; Zhai, X.; Yang, R.; Qin, W. NIR-Responsive Photocatalytic Activity and Mechanism of NaYF₄: Yb, Tm@TiO₂ Core-Shell Nanoparticles. *ACS Catal.* **2013**, *3* (3), 405–412. <https://doi.org/10.1021/cs300808r>.
- (6) Xu, D.-X.; Lian, Z.-W.; Fu, M.-L.; Yuan, B.; Shi, J.-W.; Cui, H.-J. Advanced Near-Infrared-Driven Photocatalyst: Fabrication, Characterization, and Photocatalytic Performance of β-NaYF₄: Yb³⁺, Tm³⁺@TiO₂ Core@shell Microcrystals. *Applied Catalysis B: Environmental* **2013**, *142–143*, 377–386. <https://doi.org/10.1016/j.apcatb.2013.05.062>.
- (7) Chen, Y.; Zou, L.; Zhang, X.; Huang, Q.; Yu, H. Sublattice Energy Cluster Construction for The Enhancement of NIR Photocatalytic Performance of LiYF₄: Tm@TiO₂. *ChemistrySelect* **2019**, *4* (14), 4262–4270. <https://doi.org/10.1002/slct.201900125>.
- (8) Wu, S.; Lv, J.; Wang, F.; Duan, N.; Li, Q.; Wang, Z. Photocatalytic Degradation of Microcystin-LR with a Nanostructured Photocatalyst Based on Upconversion Nanoparticles@TiO₂ Composite under Simulated Solar Lights. *Sci. Rep* **2017**, *7* (1), 14435. <https://doi.org/10.1038/s41598-017-14746-6>.

- (9) Zhang, D.; Zhao, D.; Zheng, K.; Liu, N.; Qin, W. Synthesis and Upconversion Luminescence of NaYF₄: Yb, Tm/TiO₂ Core/Shell Nanoparticles with Controllable Shell Thickness. *Journal of Nanoscience and Nanotechnology* **2011**, *11* (11), 9761–9764. <https://doi.org/10.1166/jnn.2011.5251>.
- (10) Su, W.; Zheng, M.; Li, L.; Wang, K.; Qiao, R.; Zhong, Y.; Hu, Y.; Li, Z. Directly Coat TiO₂ on Hydrophobic NaYF₄: Yb, Tm Nanoplates and Regulate Their Photocatalytic Activities with the Core Size. *J. Mater. Chem. A* **2014**, *2* (33), 13486–13491. <https://doi.org/10.1039/C4TA02756F>.
- (11) Lv, Y.; Yue, L.; Li, Q.; Shao, B.; Zhao, S.; Wang, H.; Wu, S.; Wang, Z. Recyclable (Fe₃O₄-NaYF₄: Yb, Tm) @TiO₂ Nanocomposites with near-Infrared Enhanced Photocatalytic Activity. *Dalton Trans.* **2018**, *47* (5), 1666–1673. <https://doi.org/10.1039/C7DT04279E>.
- (12) Pan, Y.; Feng, P.; Yin, M.; Fang, H.; Pan, C. Facile Synthesis of NaYF₄: Yb, Tm@TiO₂ Core-Shell Structured Composite with Enhanced Photocatalytic Activity for Degradation of RhB Dye. *ChemistrySelect* **2019**, *4* (38), 11346–11353. <https://doi.org/10.1002/slct.201902646>.
- (13) Sayevich, V.; Cai, B.; Benad, A.; Haubold, D.; Sonntag, L.; Gaponik, N.; Lesnyak, V.; Eychmüller, A. 3D Assembly of All-Inorganic Colloidal Nanocrystals into Gels and Aerogels. *Angewandte Chemie International Edition* **2016**, *55* (21), 6334–6338. <https://doi.org/10.1002/anie.201600094>.
- (14) Niederberger, M. Multiscale Nanoparticle Assembly: From Particulate Precise Manufacturing to Colloidal Processing. *Advanced Functional Materials* **2017**, *27* (47), 1703647. <https://doi.org/10.1002/adfm.201703647>.
- (15) Chen, G.; Damasco, J.; Qiu, H.; Shao, W.; Ohulchanskyy, T. Y.; Valiev, R. R.; Wu, X.; Han, G.; Wang, Y.; Yang, C.; Ågren, H.; Prasad, P. N. Energy-Cascaded Upconversion in an Organic Dye-Sensitized Core/Shell Fluoride Nanocrystal. *Nano Lett.* **2015**, *15* (11), 7400–7407. <https://doi.org/10.1021/acs.nanolett.5b02830>.
- (16) Daniel, G.-M. Polynuclear photocatalysts, a new generation? <https://mappingignorance.org/?p=6794/>.
- (17) Bogdan, N.; Vetrone, F.; Ozin, G. A.; Capobianco, J. A. Synthesis of Ligand-Free Colloidally Stable Water Dispersible Brightly Luminescent Lanthanide-Doped Upconverting Nanoparticles. *Nano Lett.* **2011**, *11* (2), 835–840. <https://doi.org/10.1021/nl1041929>.
- (18) Wilhelm, S.; Kaiser, M.; Würth, C.; Heiland, J.; Carrillo-Carrion, C.; Muhr, V.; Wolfbeis, O. S.; Parak, W. J.; Resch-Genger, U.; Hirsch, T. Water Dispersible Upconverting Nanoparticles: Effects of

Surface Modification on Their Luminescence and Colloidal Stability. *Nanoscale* **2015**, *7* (4), 1403–1410. <https://doi.org/10.1039/C4NR05954A>.

(19) Cozzoli, P. D.; Kornowski, A.; Weller, H. Low-Temperature Synthesis of Soluble and Processable Organic-Capped Anatase TiO₂ Nanorods. *J. Am. Chem. Soc.* **2003**, *125* (47), 14539–14548. <https://doi.org/10.1021/ja036505h>.

(20) Zhang, Z.; Zhong, X.; Liu, S.; Li, D.; Han, M. Aminolysis Route to Monodisperse Titania Nanorods with Tunable Aspect Ratio. *Angewandte Chemie International Edition* **2005**, *44* (22), 3466–3470. <https://doi.org/10.1002/anie.200500410>.

(21) Rojas-Gutierrez, P. A.; DeWolf, C.; Capobianco, J. A. Formation of a Supported Lipid Bilayer on Faceted LiYF₄:Tm³⁺/Yb³⁺ Upconversion Nanoparticles. *Particle & Particle Systems Characterization* **2016**, *33* (12), 865–870. <https://doi.org/10.1002/ppsc.201600218>.

(22) Liu, Y.; Moser, T.; Andres, C.; Gorjan, L.; Remhof, A.; Clemens, F.; Graule, T.; Tiwari, A. N.; Romanyuk, Y. E. Ethanolamine-Assisted Low-Temperature Crystallization of Hydroxide Nanoparticle Ink into Transparent and Conductive ITO Layers. *J. Mater. Chem. A* **2019**, *7* (7), 3083–3089. <https://doi.org/10.1039/C8TA09891C>.

(23) Porta, F.; Krpetić, Ž.; Prati, L.; Gaiassi, A.; Scari, G. Gold-Ligand Interaction Studies of Water-Soluble Aminoalcohol Capped Gold Nanoparticles by NMR. *Langmuir* **2008**, *24* (14), 7061–7064. <https://doi.org/10.1021/la8008392>.

(24) Ban, T.; Ohya, Y.; Takahashi, Y. Reaction of Titanium Isopropoxide with Alkanolamines and Association of the Resultant Ti Species. *Journal of Sol-Gel Science and Technology* **2003**, *27* (3), 363–372. <https://doi.org/10.1023/A:1024033423389>.

(25) Mishra, S.; Daniele, S. Molecular Engineering of Metal Alkoxides for Solution Phase Synthesis of High-Tech Metal Oxide Nanomaterials. *Chem. Eur. J.* **2020**, *26* (42), 9292–9303. <https://doi.org/10.1002/chem.202000534>.

(26) Kemmitt, T.; Al-Salim, N. I.; Gainsford, G. J. *N*-Methyldiethanolamine-Modified Titanium Isopropoxide: X-Ray Crystal Structure of [Ti₂(μ₂-(OCH₂CH₂)₂NCH₃)(μ₂-OPrⁱ)(OPrⁱ)₅]. *Aust. J. Chem.* **2002**, *55* (8), 513. <https://doi.org/10.1071/CH02087>.

- (27) Parra, R.; Góes, M. S.; Castro, M. S.; Longo, E.; Bueno, P. R.; Varela, J. A. Reaction Pathway to the Synthesis of Anatase via the Chemical Modification of Titanium Isopropoxide with Acetic Acid. *Chem. Mater.* **2008**, *20* (1), 143–150. <https://doi.org/10.1021/cm702286e>.
- (28) Odziomek, M.; Chaput, F.; Lerouge, F.; Dujardin, C.; Sitarz, M.; Karpati, S.; Parola, S. From Nanoparticle Assembly to Monolithic Aerogels of YAG, Rare Earth Fluorides, and Composites. *Chem. Mater.* **2018**, *30* (15), 5460–5467. <https://doi.org/10.1021/acs.chemmater.8b02443>.
- (29) Arnau del Valle, C.; Felip-León, C.; Angulo-Pachón, C. A.; Mikhailov, M.; Sokolov, M. N.; Miravet, J. F.; Galindo, F. Photoactive Hexanuclear Molybdenum Nanoclusters Embedded in Molecular Organogels. *Inorg. Chem.* **2019**, *58* (14), 8900–8905. <https://doi.org/10.1021/acs.inorgchem.9b00916>.
- (30) Felip-León, C.; Guzzetta, F.; Julián-López, B.; Galindo, F.; Miravet, J. F. Multimodal Light-Harvesting Soft Hybrid Materials: Assisted Energy Transfer upon Thermally Reversible Gelation. *J. Phys. Chem. C* **2017**, *121* (39), 21154–21159. <https://doi.org/10.1021/acs.jpcc.7b06441>.
- (31) Wadhavane, P. D.; Galian, R. E.; Izquierdo, M. A.; Aguilera-Sigalat, J.; Galindo, F.; Schmidt, L.; Burguete, M. I.; Pérez-Prieto, J.; Luis, S. V. Photoluminescence Enhancement of CdSe Quantum Dots: A Case of Organogel–Nanoparticle Symbiosis. *J. Am. Chem. Soc.* **2012**, *134* (50), 20554–20563. <https://doi.org/10.1021/ja310508r>.
- (32) Segarra-Maset, M. D.; Nebot, V. J.; Miravet, J. F.; Escuder, B. Control of Molecular Gelation by Chemical Stimuli. *Chem. Soc. Rev.* **2013**, *42* (17), 7086–7098. <https://doi.org/10.1039/C2CS35436E>.
- (33) Konishi, J.; Fujita, K.; Nakanishi, K.; Hirao, K. Monolithic TiO₂ with Controlled Multiscale Porosity via a Template-Free Sol–Gel Process Accompanied by Phase Separation. *Chem. Mater.* **2006**, *18* (25), 6069–6074. <https://doi.org/10.1021/cm0617485>.
- (34) El Mir, L.; Amlouk, A.; Elaloui, E.; Saadoun, M.; Pierre, A. C. Preparation and Optical Characterization of Transparent, Microporous TiO₂ Xerogel Monoliths. *Materials Science and Engineering: B* **2008**, *146* (1), 69–73. <https://doi.org/10.1016/j.mseb.2007.07.055>.
- (35) Isley, S. L.; Penn, R. L. Relative Brookite and Anatase Content in Sol–Gel-Synthesized Titanium Dioxide Nanoparticles. *J. Phys. Chem. B* **2006**, *110* (31), 15134–15139. <https://doi.org/10.1021/jp061417f>.
- (36) Alphonse, P.; Varghese, A.; Tendero, C. Stable Hydrosols for TiO₂ Coatings. *J Sol-Gel Sci Technol* **2010**, *56* (3), 250–263. <https://doi.org/10.1007/s10971-010-2301-y>.

- (37) Balushev, S.; Nelles, G.; Landfester, K.; Miteva, T. Sun-Light Upconversion in Multi-Component Organic Systems: Development towards Application for Solar Cells Outcome Enhancement; Tsakalakos, L., Ed.; San Diego, California, USA, **2012**; p 84710E. <https://doi.org/10.1117/12.928929>.
- (38) Wang, F.; Wang, J.; Liu, X. Direct Evidence of a Surface Quenching Effect on Size-Dependent Luminescence of Upconversion Nanoparticles. *Angewandte Chemie International Edition* **2010**, *49* (41), 7456–7460. <https://doi.org/10.1002/anie.201003959>.
- (39) Bian, W.; Lin, Y.; Wang, T.; Yu, X.; Qiu, J.; Zhou, M.; Luo, H.; Yu, S. F.; Xu, X. Direct Identification of Surface Defects and Their Influence on the Optical Characteristics of Upconversion Nanoparticles. *ACS Nano* **2018**, *12* (4), 3623–3628. <https://doi.org/10.1021/acsnano.8b00741>.
- (40) Mai, H.-X.; Zhang, Y.-W.; Sun, L.-D.; Yan, C.-H. Highly Efficient Multicolor Up-Conversion Emissions and Their Mechanisms of Monodisperse NaYF₄: Yb, Er Core and Core/Shell-Structured Nanocrystals. *J. Phys. Chem. C* **2007**, *111* (37), 13721–13729. <https://doi.org/10.1021/jp073920d>.
- (41) Wilhelm, S.; Kaiser, M.; Würth, C.; Heiland, J.; Carrillo-Carrion, C.; Muhr, V.; Wolfbeis, O. S.; Parak, W. J.; Resch-Genger, U.; Hirsch, T. Water Dispersible Upconverting Nanoparticles: Effects of Surface Modification on Their Luminescence and Colloidal Stability. *Nanoscale* **2015**, *7* (4), 1403–1410. <https://doi.org/10.1039/C4NR05954A>.
- (42) Sun, Y.; Chen, Y.; Tian, L.; Yu, Y.; Kong, X.; Zeng, Q.; Zhang, Y.; Zhang, H. Morphology-Dependent Upconversion Luminescence of ZnO: Er³⁺ Nanocrystals. *Journal of Luminescence* **2008**, *128* (1), 15–21. <https://doi.org/10.1016/j.jlumin.2007.04.011>.
- (43) Houas, A. Photocatalytic Degradation Pathway of Methylene Blue in Water. *Applied Catalysis B: Environmental* **2001**, *31* (2), 145–157. [https://doi.org/10.1016/S0926-3373\(00\)00276-9](https://doi.org/10.1016/S0926-3373(00)00276-9).

Chapter 6 Experimental

6.1. Chemicals and general instrumentation procedures

All the syntheses were carefully carried out in an argon atmosphere using standard Schlenk lines and glovebox techniques. During the synthesis of anhydrous precursors, the solvents used were dried with the help of MB SPS-800 and used without any further purifications. The chemicals (in bracket their supplier) such as Gadolinium oxide (Gd_2O_3 ; Alfa Aesar), Ytterbium oxide (Yb_2O_3 ; Strem Chemicals), Yttrium oxide (Y_2O_3 ; Strem Chemicals), Thulium oxide (Tm_2O_3 ; Strem Chemicals), Yttrium nitrate ($Y(NO_3)_3 \cdot 4H_2O$; Prolabo), Ytterbium nitrate ($Yb(NO_3)_3 \cdot 5H_2O$; Sigma Aldrich), Gadolinium nitrate ($Gd(NO_3)_3 \cdot 6H_2O$; Sigma Aldrich), Thulium nitrate ($Tm(NO_3)_3 \cdot 5H_2O$; Sigma Aldrich), Sodium nitrate ($NaNO_3$; Sigma Aldrich), Ammonium fluoride (NH_4F ; Sigma Aldrich), trifluoroacetic acid (TFA-H; Sigma Aldrich), Lithium trifluoroacetate ($LiTFA \cdot H_2O$; Strem Chemicals), Lithium hydroxide ($LiOH \cdot H_2O$; Alfa Aesar), Dimethoxyethane (anhydrous monoglyme; Sigma Aldrich), di(2-methoxyethyl)ether (diglyme; Sigma Aldrich), anhydrous ethanol (EtOH; Carlo Erba), oleic acid ($C_{18}H_{34}O_2$; 90%, Alfa Aesar), Oleylamine ($C_{18}H_{35}NH_2$; Alfa Aesar), 1-Octadecene ($C_{18}H_{36}$; 90%, Acros organics), ethylene glycol ($(CH_2OH)_2$; Sigma Aldrich) were used without any further purification. These chemicals were opened carefully around the argon atmosphere to minimize the risk of contamination due to moisture and then sealed with parafilm after use.

1H NMR spectra were recorded in $CDCl_3$ on a Bruker AC-300 spectrometer. The infrared spectra were obtained as Nujol mulls on a Bruker Vector 22 FT-IR spectrometer at room temperature and registered from 4000 to 400 cm^{-1} . TEM experiments were performed using a JEM-2100HT at 200 kV. We used a Bruker D8 Advance A25 with $Cu\ K\alpha_1 + 2$ ($\lambda = 0.154184\text{ nm}$) to measure the X-ray diffraction (XRD) patterns of the powdered crystals. During XRD, for the gadolinium sample, we used a special discrimination window to reduce the autofluorescence. The nitrogen adsorption and desorption isotherms were measured using an ASAP 2020 system. We employed the linear part of the Brunauer-Emmett-Teller (BET) method to calculate the specific surface area of these nanocomposites, while the Barrett-Joyner-Halenda (BJH) method provided their pore size distribution. Thermogravimetric analyses (TGA) were performed with a TGA/differential scanning calorimetry 1 STARE system from Mettler Toledo. For anhydrous precursors, around 5-10 mg of the sample was sealed in a 100 μL aluminium crucible in the glovebox and heated under an argon atmosphere at a heating rate of $5\text{ }^\circ\text{C}/\text{min}$, whereas for the powder samples, around 5-10 mg sample taken in an alumina crucible and heated in air or argon at a constant heating rate of $5\text{ }^\circ\text{C}/\text{min}$.

For the measurement of temperature variation upconversion studies, the sample was placed on a heating/cooling stage from LINKAM Ltd. DSC600, which allowed one to vary the temperature from -190°C up to 300°C using liquid nitrogen and a small built-in furnace. The stage is well covered and sealed with a sapphire window, to reduce the interference of moisture and other impurities.

X-ray crystallography: Crystals of molecular complexes **2**, **4** and **6** were obtained as described in the synthetic procedure. Crystal structures were determined using molybdenum radiation ($\lambda = 0.71073 \text{ \AA}$) on an Oxford Diffraction Gemini diffractometer equipped with an Atlas CCD. Intensities were collected at 200, 100 and 150 K for **2**, **4** and **6**, respectively, using CrysAlisPro software.¹ Reflection indexing, unit-cell parameter refinement, Lorentz-polarization correction, peak integration, and background determination were carried out with CrysAlisPro software.² An analytical absorption correction was applied using the modelled faces of the crystal.² The resulting sets of hkl were used for structure solutions and refinements. The structures were solved with the ShelXT³ structure solution program using intrinsic phasing and by using Olex2⁴ as the graphical interface. The model was refined with version 2018/3 of ShelXL⁵ using least-squares minimization. Some selected crystallographic and refinement data of the molecular complexes **2**, **4** and **6** are listed in Table 6.1.

Table 6.1: Crystallographic and refinement data for complexes 2, 4 and 5.

Compound	2	4	6
Formula	C ₆ H ₈ F ₃ LiO ₃	C ₄₂ HO ₁₄ F ₃₀ Gd ₂	C ₂₀ H ₂₀ F ₁₈ O ₁₆ Yb ₂
$D_{calc.}/g\text{ cm}^{-3}$	1.426	2.238	2.328
μ/mm^{-1}	0.147	3.941	5.574
Formula Weight	192.06	1172.5	1204.44
Size/mm ³	0.88×0.23×0.05	0.24×0.11×0.07	0.16×0.07×0.05
Temperature	200 K	100 K	150 K
Crystal System	triclinic	monoclinic	monoclinic
Space Group	<i>P</i> -1	<i>C</i> 2/ <i>c</i>	<i>C</i> 2/ <i>c</i>
<i>a</i> (Å)	5.3762(8)	12.4542(17)	12.3526(9)
<i>b</i> (Å)	8.5920(15)	16.5298(18)	16.4467(10)
<i>c</i> (Å)	10.1685(13)	17.658(2)	17.7047(13)
α (°)	100.357(13)	90	90
β (°)	104.038(13)	106.761(14)	107.167(8)
γ (°)	90.957(13)	90	90
$V(\text{Å}^3)$	447.36(12)	3480.7(8)	3436.6(4)
<i>Z</i>	2	4	4
<i>Z'</i>	1	0.5	0.5
Measured Refl's.	15508	22471	44587
Ind't Refl's	2317	4447	4615
Refl's with $I > 2(I)$	1338	3531	4141
R_{int}	0.0398	0.0673	0.0608
Parameters	184	283	284
Restraints	66	93	75
Largest Peak	0.358	2.929	1.768
Deepest Hole	-0.215	-2.025	-2.261
Goof	1.066	1.081	1.213
wR_2 (all data)	0.2818	0.1359	0.1085
wR_2	0.2373	0.1133	0.1009
R_1 (all data)	0.1176	0.0701	0.0492
R_1	0.0771	0.0482	0.0422

6.2. Experimental setup

6.2.1. Upconversion measurements

The up-conversion studies were carried out using a homemade spectrofluorometer on dried and properly ground powders, which were placed on a sample holder with utmost care to ensure a flat and uniform deposition. The samples were irradiated with a continuous wave (CW) laser at 972 nm which was focused to a square spot of $1 \times 1\text{ mm}^2$ on the sample with quasi-top-hat energy distribution. The emitted signal was then collected using Jobin-Yvon (TRIAX 320) monochromator equipped with automatic order removing filters and coupled to a cooled photomultiplier (Hamamatsu R943-02). The

signal from the photomultiplier was sent to an SR400 counting module from Stanford Research Systems.

To measure the upconversion quantum yield, the chosen Ln³⁺-doped NaGdF₄ and LiYF₄ samples were placed in an integrating sphere (IS200-4 from Thorlabs) and excited from above with one end of the sphere connected to the detection system. To ensure that the detection system obtains the absolute response at each wavelength, it was calibrated using an Oriel QT 63358 tungsten lamp traceable by NIST over the range 250–1000 nm. To determine the absorption of 972 nm photons by the above samples, an undoped NaGdF₄ and LiYF₄ were prepared under identical conditions. The difference in laser scattering compared to doped and undoped samples gave us an estimate of the actual absorption of the laser by the sample. Thus, the actual number of absorbed photons (respective energy absorbed) and the actual number of emitted photons (respective energy emitted) were measured over the wavelength range from 250 nm to 1000 nm. The quantum up-conversion efficiency (energy conversion efficiency) is the ratio of emitted photons (emitted power) to absorbed photons (absorbed power).

6.2.2. Photocatalysis setup

Photocatalysis measurement for the degradation of methylene blue was done under only visible and only infrared radiation using different filters on a standard Xenon lamp from CEALIGHT CEL-S500 which has the spectral distribution ranging from 300 nm to 2500 nm. We used the HWB-800 filter for infrared only transmission. For the photocatalytic degradation, as shown in Figure 5.11, the sample was placed beneath the lamp in a glass beaker with continuous stirring in the air. The distance between the source and the sample was always kept constant for all the measurements, to make it easy for comparison. The setup was well covered with a black box in a dark room to limit the interference of any other source of light. The sample was placed on a water-jacketed glass platform to keep the temperature of the solution constant during the photocatalysis reaction. During the photocatalysis experiment, a small amount (1 ml) of sample is taken out at different time intervals and their UV-Vis spectra were measured using Agilent 8453 spectrometer.

6.3. Synthesis of anhydrous precursors

The single-source precursors [NaLn(TFA)₄(diglyme)] (Ln = Gd, Tm, Yb; TFA = trifluoroacetate), were prepared using the method presented in the previous publications by our group^{6,7}. The anhydrous lithium and lanthanide trifluoroacetate precursors for lithium-based upconverting nanoparticles were synthesized using two different strategies. The first strategy involves ligand exchange of the water molecules in Li(TFA)(H₂O) and Ln(TFA)₃(H₂O)₃ with monoglyme ligand (method A). The second method of the synthesis involves refluxing of lanthanide oxides in monoglyme (for Y)

or a mixture of monoglyme + THF (for Gd, Tm and Yb), followed by crystallization by layering the concentrated mother solution with diethyl ether or any other suitable solvent (method B).

6.3.1. Method A

[Li(TFA)(monoglyme)] (1):

For the synthesis of **(1)**, we dissolved 0.28 g (2 mmol) of commercial Li(TFA)(H₂O) in 1 ml of monoglyme (9.3 mmol) and stirred the solution for 2 hr. The obtained clear solution was concentrated to a minimum amount and carefully layered with diethylether (Et₂O) to obtain colourless crystals of **1**. Yield, 0.36 g (86%). Anal. Calcd. for C₆H₁₀F₃LiO₄ (210): C, 34.28; H, 4.76; Found: C, 33.78; H, 4.61%. FT-IR (Nujol, cm⁻¹): 1704 (s) (ν_{as}CO₂), 1462 (s), 1372 (s), 1208 (w), 1147 (s) (νC–F, νC–O), 1072 (w), 1052 (w), 894 (w), 851 (m), 803 (s), 726 (s), 606 (w), 522 (w). ¹H NMR (CDCl₃, ppm): δ 3.28 (s, 6 H, CH₃), 3.46 (t, 4 H, CH₂).

[Li(TFA)(THF)] (2):

When Li(TFA)(H₂O) (0.577 g, 4.2 mmol) was dissolved in a mixture of THF and monoglyme (5 ml each), followed by crystallization by layering with Et₂O, it afforded colourless crystals of **2**. Yield, 0.63 g (78%). Anal. Calcd. for C₆H₈F₃LiO₃ (192.1): C, 37.48; H, 4.16; Found: C, 37.0; H, 4.05%. FT-IR (Nujol, cm⁻¹): 1702 (s) (ν_{as}CO₂), 1459 (s), 1378 (s), 1207 (w), 1145 (s) (νC–F, νC–O), 1054 (s), 894 (w), 853 (m), 804 (s), 724 (s), 607 (w), 520 (w). ¹H NMR (CDCl₃, ppm): δ 1.85 (t, 4 H, β-H of THF), 3.68 (t, 4 H, α-H of THF).

[Y(TFA)₃(monoglyme)] (3):

Y(TFA)₃(H₂O)₃ (0.25 g, 0.52 mmol) was stirred in 1 ml monoglyme for 2 h followed by crystallization by carefully layering with Et₂O. Yield, 0.21 g (78%). Anal. Calcd. for C₁₀H₁₀F₉O₈Y (518): C, 23.17; H, 1.93; Found: C, 23.34; H, 2.05%. FT-IR (Nujol, cm⁻¹): 1756 (s), 1676 (m), 1648 (w) (ν_{as}CO₂), 1460 (s), 1377 (s), 1207 (s), 1150 (s) (νC–F, νC–O), 1020 (m), 921 (w), 868 (m), 851 (m), 797 (s), 720 (s), 612 (s), 522 (s), 463 (m), 439 (m) (νM–O). ¹H NMR (CDCl₃, ppm): δ 3.28 (s, 6 H, CH₃), 3.46 (t, 4 H, CH₂).

By adopting the similar procedure as described for **3**, complexes [Gd(TFA)₃(monoglyme)] (**4**), [Tm(TFA)₃(monoglyme)] (**5**) and [Yb(TFA)₃(monoglyme)] (**6**) were also synthesized using appropriate quantity (given below in parentheses) of Ln(TFA)₃(H₂O)₃ (Ln = Gd, Tm and Yb) in a mixture of monoglyme and THF and crystallized by layering the concentrated mother solution with Et₂O.

[Gd(TFA)₃(monoglyme)] (4):

Gd(TFA)₃(H₂O)₃ (1.16 g, 2.12 mmol) in monoglyme (0.5 ml, 4.8 mmol) and 5 ml THF). Yield, 1.1 g (86%). Anal. Calcd. for C₁₀H₁₀F₉GdO₈ (586.2): C, 20.47; H, 1.70; Found: C, 20.17; H, 1.61%. FT-IR (Nujol, cm⁻¹): 1712 (s), 1625 (w), (ν_{as}CO₂), 1459 (s), 1376 (s), 1209 (m), 1148 (m) (νC–F, νC–O), 1052 (m), 867 (w), 845 (m), 799 (s), 722 (s), 608 (s), 522 (m), 455 (m) (νM–O).

[Tm(TFA)₃(monoglyme)] (5):

Tm(TFA)₃(H₂O)₃ (0.4 g, 0.7 mmol) in monoglyme (5 ml) and THF (5 ml). Yield, 0.35 g (82%). Anal. Calcd. for C₁₀H₁₀F₉O₈Tm (598): C, 20.1; H, 1.67; Found: C, 19.91; H, 1.61%. FT-IR (Nujol, cm⁻¹): 1742 (w), 1711 (s), 1674 (w), (ν_{as}CO₂), 1463 (s), 1376 (s), 1209 (w), 1150 (w), 1105 (w) (νC–F, νC–O), 1052(m), 1025 (w), 872 (s), 848 (s), 797 (s), 722 (s), 611 (s), 523 (s), 459 (m), 438 (m) (νM–O).

[Yb(TFA)₃(monoglyme)] (6):

Yb(TFA)₃(H₂O)₃ (0.5 g, 0.88 mmol) in a mixture of monoglyme (0.35 ml, 3.3 mmol) and THF (5 ml). Yield, 0.42 g (80%). Anal. Calcd. for C₁₀H₁₀F₉O₈Yb (603): C, 19.90; H, 1.66; Found: C, 19.83; H, 1.61%. FT-IR (Nujol, cm⁻¹): 1743 (w), 1715 (s), 1676 (w), (ν_{as}CO₂), 1454 (s), 1377 (s), 1206 (s), 1149 (m), 1105 (w) (νC–F, νC–O), 1050(w), 1025 (w), 873 (m), 848 (m), 798 (s), 722 (s), 610 (s), 522 (s), 459 (m), 438 (m) (νM–O).

6.3.2. Method B for the synthesis of (3)-(6)

Alternatively, the anhydrous lanthanide derivatives (3)-(6) could also be synthesized by a one-pot reaction of Ln₂O₃ with trifluoroacetic acid under reflux in a mixture of monoglyme and THF. As mentioned earlier, the coordinating solvent THF, which promotes the formation of [Y(TFA)₃(THF)₂], needs to be avoided for the synthesis of the yttrium complex (3). For other complexes (4)-(6), the presence of THF has no adverse effects. Due to the similarity of the synthetic procedure, the synthesis of only yttrium complex (3) is described in detail below:

[Y(TFA)₃(monoglyme)] (3):

A reaction mixture containing Y₂O₃ (0.5 g, 2.2 mmol), trifluoroacetic acid (1.1 ml, 14.4 mmol) and monoglyme (20 ml) was refluxed for 12 h at 85 °C. After cooling and filtering the reaction mixture, the filtrate was concentrated and layered carefully with diethyl ether to obtain colourless crystals in a 75% yield. The elemental analyses and the FT-IR spectra of (3)-(6) isolated by method B were consistent with the same products isolated by method A.

6.4. Synthesis of sodium-based UCNPs

6.4.1. Using anhydrous precursors

A typical method of preparing undoped NaGdF₄ nanoparticles involved taking the precursor [NaGd(TFA)₄(diglyme)] in 4 ml of 1-octadecene (or a mixture of 2 ml each of ODE + OM or ODE + OA) to obtain solution A, which was then kept at 120 °C for 1 h to obtain a clear and homogeneous solution. In parallel, 6 ml of 1-octadecene (or a mixture of 3 ml each of ODE + OM or ODE + OA) was purged with argon and heated to 290 °C (solution B). When the temperature became constant at 290 °C for solution B, the pre-heated solution A (at 120 °C) was injected all at once. The reaction mixture was then stirred at 290 °C for 1 h. It was then gradually cooled down to room temperature under a constant flow of argon. To collect the nanocrystals, ethanol was added as a precipitating agent, followed by centrifugation at 4500 rpm for 5 min. The resulting powder was washed three times with ethanol to remove any organic impurities and then air-dried at room temperature for 24 h.

To prepare doped NaGdF₄ nanoparticles, the precursors of Gd, Tm and Yb were taken in an appropriate amount and decomposed simultaneously. Table 6.2 and Table 6.3 summarize the amount of precursors used to synthesize NaGdF₄: x% Yb, y% Tm_{anhyd} in the mixture of 1-octadecene and oleylamine (Table 6.2) and 1-octadecene and oleic acid (Table 6.3), respectively.

Table 6.2: Synthesis of NaGdF₄: x% Yb³⁺, y% Tm³⁺_{anhyd} in the mixture of 1-octadecene and oleylamine

Sample	Reagents	Amount taken (g)	Millimoles taken
NaGd _{5/6} Yb _{1/6} F ₄ : 0.4% Tm	[NaGd(TFA) ₄ (diglyme)]	1.780	2.30
	[NaYb(TFA) ₄ (diglyme)]	0.362	0.46
	[NaTm(TFA) ₄ (diglyme)]	0.009	0.011
NaGd _{5/6} Yb _{1/6} F ₄ : 0.8% Tm	[NaGd(TFA) ₄ (diglyme)]	1.220	1.59
	[NaYb(TFA) ₄ (diglyme)]	0.250	0.32
	[NaTm(TFA) ₄ (diglyme)]	0.012	0.015
NaGd _{5/6} Yb _{1/6} F ₄ : 1.2% Tm	[NaGd(TFA) ₄ (diglyme)]	1.025	1.33
	[NaYb(TFA) ₄ (diglyme)]	0.201	0.25
	[NaTm(TFA) ₄ (diglyme)]	0.015	0.019
NaGd _{2/3} Yb _{1/3} F ₄ : 0.3% Tm	[NaGd(TFA) ₄ (diglyme)]	0.827	1.07
	[NaYb(TFA) ₄ (diglyme)]	0.430	0.55
	[NaTm(TFA) ₄ (diglyme)]	0.004	0.005
NaGd _{2/3} Yb _{1/3} F ₄ : 0.6% Tm	[NaGd(TFA) ₄ (diglyme)]	0.620	0.80
	[NaYb(TFA) ₄ (diglyme)]	0.316	0.40
	[NaTm(TFA) ₄ (diglyme)]	0.006	0.007

Table 6.3: Synthesis of NaGdF₄: x% Yb³⁺, y% Tm³⁺_anhyd in the mixture of 1-octadecene and oleic acid

Sample	Reagents	Amount taken (g)	Millimoles taken
NaGd _{5/6} Yb _{1/6} F ₄ : 1% Tm	[NaGd(TFA) ₄ (diglyme)]	0.918	1.19
	[NaYb(TFA) ₄ (diglyme)]	0.018	0.23
	[NaTm(TFA) ₄ (diglyme)]	0.011	0.014
NaGd _{3/4} Yb _{1/4} F ₄ : 1% Tm	[NaGd(TFA) ₄ (diglyme)]	1.471	1.91
	[NaYb(TFA) ₄ (diglyme)]	0.464	0.593
	[NaTm(TFA) ₄ (diglyme)]	0.015	0.019
NaGd _{2/3} Yb _{1/3} F ₄ : 1% Tm	[NaGd(TFA) ₄ (diglyme)]	0.716	0.934
	[NaYb(TFA) ₄ (diglyme)]	0.353	0.451
	[NaTm(TFA) ₄ (diglyme)]	0.010	0.012

6.4.2. Using hydrous precursors

For the preparation of doped NaGdF₄ nanoparticles using hydrated inorganic salts, we prepared two different ethylene glycol solutions. Solution A consists of appropriate amounts of Gd(NO₃)₃, Yb(NO₃)₃, Tm(NO₃)₃ and NaNO₃ in 10 ml of ethylene glycol, and solution B consists of an appropriate amount of NH₄F in 20 ml of ethylene glycol. Solution A, containing all the nitrate precursors, was then added dropwise to solution B with vigorous stirring. This mixture was then stirred for 3 h at room temperature, producing a transparent colloidal suspension. Finally, the NaGdF₄: x% Yb³⁺, y% Tm³⁺ nanoparticles were collected by centrifugation (5000 rpm, 10 min), and further washed three times with ethanol and deionized water to remove any impurities. The resulting powder was then dried overnight at room temperature. The synthetic details of NaGdF₄ NPs doped with different amount of Yb³⁺ and Tm³⁺ ions are summarized in Table 6.4.

Table 6.4: The amount of precursors used to synthesize NaGdF_4 : $x\% \text{Yb}^{3+}$, $y\% \text{Tm}^{3+}$ in ethylene glycol at room temperature.

Sample	Reagents	Amount taken (g)	Millimoles taken
NaGd _{5/6} Yb _{1/6} F ₄ : 0.4% Tm	Gd(NO ₃) ₃ .6H ₂ O	0.2	0.44
	Yb(NO ₃) ₃ .5H ₂ O	0.04	0.089
	Tm(NO ₃) ₃ .5H ₂ O	0.0010	0.002
	NaNO ₃	0.075	0.88
	NH ₄ F	0.361	9.7
NaGd _{5/6} Yb _{1/6} F ₄ : 0.8% Tm	Gd(NO ₃) ₃ .6H ₂ O	0.2	0.44
	Yb(NO ₃) ₃ .5H ₂ O	0.04	0.89
	Tm(NO ₃) ₃ .5H ₂ O	0.0019	0.004
	NaNO ₃	0.75	0.88
	NH ₄ F	0.361	9.7
NaGd _{5/6} Yb _{1/6} F ₄ : 1.2% Tm	Gd(NO ₃) ₃ .6H ₂ O	0.2	0.44
	Yb(NO ₃) ₃ .5H ₂ O	0.04	0.089
	Tm(NO ₃) ₃ .5H ₂ O	0.003	0.006
	NaNO ₃	0.075	0.88
	NH ₄ F	0.361	9.7
NaGd _{2/3} Yb _{1/3} F ₄ : 0.3% Tm	Gd(NO ₃) ₃ .6H ₂ O	0.2	0.44
	Yb(NO ₃) ₃ .5H ₂ O	0.1	0.22
	Tm(NO ₃) ₃ .5H ₂ O	0.0010	0.002
	NaNO ₃	0.075	0.88
	NH ₄ F	0.361	9.7
NaGd _{2/3} Yb _{1/3} F ₄ : 0.6% Tm	Gd(NO ₃) ₃ .6H ₂ O	0.2	0.44
	Yb(NO ₃) ₃ .5H ₂ O	0.1	0.22
	Tm(NO ₃) ₃ .5H ₂ O	0.0019	0.004
	NaNO ₃	0.075	0.88
	NH ₄ F	0.361	9.7

6.5. Synthesis of lithium-based UCNPs

In this section, we first present the general method of synthesis of lithium-based upconverting nanomaterials (UCNPs). We will describe the detailed synthesis methodology for undoped LiYF₄ nanoparticles, which could be extended to synthesize LiY_{5/6}Yb_{1/6}F₄: $x\% \text{Tm}^{3+}$ by mixing the appropriate amounts of Y, Yb and Tm precursors during the reaction. For this, we prepare two different solutions, A and B. Solution A was prepared by taking equivalent amounts of [Li(TFA)(monoglyme)] (1.76 g, 3.4 mmol) and [Y(TFA)₃(monoglyme)] (0.71 g, 3.40 mmol), in a round bottom schlenk containing 2 ml each of oleic acid (OA) and 1- octadecene (ODE). This solution was maintained at 120 °C for 30 min under an inert atmosphere to obtain a clear homogeneous and transparent solution. Solution B was prepared in another round bottom schlenk containing 3 ml each of OA and ODE. Unless specified otherwise, the ratio of OA and ODE was kept 1:1 for all the

decompositions. This solution was first degassed with constant stirring under argon flow and then heated to 290 °C. Once the temperature became stable at 290 °C, we injected then pre-heated precursor solution A into the decomposition solution B all at once. This solution was kept under constant stirred at 290 °C for 1 h, after which it was gradually cooled down to room temperature under argon flow. The nanocrystals were then precipitated out by adding ethanol and were separated using centrifugation (4500 rpm, 5 min). The powder obtained was washed three times with ethanol to remove any organic impurities and then dried under air at room temperature for 24 hours. The nanocrystals obtained were phase-pure tetragonal (ICDD# 04-007-5501). A similar method was adopted to prepare undoped LiYbF₄ also (ICDD# 04-010-3625). To obtain the host matrix LiYF₄ NCs co-doped with x mol% Yb³⁺ and y mol% Tm³⁺ cations, the derivatives **1**, **3**, **5** and **6** were taken in appropriate amounts and then decomposed simultaneously. The details of each synthesis are summarized in the following tables.

Table 6.5: The amount of precursors used to synthesize undoped LiYF₄ and LiYbF₄ matrices using anhydrous precursors by thermal decomposition at 290°C.

LiYF ₄	LiYbF ₄
[Li(TFA)(monoglyme)] = 1.76 g (3.4 mmol)	[Li(TFA)(monoglyme)] = 1.35 g (2.23 mmol)
[Y(TFA) ₃ (monoglyme)] = 0.71 g (3.40 mmol)	[Yb(TFA) ₃ (monoglyme)] = 0.47 g (2.24 mmol)

6.5.1. Synthesis of Yb³⁺, Tm³⁺ doped LiYF₄ matrices with different synthesis conditions

This section details the synthesis of Yb³⁺ and Tm³⁺ doped LiYF₄ matrices under different synthesis conditions.

6.5.1.1. Influence of ratio of activator ions.

The following table presents the amounts of precursors used for the synthesis of Yb³⁺ and Tm³⁺ doped LiYF₄ matrices. The suitable amount of precursors (as mentioned in Table 6.6) were also decomposed in a 1:1 mixture of 1-octadecene (5 ml) and oleic acid (5 ml).

Table 6.6: The amount of precursors used to synthesize doped LiYF_4 with varying ratio of Tm^{3+} using anhydrous precursors by thermal decomposition at 290°C .

Sample	Reagents	Amount taken (g)	Millimoles taken
$\text{LiY}_{5/6}\text{Yb}_{1/6}\text{F}_4$: 0.4% Tm	[Li(TFA)(monoglyme)]	1.075	5.12
	[Y(TFA) ₃ (monoglyme)]	2.650	5.11
	[Yb(TFA) ₃ (monoglyme)]	0.617	1.02
	[Tm(TFA) ₃ (monoglyme)]	0.017	0.028
$\text{LiY}_{5/6}\text{Yb}_{1/6}\text{F}_4$: 0.8% Tm	[Li(TFA)(monoglyme)]	0.365	1.73
	[Y(TFA) ₃ (monoglyme)]	0.90	1.74
	[Yb(TFA) ₃ (monoglyme)]	0.20	0.34
	[Tm(TFA) ₃ (monoglyme)]	0.010	0.017
$\text{LiY}_{5/6}\text{Yb}_{1/6}\text{F}_4$: 1.2% Tm	[Li(TFA)(monoglyme)]	0.41	1.95
	[Y(TFA) ₃ (monoglyme)]	1.01	1.95
	[Yb(TFA) ₃ (monoglyme)]	0.234	0.39
	[Tm(TFA) ₃ (monoglyme)]	0.016	0.028

6.5.1.2. Influence of ratios of ODE and OA

As discussed in chapter 3, we continued all the following studies for a particular ratio of dopant ions. This section presents the amounts of anhydrous precursors used for the study of $\text{LiY}_{5/6}\text{Yb}_{1/6}\text{F}_4$: 0.4% Tm^{3+} with varying the solvent composition during thermal decomposition (Table 6.7).

Table 6.7: The amount of precursors used to synthesize $\text{LiY}_{5/6}\text{Yb}_{1/6}\text{F}_4$: 0.4% Tm^{3+} in a decomposition mixture containing a different ratio of 1-octadecene and oleic acid.

Precursors	ODE: OA		
	1:1	1:3	3:1
[Li(TFA)(monoglyme)]	0.447 g (2.12 mmol)	0.737 g (3.50 mmol)	0.796 g (3.8 mmol)
[Y(TFA) ₃ (monoglyme)]	1.097 g (2.11 mmol)	1.812 g (3.51 mmol)	1.957 g (3.77 mmol)
[Yb(TFA) ₃ (monoglyme)]	0.255 g (0.42 mmol)	0.422 g (0.70 mmol)	0.455 g (0.75 mmol)
[Tm(TFA) ₃ (monoglyme)]	0.006 g (0.010 mmol)	0.010 g (0.017 mmol)	0.10 (0.017 mmol)

6.5.1.3. Influence of precursor's concentration

For this particular study, the total amount of mixture of oleic acid and 1-octadecene was varied. For the precursor concentration of 0.175 mmol/ml and 0.512 mmol/ml, we took 20 ml and 10 ml of this mixture, respectively (Table 6.8).

Table 6.8: The amount of precursors used for studying the effect of their concentration on the resultant $\text{LiY}_{5/6}\text{Yb}_{1/6}\text{F}_4$: 0.4% Tm^{3+} UCNPs.

Precursor's concentration variation		
Precursors	0.175 mmol/ml	0.512 mmol/ml
[Li(TFA)(monoglyme)]	0.734 g (3.5 mmol)	1.075 g (5.11 mmol)
[Y(TFA) ₃ (monoglyme)]	1.80 g (3.49 mmol)	2.65 g (5.12 mmol)
[Yb(TFA) ₃ (monoglyme)]	0.42 g (0.70 mmol)	0.617 g (1.02 mmol)
[Tm(TFA) ₃ (monoglyme)]	0.010 g (0.017 mmol)	0.17 (0.028 mmol)

6.5.1.4. Influence of decomposition temperature

For this study, we took 5 ml each of 1-octadecene and oleic acid during the thermal decomposition. The following Table 6.9 presents the amounts of precursors used for this temperature-dependent study. It is to be noted that, for the decomposition at higher temperature (such as 295 °C and 315 °C), we took 1.5 equivalent of the lithium complex for the reasons mentioned in chapter 3.

Table 6.9: The amount of precursors used for studying the effect of decomposition temperature on the resultant $\text{LiY}_{5/6}\text{Yb}_{1/6}\text{F}_4$: 0.4% Tm^{3+} UCNPs.

Decomposition temperature variation				
Precursors	270°C	290°C	295°C	315°C
[Li(TFA)(monoglyme)]	0.606 g (2.88 mmol)	0.447 g (2.12 mmol)	0.988 g (4.70 mmol)	0.66 g (3.14 mmol)
[Y(TFA) ₃ (monoglyme)]	1.49 g (2.87 mmol)	1.097 g (2.11 mmol)	1.626 g (3.13 mmol)	1.08 g (2.09 mmol)
[Yb(TFA) ₃ (monoglyme)]	0.346 g (0.57 mmol)	0.255 g (0.42 mmol)	0.382 g (0.635 mmol)	0.252 g (0.42 mmol)
[Tm(TFA) ₃ (monoglyme)]	0.008 g (0.014 mmol)	0.006 g (0.010 mmol)	0.009 g (0.016 mmol)	0.006 g (0.010 mmol)

6.5.1.5. Influence of reaction time

The amount of precursors used for studying the effect of reaction time on $\text{LiY}_{5/6}\text{Yb}_{1/6}\text{F}_4$: 0.4% Tm^{3+} nanoparticles is presented in Table 6.10. A total of 10 ml solution mixture of 1-octadecene and oleic acid is used for decomposition.

Table 6.10: The amount of precursors used for studying the effect of time of decomposition on the resultant $\text{LiY}_{5/6}\text{Yb}_{1/6}\text{F}_4$: 0.4% Tm^{3+} UCNPs.

Reaction time influence		
Precursors	Amount taken (g)	Millimoles taken
[Li(TFA)(monoglyme)]	0.726	3.45
[Y(TFA) ₃ (monoglyme)]	1.785	3.44
[Yb(TFA) ₃ (monoglyme)]	0.415	0.690
[Tm(TFA) ₃ (monoglyme)]	0.010	0.017

6.6. Synthesis of UCNPs-TiO₂ nanocomposites

6.6.1. Oleic acid-modified TiO₂@UCNPs nanocomposites

For this study, we started with the modification of titanium precursor with oleic acid. In a round bottom schlenk, we took 10 mmol of oleic acid (OA) and heated it to 120 °C in an inert atmosphere for one hour. After 1 hour, we cooled this solvent up to 100 °C. and injected 2 mmol (0.6 ml) of titanium isopropoxide (TIP) under vigorous stirring. This solution is then brought to room temperature with continuous stirring in an inert atmosphere. The obtained pale-yellow solution of titanium oleate was dissolved in 5 ml of anhydrous hexane. This resultant solution was then injected into another solution containing 8 mmol of core UCNPs in 7 ml of isopropanol and stirred the resulting solution for 20 minutes. This was followed by the addition of a hydrolysis mixture of 0.02 ml acetic acid, 0.14 ml H₂O and 1.9 ml isopropanol, which resulted in a white solution. After stirring for about 40 minutes, the obtained transparent sol solution was heated for 2 hours at 98 °C. The obtained TiO₂@LiY_{5/6}Yb_{1/6}F₄: 0.4%Tm³⁺ core-shell NPs were isolated by centrifugation, washed three times with ethanol and then dried in the open air for further use.

6.6.2. Aminoalcohols modified TiO₂@UCNPs nanocomposites

We followed a modified sol-gel approach for the synthesis of UCNPs-TiO₂ nanocomposites using amino alcohols. Two different solutions were prepared. In solution A, we prepared surface-modified UCNPs by treating 0.020 g (10 mmol) of UCNPs with 0.23 ml mdeaH₂ under continuous stirring in 10 ml of chloroform. Solution B contains 0.6 ml (2 mmol) of titanium isopropoxide (TIP) mixed with 0.23 ml of mdeaH₂ ligand in 10 ml of isopropanol. After 10 minutes of stirring, solution A (containing UCNPs) was taken by a syringe under argon flow and was added to solution B (containing titanium isopropoxide) under magnetic stirring at 750 rpm. Then a hydrolysis mixture of 0.1: 2.7: 2 ml

acetic acid (CH_3COOH), deionized water (H_2O) and isopropanol (iPrOH), respectively, was added dropwise under vigorous stirring to the above mixture resulting in a suspended solution which was further refluxed for 2 h under constant stirring to produce a core-shell solution. This final product was washed with ethanol and centrifuged three times at 5000 rpm to isolate UCNPs- TiO_2 nanocomposites. The precipitate was then dried in the air for 24 h. We used the same protocol for the synthesis of UCNPs- TiO_2 nanocomposites capped with dmeaH ligand also. The only difference was that we used chloroform instead of isopropanol as a solvent.

6.6.3. UCNPs embedded TiO_2 metallogels

We synthesized transparent metallogel of TiO_2 by hydrolysing $\text{Ti}(\text{OEt})_4$ with $\text{H}_2\text{O}/\text{EtOH}$ hydrolysis solution ($h=2$) in the presence of HCl ($R = 0.04$). As the hydrolysis rate of $\text{Ti}(\text{OEt})_4$ is high, the formation of TiO_2 can be chemically controlled by adding HCl .⁸ For the preparation of pure TiO_2 , we prepared 1M solution of titanium ethoxide ($\text{Ti}(\text{OEt})_4$) in anhydrous ethanol (EtOH). 2 ml solution of 1M $\text{Ti}(\text{OEt})_4$ is then mixed with 0.1 ml of 1M HCl solution. After 30 minutes of this addition, a transparent solid gel-like network is formed. We dried this gel at room temperature to obtain a powder. For the preparation of UCNPs- TiO_2 doped transparent gel, we chose a different ratio of UCNPs to be added in the initial 1M solution of titanium ethoxide ($\text{Ti}(\text{OEt})_4$). The remaining process is similar to used for the preparation of pure TiO_2 gel.

6.7. References

- (1) CrysAlis Pro | Rigaku Global Website <https://www.rigaku.com/products/smc/crysalis>.
- (2) Clark, R. C.; Reid, J. S. The Analytical Calculation of Absorption in Multifaceted Crystals. *Acta Crystallographica Section A* **1995**, *51* (6), 887–897. <https://doi.org/10.1107/S0108767395007367>.
- (3) Sheldrick, G. M. *SHELXT* – Integrated Space-Group and Crystal-Structure Determination. *Acta Crystallogr A Found Adv* **2015**, *71* (1), 3–8. <https://doi.org/10.1107/S2053273314026370>.
- (4) Dolomanov, O. V.; Bourhis, L. J.; Gildea, R. J.; Howard, J. a. K.; Puschmann, H. OLEX2: A Complete Structure Solution, Refinement and Analysis Program. *J Appl Cryst* **2009**, *42* (2), 339–341. <https://doi.org/10.1107/S0021889808042726>.
- (5) Sheldrick, G. M. Crystal Structure Refinement with SHELXL. *Acta Cryst C* **2015**, *71* (1), 3–8. <https://doi.org/10.1107/S2053229614024218>.
- (6) Mishra, S.; Daniele, S.; Ledoux, G.; Jeanneau, E.; Joubert, M.-F. Heterometallic Na–Y(Ln) Trifluoroacetate Diglyme Complexes as Novel Single-Source Precursors for Upconverting NaYF₄ Nanocrystals Co-Doped with Yb and Er/Tm Ions. *Chem. Commun.* **2010**, *46* (21), 3756–3758. <https://doi.org/10.1039/B921474G>.
- (7) Mishra, S.; Ledoux, G.; Jeanneau, E.; Daniele, S.; Joubert, M.-F. Novel Heterometal–Organic Complexes as First Single Source Precursors for Up-Converting NaY(Ln)F₄ (Ln = Yb, Er, Tm) Nanomaterials. *Dalton Trans.* **2012**, *41* (5), 1490–1502. <https://doi.org/10.1039/C1DT11070E>.
- (8) Livage, J.; Henry, M.; Sanchez, C. Sol-Gel Chemistry of Transition Metal Oxides. *Progress in Solid State Chemistry* **1988**, *18* (4), 259–341. [https://doi.org/10.1016/0079-6786\(88\)90005-2](https://doi.org/10.1016/0079-6786(88)90005-2).

Chapter 7: Conclusions and perspectives

7.1. Conclusions

To use solar energy for real applications, the main objective of this thesis was to design materials that allow the conversion of the solar photons that are not used by classical TiO₂-based photocatalyst to useful ones. We addressed this objective using an upconversion-based approach: by combining upconverting nanomaterial with TiO₂.

Structure-wise, we broadly divided this thesis into two parts. The first part emphasizes the enhancement of upconversion emission intensity, whereas the second part presents the ideas and strategies of incorporation of upconverting nanostructures into titania to synthesize novel composite catalysts for NIR-induced photocatalytic applications.

In the scope of this thesis, initially, a detailed emphasis has been given to the necessity and usefulness along with the synthetic techniques for anhydrous precursors to prepare upconverting nanomaterials based on MLnF₄ (M = Li, Na; Ln = Y, Gd) matrices. In comparison with the widely used hydrous precursors, these precursors possess definite advantages concerning the higher upconversion emission from identically doped nanoparticles. The detrimental role of OH⁻ ions on the upconversion performance is addressed by comparing quantitative study of emitted upconversion light. The upconversion quantum efficiency of 1.8% and 0.04% of the NaGd_{5/6}Yb_{1/6}F₄: 0.8% Tm³⁺ UCNPs synthesized using anhydrous and hydrous precursors, respectively, further justified that the anhydrous method of synthesizing UCNPs is indeed significantly better than those prepared *via* hydrous precursors.

After establishing in sodium-based UCNPs that to get brighter upconverting nanoparticles, the key is to avoid OH⁻ ions during the reactions as much as possible, we switched to lithium-based UCNPs, which are more effective in the absorption range of TiO₂ i.e., UV-region. To achieve this objective, we first prepared novel anhydrous molecular precursors directly from oxides in a one-pot reaction and characterized them thoroughly using physicochemical techniques such as single-crystal X-ray structure, Thermo-gravimetric analysis (TGA), Fourier Transform Infrared Spectroscopy (FTIR), etc. . These well-defined anhydrous molecular precursors were then decomposed to obtain upconverting LiYF₄:xYb³⁺, γTm³⁺ NPs in a variety of different conditions. The influences of reaction conditions such as the ratio of solvents, precursor's concentration, reaction time, temperature, etc. over crystalline phase, size, shape, morphology and upconverting properties of nanoparticles were

systemically studied. This contributed enormously to our overall understanding of various aspects of these UCNPs, and in particular, the mechanism of formation of diamond and spherical shaped LiYF_4 : $x\text{Yb}^{3+}$, $y\text{Tm}^{3+}$ UCNPs. Another sub-objective of this thesis was to determine the upconversion efficiency both qualitatively and quantitatively. In this regard, we compared the upconversion of these nanocrystals with their bulk counterpart and further prioritized the need for anhydrous precursors for synthesizing higher quality upconverting nanoparticles.

To understand how this upconversion-based approach is beneficial for improving the photocatalytic activity of the catalyst, we presented a thorough study to show that this method is fully suitable for solar light photocatalysis. We demonstrated, using excited state excitation spectroscopic studies, that the process of broad light to UV upconversion is the addition of one IR and one visible photon and not necessarily a successive addition of IR photons which, in the literature, is generally considered a mechanism for such upconversion. In other words, we showed that under broadband and low power excitation it becomes a first-order process for the IR photons. This study essentially made the necessary ground for the use of upconverting nanoparticles based approach for NIR-induced photocatalysis.

Finally, we synthesized the nanocomposites of the most efficient $\text{LiY}_{5/6}\text{Yb}_{1/6}\text{F}_4$: 0.4% Tm^{3+} UCNPs with TiO_2 . We used two different approaches for nanocomposite formation, namely, core-shell and transparent metallogel strategy. We performed some preliminary upconversion and photocatalytic studies on these nanocomposites and showed that the metallogel strategy to synthesize UCNPs- TiO_2 nanocomposite is a good way to obtain nanocomposites with high surface area and uniform distribution making them a suitable candidate for photocatalytic applications.

Overall, we presented strategies and materials to improve the upconversion emission of nanoparticles by mainly focusing on the anhydrous synthetic methods and, later on, we investigated the methods to obtain UCNPs- TiO_2 nanocomposites for their application in NIR-induced photocatalysis.

7.2. Perspectives

The above-presented results opened up a wide range of possibilities for many lateral projects which were not possible to be completed within the stipulated time of the project. Some of these are presented below:

7.2.1. Optimization of energy transfer between UCNPs and TiO_2 for efficient photocatalysis

For photocatalytic and some biological applications, the energy transfer process becomes very crucial. In most such studies the energy transfer process is partly based on non-radiative transfer, but often also contains contributions from reabsorption.^{1,2} For example, In photocatalytic processes, the upconverting nanoparticles need to transfer the upconverted UV to the classical photocatalyst

(such as TiO_2) so that its performance can be enhanced. This energy transfer can rely on radiative transfer (re-absorption) or non-radiative energy transfer. The former is inefficient and competitive with many other non-radiative processes. As the transfer of excitation from UCNPs to the photocatalyst is highly dependent on how they interact,³ this aspect of energy transfer could be addressed by optimizing the distance between the upconverting nanoparticle and photocatalyst.

In this regard, we designed an experiment to have a systematic study of the transfer of energy from single layers of GdF_3 and TiO_2 grown using the atomic layer deposition technique (ALD). We chose this system because the Gd^{3+} excited states show good resonance with the energy band of TiO_2 . These studies were performed in collaboration with Dr Per-Anders Stensby Hansen from the Department of Chemistry, University of Oslo, who welcomed me for three weeks in his team. During this study, we varied the separation (from 1 nm to 4 nm) distance between these monolayers by introducing the buffer Y layer (which is optically inactive). These samples were denoted as Y-G- Y_x - TiO_2 , where x is the separation distance between these layers in nm. The Experimental setup and representative figure are shown here (Figure 7.1).

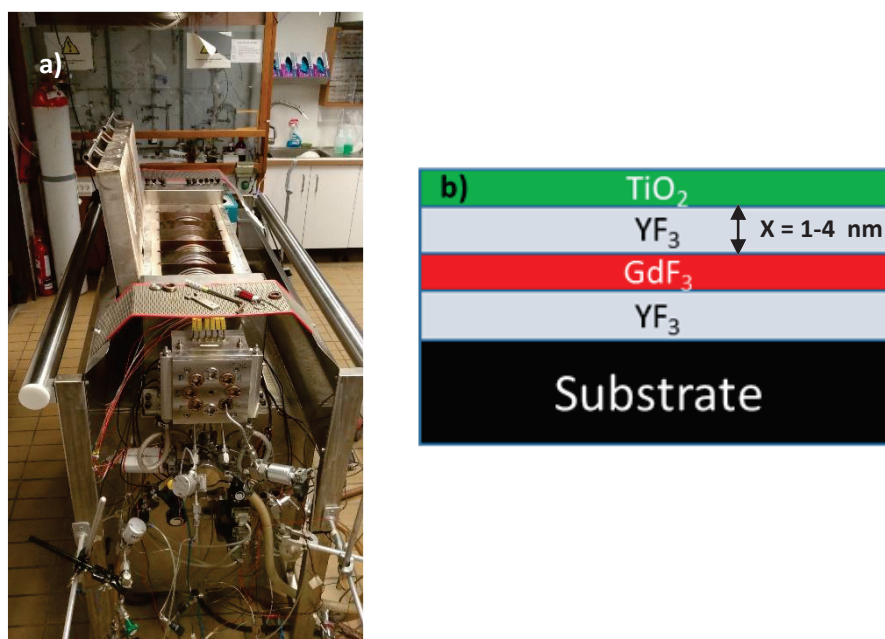


Figure 7.1: Experimental setup a) and representative figure for the different sample prepared by varying the thickness of the yttrium layer using atomic layer deposition (ALD) technique b).

Then to observe the energy transfer between them we performed some basic fluorescence spectroscopic measurements on a homemade apparatus. The detailed experimental setup is described as follows. The deposited thin films were kept with GdF_3 side facing to the illumination from an optical

parametric oscillator (OPO) from EKSPLA (model NT230-50-SH) with a fixed repetition rate of 50 Hz and a pulse width of 3 ns. The spot size has a 5 mm diameter on the sample with a Gaussian intensity distribution. The emitted light from the sample is collected by an optical fibre connected to a Jobin-Yvon TRIAX320 monochromator equipped with a cooled CCD detector. At the entrance of the monochromator, various long and bandpass filters were chosen to eliminate the excitation light.

We then excited these samples with 272.5 nm excitation (corresponding to ${}^6I_1 \rightarrow {}^8S_{7/2}$ transition in Gd^{3+}) with GdF_3 side facing upwards and recorded the emission spectra (Figure 7.2). Interestingly, the samples with different buffer layer thickness showed different emission intensities. As expected, the samples with greater separation between GdF_3 and TiO_2 showed a higher emission peak at 312 nm, corresponding to ${}^6P_{7/2} \rightarrow {}^8S_{7/2}$ transition in Gd^{3+} transition. When the separation between these layers is 1 nm, the transfer of energy from Gd to the nearby Ti layer is more probable compared to when the distance is 4 nm (see Figure 7.2). Hence, we can say that the more separated these layers are the less will be the probability of transfer of energy from Gd to Ti layer, which has been also been shown theoretically (*via* modelling the energy transfer process between these ions in similar fluoride-based systems) by Ledoux et al.³ in 2018.

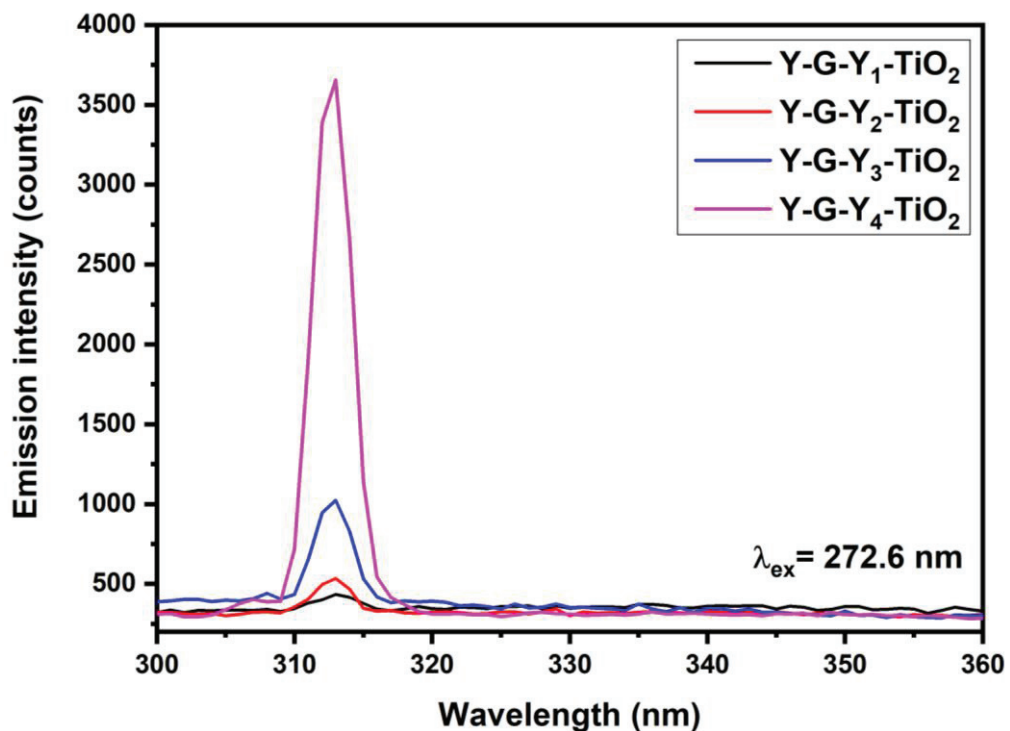


Figure 7.2: Emission spectra for different thin film samples with varying separation layer (YF_3) thickness.

From this study, we can speculate that further exploration of the system comprising Gd^{3+} and Tm^{3+} ions (e.g. $NaGdF_4: Yb^{3+}, Tm^{3+}$) and their composite with TiO_2 would open a new gateway to

understanding the energy transfer mechanism between UCNPs and photocatalysts, which indeed increase our understanding towards solar-driven photocatalysis. Unfortunately because of the COVID pandemic, I could not return to Oslo to pursue this study but it would be interesting in the future to study more thoroughly the energy transfer between the different component of our system to optimize it.

7.2.2. Photocatalytic experiments under direct sunlight

In the real world situation, such as degradation of organic pollutants or water splitting, the photocatalyst is needed to be robust as well as optically efficient. In this regard, heterogeneous photocatalysis has proved to be an efficient tool. The performance of classical and most widely used photocatalyst, TiO₂, which works only under UV irradiation (due to its large bandgap (~3.2 eV for anatase)), could be enhanced by the incorporation of upconverting nanoparticles with such photocatalyst. Some preliminary (dye degradation) results based on this strategy has already been shown in chapter 5, where we evaluated the performance of such modified catalyst under only IR irradiation.

From a future perspective, it would be interesting to extend these studies step-by-step, by performing dye degradation under only UV, only visible, and then complete solar spectrum. This would give us an understanding of how the process of upconversion is accelerating the remediation of environmental contaminants under sunlight. We tested our samples for photocatalytic dye degradation under only visible light (420 – 780 nm) using UVIRCUT 420 filter on a standard xenon lamp from CEALIGHT CEL-S500 (which has spectral distribution from 300 nm to 2500 nm). In Figure 7.3, the change in concentration of methylene blue with only TiO₂ and 10% mixing ratio of UCNPs in TiO₂ is represented. Here we observed a significant reduction (~35%) in the concentration of methylene blue for the 10% UCNPs-TiO₂ sample. These and the results presented in chapter 5, supports the idea of having an overall enhanced photocatalytic performance under the full solar spectrum.

It would also be interesting to introduce in the above UCNPs-TiO₂ photocatalyst a luminescent molecule that absorbs in the near IR region (e.g., IR-806), which would improve further the efficiencies of these photocatalysts by acting as an antenna to widen the absorption range. The metallo gel strategy may be useful in achieving this as the luminescent molecule can easily be incorporated during the gelation stage.⁴

Furthermore, in a broad view, these UCNPs-TiO₂ composite could also serve as an efficient photocatalyst for water splitting application. It was originally planned to be included in this thesis but it had to be postponed for the future because of a delay in the delivery of a gas chromatograph.

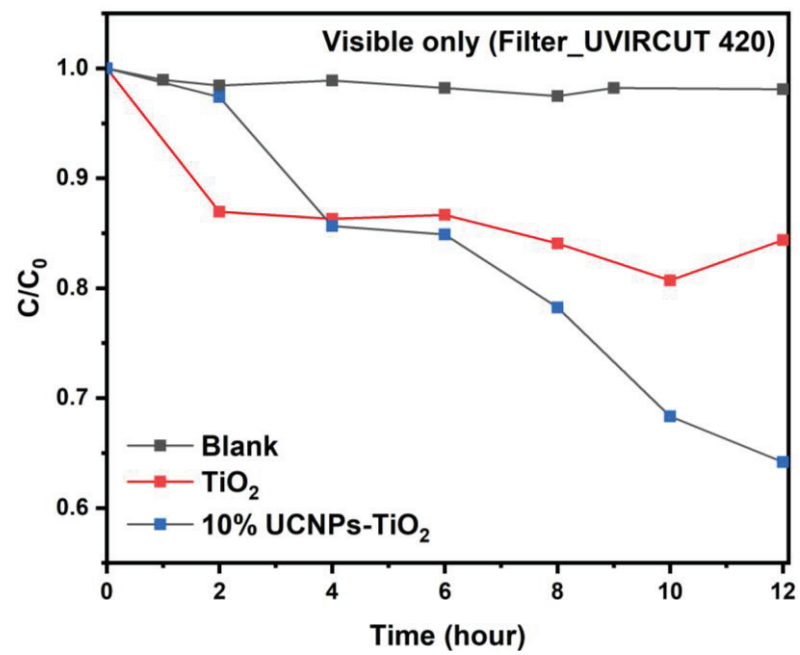


Figure 7.3: Photodegradation study of methylene shown by the relative change in concentration blue using Xe lamp under visible irradiation band (420 - 780 nm)

7.3. References

- (1) Lahtinen, S.; Wang, Q.; Soukka, T. Long-Lifetime Luminescent Europium(III) Complex as an Acceptor in an Upconversion Resonance Energy Transfer Based Homogeneous Assay. *Anal. Chem.* **2016**, *88* (1), 653–658. <https://doi.org/10.1021/acs.analchem.5b02228>.
- (2) Wang, Y.; Liu, K.; Liu, X.; Dohnalová, K.; Gregorkiewicz, T.; Kong, X.; Aalders, M. C. G.; Buma, W. J.; Zhang, H. Critical Shell Thickness of Core/Shell Upconversion Luminescence Nanoplatform for FRET Application. *J. Phys. Chem. Lett.* **2011**, *2* (17), 2083–2088. <https://doi.org/10.1021/jz200922f>.
- (3) Ledoux, G.; Amans, D.; Joubert, M.-F.; Mahler, B.; Mishra, S.; Daniele, S.; Dujardin, C. Modeling Energy Migration for Upconversion Materials. *J. Phys. Chem. C* **2018**, *122* (1), 888–893. <https://doi.org/10.1021/acs.jpcc.7b10113>.
- (4) Chen, G.; Damasco, J.; Qiu, H.; Shao, W.; Ohulchanskyy, T. Y.; Valiev, R. R.; Wu, X.; Han, G.; Wang, Y.; Yang, C.; Ågren, H.; Prasad, P. N. Energy-Cascaded Upconversion in an Organic Dye-Sensitized Core/Shell Fluoride Nanocrystal. *Nano Lett.* **2015**, *15* (11), 7400–7407. <https://doi.org/10.1021/acs.nanolett.5b02830>.

Appendix A: Research output related to this thesis

A1. Publications

(1) Purohit, B.; Guyot, Y.; Amans, D.; Joubert, M.-F.; Mahler, B.; Mishra, S.; Daniele, S.; Dujardin, C.; Ledoux, G. Multicolor Solar Absorption as a Synergetic UV Upconversion Enhancement Mechanism in $\text{LiYF}_4: \text{Yb}^{3+}, \text{Tm}^{3+}$ Nanocrystals. *ACS Photonics* **2019**, *6* (12), 3126–3131. <https://doi.org/10.1021/acsp Photonics.9b01151>.

(2) Purohit, B.; Amans, D.; Guyot, Y.; Mahler, B.; Joubert, M.-F.; Dujardin, C.; Daniele, S.; Ledoux, G.; Mishra, S. Quest to Enhance Up-Conversion Efficiency: A Comparison of Anhydrous vs. Hydrated Synthesis of $\text{NaGdF}_4: \text{Yb}^{3+}$ and Tm^{3+} Nanoparticles. *Materials Today Chemistry* **2020**, *17*, 100326. <https://doi.org/10.1016/j.mtchem.2020.100326>.

A2. Oral Presentations

1. Enhanced upconversion efficiency in $\text{LiYF}_4: \text{Yb}^{3+}, \text{Tm}^{3+}$ nanocrystals by using anhydrous molecular precursors.

Bhagyesh Purohit, Shashank Mishra, Gilles Ledoux, Erwann Jeanneau, Yannick Guyot, Benoit Mahler, David Amans, Marie-France Joubert, Christophe Dujardin, Stephane Daniele

MSE 2020 - Materials Science and Engineering (22-25 September) from Deutsche Gesellschaft für Materialkunde e.V., Cologne, Germany.

2. Precursor-directed synthesis of upconverting $\text{LiYF}_4: \text{Yb}^{3+}, \text{Tm}^{3+}$ nanoparticles and their composites designed for near infra-red driven photocatalysis.

Bhagyesh Purohit, Shashank Mishra, Gilles Ledoux, Erwann Jeanneau, Yannick Guyot, Benoit Mahler, David Amans, Marie-France Joubert, Christophe Dujardin, Stephane Daniele,

8th International Workshop on Photoluminescence of Rare-Earth PRE'19, September 2019, Nice, France.

A3. Poster presentation

1. Poster: G. Ledoux, B. Purohit, S. Mishra, D. Amans, S. Daniele, C. Dujardin, Y. Guyot, M. F. Joubert, B. Mahler “HARVESTING LIGHT THROUGH UPCONVERSION FOR PHOTOCATALYSIS”, **UPCON 2018**, 2-5th April 2018, Valencia, Espagne

2. Poster: B. Purohit, G. Ledoux, S. Mishra, D. Amans, S. Daniele, C. Dujardin, Y. Guyot, M. F. Joubert, B. Mahler “HARVESTING LIGHT THROUGH UPCONVERSION FOR PHOTOCATALYSIS”, **Journée de printemps de la SCF**, 11th June 2018, Lyon, France.

3. Participation in CCRA: Journée de coordination en Rhone-Alpes – Grenoble, France April 4th, 2019.

A4. Awards and Grants

Received research visit grant for 1 month at Department of Chemistry, University of Oslo, Norway in May 2019.